Development of a Three-Dimensional Numerical Model for Sediment Transport and Morphological Evolution : Application to the Study of Scouring around Hydraulic Structures

Matthias Renaud

▶ **To cite this version:**

Matthias Renaud. Development of a Three-Dimensional Numerical Model for Sediment Transport and Morphological Evolution : Application to the Study of Scouring around Hydraulic Structures. Environmental Sciences. Université Grenoble Alpes [2020-..], 2025. English. ⟨NNT : 2025GRALU031⟩. ⟨tel-05567679⟩

HAL Id: tel-05567679

https://theses.hal.science/tel-05567679v1

Submitted on 26 Mar 2026

HAL is a multi-disciplinary open access archive for the deposit and dissemination of scientific research documents, whether they are published or not. The documents may come from teaching and research institutions in France or abroad, or from public or private research centers.

L'archive ouverte pluridisciplinaire **HAL**, est destinée au dépôt et à la diffusion de documents scientifiques de niveau recherche, publiés ou non, émanant des établissements d'enseignement et de recherche français ou étrangers, des laboratoires publics ou privés.

HAL Authorization

THÈSE

Pour obtenir le grade de

DOCTEUR DE L'UNIVERSITÉ GRENOBLE ALPES

École doctorale : STEP - Sciences de la Terre de l'Environnement et des Planètes
Spécialité : Sciences de la Terre et de l'Environnement
Unité de recherche : Laboratoire des Ecoulements Géophysiques et Industriels

Développement d'un modèle numérique tridimensionnel de transport sédimentaire et d'évolution morphologique : Application à l'étude de l'affouillement autour de structures hydrauliques

Development of a Three-Dimensional Numerical Model for Sediment Transport and Morphological Evolution: Application to the Study of Scouring around Hydraulic Structures

Présentée par :

Matthias RENAUD

Direction de thèse :

Julien CHAUCHAT Directeur de Recherche, INRAE Lyon-Grenoble Auvergne-Rhône-Alpes	Directeur de thèse
Cyrille BONAMY Expert calcul scientifique,	Co-encadrant de thèse
Olivier BERTRAND Artelia	Co-encadrant de thèse

Rapporteurs :

David FUHRMAN
FULL PROFESSOR, Danmarks Tekniske Universitet
Ivana VINKOVIC
PROFESSEURE DES UNIVERSITES, Université Lyon 1 - Claude Bernard

Thèse soutenue publiquement le **5 décembre 2025**, devant le jury composé de :

Eric BARTHELEMY, PROFESSEUR DES UNIVERSITES, Université Grenoble Alpes	Président
Julien CHAUCHAT, DIRECTEUR DE RECHERCHE, INRAE Lyon-Grenoble Auvergne-Rhône-Alpes	Directeur de thèse
David FUHRMAN, FULL PROFESSOR, Danmarks Tekniske Universitet	Rapporteur
Ivana VINKOVIC, PROFESSEURE DES UNIVERSITES, Université Lyon 1 - Claude Bernard	Rapporteure
Benoît CAMENEN, DIRECTEUR DE RECHERCHE, INRAE Lyon-Grenoble Auvergne-Rhône-Alpes	Examinateur
Magali JODEAU, INGENIEURE DOCTEURE, EDF	Examinatrice
Stéphane POPINET, DIRECTEUR DE RECHERCHE, CNRS délégation Paris Centre	Examinateur

Invités :

Cyrille Bonamy
INGENIEUR DE RECHERCHE, Laboratoire des Écoulements Géophysiques et Industriels
Olivier Bertrand
INGENIEUR DOCTEUR, ARTELIA

Contents

Abbreviations and symbols **9**

Introduction **19**
Example study, the Dordogne viaduct 20
Objectives and methodology 21
Outline of the thesis 23

1 State of the art review **24**
1.1 Flow and scour around a pier 24
1.2 Experimental study of the scour process 28
1.3 Pier scour formulas for engineering studies 31
1.4 Sediment transport modeling and methods 33
1.5 Hydrodynamics processes 37
1.5.1 Navier-Stokes equations 37
1.5.2 The law of the wall 43
1.5.3 Wall boundary condition for turbulence 47
1.6 Sediment transport modeling 50
1.6.1 Threshold of motion 51
1.6.2 Entrainment of sediments 54
1.6.3 Saturation of the bedload flux 56
1.7 Conclusion 58

2 Model description **59**
2.1 Model mathematical description 59
2.2 Hydrodynamics and turbulence 59
2.2.1 Turbulence models 60
2.2.2 Wall boundary condition for turbulent quantities 64
2.3 bedload transport 65
2.4 Suspended transport 71
2.4.1 Erosion/Deposition condition 73
2.5 Morphology evolution 76
2.6 Numerical methods 76

2.6.1 Finite Volume Method . . . 78
2.6.2 Advection schemes . . . 81
2.6.3 Pressure-velocity coupling . . . 82
2.6.4 Exner equation and finite-area . . . 85
2.7 Conclusion . . . 89

3 Model validation **90**
3.1 Idealized dune transport . . . 90
3.2 Settling of particles in a quiescent fluid . . . 97
3.3 Suspension under equilibrium conditions . . . 99
3.4 Development of the suspension . . . 106
3.5 Deposition and mass conservation . . . 111
3.6 Erosion in a channel . . . 114
3.7 Conclusion . . . 117

4 Dune migration **118**
4.1 2D dune migration in a straight flume . . . 118
4.1.1 Experimental configuration . . . 119
4.1.2 Numerical configuration . . . 122
4.1.3 Hydrodynamics . . . 125
4.1.4 Morphological evolution . . . 130
4.1.5 Other relevant fitting parameters . . . 140
4.1.6 Mass loss scenario . . . 143
4.2 Formation and migration of a subaqueous barchan . . . 145
4.2.1 Experimental setup . . . 146
4.2.2 Numerical configuration . . . 147
4.2.3 Results and discussion . . . 149
4.3 Conclusion . . . 150

5 Scour around a cylinder **153**
5.1 Description of the experimental and numerical configurations . . . 153
5.1.1 Rigid bed experiments . . . 154
5.1.2 Numerical setup, rigid bed simulations . . . 155
5.1.3 Numerical setup, live-bed simulations . . . 159
5.2 Simulation of the flow around a wall mounted cylinder . . . 161
5.3 Simulation of the scour process . . . 171
5.4 Conclusion . . . 174

Conclusion and perspectives **177**

List of Figures

1 Bridge crossing the Saint-Étienne river. . . . 20
2 Physical model of the Dordogne bridge 21
3 Numerical study of scour around a pier 22

1.1 Flow and scour around a cylindrical pile 25
1.2 Horseshoe vortex system. . . . 26
1.3 Coherent structures around piers 27
1.4 Flow regimes, cylinder in steady current 28
1.5 Strouhal number as a function of the Reynolds number 29
1.6 Scour around an vertical cylinder in a steady flow 30
1.7 Vortices in a scour hole issued obtained with LES 31
1.8 Equilibrium scour hole for cohesive sediments 32
1.9 Sediment transport models and scales 34
1.10 CFD-DEM simulations 35
1.11 Illustration of turbulence 39
1.12 Turbulent boundary layer, fluctuations and averaged fields 41
1.13 Boundary layer flow above a smooth surface 43
1.14 Turbulent flows over rough surfaces 46
1.15 B as a function of rough Reynolds number 46
1.16 Bedload and suspended load sediment transport 51
1.17 Forces exerted on a spherical particle on the sediment bed 52
1.18 Threshold of motion on a flat bed 53
1.19 Schematic of the saturation length 57

2.1 Critical Shields number formulas 67
2.2 Angles definition for slope correction 68
2.3 Effect of slope on Shields and bedload 69
2.4 Bedload formulas in *sedExnerFoam* 70
2.5 Terminal settling velocity formulas 72
2.6 Hindrance models available in *sedExnerFoam* 73
2.7 Schematic of a channel flow with suspended sediments 74
2.8 Extrapolation of the reference concentration 75
2.9 Model flow chart 77

2.10 Polyhedral control volume . . . 78
2.11 Representation of the basic advection schemes . . . 82
2.12 Polygonal control area . . . 86
2.13 Projection of the finite-area mesh . . . 86
2.14 Dual mesh decomposition . . . 88

3.1 Schematic of the idealized dune transport case. . . . 91
3.2 Characteristic lines . . . 92
3.3 Idealized dune mesh . . . 93
3.4 Idealized dune morphological evolution . . . 94
3.5 Effect of avalanche model on idealized dune migration . . . 94
3.6 Dune migration sensitivity to numerical schemes . . . 95
3.7 Idealized dune sensitivity to schemes and mesh resolution . . . 96
3.8 Settling of particles, position of upper/lower interfaces . . . 98
3.9 Volume fraction profiles during settling . . . 100
3.10 Suspended sediment at equilibrium with classical closure . . . 103
3.11 Effect of fine grid resolution on suspended sediments . . . 103
3.12 Effect of near bed additional diffusivity for suspended sediments . . . 104
3.13 Suspended sediments profiles, comparison with experiments . . . 105
3.14 Suspension development at the transition from rigid to sediment bed . . . 106
3.15 Isolines of concentration, idealized flow conditions . . . 108
3.16 Isolines of concentration . . . 110
3.17 Relaxation toward a Rouse profile . . . 110
3.18 Mass conservation in 1D sedimentation case . . . 112
3.19 Mesh motion during sedimentation in an hourglass . . . 113
3.20 Hourglass deposition, mass conservation . . . 114
3.21 Erosion in a channel . . . 116

4.1 Dune migration experimental setup . . . 119
4.2 Schematic of dune characteristics definition . . . 120
4.3 Stationary regime experiment . . . 121
4.4 Mass lost scenario experiment . . . 121
4.5 Undisturbed velocity profiles . . . 123
4.6 Example of mesh for dune migration . . . 124
4.7 Initial dune geometry . . . 125
4.8 Effect of bed roughness on flow profiles . . . 126
4.9 Mesh resolution effect for different roughness conditions . . . 127
4.10 Flow over a dune . . . 128
4.11 Effect of mesh resolution and bed roughness BC on friction velocity . . . 129
4.12 Exner instabilities at the crest of a dune . . . 131
4.13 Bed level temporal evolution for different bed roughness conditions . . . 132
4.14 Dune morphological evolution, influence of bottom roughness . . . 132
4.15 Analysis of the causes the mechanisms driving bedload transport . . . 133
4.16 Effect of suspended load on the dune migration . . . 134

4.17 Bedload equilibrium upstream of the dune's crest . . . 134
4.18 Effect of advection scheme on dune migration . . . 135
4.19 Upwind scheme effect on dune migration . . . 135
4.20 Dune morphological response to maximum bedload position . . . 137
4.21 Rough boundary condition effect on dune migration . . . 137
4.22 Effect of saturation length in rough bed cases . . . 138
4.23 Effect of saturation length in smooth bed cases . . . 139
4.24 Relaxation of the bedload flux at the crest of a dune . . . 139
4.25 Stationary regime dune migration, flow streamlines visualization . . . 141
4.26 Bed elevation with and without suspension . . . 141
4.27 Dune morphological characteristics in time . . . 142
4.28 Mass loss, streamlines and suspended load . . . 144
4.29 Dune mass over time . . . 145
4.30 Sketch of a barchan dune . . . 146
4.31 Satellite view of barchans . . . 147
4.32 Top views of subaqueous barchans in a channel . . . 148
4.33 Barchan computational domain . . . 149
4.34 Inlet profiles, barchan simulation . . . 150
4.35 Barchan migration, bedload transport only . . . 151

5.1 Computational domain for rigid bed cases . . . 156
5.2 Undisturbed velocity profiles at inlet, smooth and rough bed cases . . . 156
5.3 Flow surface streamlines around a cylinder . . . 157
5.4 Test setup scour experiment . . . 158
5.5 Computational domain for live bed simulation . . . 160
5.6 Inlet profiles for live bed case . . . 160
5.7 Coherent structures around cylinder . . . 162
5.8 Horseshoe vortex streamlines . . . 163
5.9 Smooth bed, stream-wise velocity component . . . 164
5.10 Smooth bed, vertical velocity component . . . 164
5.11 Rough bed, stream-wise velocity component . . . 166
5.12 Rough bed, vertical velocity component . . . 167
5.13 Velocity probes, smooth bed case . . . 168
5.14 Velocity probes, rough bed case . . . 169
5.15 Shear stress amplification upstream of pile, smooth bed case . . . 170
5.16 Shear stress amplification upstream of pile, rough bed case . . . 170
5.17 Bed shear stress amplification around a cylinder . . . 171
5.18 3D visualization of scour around a cylinder . . . 172
5.19 Exner instabilities in scour hole . . . 173
5.20 Avalanche in the horseshoe vortex . . . 174
5.21 Initial Scour evolution . . . 175
5.22 Maximum scour depth temporal evolution . . . 175
5.23 3D view of scour around various geometries . . . 176

5.24 Suspension at equilibrium, mesh sensitivity 182
5.25 Mesh decomposition 183

List of Tables

2.1 Turbulence models in *OpenFOAM* 61
2.2 Turbulence models coefficients 62
2.3 Blending functions for ω 64
2.4 Wall functions for rough walls 66
2.5 Formulas for critical Shields and bedload 67
2.6 Terminal settling velocity and hindrance formulas 72

3.1 Suspension at equilibrium experiments 102

4.1 Characteristic of the glass beads 119
4.2 Parameters of the experimental configurations 121
4.3 Mesh characteristics for dune migration 123

5.1 Smooth bed experiments conditions 154
5.2 Meshes for rigid bed cases 157
5.3 Scour experiment conditions 159

Abbreviations and symbols

Abbreviations

ALE	Arbitrary Lagrangian Eulerian
CFD	Computational Fluid Dynamics
DEM	Discrete Element Method
DNS	Direct Numerical Simulation
FAM	Finite Area Method
FEM	Finite Element Method
FVM	Finite Volume Method
IBM	Immersed Boundary Method
LDA	Laser Doppler Anemometer
LEGI	Laboratoire des Écoulements Géophysiques et Industriels
LES	Large Eddy Simulation
RANS	Reynolds-Averaged Navier-Stokes
RMSE	Root Mean Square Error

Nomenclature

B	Integration constant in the log law for a rough wall
d	Diameter of the sediments $[m]$
d_0	Hydrodynamic roughness length $[m]$
$\tilde{d_0}$	Modified hydrodynamic roughness length $[m]$
D	Deposition flux $[m.s^{-1}]$
D_{cyl}	Diameter of the pier $[m]$

D_h	Hydraulic diameter, 4 times the ratio of the wet area to the wet perimeter $[m]$
D_*	Dimensionless sediment diameter
c	Celerity of bedforms $[m.s^{-1}]$
c_s	Suspended sediment volume fraction
c_s^{max}	Maximum sediment volume fraction
c_b^*	Reference concentration
C	Integration constant in the log law for a smooth wall
C_o	Courant number
E	Erosion flux $[m.s^{-1}]$
f_v	Vortex shedding frequency $[s^{-1}]$
F_h	Hindrance function
F_r	Froude number
$\boldsymbol{g}$	Gravity acceleration $[m.s^{-2}]$
h_d	Height of the dune $[m]$
H	Water depth $[m]$
k	Specific turbulent kinetic energy $[m^2.s^{-2}]$
k_s	Nikuradse equivalent roughness height $[m]$
k_s^+	Roughness Reynolds number
k_{Rough}^+	Lower limit of the roughness Reynolds number for hydraulically rough flow
k_{Smooth}^+	Upper limit of the roughness Reynolds number for hydraulically smooth flow
L_d	Length of the dune $[m]$
L_{sat}	Saturation length $[m]$
p	Pressure of the fluid $[kg.m^{-1}.s^{-2}]$
P	Turbulent kinetic energy production rate $[m^2.s^{-3}]$
$\boldsymbol{q_{av}}$	Avalanche related bedload flux $[m^2.s^{-1}]$
q_{av}^0	Maximum avalanche related bedload flux $[m^2.s^{-1}]$
$\boldsymbol{q_b}$	Bedload flux $[m^2.s^{-1}]$
$\boldsymbol{q_{sat}}$	Saturated bedload flux $[m^2.s^{-1}]$
Re	Reynolds number
Re_D	Pile Reynolds number

Re_p	Reynolds number based on particle diameter and settling velocity
Re_*	Reynolds number based on the friction velocity
R_o	Rouse number, ratio of the settling velocity to the upwards velocity of the grains
s	Ratio of sediment to fluid density
$\boldsymbol{S}$	Strain rate tensor $[s^{-1}]$
S_R	Roughness coefficient in rough wall functions for ω
S_t	Strouhal number, dimensionless vertex shedding frequency
T_{sat}	Saturation time $[s]$
$\boldsymbol{u}$	Velocity field $[m.s^{-1}]$
$\boldsymbol{u'}$	Velocity field fluctuations $[m.s^{-1}]$
u_*	Friction velocity $[m.s^{-1}]$
V_f	Volume of fluid $[m^3]$
V_s	Volume of sediments $[m^3]$
$\boldsymbol{w_s}$	Settling velocity of suspended sediments $[m.s^{-1}]$
$\boldsymbol{w_s^0}$	Terminal settling velocity of a lone particle in a quiescent fluid $[m.s^{-1}]$
W_c	Width of the channel $[m]$
z_b	Sediment bed elevation $[m]$
z_{fs}	Free surface elevation $[m]$
z_s	Maximal scour depth $[m]$
α_s	Angle between the steepest slope direction and the shear direction
β_r	Repose angle of the granular material
β_s	Bed slope angle
δ_t	Time step $[t]$
δz_b^*	Reference level $[m]$
ϵ	Rate of dissipation of turbulence kinetic energy $[m^2.s^{-3}]$
ϵ_s	Turbulent diffusivity for suspended load $[m^2.s^{-1}]$
ϵ_w	Additional near bed diffusivity for suspended sediments $[m^2.s^{-1}]$
θ	Shields number, dimensionless shear stress
θ_c^0	Critical Shields number on a flat bed
θ_c	Critical Shields number with slope correction

κ	Von Kármán constant
λ_s	Porosity of the granular material
μ_s	Static friction coefficient
ν	Kinematic viscosity of the fluid $[m^2.s^{-1}]$
ν_t	Turbulent eddy viscosity $[m^2.s^{-1}]$
ρ_f	Density of the fluid $[kg.m^{-3}]$
ρ_s	Density of the sediments $[kg.m^{-3}]$
σ_c	Schmidt number, ratio of eddy viscosity to turbulent diffusivity of suspended sediments
$\boldsymbol{\tau_b}$	Shear stress exerted on the bed $[kg.m^{-1}.s^{-2}]$
$\boldsymbol{\tau_f}$	Filtering tensor in Navier-Stokes equation $[m^2.s^{-2}]$
ϕ_b	Dimensionless bedload flux
ω	Specific dissipation rate of turbulent kinetic energy $[s^{-1}]$

Abstract

Scouring, i.e., localized erosion around a structure obstructing flow, is a subject of paramount importance for the safety of hydraulic structures, particularly bridges, as it is the main cause of failure. Although it has been the subject of numerous studies in the past, it remains poorly understood and difficult to predict accurately. As part of the OXALIA industrial chair, supported by the Grenoble INP Foundation, thanks to the sponsorship from the Artelia engineering group, this doctoral thesis aims to develop a numerical model to simulate the scouring process. Ultimately, this tool should help in the design of hydraulic structures that are more resilient to extreme events.

The main contribution of this work is the development of an open-source numerical model called *sedExnerFoam*, implemented in the open-source C++ multi-physics simulation toolkit *OpenFOAM*. This model combines high-resolution hydrodynamics, a transport equation for suspended sediment concentration, and a morphological evolution module based on the Exner equation. The sediment bed constitutes one of the boundaries of the computational domain, whose geometry varies over time. The evolution of the bed in turn affects the hydrodynamics through mesh deformation. The development of the numerical model was validated against numerous benchmarks to ensure the proper functioning of its various components and their coupling. A crucial point for the sediment transport part is the conservative nature of the model with regard to sediment mass.

Subsequently, more complex problems were addressed, such as the migration of an isolated dune, subjected to unidirectional flow or scouring around a cylindrical obstacle. The numerical study of the different dune migration regimes identified three important parameters for predicting the morphological evolution of bedforms with this model: the rough boundary condition on the bed, the position of the boundary layer detachment, and the inertia of the grains transported as bedload. The use of the saturated bedload flux, which neglects particle inertia, shows unrealistic behavior in the presence of flow detachment upstream of the dune's crest, which causes sediment accumulation at the top of the dune, a steepening of the upstream slope, and then avalanches that compensate for the bedload transport. To correct these effects, the concept of bedload flux saturation, borrowed from aeolian sand transport, was implemented. Saturation causes the bedload flux to react more gradually to variations in bed shear stress, enabling sediments to reach the downstream face of the dune before being picked up by avalanches. In the configuration of a three-dimensional crescentic dune (barchan), the effect of saturation appears less critical. However, the formation and growth of the barchan's horns without saturation leads to excessive lateral dispersion.

In the last chapter, preliminary results of the application of the model to the simulation of the scouring process are presented. Although these results are very encouraging, the implementation of this method on complex obstacle geometries is nevertheless made difficult by constraints related to the quality of the mesh required for its proper functioning. Several areas for improvement have been identified to enable the use of *sedExnerFoam* in engineering applications. The priorities concern the quality of the mesh, as its deformation can sometimes cause simulations to fail. A 3D formulation of bedload

saturation has been proposed, but it still needs to be validated. The diffusivity near the bed, introduced to model the erosion flux, remains empirical for the time being, and a formulation inspired from two-phase modeling approach has yet to be developed. Other improvements are also discussed, which could serve as a basis for future developments of this open-source model.

Résumé

L'affouillement, c'est-à-dire l'érosion localisée autour d'une structure faisant obstacle à un écoulement, est un sujet d'une importance capitale pour la sécurité des ouvrages hydrauliques, notamment des ponts, car il en est la principale cause de défaillance. Bien qu'il ait fait l'objet de nombreuses études par le passé, il reste mal compris et difficile à prévoir avec précision. Dans le cadre de la chaire industrielle OXALIA, portée par la Fondation Grenoble INP grâce au mécénat du groupe d'ingénierie Artelia, cette thèse de doctorat vise à développer un modèle numérique permettant de simuler le processus d'affouillement. À terme, cet outil doit permettre d'aider à la conception d'ouvrages plus résilients face aux événements extrêmes.

La contribution principale de ce travail est le développement d'un modèle numérique open source nommé *sedExnerFoam* implémenté dans la boîte à outils de simulation multi-physique open source C++ *OpenFOAM*. Ce modèle associe une résolution fine de l'hydrodynamique, une équation de transport pour la concentration de sédiments en suspension et un module d'évolution morphologique basé sur l'équation d'Exner. Le fond sédimentaire constitue une frontière mobile pour le domaine de calcul. Son évolution affecte en retour l'hydrodynamique par la déformation du maillage. Le développement du modèle numérique a été jalonné par de nombreux tests de validation afin de garantir le bon fonctionnement de ses différentes composantes ainsi que de leur couplage.

Par la suite, des problèmes plus complexes ont été abordés, comme la migration d'une dune isolée soumise à un écoulement unidirectionnel ou l'affouillement autour d'un obstacle. L'étude des différents régimes de migration de dunes a permis d'identifier trois paramètres clés pour prédire l'évolution morphologique des formes de fond: la condition limite de rugosité sur le lit sédimentaire, la position du décrochement de la couche limite et l'inertie des grains transportés par charriage. L'utilisation du flux de charriage saturé, qui néglige l'inertie des particules, crée des comportements non réalistes en cas de détachement de l'écoulement en amont de la crête, provoquant une accumulation de sédiments, un redressement de la pente, puis des avalanches qui compensent le flux de charriage. Pour corriger ces effets, un modèle de saturation a été implémenté et permet au flux de charriage de ne plus réagir instantanément aux variations de contrainte. Les sédiments sont alors transportés jusqu'à la face aval avant d'être repris par les avalanches. Dans le cas de la migration d'une dune tridimensionnelle en forme de croissant, il a été montré que l'effet de la saturation est moins critique, car les sédiments peuvent également être transportés dans les directions latérales. Cependant, la formation et la croissance des cornes de la barkhane, sans prendre en compte la saturation, conduisent à une dispersion latérale excessive.

Dans le dernier chapitre, des résultats préliminaires de l'application du modèle à la simulation du processus d'affouillement sont présentés. Bien que ces résultats soient très encourageants, la mise en œuvre de cette méthode sur des géométries d'obstacles complexes est toutefois rendue difficile par les contraintes liées à la qualité du maillage nécessaire à son bon fonctionnement. Plusieurs pistes d'amélioration ont été identifiées pour permettre l'utilisation de *sedExnerFoam* dans le cadre d'applications d'ingénierie.

Les priorités concernent la qualité du maillage, dont la déformation provoque parfois l'échec des simulations. Une formulation 3D de la saturation du flux de charriage a été proposée, mais doit encore être validée. La diffusivité proche du lit, introduite pour modéliser le flux d'érosion, reste pour l'instant empirique et une approche fondée sur la modélisation diphasique reste à développer. D'autres améliorations sont également évoquées, qui pourront servir de base aux futurs développements de ce modèle open source.

Remerciements

Déjà plusieurs années avant de me lancer dans cette aventure qu'est la réalisation d'une thèse, je savais déjà avec certitude que je souhaitais m'orienter vers un travail scientifique technique, que ce soit dans la recherche académique ou bien dans le privé. C'est grâce à un stage de fin d'études, proposé par ceux qui allaient devenir mes encadrants, que la thèse s'est imposée comme une évidence. Je ne savais pas encore tout à fait dans quoi je m'engageais, et à quel point ce sujet allait devenir une part de moi-même. Trois ans, c'est court. Par moments, j'aurais aimé que cela continue et que je puisse emmener le sujet plus loin. Mais ces trois années ont aussi été longues. J'ai rencontré beaucoup de personnes qui ont participé de près ou de loin à cette période de ma vie, et qui en ont fait une expérience dont je garderai de très bons souvenirs. Je tiens donc ici à remercier ces personnes qui ont fait partie de cette aventure.

Premièrement, je remercie l'ensemble des membres de mon jury qui ont pris le temps de me lire, de comprendre mon travail et de l'évaluer. Je tiens tout d'abord à remercier Éric Barthélemy, qui, avant d'être le président de mon jury de thèse, a été un super professeur d'hydraulique. Je remercie Magalie Jodeau et Benoît Camenen, avec qui j'ai eu l'occasion d'interagir plusieurs fois au cours de ma thèse, pour l'expertise qu'ils m'ont apportée. Je tiens également à remercier Stéphane Popinet, dont j'apprécie tout particulièrement le travail et dont j'ai beaucoup apprécié la présence dans le jury. Enfin, j'adresse un remerciement particulier à David Fuhrman et Ivana Vinkovic, qui ont accepté de rapporter ma thèse, et dont les compliments comme les critiques m'ont permis de renforcer ma maîtrise de mon sujet et d'être fier du travail accompli.

Dans une thèse, le sujet est bien sûr important, mais selon moi, l'équipe encadrante l'est bien plus. Je remercie Olivier, Cyrille et Julien, que je recommanderais sans hésiter à tout étudiant.e qui souhaiterait se lancer dans une thèse en modélisation du transport sédimentaire. Je n'ai jamais eu l'impression d'avancer seul. Vos conseils et réflexions m'ont permis de ne jamais être à court d'idées et de vivre sereinement ces trois années. Je vous remercie pour votre bienveillance et je suis heureux de pouvoir continuer à travailler avec vous à l'avenir.

Je remercie bien sûr l'ensemble de mes camarades du LEGI et d'Artelia, qui m'ont permis d'aborder ces trois années dans les meilleures conditions. Mes deux co-bureaux, Marie et Emma, à qui je souhaite le meilleur pour leurs thèses respectives. Les cyclistes de la pause midi, Alban, Valentin, Rémi et Alexis, avec lesquels j'espère continuer à rouler. Ivan, le plus vieux jeune du LEGI, pour son travail de photographe et les memes quotidiens à l'heure du café. Et les autres membres de l'équipe sedFoam, Maxime, George, Manohar et en particulier Eduard, qui est devenu un ami proche.

Enfin, je remercie ma famille, mes deux parents Sylvie et Xavier, pour leur soutien inconditionnel et les nombreux moments passés ensemble. Ma sœur Solweig, que j'ai forcée à travailler pour préparer le pot de thèse et sans qui je ne m'en serais très certainement pas sorti. Sarah enfin, qui fait maintenant partie de ma vie depuis 6 ans, pour tous les bons moments, le réconfort apporté dans les moments plus difficiles et pour la joie que tu me procures.

Acknowledgements

This thesis work was carried out within the framework of the Oxalia industrial chair, supported by the Grenoble INP Foundation, thanks to sponsorship from the Artelia engineering group. The authors would like to thank the developers of *OpenFOAM*, which offers a wide variety of tools to solve partial differential equations. The software ParaView and the Python package Fluidfoam [Bonamy et al., 2025] were invaluable visualisation tools for processing and analysing the simulation results presented in this work. The dedication of these development communities to open-source innovation has made high-quality computational tools accessible to researchers and engineers around the world. Their work is greatly valued.

Introduction

In 2007, Cyclone Gamede passed over La Réunion Island, causing heavy rainfall and the subsequent collapse of the Saint-Étienne River bridge, which was built in 1992-1993. This occurred only 10 years after its construction. Following the event, the Director General of Roads requested an investigation by the General Council of Ponts et Chaussées to determine the causes and consequences of this failure. The report concluded that the collapse of the bridge was the result of significant scouring of one of the piers. This is the erosion of the riverbed by the flow of water in the vicinity of the hydraulic work. The pier collapsed, bringing down the two adjacent spans with it. The entire structure then followed as the other piers were unable to withstand the drag effect of the deck along the structure's axis. Perhaps the most surprising fact is that the estimated river discharge corresponds to a flood with a return period of only 10 years. Yet this was sufficient to completely wash away the bridge (see Figure 1). In order to quickly restore the traffic, a temporary submersible foundation was built before being in turn destroyed by Cyclone Dumile in 2013. A new bridge was finally inaugurated that same year. Spanning almost 700 meters, it is supported by eight piers with foundations buried up to 36 meters below the riverbed to prevent scour. This major circulation infrastructure project, used by around 70,000 vehicles every day, was built for a total cost of 113 million euros.

This event is by no means an isolated case. In fact, scour is often identified as a major factor in bridge failure. In their work, Wardhana and Hadipriono [2003] conducted an analysis of bridge failures in the United States, attempting to identify the reasons for the collapse of a collection of 503 bridges between the years 1989 and 2000. The study identified the combined effect of flooding and scouring as the cause of failure for 266 bridges, representing 53% of the total sample. Many other examples can be found, such as the Malahide Viaduct in Dublin and the Zava Bridge in Zagreb, which both failed in 2009 [Prendergast and Gavin, 2014]. By understanding how flowing water removes sediment around bridge foundations, engineers can design safer structures, assess existing risks, and implement effective countermeasures. This ensures the long-term stability of bridges, protects public safety, and reduces maintenance and repair costs. Scour affects not only bridge piers, but also many other hydraulic structures. The rapid development of offshore wind farms, in particular, has created a growing interest in studying scour around the foundations, which is caused by both waves and tidal currents.

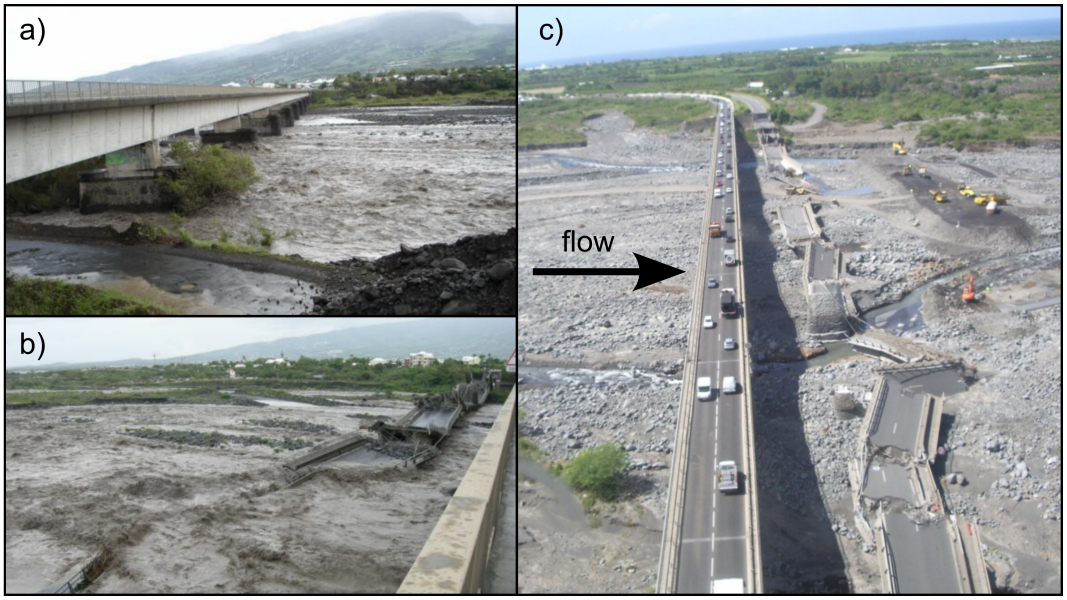

Figure 1: Images of the Saint-Étienne river bridge in La Réunion island after the passage of the Gamede cyclone in 2007. Images taken from Binet-Tarbé de Vauxclairs [2007].

Example study, Dordogne viaduct

The following section provides an example of the type of engineering study that can be carried out to address scour-related issues.

ARTELIA Water & Environment assisted COSEA with hydraulic studies for major crossings on the new South Europe Atlantic high-speed rail line infrastructure over the Indre, Vienne, and Charente valleys and the Dordogne. In early 2012, one of the piers of the viaduct over the Dordogne River underwent physical modeling with movable bottoms to quantify scouring and determine a protection solution. The viaduct over the Dordogne River was subsequently constructed, and the high-speed rail line has been operational since 2017 (see Figure 2).

In the years following, the bathymetry monitoring of the Dordogne riverbed revealed unexpected scour depths for one pier in particular that had not been anticipated during the physical study conducted prior to the construction. These observations prompted the development of new expertise using numerical modeling to provide the best possible guarantees for the refilling solution to be implemented to limit future scouring. This study was conducted through numerical modeling by the engineering group Artelia using the Computational Fluid Dynamics (CFD) C++ toolbox *OpenFOAM*.

Due to the lack of tools to perform numerical simulation of the local scour phenomenon, only the hydrodynamics was simulated. The shear stress exerted by the flow on the bed was used to dimension the minimum size of the rocks protecting the pier to avoid further scouring. Firstly, the physical model of the 2012 study was reproduced numerically to verify that the same conclusions regarding the stability of the rocks could be

Figure 2: On the left, configuration of the physical model during construction phase testing with scour protection (Artelia 2012). On the right, an image on the viaduct and the Dordogne River.

drawn. In a second phase, the flow around the actual pier was simulated by considering more realistic current conditions. The bridge being located close to the estuary, the flow is subject to marine influences. The tides, in particular, are strongly influencing the river discharge. To force the local model boundary conditions, a large-scale simulation covering more than 10 km of the Dordogne river was realized using the TELEMAC-MASCARET software. Images illustrating the numerical model results are presented in Figure 3.

This study allowed Artelia to confirm the initial instability of the rockfill and to predict the stabilization of the scour pit. The potential of a new refilling solution in the event of the pit being deepened in the future due to interaction with bedforms was also investigated. The study of hydrodynamics is only sufficient to identify areas of high shear stress where sediment erosion from the bed is expected, and engineers are able to study scour protection solutions for various flow conditions. However, it is difficult to accurately predict the morphological response of the riverbed and its impact on flow through hydrodynamic studies alone. A sediment transport and morphological model would enable the feedback between the formation of the scour hole and the flow to be considered, allowing the maximum scour depth to be estimated more accurately and the risk of pier instability to be assessed.

Objectives and methodology

With the rapid surge in computational power, many sediment transport numerical models have been developed over the past few decades. However, to the author's knowledge, none of the models suited for the local study of scour around hydraulic structures, for which a precise three-dimensional description of turbulent flow is required, is open source. The

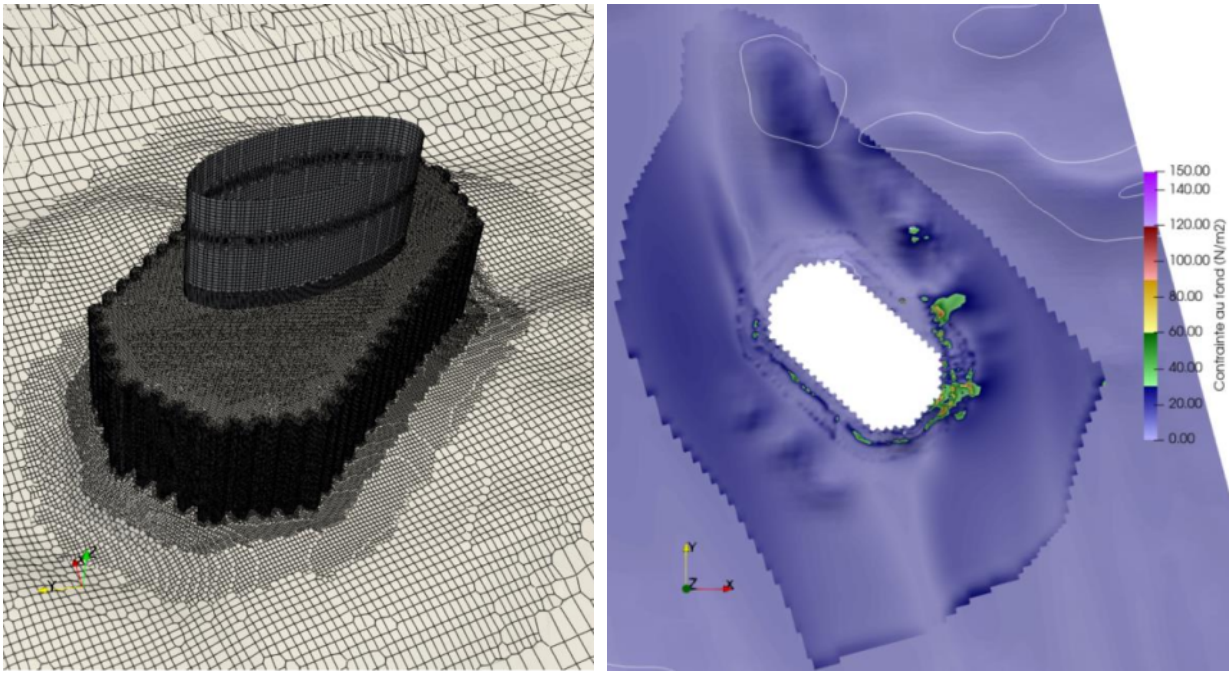

Figure 3: On the left, representation of a mesh used for the numerical study of the stability of the scour protection. On the right, the shear stress exerted on the bed around in the vicinity of pier. Images taken from the study of Artelia.

objective of this thesis is therefore to develop a sediment transport and morphological evolution numerical model able to tackle scour problems in order to address real engineering applications, such as those involving bridge piers. The ambition to scale up beyond the laboratory level creates constraints on computational costs. This has influenced the modeling choices made in this study. The objective can be summarized as developing a precise model that allows scour to be studied at a reasonable computational cost.

To pursue this objective, it was decided to develop a sediment transport model within the C++ open source library *OpenFOAM* using the version developed and distributed by OpenCFD Ltd (v2506). *OpenFOAM* is based on the finite volume method (FVM) and provides many utilities to solve a vast range of physical problems, particularly those related to fluid mechanics, but not exclusively. The sediment transport model being the subject of this work was named *sedExnerFoam* [Renaud et al., 2025] and is rendered open source with the hope that it will be useful to the sediment transport community. A native *OpenFOAM* model named *pimpleFoam*, used for incompressible, single-phase turbulent flows, was the basis for its development. Sediment transport is initially divided into two parts that were initially developed separately. The suspended load transport and bedload transport, as well as the morphological evolution. To ensure consistent code quality and behavior over time, a variety of tests were implemented based on the principle of verifying each process individually. These tests are part of a continuous integration strategy, and, together with the code development, represent the main contribution of this work.

Outline of the thesis

The thesis is organized into five chapters, which are structured as follows: The first chapter is a state of the art review. It begins with a description of the flow around an obstacle, focusing particularly on the case of a vertical cylinder. It then provides a review of different laboratory scour experiments, as well as existing sediment transport models, and analyses their respective strengths and shortcomings. This review forms the basis for justifying the chosen modeling approach. The second part focuses on the physical processes to be modeled, including hydrodynamics, turbulence, sediment transport processes, and morphological evolution. The second chapter delivers a detailed description of *sedExnerFoam*, covering both mathematical and numerical aspects. It is followed by the review of different benchmarks and validation test cases, which make up a third chapter. These are simple simulations designed to isolate the different model components and validate them separately. The fourth chapter presents a first application of the fully coupled model to the migration of a lone dune under the influence of an unidirectional flow. As the flow passes over the lee side of the dune, a wake is formed with adverse pressure gradients, which, depending on the mass of the dune and the velocity of the flow, can lead to flow separation. It was found that the position at which the flow separates dramatically affects the migration process. The fifth and final chapter focuses on the classic example of flow and scour around a cylindrical pile to highlight the model's potential to target scour applications. However, limitations remain that prevent the model from being used for more complex geometries. Different improvement strategies and perspectives are discussed in the concluding section.

Chapter 1

State of the art review

1.1 Flow and scour around a pier

The presence of a bridge pier disrupts the natural flow of the river, forcing it to deviate from its course. This creates turbulent structures and high velocities around the pier, resulting in excess shear stress exerted on the granular bed, which can dislodge and carry away sediments. This excavation process leads to the formation of a scour hole around the pier. The scour process is due to two mechanisms. Firstly, the pier's presence locally reduces the available space for the flowing fluid, which significantly increases the fluid velocity as it passes on the sides of the obstacle. The other reason is the presence of turbulent structures around the pier, divided into three different vortex systems [Breusers et al., 1977]. These are the horseshoe vortex system, the wake-vortex system, and the trailing vortices (see Figure 1.1). In particular, the horseshoe vortex and the wake-vortex systems strongly affect sediment transport. Trailing vortices, on the other hand, only exist for submerged obstacles and is therefore not relevant for bridge scour.

The existence and the characteristics of these vortex systems depend strongly on the obstacle geometry and on the bulk flow velocity. For a cylindrical pile, the turbulent structures of the flow are characterized by the pile Reynolds number defined as follows:

$$Re_D = \frac{\overline{u} D_{cyl}}{\nu}\,, \tag{1.1}$$

where D_{cyl} is the cylinder diameter, $\overline{u}$ is the undisturbed bulk velocity, and ν the fluid kinematic viscosity. If the pier is not cylindrical, the characteristic length scale used to define the pile Reynolds number is taken as the pier's projected width in the plane perpendicular to the flow mean direction.

Horseshoe vortex system

The presence of the pier creates a stagnation point for the flow, resulting in a local increase in the water level on the upstream side of the obstacle. Because of the higher pressure associated, the flow dives to the bottom. The downflow and the adverse pressure gradient

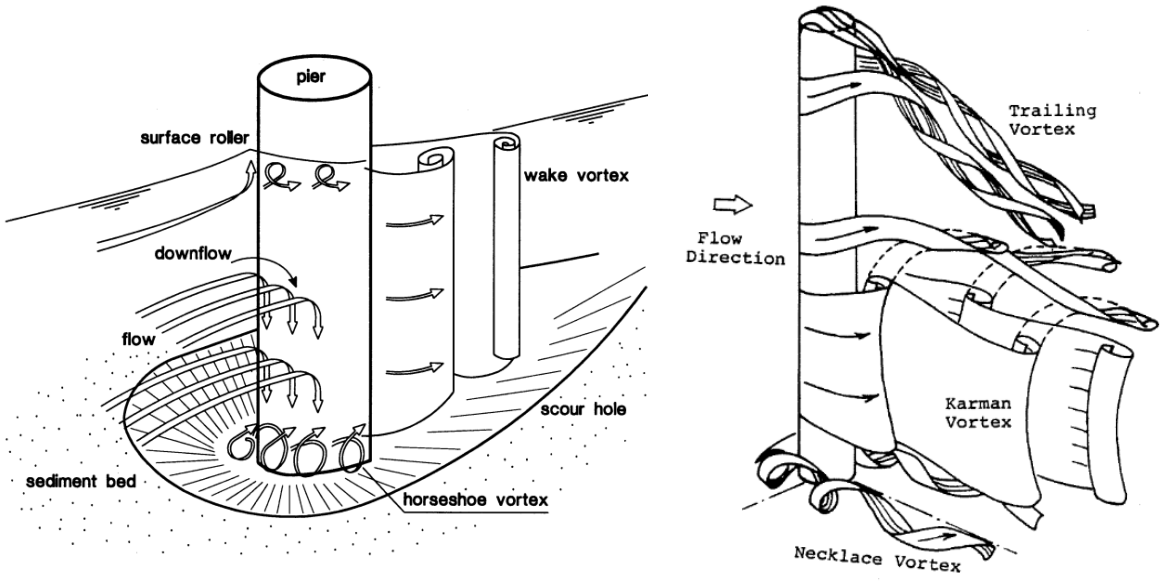

Figure 1.1: On the left, schematic of the scour process around a cylindrical pile. The image is taken from the work of van Rijn [2005]. On the right, another schematic showing the three different vortex systems, horseshoe, wake vortex and trailing vortices. The image is issued from the work of Kawamura et al. [1984].

upstream of the pier generate a vortex rotating in the spanwise direction. The flow sweeps the ends of this vortex downstream, creating the horseshoe shape that gives it its name. It is also sometimes referred to as a necklace vortex. In reality, it does not consist in a single vortex but in a complex system made of a varying number of vortices. An image issued from an experiment made by E. P. Sutton in 1960, but only reported in the work of Baker [1980], is shown in Figure 1.2. It shows a laminar boundary layer reaching an obstacle and generating a horseshoe vortex system at its foot.

Baker [1980] conducted experiments in a wind tunnel of a flow with a growing boundary layer encountering an obstacle. The aim of the experiments was to observe the horseshoe vortex system. To visualize the streamlines pattern on the bottom surface, he used an oil visualization method. He spread over the bottom surface a suspension of titanium dioxide in paraffin to observe how it moves once the air flow starts up. From this experiment, he could identify a total of four vortices and drew the sketch presented in Figure 1.2. The smallest one is stuck at the limit between the bottom surface and the obstacle and is referred to as the bottom attached vortex. According to Baker, this small vortex is caused by the separation of the boundary layer on the upstream face of the obstacle, that is, the downflow detaching before reaching the bottom surface. He identified three other vortices in the core of the system and suggested that smaller ones may exist but were not revealed by the oil flow visualization method.

Another characteristic of the horseshoe vortex system is that as the pile Reynolds number increases, it starts to oscillate. Experimental results from Schwind [1962] and

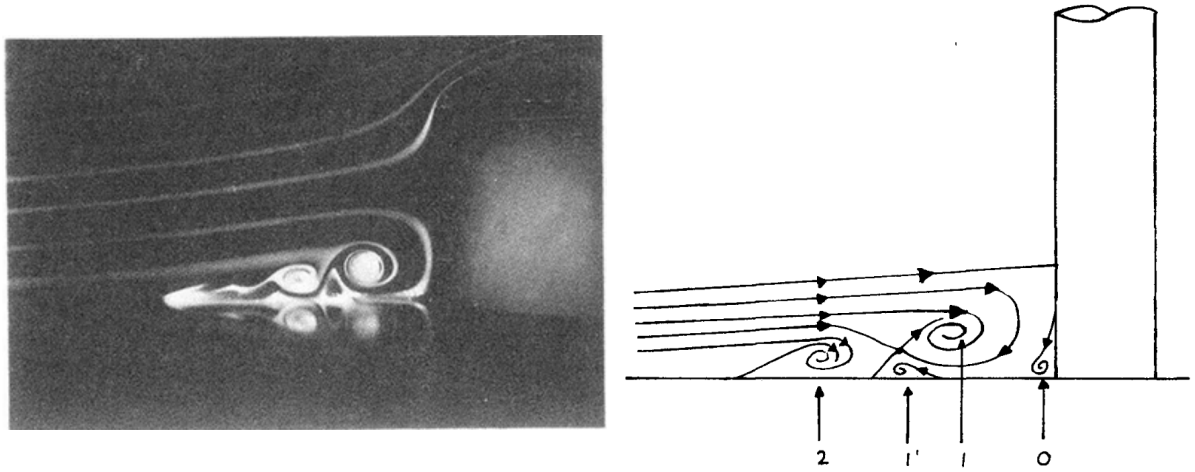

Figure 1.2: On the left, a visualization of a horseshoe vortex system at the foot of an obstacle in a laminar boundary layer flow. On the right, a schematic of the horseshoe vortex system at the foot of a wall mounted cylinder. Images taken from [Baker, 1991] and Baker [1980] respectively.

Baker [1979] suggest that for given flow conditions, two kind of oscillations exist and that the flow intermittently switches from one type of oscillation to the other [Baker, 1991]. This is known as the bi-modal oscillation of the horseshoe vortex system. There is clear evidence that the number of horseshoe vortices in the system depends on the Reynolds number. However, the relationship is complex, and an increase in the Reynolds number can lead to either more or fewer vortices [Baker, 1991].

The horseshoe vortex system is often identified as one of the main drivers of the scour process. Unlike the acceleration of the flow on the pier's sides, which is important in the early stages of scour development, but it loses intensity once the scour hole has developed sufficiently. The horseshoe vortex continues to erode sediments upstream of the pile in the latter stages of scour development. Its intensity is strongly influenced by the pier geometry. In the case of a blunt-nosed pier, the pressure gradient due to flow blockage is stronger, resulting in an exacerbation of the horseshoe system. In contrast, a sharp geometry clearly reduces the erosive capacity of the vortex. In Figure 1.3 are represented the coherent turbulent structures of the flow around a cylindrical pile and a diamond pile obtained by Lai et al. [2003] using numerical simulations. The coherent structures are represented by iso-surfaces of vorticity, which allow for visualization of the horseshoe vortex, which appears smaller for the diamond geometry.

Wake vortices

As previously mentioned, another key feature of flows around a pier is the presence of wake vortices. For a very low Reynolds number ($Re_D < 5$), there is no vortex at all, and the flow remains attached to the cylinder. However, as soon as the Reynolds number increases, the adverse pressure gradient downstream of the cylinder causes the boundary

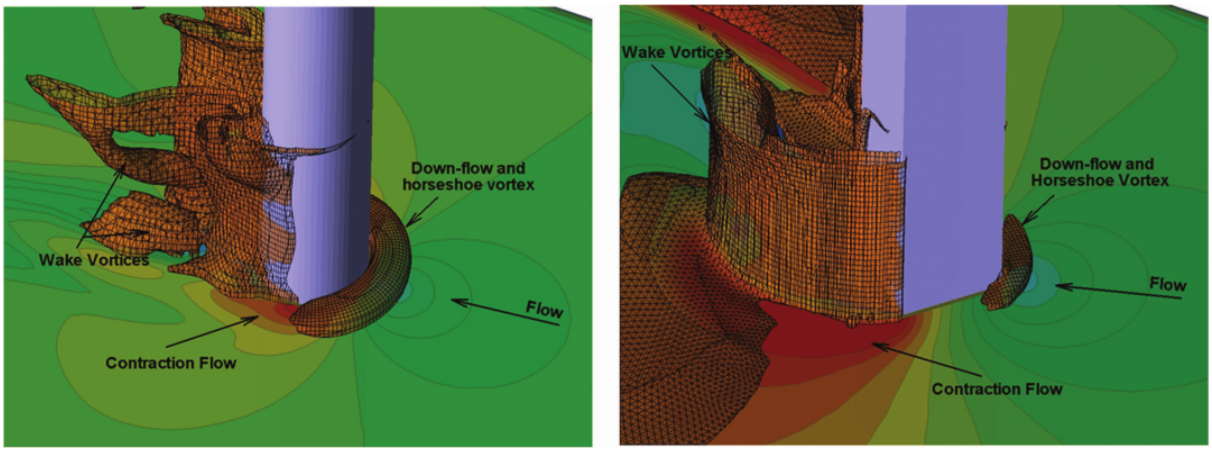

Figure 1.3: Representation of the flow features around two piers with different geometries, a cylindrical pier on the left and a diamond pier on the right, issued from RANS simulations. Three dimensional iso-surfaces of vorticity are represented as well as 2D iso-lines of near bed velocity on the bottom surface. Image taken from Lai et al. [2022].

layer to detach on both sides of the cylinder, creating a pair of symmetrical attached vortices. As the Reynolds number further increases, these two vortices grow in size and become unstable for a pile Reynolds number about $Re_D = 40$. They begin to slowly oscillate and detach from the cylinder. This creates a series of vortices known as the Kármán vortex street, consisting of alternating clockwise and anticlockwise vortices that are carried downstream by the mean flow. For $Re_D < 200$, the vortex street is laminar, which implies that the flow does not vary in the spanwise direction. The flow then slowly transitions until the wake is totally turbulent. These different flow regimes are represented on the schematic in Figure 1.4. At higher Reynolds number the boundary layer progressively becomes turbulent, which causes the boundary layer detachment to happen more upstream. For a pile Reynolds number between 10^5 and $3.5\,10^5$, only one of the two boundary layer detachments is turbulent. This asymmetry in the vortex shedding creates a non-zero mean lift [Sumer et al., 2006]. For $Re_D > 3.5\,10^5$, both boundary layer detachments are turbulent.

The frequency of the vortex detachment is usually expressed as a dimensionless number, calculated using the mean undisturbed flow velocity and the cylinder diameter. This dimensionless number is the Strouhal number:

$$S_t = \frac{f_v \overline{u}}{D_{\text{cyl}}}\,, \tag{1.2}$$

where f_v is the vortex shedding frequency. In the subcritical Reynolds number range (10^3 to 10^5), the Strouhal number remains relatively constant with a value of around 0.2. For a higher Reynolds number, the flow regime becomes supercritical, which corresponds to the boundary layer separation being turbulent on both sides of the cylinder. The Strouhal number suddenly increases when the regime transitions from subcritical to supercritical. The relation between the Strouhal number and the pile Reynolds number is represented

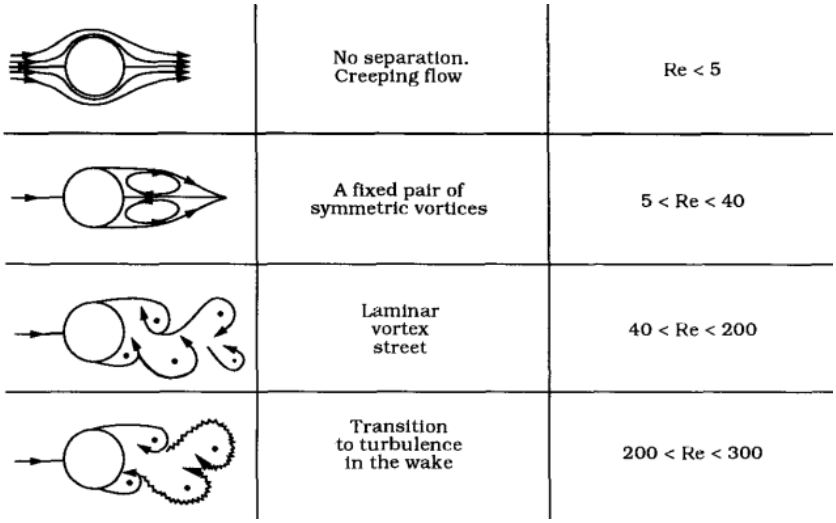

Figure 1.4: Regimes of flow around a smooth, circular cylinder in steady current for different pile Reynolds numbers. Image taken from Sumer et al. [2006].

in Figure 1.5 issued from the book of Sumer et al. [2006]. Understanding the behavior of the wake vortex shedding is crucial for predicting flow-induced vibrations and designing structures to withstand unsteady fluid forces.

1.2 Experimental study of the scour process

The scour around piers has been extensively studied in laboratory flumes in order to understand the effects of flow velocity, sediment size, and pier geometry on the onset, evolution, and equilibrium of scour. The most commonly studied geometry is the vertical cylinder pier. These experiments generally involve one of the following types of flow: Steady currents, waves, or both. The experiments are divided into two categories according to the sediment transport conditions: live bed and clear water, respectively. Live bed corresponds to flow conditions in which sediments are transported everywhere, even outside the area of influence of the cylinder. The second category is clear-water scour, which occurs when the bed shear stress exceeds the motion threshold only in the immediate vicinity of the pier. For clear water scour, the undisturbed flow is too weak to cause morphological changes, and there is therefore no motion of sediments outside the area of influence of the pier.

Chiew and Melville [1987] performed experiments of scour around a cylinder facing a steady current and studied the influence of different parameters on the equilibrium scour depth, the diameter of the sediments, and the bulk flow velocity. Their results showed an initial reduction in scour depth for conditions just exceeding the transition from clear water to live bed conditions. As the flow velocity is further increased, the scour hole deepens again until a maximum is reached for high bed shear stress. Roulund et al. [2005] conducted both experimental and numerical investigations of local scour around

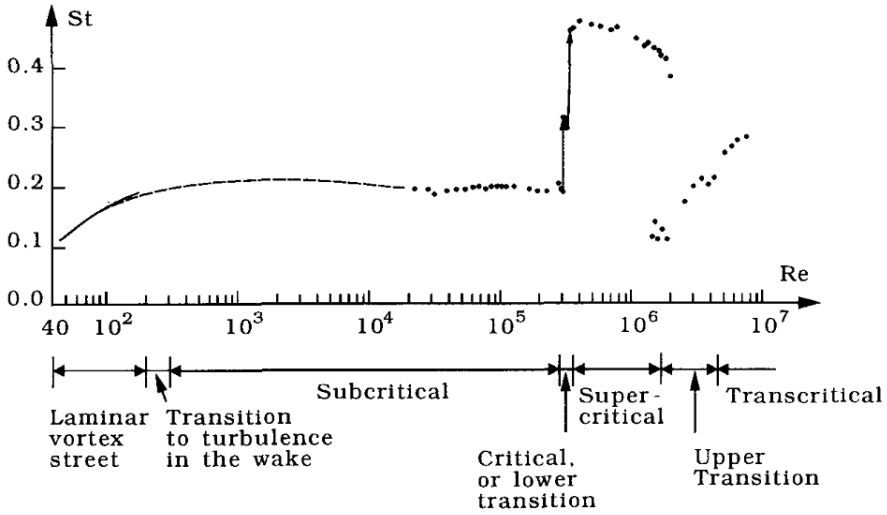

Figure 1.5: Strouhal number (dimensionless vortex shedding frequency) for a smooth circular cylinder as a function of the pile Reynolds number. Experimental data from: Solid curve: Williamson [1989]. Dashed curve: Roshko [1961]. Dots: Schewe [1983]. Image taken from Sumer et al. [2006].

a vertical cylinder mounted on a sediment bed made of sand particles of mean diameter $d = 0.26\,mm$. The experiment was conducted in the live bed regime with a cylinder of diameter $D_{\text{cyl}} = 10\,cm$ and a pile Reynolds number $Re_D = 4.6\,10^4$. Their findings showed that the boundary layer thickness relative to the pile diameter affects the size and strength of the horseshoe vortex. At equilibrium, the maximum scour depth was approximately 1.2 times the diameter of the pile. A picture of the equilibrium scour hole is shown in Figure 1.6.

A similar study was conducted by Zhao et al. [2010], combining experimental and numerical investigations of local scour around a submerged vertical circular cylinder in steady currents. For their experiment, they used sand with a median grain size $d = 0.4\,mm$. They used two different cylinders of diameter $D_{\text{cyl}} = 10\,cm$ and $D_{\text{cyl}} = 6\,cm$, respectively, and two different incoming flow velocities. The water depth in the test section was maintained at $50\,cm$ for all cases. A particularity of their experiments is the fact that the cylinder is totally submerged by water, allowing for the study of the impact of the cylinder height-to-diameter ratio on the scour process. They performed a set of 28 experiments and found that for height to-diameter-ratios smaller than 2, the scour depth at the stagnation point of the cylinder, which is the most upstream point of the cylinder surface, does not depend much on that ratio. Also, for height to-diameter-ratio smaller than 0.5, no scour was observed in the wake of the cylinder due to the absence of vortex shedding. This behavior was already explained by Kawamura et al. [1984], who pointed out that a critical height to diameter ratio value exists under which the wake zone is dominated by the trailing vortices (see Figure 1.1), which suppress the formation of the vortex streets.

Figure 1.6: On the left, equilibrium scour hole issued from the experiment of Roulund et al. [2005]. On the right bed pattern obtained by Zhao et al. [2010] using a cylinder of diameter 10 cm, an incoming flow velocity of 0.362 $m.s^{-1}$ and a cylinder height to diameter ratio of 1.5.

Many other authors have studied the scour around a cylinder in a steady flow. Ahmed and Rajaratnam [1998] performed a total of ten experiments and investigated the effect of bed roughness on the maximum amplification of shear stress. During a flood, the flow of the river is not steady, but varies over time. It is generally characterized by a rising phase, followed by a falling phase. Investigating the effect of flow unsteadiness on the hydrodynamics and local scour around a pier is the topic of the work of Misuriya and Eldho [2023]. They used a cylindrical pier with a diameter of 5 cm over a gravel bed with a mean grain size of 4.9 mm and conducted various experiments by varying the time taken for the discharge to reach its peak value, but limited their study to triangular-shaped flood hydrographs. Some studies have also provided results for piles of different geometries, such as in the work of Kirkil and Constantinescu [2010], who performed LES simulations of the flow around a blunt obstacle of rectangular section. They conducted an experiment to obtain the equilibrium scour hole and then meshed the bathymetry to run a high-resolution LES simulation revealing the unsteady dynamics of the coherent structures present in the vicinity of the obstacle and, in particular, the horseshoe vortex system located in the scour hole (see Figure 1.7).

In marine and estuarine environments, local scour occurs due to waves and tidal currents. In their book, Fredsoe and Sumer [2002] provide an exhaustive description of the scour process around a wide variety of hydraulic structures encountered in marine environments, such as pipelines or slender piles, which are commonly used to support a bigger structure, breakwaters, etc. The study of scour around a vertical cylinder subjected to an oscillatory flow, in particular, is a growing area of interest due to the rapid development of offshore wind farms. A wind turbine foundation could also consist of a more complex structure, such as in the work of Stahlmann [2013], where a tripod structure supports

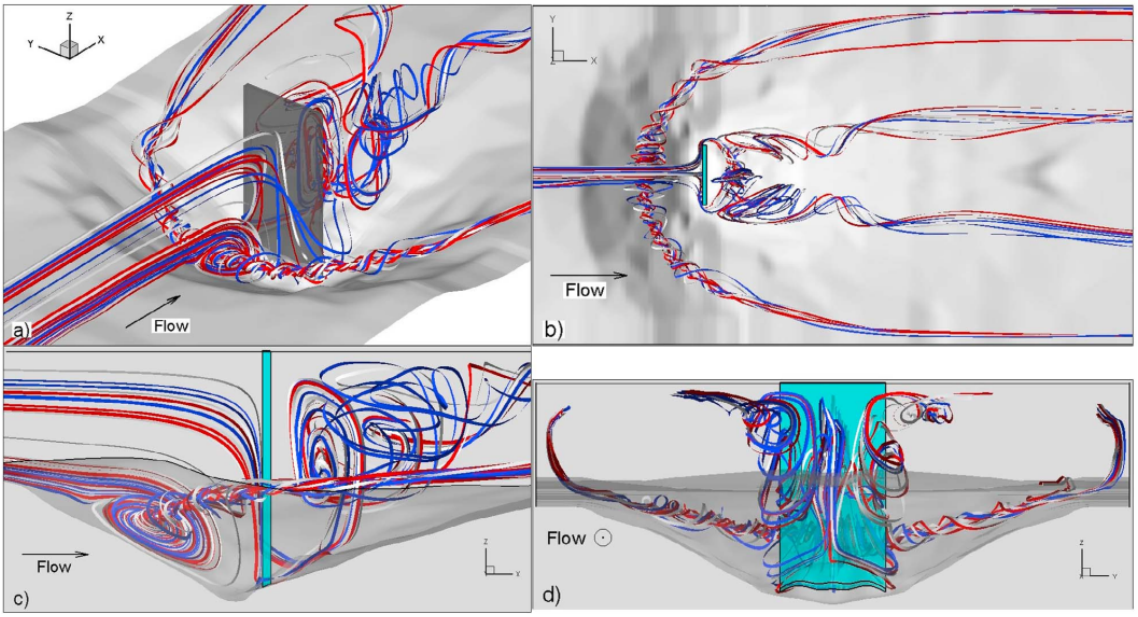

Figure 1.7: Visualization of the primary horseshoe vortex and of the U-shaped vortex behind the cylinder in the mean flow using 3D streamlines. (a) A 3D view; (b) top view; (c) lateral view; (d) back view. Image taken from Kirkil and Constantinescu [2010].

the offshore wind turbine. The scour below pipelines has been investigated by various authors [Mao, 1987, Sumer and Fredsøe, 1990, Dey and Singh, 2007], where the pipeline is generally a rigid horizontal cylinder facing the current. Xu and Huang [2023] investigated scour around pile breakwaters, which are structures designed to protect the shore against coastal erosion and are made up of an array of vertical cylinders that dissipate wave energy. More recently, Xie et al. [2025] showcased the potential of artificial reefs made of discarded oyster shells to protect pier foundations against local scour by carrying out a series of scour experiments in a flume.

Sediment type and cohesive elements also play a strong role in the scour process. Debnath and Chaudhuri [2010] explored scour for clay-sand mixed beds and found that increasing clay content reduces maximum equilibrium scour depth, modifies the geometry of the scour hole, and alters the time evolution of the process. In fully cohesive beds, scour is generally much less deep than in non-cohesive sand beds under similar hydraulic forcing. An example of the equilibrium scour holes obtained by Debnath and Chaudhuri [2010] for different clay percentages in the clay–sand mixture. In the rest of this work, only non-cohesive particles are considered.

1.3 Pier scour formulas for engineering studies

In practice, engineers heavily rely on empirical formulas to estimate the risk of scour for a wide variety of situations. Technical reports, as Richardson et al. [2001], CEREMA

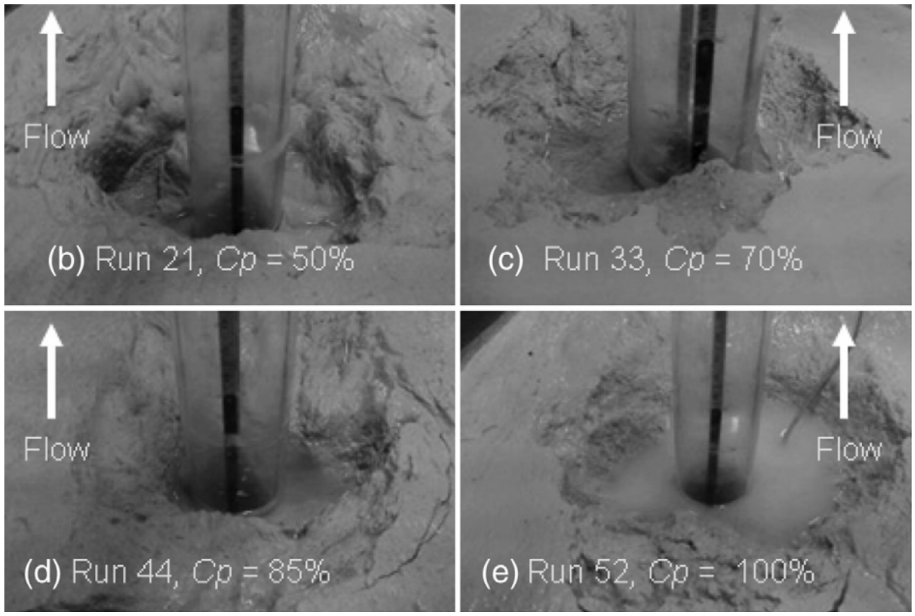

Figure 1.8: Photographs of equilibrium scour holes for 4 different experiments with different clay percentages in the clay-sand mixture. Image taken from Debnath and Chaudhuri [2010].

[2019], help to provide an overview of the existing methods. The following equation, known as the Colorado State University equation is provided as an example of an existing engineering formula to estimate the maximum local scour depth in the direct vicinity of a pier:

$$\frac{z_s}{H} = 2K_1K_2K_3K_4\left(\frac{H}{D_{\text{cyl}}}\right)^{0.35} F_r^{0.43}, \tag{1.3}$$

where z_s is the scour depth, H is the water depth upstream of the pier, F_r is the Froude number, D_{cyl} is the width of the pier, and K_1, K_2, K_3 and K_4 are correction factors. The value of K_1 depends on the pier geometry, K_2 on the angle of attack of the flow. K_3 depends on the bed conditions (clear water, plane bed, presence of small dunes, large dunes...), and K_4 is a correction factor for armouring by bed material, which depends on the grain size distribution.

Many other formulas have been developed and are not reviewed in this work. These are empirical and derived primarily from laboratory experiments under simplified, controlled conditions. As a result, their applicability is often limited to steady, uniform flows over non-cohesive, homogeneous sediment beds, with idealized pier geometries and well-aligned flow. These conditions rarely reflect the complexity of real river environments, which commonly feature unsteady hydrographs [Misuriya and Eldho, 2023], variable sediment supply, mixed or stratified bed materials, and skewed or compound flow patterns around bridges or piers. Also, many formulas assume a well-defined critical shear stress or velocity for sediment motion, yet this threshold is known to vary significantly with grain packing, armoring, and bedform development, leading to uncertainty in predictions.

Moreover, most equations predict only the final (equilibrium) scour depth and do not capture the temporal evolution of scour during transient flow events such as floods, nor do they account for backfilling after peak flow subsides. These formulas can significantly over or underpredict scour depth if applied without careful consideration of site-specific conditions, and they should be supplemented with field data, physical modeling, or numerical simulations where possible.

1.4 Sediment transport modeling and methods

This section reviews existing sediment transport modeling methods, providing an overview of the different possibilities and their respective advantages and drawbacks. The aim is to select the most suitable method for the objective of this PhD thesis, that is, the study of local scour at an affordable computational cost. Sediment transport problems involve multiple scales, from the interactions between sand grains to large submarine avalanches or large dunes spanning hundreds of meters to kilometers, migrating at a rate of only a few meters each year [Bourke, 2010]. Figure 1.9 shows a schematic representation of the various modelling approaches, organised according to their respective spatial scales.

The discrete element method (DEM) enables each grain to be represented as a Lagrangian particle, the motion of which is determined by Newton's second law. One difficulty of this method is to capture the collision of the particles. If they are considered perfectly rigid, then the time step of the simulation must be controlled so that each moment when two particles collide is captured. As the number of particles increases, this can lead to really small time steps and a considerable increase in the computational cost. To avoid this issue, soft particles are used in many studies. The particles can overlap and repel each other via an elastic force, which depends linearly on the thickness of the overlap [Mazzuoli and Lacaze, 2024]. To represent the fluid particles' interactions, there are two methods with different mesh refinement requirements. The immersed boundary method (IBM) can be used when particles are typically at least 20 times bigger than the grid spacing. It consist in a penalization of the Navier-Stokes equations to take into account the presence of the particles. This method, named particle resolved DNS, allows the precise computation of the drag force by integrating the stress exerted by the fluid on the surface of each particle. Kidanemariam and Uhlmann [2017] applied this method to study sediment patterns in a periodic channel. Conversely, when the particles are small compared to the grid size, it is possible to model the fluid-particle interactions using formulas to estimate the drag and lift forces. Figure 1.10 shows a schematic of these two possibilities. The main inconvenience of using DEM models is the strong limitation on the number of particles. For instance, considering monodispersed spherical particles of diameter $d = 1\,mm$, which corresponds to coarse sand, with a porosity of 40%, there are a total of 1.14 billion of particles in one cubic meter. This shows the impossibility to apply DEM at the scale of an actual hydraulic work.

To avoid this limitation on the number of particles, a possibility is to use an Eulerian-Eulerian approach, also called two-fluid approach [Chauchat et al., 2017]. The granular

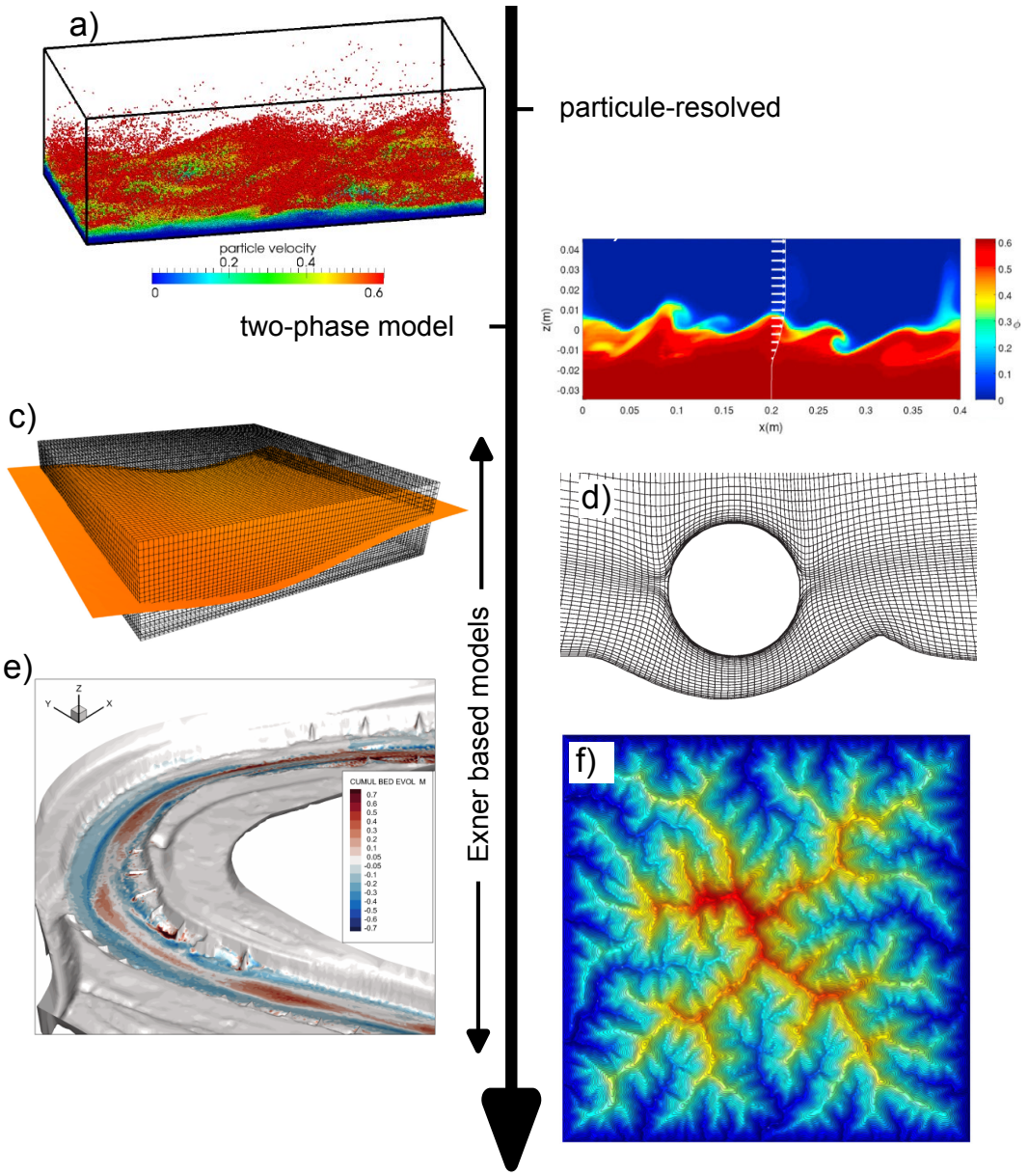

Figure 1.9: The different scales of sediment transport modeling. a) CFD–DEM simulation of sediment transport in a periodic channel [Sun and Xiao, 2016] b) instabilities of the near bed transport layer [Cheng et al., 2017], c) schematic view of a 3D background mesh and an embedded immersed boundary for a mobile sediment bed [Song et al., 2022], d) scour under a pipeline [Liang et al., 2005], e) bed evolution in the Gironde estuary simulated with GAIA Tassi et al. [2023], f) landscape after 30 million year of fluvial erosion and hill-slope mass wasting [Egholm et al., 2012].

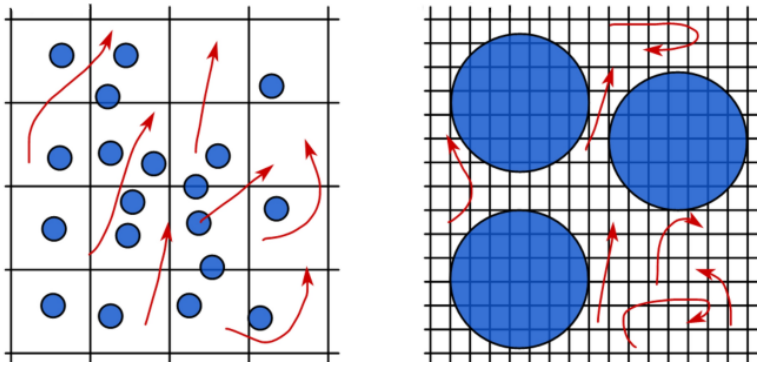

Figure 1.10: Schematic representing point-particle (left), for which particles can be smaller than the grid size, and particle-resolved DNS simulations on the right, for which the grid size must be smaller than the particle's diameter (at least 10 times smaller) to accurately solve fluid-particles interactions. Images taken from Zhao et al. [2024].

material is modeled as a continuum with a specific rheology, such has the famous $\mu(I)$ rheology [Jop et al., 2006] for dense granular flows, or the Kinetic Theory of granular gases [Jenkins and Berzi, 2010, Chassagne et al., 2023] for dilute granular flows. The fluid and granular phases interact through a drag force for which a drag coefficient needs to be specified, generally by means of an empirical formula. The main benefits of the Eulerian-Eulerian approach is that it allows for modeling all the different granular processes, particle-particule and fluid-particle interactions, in the water column and in the porous media. The bed interface is not explicit and corresponds to an iso-surface of sediment volume fraction. Although not limited by the number of particles like the DEM method, the mesh requirement to simulate the scour process around a pile with this method is quite high. Indeed, the area close to the bed interface is characterized by strong gradients of various fields (e.g. sediment volume fraction, fluid velocity, and turbulence), for which a fine mesh resolution is needed. During the scour process, the bed geometry varies considerably, so that the mesh must be refined in all areas that the bed could potentially explore. Moreover, the time step must be kept small to ensure the stability of the simulation, which also leads to a high computational cost.

Models suitable at larger scales do not resolve the granular phase, and the different sediment fluxes are computed using empirical formulas based on the bed shear stress, the local bed slope, and, eventually, other physical quantities. These models are referred to as single-phase flow models. They are based on the Exner equation for the bed evolution. The Exner equation is a mass conservation equation that describes the evolution of the sediment bed elevation in time:

$$(1-\lambda_s)\frac{\partial z_b}{\partial t} + \nabla_H . \boldsymbol{q_b} = D - E\,, \tag{1.4}$$

where z_b is the bed elevation, λ_s is the porosity of the granular material, $\boldsymbol{q_b}$ is the bedload flux, and E and D are the erosion and deposition fluxes, respectively.

Different strategies are possible to track the bed geometry evolution in time. One of

them is the immersed boundary method (IBM), where the sediment bed interface is a curved surface immersed in the three-dimensional computational domain. The equations for the fluid are penalized to consider the presence of the bed in the domain. A fine mesh is needed near the bed to correctly capture the hydrodynamics and obtain a good estimate of the bed shear stress. Song et al. [2022] developed a model based on this method, which they then used to study the scouring effect around both vertical and horizontal cylinders. For Exner-based models, it is the shear stress that drives sediment transport. In order to accurately estimate the bed shear stress, a high level of mesh resolution is required in the area close to the bed. Just as for the Eulerian–Eulerian approach, this means that a large mesh size is needed to study problems involving significant changes in bed elevation, as the mesh resolution must be kept high wherever the immersed boundary could pass during the simulation. Recently, D'Alessandro et al. [2025] used the IBM method to investigate the evolution of bedforms on a loose sediment bed under turbulent flow conditions with a LES turbulence model.

Another method is the use of σ-coordinates. It consists of operating a change of variable $\sigma = (z - z_{fs})/H$, where z is the vertical coordinate, z_{fs} the elevation of the free surface, and H the water depth. The equations for the fluid are written using the newly defined variable σ. The two drawbacks of this method are that it can only be applied to problems without sharp bed changes [Haney, 1991] and also that the sigma transform cannot be used for piers whose cross-section is not uniform in the vertical direction. Although scour around geometries that are an extrusion of a two-dimensional shape, such as rectangular or cylindrical piers, is possible, this method cannot be used to treat any pier whose section varies vertically. The last method is known as the Arbitrary Lagrangian-Eulerian (ALE) method and consists of having a dynamic mesh deforming in time so that its bottom boundary always matches the sediment bed interface [Liu and García, 2008, Liang et al., 2005]. The advantage is that, contrary to the immersed boundary method, there is no need to mesh below the bed interface. It is also not necessary to refine large areas of the mesh in anticipation of morphological changes. However, the use of a dynamic mesh can lead to tricky issues, with one main downfall being that the mesh quality could deteriorate during the scour process, and a remeshing strategy may be needed if the deformation becomes excessive. Two-phase models and the immersed boundary method made it possible to dig under solid structures. However, this is not possible with the ALE approach. This approach has been successfully applied to the study of scour around a vertical cylinder [Liu and García, 2008, Baykal et al., 2015], below a pipeline [Liang et al., 2005] or to the formation and migration of dunes in a river [van der Sande et al., 2025].

To simulate larger-scale problems, such as those affecting a section of a river or an estuary, models based on the previously mentioned 3D CFD-Exner equation are no longer applicable due to the required mesh resolution, particularly near the sediment bed and rigid walls. In order to overcome this constraint on mesh refinement, larger-scale models use boundary layer parametrizations to estimate the velocity at a certain distance from those surfaces, which enables them to use a much coarser resolution. These parametrization are generally based on certain hypothesis such as almost uniform flow conditions, and do not hold in the vicinity of a bridge pier, where the flow is not uniform at all. However,

large-scale models can be used to obtain more realistic boundary conditions to force a more local model, such as what was done in the work of Daou et al. [2018].

At even larger scales, landscape evolution models allow to simulate sediment transport processes at a geological time scale. They are usually applied to study the evolution of mountain ranges on Earth or other planets [Tucker and Hancock, 2010]. They usually introduce an extra term in the Exner equation to account for tectonic uplift and subsidence [Paola and Voller, 2005]. According to Campforts et al. [2020], landslides are the main phenomenon driving the geological evolution of mountain ranges. These rocks end up at the bottom of valleys and are conveyed by rivers. The momentum and continuity equations for the fluid are not solved, and instead, the erosion and transport of sediments by rivers are solved using either a subgrid model or a runoff model, depending on the scale of the problem to solve [Tucker and Hancock, 2010]. These models are the largest scale models possible for which all processes are modeled, and none are solved. The type of modeling varies greatly from case to case and depending on geography. For instance, Egholm et al. [2012] added sediment quarrying and bedrock abrasion by glaciers to study the formation of landscapes due to both glacial and fluvial erosion.

In conclusion, it has been shown that a wide variety of modeling approaches exist. Each one of them is relevant at a different temporal and spatial scale. There is always a trade-off between complexity/explicit representation of physical processes and computational cost. For the study of scour in the context of engineering applications, our understanding of the state-of-the-art suggests using the 3D CFD-ALE Exner equation approach.

1.5 Hydrodynamics processes

1.5.1 Navier-Stokes equations

The Navier-Stokes equations describe the motion of a fluid. They take their name after two physicists, Claude-Louis Navier (1785-1836) and Georges Gabriel Stokes (1819–1903) who derived those equations during the first half of the 19th century. They consist of two equations, one vectorial and one scalar, the momentum conservation and the mass conservation. Both equations can be obtained in their integral form by considering a small volume of fluid, applying Newton's second law, and writing the conservation of fluid mass, respectively. Then, the local form is retrieved using the divergence theorem.

As the motivation behind this work is the study of scour around bridges, the fluid considered is always water, which has a really low compressibility of approximately $4.6\,10^{-10}\,kg.m^{-1}.s^{-2}$ under ambient conditions. As an example, a pressure variation of $10^6\,kg.m^{-1}.s^{-2}$, corresponding to approximately 10 times the atmospheric pressure, the density of water is varying is only of 0.046%. For this reason, compressibility is almost always neglected when studying water flows except for acoustic studies or other specific

problems. The incompressible Navier-Stokes equations are written as:

$$\begin{aligned} \frac{\partial \boldsymbol{u}}{\partial t} + \nabla.(\boldsymbol{u} \otimes \boldsymbol{u}) = -\frac{1}{\rho_f}\nabla p + \boldsymbol{g} + \nabla.(2\nu \boldsymbol{S}\,), \\ \nabla.\boldsymbol{u} = 0\,, \end{aligned} \tag{1.5}$$

where the operator $\otimes$ is the dyadic product, $\boldsymbol{u}$ the fluid velocity, p the fluid pressure, $\boldsymbol{g}$ the gravitational acceleration, ρ_f the fluid density, and $\boldsymbol{S}$ is the strain rate tensor defined as:

$$\boldsymbol{S} = \frac{1}{2}\left(\nabla \boldsymbol{u} + (\nabla \boldsymbol{u})^T\right)\,. \tag{1.6}$$

For a given fluid mechanics problem characterized by a length scale L and a velocity scale U, the Reynolds number, named after Osborne Reynolds, is defined as:

$$Re = \frac{UL}{\nu}\,. \tag{1.7}$$

The Reynolds number describes the competition between inertial forces and viscous forces within the fluid. For small enough length scales and velocities, the viscous forces dominate, and the Navier-Stokes equations have well-behaved, steady solutions [Wilcox et al., 1998]. Such a flow is called laminar. As the Reynolds number increases, the flow transitions to turbulence, and the solution of the Navier-Stokes equations becomes chaotic with the presence of eddies of different sizes, orientations, and temporalities. Turbulence was already observed and studied by Leonardo da Vinci, who made various sketches of the phenomenon for different kinds of flows (see Figure 1.11). However, the first to derive a criterion for the appearance of turbulence was Reynolds [1883], as he identified that the birth of the eddies was associated with some definite value of the Reynolds number. He performed a famous experiment where he made water flow in glass tubes of different diameters, and he injected, along with the clear water, streaks of highly colored water. For small Reynolds numbers, the streaks would form perfectly straight lines in the tube. As the Reynolds number was increased, at some point in the glass tube, the flow would transition to turbulence, and the colored water would be mixed and fill the whole tube's section. The apparatus he used was conserved at Manchester University, which would allow his experiment to be reproduced a century later by N. H. Johannesen and C. Lowe. Images of the experiment are shown in Figure 1.11.

As stated before, turbulent regimes are characterized by the presence in the flow of chaotic secondary currents inducing the turbulent agitation [Chassaing, 2000]. In turbulent flow, the agitation results in a vigorous mixing of momentum far stronger than that due to molecular diffusivity. Another feature of turbulence is that it operates on a wide range of scales. Through a Fourier analysis, the frequency and wavelength associated with turbulence can be represented. The size of the largest, most energetic eddies is limited by the dimension of the problem considered, that is, the diameter of a pipe, the water depth in a channel, etc. On the other hand, for the shortest wavelength, the kinetic energy associated with the eddies is dissipated by viscosity. The size of the smallest existing eddies is determined by the balance of viscous and inertial forces. These eddies dissipate into

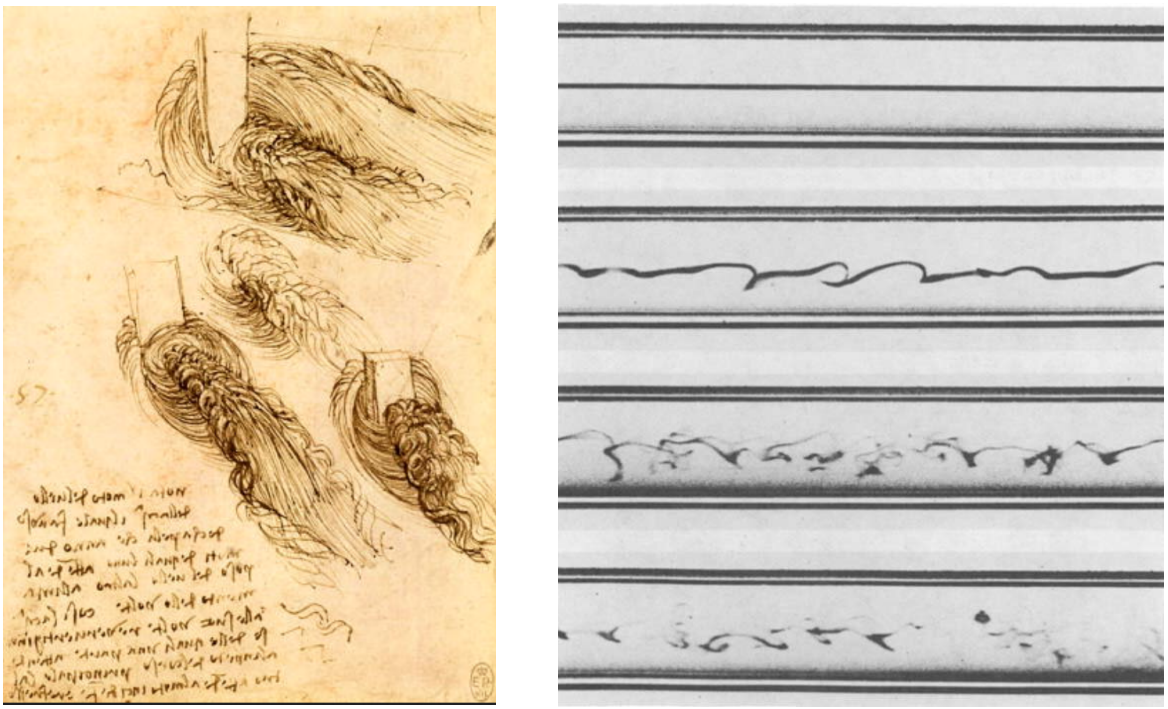

Figure 1.11: On the left, sketch of turbulence in wake flows drawn by Leonardo da Vinci. On the right, repetition of Reynolds dye experiment. Image taken from An Album of Fluid Motion Van Dyke [1982].

heat at a rate determined by the rate at which larger wavelengths transfer kinetic energy to the smaller ones $\epsilon = -dk/dt$. The scale of the smallest eddies is named after the soviet mathematician Andreï Kolmogorov, who first introduced it in his universal equilibrium theory in 1941b:

$$l = \left(\frac{\nu^3}{\epsilon}\right)^{1/4}, \quad t = \left(\frac{\nu}{\epsilon}\right)^{1/2}, \tag{1.8}$$

where l and t are the length and time scales of the smallest eddies.

Solving the Navier-Stokes equations numerically requires representing all the scales of the turbulent fluctuating motions. Therefore, the elements constituting the computational mesh should be of the same size or smaller than the Kolmogorov scale. Such a simulation is called a Direct Numerical Simulation (DNS). For problems of small dimensions and relatively low Reynolds numbers, this can be achieved. However, as the rate of energy transfer in the cascade process increases with the Reynolds number, the size of the smallest eddies diminishes, and consequently, the mesh resolution must be increased. For a given problem defined by a Reynolds number Re an estimation of the number of grid points N^3 needed to perform a DNS is given by the relation $N^3 \geq R_e^{9/4}$. Following this relation, at least 10^{13} grid points would be needed to study the flow in a river with a water height of 2 meters and a flow velocity of $0.5\,m.s^{-1}$. Other, more specific estimations can be found in the literature, such as Choi and Moin [2012], who proposed that for DNS of wall-bounded turbulent flows, the resolution must verify $N^3 \geq R_e^{37/14}$. The exponential increase of the grid resolution with the Reynolds number limits the use of DNS simulations to small scales, really far from the bridge scour application.

The turbulent agitation is composed of many secondary current fluctuations, swirling motions that cannot be simulated at an affordable computational cost. However, from a practical point of view, having knowledge of the flow mean properties is sufficient to treat many problems. Indeed, even though the instantaneous flow properties are extremely sensitive to initial conditions, the statistically averaged ones are not [Wilcox et al., 1998]. This difference between the extreme irregularity of the instantaneous fields and the well-behaved averaged flow is illustrated in Figure 1.12. It shows different instantaneous velocity profiles of a boundary layer flow over a flat surface. When these profiles are superposed, the theoretical logarithmic profile is retrieved. Cebeci [2012] obtained these results using the hydrogen bubble technique, which involves placing a fine electric wire perpendicular to the wall and using a small electrical impulse to electrolyze the water, creating small hydrogen bubbles along the wire. These bubbles are then advected by the flow, and the local velocity profile can be inferred from the displacement of the bubbles downstream of the wire.

Reynolds [1895] proposed to decompose the hydrodynamics into two parts. Each quantity f describing the flow is decomposed into a mean component noted $\langle f \rangle$ and a fluctuation f'.

$$f = \langle f \rangle + f'. \tag{1.9}$$

In the case of an incompressible flow, that would be the velocity $\boldsymbol{u}$ and the pressure p fields. The averaged field is obtained by applying an averaging operator, which could be

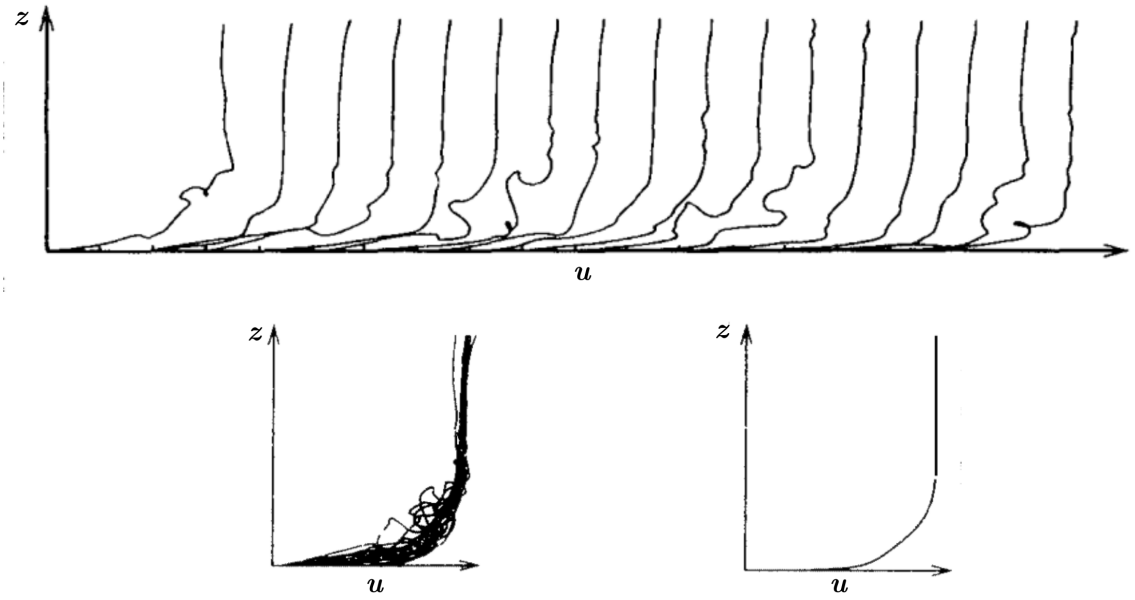

Figure 1.12: On the top, various instantaneous velocity profiles taken at the same position for a boundary layer flow. On the bottom, the superposition of these profiles is compared to a theoretical logarithmic boundary layer flow profile. Taken from Cebeci [2012]

a spatial, temporal, or statistical averaging. Here, the following temporal average is used:

$$\langle f \rangle = \frac{1}{T} \int_{t-T/2}^{t+T/2} f dt \,, \tag{1.10}$$

where T is the time window over which the field f is averaged. It is never given a definite value, but conceptually it should be large compared with the turbulent temporal fluctuations of the flow. The average operator is linear, and the average of a fluctuation is null. This yields the following properties:

- $\langle f_1 + f_2 \rangle = \langle f_1 \rangle + \langle f_2 \rangle$
- $\langle f_1 f_2 \rangle = \langle f_1 \rangle \langle f_2 \rangle + \langle f_1' f_2' \rangle$

Applying the averaging operator to the fluid momentum and continuity equations (eq. 1.5) yields:

$$\begin{aligned} \frac{\partial \langle \boldsymbol{u} \rangle}{\partial t} + \nabla . \left(\langle \boldsymbol{u} \rangle \otimes \langle \boldsymbol{u} \rangle \right) &= -\frac{1}{\rho_f} \nabla \langle p \rangle + \boldsymbol{g} + \nabla . \left(2\nu \langle \boldsymbol{S} \rangle - \langle \boldsymbol{u'} \otimes \boldsymbol{u'} \rangle \right) \,, \\ \nabla . \langle \boldsymbol{u} \rangle &= 0 \,. \end{aligned} \tag{1.11}$$

The continuity equation is unchanged, and the momentum equation is very similar except for one new term resulting from applying the average operator to the non-linear advection term. This new term, written on the right-hand side of the equation, together with the viscous stress tensor, involves the correlation of the velocity fluctuations. This tensor is

called the specific Reynolds tensor:

$$\boldsymbol{\tau_f} = -\left\langle \boldsymbol{u'} \otimes \boldsymbol{u'} \right\rangle . \tag{1.12}$$

It represents the effect of fluctuations on the mean flow and is generally considered as an effective turbulent stress with an isotropic part acting as a pressure and an off-diagonal part acting as an effective viscosity. The trace of this tensor is linked to the turbulent kinetic energy as follows:

$$\mathrm{tr}(\boldsymbol{\tau_f}) = -\left(\overline{u'u'} + \overline{v'v'} + \overline{w'w'}\right) = -2k\,, \tag{1.13}$$

where tr is the trace operator and u', v' and w' the three components of the fluctuating velocity $\boldsymbol{u'}$.

The problem as such is unclosed, as the Reynolds tensor brings 6 new unknowns for a total of 10 unknowns and 4 equations. To close the problem, the Boussinesq assumption is used to express the Reynolds stress tensor as an hydrostatic part by assuming isotropy of turbulence, which is $\left\langle {u'}^T u' \right\rangle = \left\langle {v'}^T v' \right\rangle = \left\langle {w'}^T w' \right\rangle$ and a deviatoric part expressed using an eddy vscosity ν_t and the averaged strain rate tensor $\langle \boldsymbol{S} \rangle$ which is traceless as $\mathrm{tr}(\langle \boldsymbol{S} \rangle) = \nabla . \langle \boldsymbol{u} \rangle = 0$ (see eq. 1.11). The Boussinesq assumption provides the following expression for the Reynolds stress:

$$\boldsymbol{\tau_f} = 2\nu_t \boldsymbol{S} - \frac{2}{3} k\, \boldsymbol{I_3}\,, \tag{1.14}$$

where $\boldsymbol{I_3}$ is the identity matrix.

Over the last century, many different turbulence models of various complexities have been proposed to express the eddy viscosity and close the RANS equations. The most classic example is the mixing length model introduced by the German physicist Ludwig Prandtl in 1925. Considering a shear flow $\langle \boldsymbol{u} \rangle = \langle u \rangle \, \boldsymbol{e_x}$, the mixing length hypothesis is written as follows:

$$\nu_t = l_{\mathrm{mix}}^2 \left\| \frac{d \langle u \rangle}{dz} \right\| , \tag{1.15}$$

where l_{mix} is the mixing length which corresponds to the distance over which the turbulent structures will retain their coherence before dispersing. Prandtl suggested that for flow near a solid wall, the mixing length is proportional to the distance to the wall. Despite its simplicity, this model has been applied to a wide range of problems in fluid mechanics.

More advanced turbulence models involve additional transport equations for turbulent quantities used to express the turbulent eddy viscosity. Kolmogorov [1941a] was the first to propose a two-equation model for turbulence. A classical one-equation model is the Spalart and Allmaras [1992] model, which uses the expression $\nu_t = \tilde{\nu} f_{v1}$ where the field $\tilde{\nu}$ temporal and spatial evolution is described by a transport equation and f_{v1} is a function of the ratio of $\tilde{\nu}$ to the kinematic viscosity of the fluid. The most widely used turbulence models in environmental fluid dynamics are two-equation models like the classical $k-\omega$ and $k-\epsilon$ models [Wilcox et al., 1998, Launder and Spalding, 1983]. Models with a higher number of equations exist up to 6 equations. A 6-equations model is referred as a Reynolds

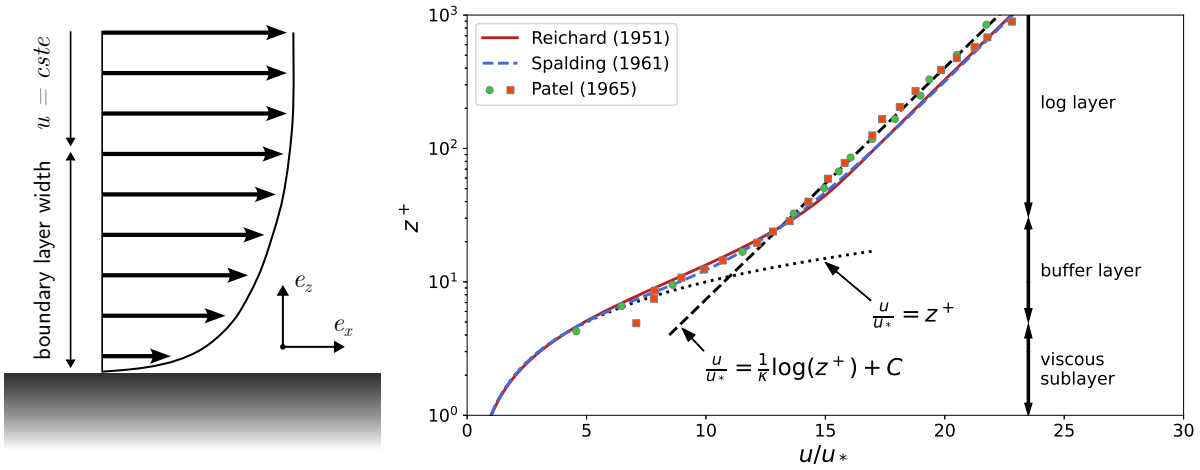

Figure 1.13: On the left, schematic of a boundary layer flow above a smooth plane surface. On the right, representation of the theoretical velocity profile in the viscous sublayer and in the log layer. The points are experimental results from Patel [1965] of mean flow velocity, in a circular tube (∘) and above a plane surface (□).

stress equation model for which there is a transport equation corresponding to every component of the Reynolds stress tensor, therefore avoiding the use of the Boussinesq assumption expressing the eddy viscosity and allowing for the account of the anisotropy of turbulence.

For the simplicity of the notation, the average operator $\langle\ \rangle$ is implicit in the rest of this work.

1.5.2 The law of the wall

This section provides a description of the flow in the vicinity of a plane surface. The flow is assumed unidirectional along the x direction, so that $\boldsymbol{u} = u(z)\boldsymbol{e_x}$, where z is the normal distance from the wall and $\boldsymbol{e_x}$ a unit vector tangential to the wall surface (see Figure 1.13).

Smooth wall

When a fluid flows over a surface, it forms a layer over which the flow velocity transitions from $u = 0$ at the wall, where the interaction with the wall yields a no-slip condition, to the position where the undisturbed velocity is reached. This transition zone is known as the boundary layer. The different physical quantities describing the problem are the fluid density ρ_f, the fluid kinematic viscosity ν, the shear stress exerted on the surface τ_b and the boundary-layer width δ_{bl}. From a dimensional analysis, a velocity scale $u_* = \sqrt{\tau_b/\rho_f}$ called the friction velocity can be defined, as well as a typical length scale for the flow ν/u_*. This is the characteristic length scale of the flow region directly in contact with

the wall, where viscous forces dominate over inertial forces [Chassaing, 2000]. This small layer, where turbulence completely vanishes due to viscous forces, is called the viscous sublayer. This means that the transfer of momentum between the fluid and the wall is only due to viscous stress. The RANS momentum equation (eq. 1.11) then simplifies to:

$$\nu \frac{\partial u}{\partial z} = \text{constant}\,, \quad \nu \left.\frac{\partial u}{\partial z}\right|_{z=0} = u_*^2\,. \tag{1.16}$$

In the viscous sublayer, the viscous shear stress is constant and equal to the shear stress exerted on the wall. This yields that the velocity increases linearly with the wall distance (see Figure 1.13):

$$\frac{u}{u_*} = \frac{z u_*}{\nu} = z^+\,, \tag{1.17}$$

where $z^+ = z u_*/\nu$ is called the dimensionless wall distance. This relation is valid for wall distances smaller than five times the viscous length scale ν/u_*, $z^+ < 5$.

At a larger distance from the wall, measurements have shown that the mean velocity varies logarithmically with the wall distance. This relation is called the law of the wall:

$$\frac{u}{u_*} = \frac{1}{\kappa} \ln\left(\frac{z}{z_0}\right)\,, \tag{1.18}$$

where z_0 is an integration constant, and κ is the von Kármán constant, which is estimated to $\kappa \approx 0.4$. When the surface is smooth, z_0 is proportional to ν/u_* and the law of the wall can be written as:

$$\frac{u}{u_*} = \frac{1}{\kappa} \ln\left(z^+\right) + C\,, \tag{1.19}$$

where C is a constant, which, in the case of a perfectly smooth surface, verifies $C \approx 5$. The logarithmic law of the wall is valid for $z^+ > 30$. The transitional layer, or buffer layer, is found between the viscous sublayer and the log layer ($5 < z^+ < 30$), where neither law applies. Different authors have proposed expressions to describe the velocity profile in these three layers with a unique formula, such as the following fit on experimental data proposed by Reichardt [1951]:

$$\frac{u}{u_*} = \frac{1}{\kappa} \ln(1 + \kappa z^+) + 7.8 \left(1 - e^{-\frac{z^+}{11}} - \frac{z^+}{11} e^{-0.33 z^+}\right)\,. \tag{1.20}$$

10 years later, Spalding et al. [1961] proposed another formula, which represents z^+ as a function of u/u_* instead of the opposite.

$$z^+ = \frac{u}{u_*} + 0.1108 \left[e^{\kappa \frac{u}{u_*}} - 1 - \kappa \frac{u}{u_*} - \frac{1}{2}\left(\kappa \frac{u}{u_*}\right)^2 - \frac{1}{6}\left(\kappa \frac{u}{u_*}\right)^3 - \frac{1}{24}\left(\kappa \frac{u}{u_*}\right)^4\right]\,. \tag{1.21}$$

The two formulas from Reichardt [1951] and Spalding et al. [1961] are represented in Figure 1.13 together with velocity measurements issued from the work of Patel [1965].

Rough wall

If the wall surface is rough, a new length scale is introduced in the problem, that is, the size of the roughness elements k_s, or roughness length/height. The roughness Reynolds number is defined as the ratio of the roughness length to the characteristic viscous length scale ν/u_*:

$$k_s^+ = \frac{k_s u_*}{\nu} \,. \tag{1.22}$$

Depending on the value of k_s, three different flow regimes can be identified. The distinction between these regimes is defined by two critical values of k^+_{Smooth} and k^+_{Rough}, which depend on the type of roughness. For sand grain roughness, the values $k^+_{Smooth} = 2.5$ and $k^+_{Rough} = 90$ are generally used. In the review work of Kadivar et al. [2021], the three roughness regimes are described as follows:

- For $k_s^+ \leq k^+_{Smooth}$, the roughness elements are fully embedded within the viscous sublayer, and the flow is said to be hydraulically smooth.
- For $k^+_{Smooth} < k_s^+ < k^+_{Rough}$, both the viscous effect and the roughness elements affect the velocity profile, and the flow is said to be transitionally rough.
- For $k_s^+ \geq k^+_{Rough}$, the roughness are big compared to the viscous length scale ν/u_*.

These different roughness regimes are summarized in Figure 1.14). For fully rough flows, the law of the wall still holds but the constant C is a function of k_s^+. For fully rough flows ($k_s^+ > k^+_{Rough}$), measurements from Nikuradse [1933] point to the relation:

$$C = B - \frac{1}{\kappa} \ln(k_s^+) \,, \tag{1.23}$$

where B is a constant which verifies $B \approx 8.5$. Different values are found in the literature, Wilcox et al. [1998] suggest $B = 8$, whereas Schlichting and Kestin [1961] $B = 8.5$. The values taken by B depend on how the equivalent roughness length was estimated. For sand roughness, k_s is proportional to the grain diameter d, and the coefficient can vary depending on the study. For instance, van Rijn [1984a] suggested the use of $k_s = 2.5 d_{90}$ and Roulund et al. [2005] used $k_s = 2.5 d_{50}$ in their work, where d_{50} and d_{90} are the diameters for which 50% and 90% of the particles are smaller, respectively. The law of the wall for fully rough flows can be rewritten as:

$$\frac{u}{u_*} = \frac{1}{\kappa} \ln\left(\frac{z}{k_s}\right) + B \,. \tag{1.24}$$

To extend this relation to describe boundary layer flows for all three roughness regimes, Ligrani and Moffat [1986] proposed a formula for B, which depends on k_s^+, that the authors fitted to match experimental results from Nikuradse [1933].

$$B = \left[C + \frac{1}{\kappa} \ln(k_s^+)\right] \left(1 - \sin\left(\frac{\pi \sigma_{sr}}{2}\right)\right) + 8.5 \sin\left(\frac{\pi \sigma_{sr}}{2}\right) \,, \tag{1.25}$$

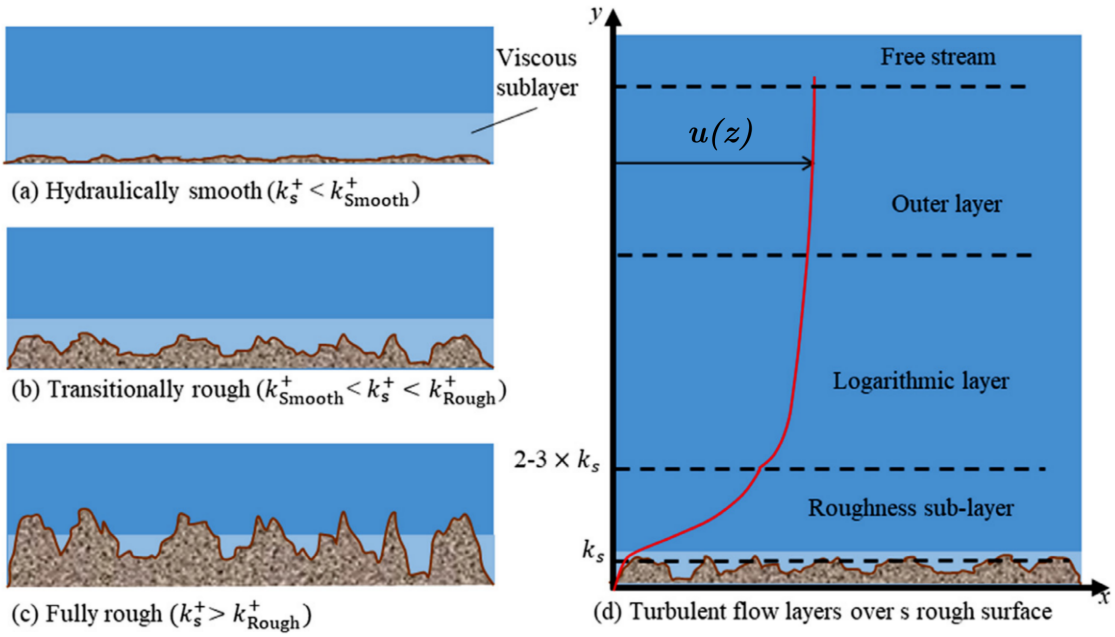

Figure 1.14: Turbulent flows over rough surfaces; (a) hydraulically smooth regime with roughness embedded under the viscous sublayer, (b) transitionally rough regime with partially destroyed viscous sublayer, (c) fully rough regime with completely destroyed viscous sublayer, (d) representation of the velocity profile and its three constituent layers, roughness sublayer, logarithmic layer and outer layer. Image taken from Kadivar et al. [2021].

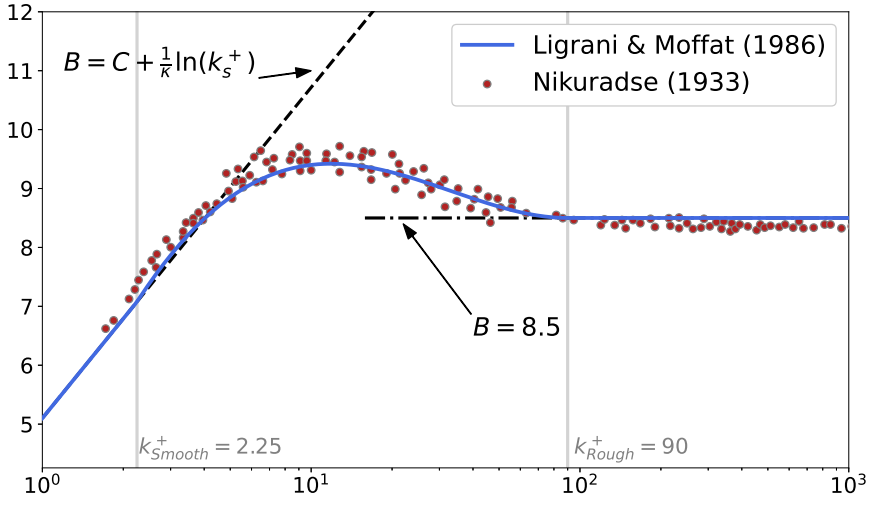

Figure 1.15: Fully rough flow log profile constant B as a function of the roughness Reynolds number k_s^+. Formula from Ligrani and Moffat [1986] and comparison with experimental data from Nikuradse [1933] for flows in rough pipes.

where $C = 5.1$ is considered constant, and σ_{sr} is a blending function allowing for a transition from a hydraulically smooth to rough regime. It is defined as:

$$\sigma_{sr} = \begin{cases} 0 & \text{if } k_s^+ < k_{smooth}^+ \,, \\ \frac{\ln(k_s^+/k_{smooth}^+)}{\ln(k_{rough}^+/k_{smooth}^+)} & \text{if } k_{smooth}^+ < k_s^+ < k_{rough}^+ \,, \\ 1 & \text{if } k_s^+ > k_{rough}^+ \,. \end{cases} \tag{1.26}$$

For $k_s^+ < k_{Smooth}^+$, equation 1.25 simplifies to $B = C + \frac{1}{\kappa}\ln(k_s^+)$ and equation 1.19 is retrieved. The formula from Ligrani and Moffat [1986] is represented in Figure 1.15 alongside experimental results from Nikuradse [1933].

These results will be useful to derive boundary conditions for turbulent models in the next section.

1.5.3 Wall boundary condition for turbulence

When using RANS modelling, additional turbulent variables are added to the problem, such as $\tilde{\nu}$ for the Spalart and Allmaras [1992], k and ϵ for the $k-\epsilon$ [Launder and Spalding, 1983] or k and ω for the $k-\omega$ model [Wilcox et al., 1998] or the $k-\omega\,SST$ from Menter [1994]. The eddy viscosity is expressed with these variables, for instance, $\nu_t = k/\omega$ for the $k-\omega$ model, and specific boundary conditions are needed to damp turbulence close to the wall and retrieve the law of the wall. This specific wall treatment is done through wall function. One difficulty for a lot of turbulence models is that the turbulent variables do not have a finite value at the wall surface, except for ω, as will be seen later. For this reason, wall functions are applied at a distance from the wall surface (the first grid point), and the boundary conditions therefore depend on the distance from the wall. In particular, the wall functions depend on whether the position where the boundary condition is applied is located in the viscous sublayer or further away from the wall in the logarithmic zone.

Turbulence models based on k and ω are known for their good performance in the presence of adverse pressure gradients and are therefore suited to simulate flows around obstacles or above bedforms. The $k-\omega\,SST$ turbulence model, in particular, has the ability to handle both free shear and boundary layer flows. For these reason it is the only turbulence model used throughout this work. The exhaustive presentation of the $k-\omega\,SST$ (transport equations, blending functions, and coefficients) is provided in the chapter 2, dedicated to the description of *sedExnerFoam*. This section focuses on the wall boundary conditions for k and ω to handle both smooth and rough surfaces.

Smooth wall conditions

Beginning with the case of a smooth wall, the most classical wall functions are detailed in the work of Wilcox et al. [1998]. He simplified the equation for the $k-\omega$ model in the

log layer to derive the boundary conditions:

$$k = \frac{u_*^2}{\sqrt{\beta_*}}, \quad \omega = \frac{u_*}{\sqrt{\beta_*}\kappa z_1} \tag{1.27}$$

where $\beta_* = 0.09$ is a constant of the model. Combining these two equations yields the following linear relation for the eddy viscosity in the log layer:

$$\nu_t = \kappa u_* z_1 . \tag{1.28}$$

By expressing u_* as a function of k and injecting it in the expression of ω, the boundary condition for ω in the log-layer is obtained:

$$\omega_{log} = \frac{\sqrt{k}}{\beta_*^{1/4}\kappa z_1} \tag{1.29}$$

where z_1 is the distance of the first cell center to the wall.

The previous boundary condition does not hold when the distance to the wall is reduced. At the wall, the no-slip condition on the velocity yields $k = 0$. Examining the differential equations as the wall distance tends towards 0 shows that the quantity $\frac{\beta_* z_1^2 \omega}{\nu}$ tends toward a constant value. This constant is written as $6\beta_1$ where $\beta_1 = 0.075$ is a constant of the model, leading to the following boundary condition for ω in the viscous sublayer:

$$\omega_{vis} = \frac{6\nu}{\beta_1 z_1^2} . \tag{1.30}$$

A feature specific to $k-\omega$ models and initially recognized by Saffman [1970] is the fact that ω can also be specified at the wall. Using this feature, Menter [1993] proposed an alternative boundary condition to equation 1.30 for ω to be applied at the wall surface:

$$\omega|_{z=0} = \frac{60\nu}{\beta_1 z_1^2} \tag{1.31}$$

Numerically, imposing the boundary condition at the wall presents an advantage because there is then no need to change the solution at interior grid points.

Rough wall conditions

Once again, following the idea of Saffman [1970] that ω can be specified directly at the wall, Wilcox et al. [1998] proposed the following rough wall condition:

$$\omega = \frac{u_*^2}{\nu} S_R , \quad \text{at } y = 0 \tag{1.32}$$

where S_R is a roughness coefficient, which depends on k_s^+. In the first version of his book in 1993, he had initially proposed the following expression for S_R:

$$S_R = \begin{cases} \left(\frac{50}{k_s^+}\right)^2 & \text{if } k_s^+ < 25 , \\ \frac{100}{k_s^+} & \text{if } k_s^+ \geq 25 . \end{cases} \tag{1.33}$$

Roulund et al. [2005] used a modified version of this formula. In 2006, Wilcox et al. proposed a revision of the initial formula, which is indicated below.

$$S_R = \begin{cases} \left(\frac{200}{k_s^+}\right)^2 & \text{if } k_s^+ < 5\,, \\ \frac{100}{k_s^+} + \left[\left(\frac{200}{k_s^+}\right)^2 - \frac{100}{k_s^+}\right] e^{k_s^+ - 5} & \text{if } k_s^+ \geq 5\,. \end{cases} \tag{1.34}$$

For a hydraulically smooth flow (when k_s^+ is small), this yields the following condition at the wall:

$$\omega = \frac{40000\nu}{k_s^2}\,, \tag{1.35}$$

which is very similar to equation 1.30. Wilcox et al. [1998] suggested that this rough formulation should be preferred over equation 1.30 even for a perfectly smooth wall. This formulation was used by Fuhrman et al. [2010], who modified the coefficients and suggested that for rough flow, using a zero-gradient condition for k is preferred over the classical null condition used for hydraulically smooth flows.

The main drawback of this method is that a really fine mesh near walls is typically needed to achieve mesh convergence and accurately estimate the bed shear stress. This has motivated various authors to develop other wall functions. Knopp et al. [2009] derived boundary conditions for k and ω suited for both hydraulically smooth and rough conditions. They used the expression of the eddy viscosity in the log layer for a hydraulically rough flow proposed by Aupoix and Spalart [2003]:

$$\nu_t = \kappa u_*(z + d_0)\,, \tag{1.36}$$

where d_0 is the hydrodynamic roughness length defined as $d_0 \approx 0.03 k_s$. Using this expression of the eddy viscosity to integrate the equation $\nu_t du/dz = 0$ yields the following expression for the logarithmic velocity profile:

$$\frac{u}{u_*} = \frac{1}{\kappa} \ln\left(\frac{z + d_0}{d_0}\right)\,. \tag{1.37}$$

Using the previous formulation of the near-wall eddy viscosity, the relation $\nu_t = k/\omega$, and the fact that for fully rough flows, the viscous sublayer is completely disturbed so that k can be computed using 1.27, they obtained the following expression for ω near the wall:

$$\omega = \frac{u_*}{\beta_*^{1/2}\kappa(z + d_0)}\,. \tag{1.38}$$

In order to adapt the expression of k and ω near the rough wall to transitionally rough and smooth flows, they limited the value of ω at the wall by the solution from Menter [1993] for a smooth surface (see eq. 1.31) and introduced two blending functions. A first one, to limit the values of k for $k_s^+ < k_{Rough}^+$, and a second one to define a modified hydrodynamical roughness $\tilde{d_0}$ as:

$$\tilde{d_0} = d_0 \min\left[1, \left(\frac{k_s^+}{30}\right)^{2/3}\right] \min\left[1, \left(\frac{k_s^+}{45}\right)^{1/4}\right] \min\left[1, \left(\frac{k_s^+}{60}\right)^{1/4}\right]\,. \tag{1.39}$$

The resulting boundary conditions for k and ω at the wall are as follows:

$$k|_{z=0} = \frac{u_*^2}{\sqrt{\beta^*}} \min\left(1, \frac{k_s^+}{90}\right), \quad \omega|_{z=0} = \min\left(\frac{u_*}{\beta_*^{1/2}\kappa\tilde{d_0}}, \frac{60\nu}{\beta_1 z_1^2}\right) \tag{1.40}$$

In order to reduce the effect of mesh resolution on the formulation from Knopp et al. [2009], Lee [2018] proposed to discretize the following equation to take into account the mesh resolution in the boundary condition:

$$u_*^2 = \nu_t \frac{\partial u}{\partial z} = 0 \rightarrow u_*^2 = \nu_t|_{z=0} \frac{u|_{z=z_1}}{z_1}, \tag{1.41}$$

which is obtained considering the no slip condition $u|_{z=0} = 0$ at the wall. Now, using equation 1.37 to obtain the velocity at the first grid point above the wall $u|_{z=z_1}$, the following expression for the eddy viscosity at the wall is obtained:

$$\nu_t|_{z=0} = \frac{\kappa u_* z_1}{\ln((z_1 + d_0)/d_0)}. \tag{1.42}$$

Then, using the same methodology as Knopp et al. [2009], another boundary condition for ω is obtained:

$$\omega|_{z=0} = \min\left(\frac{u_* \ln\left(\frac{z_1+d_0}{d_0}\right)}{\beta_*^{1/2}\kappa\tilde{d_0}}, \frac{60\nu}{\beta_* z_1^2}\right). \tag{1.43}$$

When modeling the evolution of riverbed morphology using the Exner equation, the different sediment fluxes are computed using empirical formulas with bed shear stress as the input parameter. As an accurate estimation of bed shear stress depends heavily on the bed boundary conditions, the modeling of the bed roughness can significantly affect the results of morphological evolution simulations.

1.6 Sediment transport modeling

The modeling approach used in this work is based on the Exner equation (eq. 1.4). As explained previously, the granular phase is not solved, and sediment transport fluxes are computed from the shear stress exerted on the bed using empirical formulas. Sediment transport is typically categorized into two distinct modes, which are the bedload transport and the suspended load transport [Fredsoe and Deigaard, 1992]. Bedload transport refers to sediments that move along the riverbed. These sediments slide, roll, and make small jumps (saltation), but never lose contact with the riverbed for extended time periods. The suspended load comprises particles eroded from the bed and carried by the flow. A third transport mode called wash load is sometimes mentioned. Unlike suspended load, particles never come into contact with the bed in wash load transport. In the present work, no distinction is made between suspended and wash load, with both being referred to as suspended load. The following section provides a description of these processes,

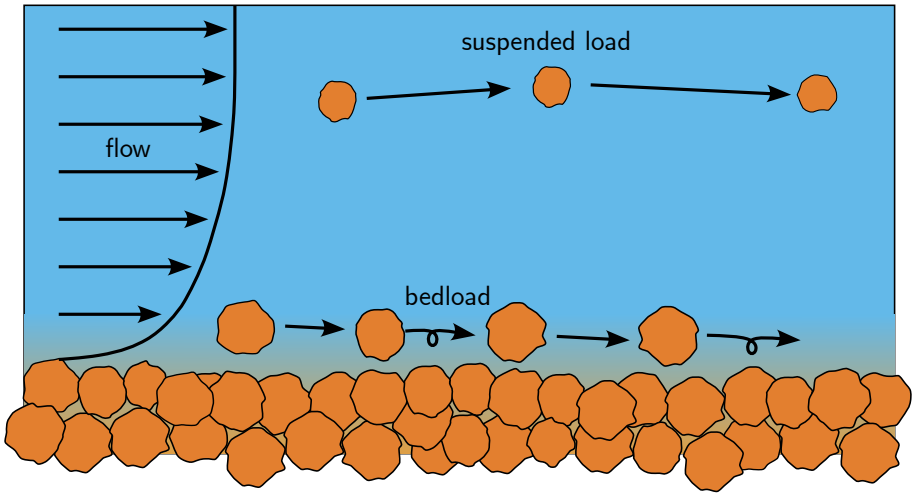

Figure 1.16: Sketch of bed load and suspended load sediment transport.

which are represented on the schematic in Figure 1.16. The final part of this state-of-the-art review begins with an explanation of the motion threshold and how it is modeled. This is followed by a description of how sediments are entrained by the flow as soon as the threshold is exceeded. Finally, the saturation of the bedload flux is described. This is a first-order approximation used to model the effect of the inertia of grains in the bedload layer.

1.6.1 Threshold of motion

The first attempt to propose a rational approach to sediment transport and morphology evolution during flood was made by Paul Du Boys, a French engineer working for the water services on the Rhone river. He was the first in 1879 to propose a mathematical approach to compute sediment transport entrainment rate as a function of the entrainment force defined as the product of the fluid density, the water depth, and the slope [Hager, 2005]. Half a century later, in the 1930's, Albert Frank Shields made measurements of the motion threshold already highlighted by du Boys in an experimental flume. The motion threshold is the result of an equilibrium between the tractive force and the resistive forces. Let us consider an equilibrium between the forces exerted by a flowing fluid of density ρ_f on a spherical particle of diameter d and of density $\rho_s > \rho_f$ positioned on a flat bed (see Figure 1.17).

- buoyancy: $\boldsymbol{F_B} = -(\rho_s - \rho_f) g \frac{\pi d^3}{6} \boldsymbol{e_z}$.
- friction force: $\boldsymbol{F_R} = -\mu_f (\rho_s - \rho_f) g \frac{\pi d^3}{6} \boldsymbol{e_x}$, where μ_f is the friction coefficient.
- drag force: $\boldsymbol{F_D} = \frac{\pi d^2}{2} \rho_f u_*^2 C_D \boldsymbol{e_x}$.

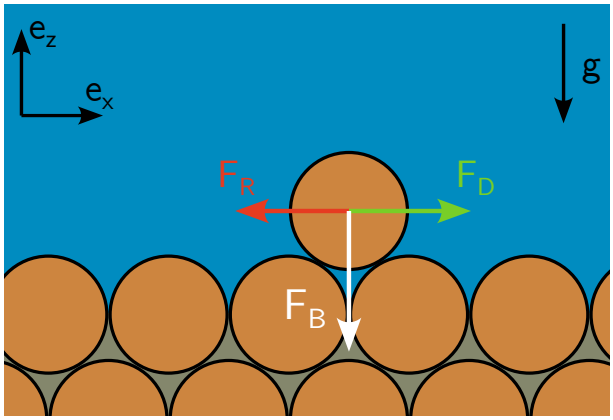

Figure 1.17: Sketch of the different forces exerted on a spherical particle on a sediment bed.

The resistive and the drag force cancel each other out so that their sum is null. By writing this equality, the following equation is obtained:

$$\frac{u_*^2}{(s-1)gd} = \frac{\mu_f}{3C_D}\,, \tag{1.44}$$

where $s = \rho_s/\rho_f$ is the density ratio. The left-hand term is the Shields number, which is the shear stress rendered dimensionless by the diameter, the fluid and sediment densities and the gravity acceleration. The particles start to move when the Shields number $\theta = \frac{u_*^2}{(s-1)gd}$ exceeds a critical value θ_c.

The precise characterization of the transport threshold is somewhat subjective [Miller et al., 1977] and several methods have been proposed to evaluate it. For laboratory measurements, the most natural method is direct visual observation. When close to the motion threshold, individual grains can be seen moving, even though the movement is not general. Therefore, there is subjectivity in identifying the moment when motion becomes a general characteristic of the flow rather than a stochastic phenomenon. In natural environments, isolated particles can be seen moving as soon as the fluid is not completely still [Paintal, 1971], due to variations in grain size and shape, as well as the presence of turbulence. Another method used by Parker and Klingeman [1982] is to set a measurable reference transport value below, which the threshold is not considered to have been reached. The subjectivity then comes from the choice of the bedload transport value used as a reference which should be as small as possible but still measurable with some accuracy.

Initially, Shields [1936] presented the critical Shields as a function of the Reynolds number associated with the grain diameter and the friction velocity, $Re_* = u_* d/\nu$. Due to the difficulty in precisely identifying the motion threshold, he represented his experimental data with a narrow band below which the bed shear stress is insufficient to cause sediment movement and the grains stay still, but above which sediments are moving. The threshold exists somewhere within the band [Miller et al., 1977] so that for a given value of Re_*,

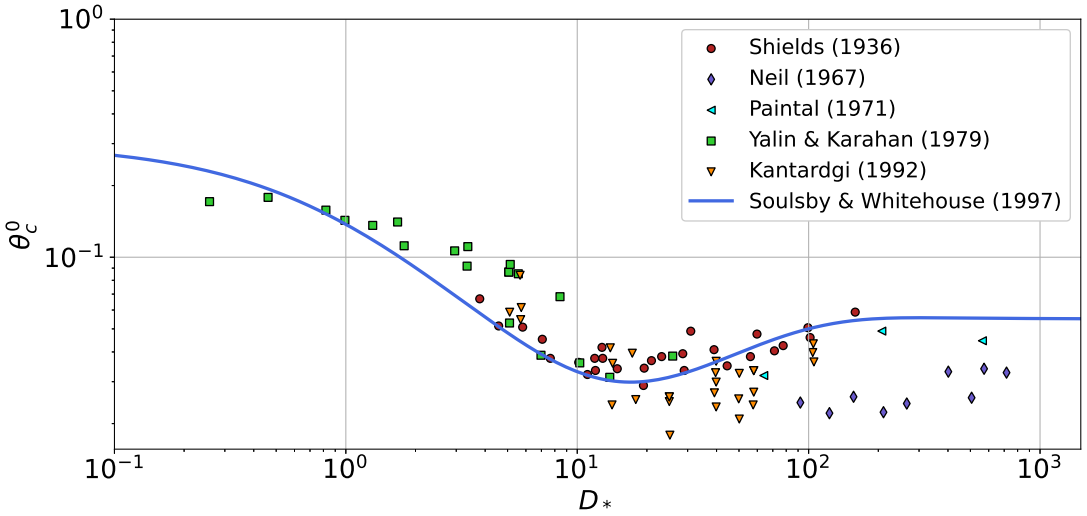

Figure 1.18: The threshold of motion as a function of the dimensionless diameter D_*. Experimental data from Shields [1936], Neill [1967], Paintal [1971], Yalin and Karahan [1979], Kantardgi [1992]. The equation proposed by Soulsby and Whitehouse [1997] is represented by a solid line.

the critical Shields number lies between two limits. His experiments were made in a channel with fully developed velocity profiles and a flat bed made of a layer of sediments. For the granular material, he used sand of different sizes, as well as other materials of different densities, such as amber, ignite, and granite. Chiew and Parker [1994] conducted experiments on an inclined bed to characterize the influence of the local bed slope on the motion threshold.

Since the pioneering work of Shields [1936], many experimental studies of the motion threshold have been conducted. Vanoni [1964] studied the incipient motion of glass beads and quartz sand in a straight channel under steady flow conditions, and Kantardgi [1992] investigated the threshold of motion under the combined influence of waves and currents. Yalin and Karahan [1979] studied the initiation of sediment motion under hydraulically smooth flow conditions, that is, when the grains at the bed interface are embedded in the viscous sublayer. For some of their experiments, they used glycerine instead of water to increase the width of the viscous sublayer. At the same time, they compiled data of various experiments under turbulent flow conditions and provided an extended Shield' diagram covering a wide range of values for Re_*. A compilation of some experimental measurements of the incipient motion of sediments is shown in Figure 1.18.

In practice, having θ_c depend on Re_* is not convenient because the friction velocity has to be known beforehand. In order to circumvent this difficulty, another dimensionless number can be defined from the previous two. Brownlie [1983] proposed a formula based

the dimensionless number $\sqrt{(s-1)gd^3}/\nu$.

$$\theta_c = 0.22 \left(\frac{\sqrt{(s-1)gd^3}}{\nu} \right)^{-0.6} + 0.06\, 10^{-7.7\left(\frac{\sqrt{(s-1)gd^3}}{\nu}\right)^{-0.6}} . \tag{1.45}$$

Afterwards, multiple authors have preferred the use of the dimensionless diameter D_* defined as follows:

$$D_* = \left(\frac{Re_*^2}{\theta} \right)^{1/3} = d \left(\frac{(s-1)g}{\nu^2} \right)^{1/3} . \tag{1.46}$$

One widely used formula to compute the motion threshold has been proposed by Soulsby and Whitehouse [1997]. It is written as follows:

$$\theta_c^0 = \frac{0.3}{1 + 1.2D_*} + 0.055 \left(1 - e^{-0.02D_*}\right) . \tag{1.47}$$

For comparison, the relation is represented in Figure 1.18 together with experimental data. Many other similar formulas can be found in the literature, such as the ones from Brownlie [1983], Zanke [2003] or Miedema [2008].

If the sediment bed is not flat, the motion threshold is modified. A slope correction of the critical Shields number can be obtained analytically using the same steps as those used to derive equation 1.44. The local slope angle is noted β_s, and the unit vectors $\boldsymbol{e_x}$ and $\boldsymbol{e_z}$ are tangential and normal to the bed, respectively, so that the gravity acceleration is $\boldsymbol{g} = \sin(\beta_s)\boldsymbol{e_x} - \cos(\beta_s)\boldsymbol{e_z}$. The different forces acting on a spherical bed particle are:

- buoyancy: $\boldsymbol{F_B} = -(\rho_s - \rho_f) g \frac{\pi d^3}{6} (\cos(\beta_s)\boldsymbol{e_z} - \sin(\beta_s)\boldsymbol{e_x})$.
- resistive force: $\boldsymbol{F_R} = -\mu_f (\rho_s - \rho_f) g \frac{\pi d^3}{6} \cos(\beta_s)\boldsymbol{e_x}$.
- drag force: $\boldsymbol{F_D} = \frac{\pi d^2}{2} \rho_f u_*^2 C_D \boldsymbol{e_x}$.

By writing the sum of these three forces, the following slope correction is obtained:

$$\frac{u_*^2}{(s-1)gd} = \frac{\mu_f \cos(\beta_s) - \sin(\beta_s)}{3C_D} = \theta_c^0 \cos(\beta_s) \left(1 - \frac{\tan(\beta_s)}{\mu_f}\right) , \tag{1.48}$$

where θ_c^0 is the critical Shields number on a flat bed. Other corrections exist, such as the one proposed by Fredsoe and Deigaard [1992], which uses the local slope angle, but also the angle between the direction of the shear stress and the steepest slope direction.

1.6.2 Entrainment of sediments

Once the shear stress applied to the bed surpasses the critical motion threshold, sediment particles begin to roll and slide along the bed, leading to an increase in the amount of material entrained by the flow. When modeling sediment transport using the Exner equation, it is essential to accurately characterize the relationship between bed shear stress and the volume of entrained sediment. As previously discussed, sediment transport occurs through two primary modes: bedload and suspended load. The partitioning between

these modes is influenced by factors such as grain size and shape, as well as the turbulent structures within the flow. The following section provides a review on the modeling of these two transport modes.

Bedload transport

One of the earliest and most influential studies was conducted by Meyer-Peter and Müller [1948], who developed a widely used bedload transport formula based on flume experiments with uniform gravel under steady flow conditions. Their results demonstrated a nonlinear relationship between sediment flux and excess shear stress, which remains a cornerstone in sediment transport modeling. Their formula expresses the dimensionless bedload transport rate as proportional to the excess Shields stress raised to the 3/2 power as:

$$\phi_b = 8\varpi(\theta - \theta_c)^{3/2}\,. \tag{1.49}$$

where ϕ_b is the Einstein number, that is, the bedload flux rendered dimensionless by dividing it by the quantity $\sqrt{(s-1)gd^3}$:

$$\phi_b = \frac{q_b}{\sqrt{(s-1)gd^3}}\,. \tag{1.50}$$

Many other authors have provided formulas following a power law, such as van Rijn [1984a], Nielsen [1992], Ribberink [1998]. More complex formulations have been proposed to capture additional physical processes. For instance, Einstein [1950] introduced a probabilistic model that incorporates the stochastic nature of particle entrainment and travel distances. Another notable formulation was proposed by Camenen and Larson [2005], which does not impose a fixed motion threshold, allowing for a residual bedload flux even when the bed shear stress is below the traditional threshold for particle motion. It is written as follows:

$$\phi_b = 12\,\theta^{1.5} e^{-4.5\theta_c/\theta}\,. \tag{1.51}$$

Later, Parker [1990] developed a surface-based bedload transport relation that accounts for the grain-size distribution of the bed surface, recognizing that the surface layer controls the initiation of motion. Building on this, Wilcock and Crowe [2003] developed a two-fraction model to describe the transport of sand and gravel mixtures, incorporating the effects of grain hiding and exposure. This model is particularly useful in natural rivers where mixed sediment beds are common, and sand infiltration affects the mobility of coarser grains.

Modeling bedload transport remains a significant challenge due to the high variability and inherent uncertainty of measured data [Recking, 2010]. Bedload flux is often characterized by large scatter, even under seemingly uniform flow conditions, resulting from the stochastic nature of particle motion, intermittent transport, and spatial heterogeneity of the riverbed. As a result, increasing the complexity of predictive formulas by incorporating more variables or finer physical detail does not necessarily lead to better performance or more accurate predictions. For this reason, simple formulas such as the one proposed by Meyer-Peter and Müller [1948] remain widely used today.

Suspended load transport

Unlike bedload, suspended load generally consists of finer particles such as silts and clays that are carried within the water column by turbulent eddies. The transport of suspended sediment is governed by the balance between downward gravitational settling and upward turbulent diffusion. The Rouse number, named after the hydraulician Hunter Rouse (March 29, 1906 – October 16, 1996) characterizes the importance of the suspended load over bedload. It is defined as the ratio of the settling velocity of particles w_s to the characteristic velocity scale associated with turbulent vertical motion estimated as κu_*. The Rouse number is written as:

$$R_o = \frac{\sigma_c w_s}{\kappa u_*} \tag{1.52}$$

where σ_c is the Schmidt number defined as the ratio of the eddy viscosity to the turbulent diffusivity for the suspended sediments. For low values of R_o, upward turbulent diffusion dominates over the settling and the major part of transport is suspended load. Conversely, large values of R_o indicate that bedload transport dominates.

The vertical distribution of suspended sediment volume fraction c_s can be described using the advection diffusion equation:

$$\frac{\partial c_s}{\partial t} + \nabla.[(\boldsymbol{u} + \boldsymbol{w_s})c_s] = \nabla.(\epsilon_s \nabla c_s)\,, \tag{1.53}$$

where $\epsilon_s = \nu_t/\sigma_c$ is the turbulent diffusivity for suspended sediments. While these formulations are widely applied in both natural and engineered systems, modeling suspended load accurately remains challenging. It requires reliable estimates of parameters such as the settling velocity, turbulence structure, and sediment availability. Furthermore, sediment entrainment from the bed into suspension must be specified through empirical relationships, such as those proposed by Smith and McLean [1977] or van Rijn [1984b], which relate reference concentration to bed shear stress and grain size.

1.6.3 Saturation of the bedload flux

Various empirical formulas have previously been proposed to estimate the bedload flux. When the flow is not uniform, for example, due to a sudden increase in discharge or the presence of bedforms, the actual sediment flux $\boldsymbol{q_b}$ does not adjust instantaneously to the new flow conditions. Instead, it relaxes toward the saturated flux $\boldsymbol{q_{sat}}$ over a characteristic spatial scale known as the saturation length L_{sat}. The schematic in Figure 1.19 illustrates the relaxation of the bedload flux in a situation where a fluid flows over a patch of sand.

In the presence of beforms, the bedload flux can be described with the following equation [Charru et al., 2013]:

$$T_{sat}\frac{\partial q_b}{\partial t} + L_{sat}\frac{\partial q_b}{\partial x} = q_{sat} - q_b\,, \tag{1.54}$$

where T_{sat} is a characteristic time needed for the grain to react to a change of the bed shear stress called saturation time. However T_{sat} is small compared to the characteristic

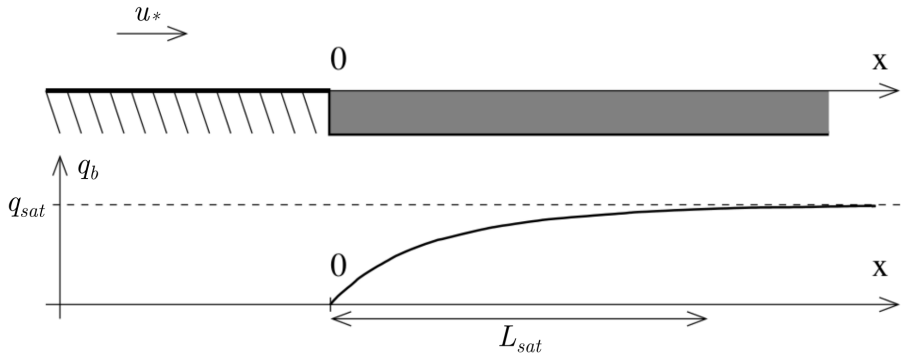

Figure 1.19: Illustration of the spatial relaxation of the bedload flux when the fluid passes from a rigid bed to an erodible sediment bed. Image taken from Andreotti et al. [2002b].

time associated with bedforms development, so that it is not taken into account in most studies [Kouakou and Lagrée, 2006, Gadal et al., 2019].

For aeolian sediment transport, the density ratio $s = \rho_s/\rho_f$ is large and the bedload transport consists in grain making large jumps instead of rolling and sliding along the bed. This specific transport mode is called saltation. There is a general consensus that the saturation length is controlled by grain inertia. L_{sat} represents the average downstream distance over which a particle, once entrained, contributes to transport before being redeposited Charru et al. [2013] so that L_{sat} is proportional to the grain size:

$$L_{sat} \propto \frac{\rho_s}{\rho_f} d\,. \tag{1.55}$$

Because of the high density difference, it leads to saturation length of the order 1 meter [Vriend and Bacik, 2025]. For subaqueous sediment transport, no definite agreement has been reached regarding the mechanism responsible for the saturation length, which could either be due to erosion-deposition competition or grain inertia as in the aeolian case. The following formula was suggested by CHARRU and HINCH [2006] to estimate L_{sat} for underwater situations:

$$L_{sat} \propto \frac{\overline{u}}{w_s} d\,. \tag{1.56}$$

More recently Pähtz et al. [2014] provided a general expression for the saturation length which can be applied both for aeolian and subaqueous studies.

The concept of bedload saturation plays a critical role in morphodynamics, particularly in modeling bed evolution and the formation of bedforms, such as dunes and ripples. Due to the finite saturation length, the distance required for sediment flux to adjust to changes in flow conditions, a spatial lag arises between the applied bed shear stress and the resulting sediment transport. This lag causes a shift in the position of the maximum bedload flux relative to bedform features. Since the growth and migration of dunes are strongly influenced by the location of this maximum flux with respect to the dune crest, accounting for the effect of saturation is essential for accurately predicting bedform dynamics.

1.7 Conclusion

Modeling scour around a cylinder or similar obstacle remains a key challenge in hydraulic and coastal engineering, due to its critical implications for the stability and safety of structures such as bridge piers, offshore platforms, and monopiles. The first part of this state-of-the-art review has been dedicated to describing the scour process and examining various sediment transport modeling approaches, with the goal of identifying the most suitable framework for this PhD thesis. The objective of the thesis is to develop a sediment transport and morphological evolution model tailored to the study of scour at engineering-relevant scales. This section also includes an overview of the complex flow structures that form around cylindrical obstacles, a synthesis of major experimental studies on scour, and a classification of the main types of existing scour models.

After identifying the Arbitrary Lagrangian–Eulerian (ALE) strategy as the most suitable approach for this study, the second part of the chapter focused on the detailed modeling of flow, turbulence, and sediment transport processes. Particular attention was given to the use of RANS equations for turbulence modeling, which provide a practical balance between computational cost and the ability to capture key flow features relevant to sediment transport. Since sediment transport is primarily driven by bed shear stress, accurately capturing the interactions between the flow and the sediment bed is essential. To this end, the treatment of boundary layer flows over both smooth and rough surfaces was addressed. This was followed by a discussion on the use of wall functions for the $k-\omega\,SST$ turbulence model, which are of primary importance to accurately capture the flow behavior near solid boundaries.

The modeling of sediment transport was then examined in detail, including the definition of the motion threshold, the characterization of both bedload and suspended load transport, and the use of empirical formulas to estimate the amount of sediment entrained by the flow. In particular, the concept of bedload flux saturation was introduced to account for the non-instantaneous adjustment of sediment transport to changes in flow conditions. This phenomenon reflects the finite distance known as the saturation length over which the bedload flux evolves toward its equilibrium value. Incorporating this concept is essential for capturing the spatial lag between the applied shear stress and the sediment response, which plays a critical role in the accurate prediction of scour patterns and bedform development.

Chapter 2

Model description

This chapter presents a comprehensive description of the developed model, structured into two main parts, each serving a distinct purpose. The first part focuses on the mathematical formulation of the model. It begins with the governing equations of hydrodynamics, including the treatment of turbulence and the implementation of wall functions for near-wall turbulent quantities. This is followed by a detailed discussion of sediment transport processes, covering the threshold of motion and various empirical formulas for bedload and suspended load transport. The second part introduces the numerical framework, with an overview of the finite volume and finite area methods employed. Key numerical aspects are then discussed, including the pressure–velocity coupling algorithm used to solve the fluid momentum and continuity equations. Finally, the specific numerical treatment of the Exner equation, which governs the sediment bed evolution, is presented in detail.

2.1 Model mathematical description

2.2 Hydrodynamics and turbulence

The model presented in this work has been developed starting from an existing solver named *pimpleFoam*, a transient solver for one-phase incompressible flows, and based on the PIMPLE algorithm, which is detailed later in this work. The hydrodynamics is described by the incompressible filtered Navier-Stokes equations:

$$\begin{aligned} \frac{\partial \boldsymbol{u}}{\partial t} + \nabla.(\boldsymbol{u} \otimes \boldsymbol{u}) = -\frac{1}{\rho_f}\nabla p + \boldsymbol{g} + \nabla.(2\nu \boldsymbol{S} + \boldsymbol{\tau_f})\,, \\ \nabla.\boldsymbol{u} = 0\,, \end{aligned} \tag{2.1}$$

where $\boldsymbol{\tau_f}$ is a tensor, whose definition depends on the type of filter used. It can either be the specific Reynolds stress tensor to run Reynolds Averaged Navier-Stokes (RANS) simulations, a subgrid scale stress tensor when performing LES, or the null tensor in case of laminar simulation or DNS. The model makes use of the vast range of possibilities offered by *OpenFOAM*, and lets the user choose freely the kind of filtering to be applied to

equation 2.1. This is done by changing entries in a file *turbulenceProperties*. In this work however, the numerical simulations presented are either laminar cases (no filtering of the Navier-Stokes equations) or unsteady RANS simulations. It should be pointed out that the major part of the uncertainties in sediment transport simulation relying on the Exner equation comes from the empirical sediment transport closures described in sections 2.4 and 2.3. Those formulas were fitted on experimental measurements of sediment transport in straight channels where the flow is uniform. Therefore, they establish a link between the mean quantities transported and the mean shear stress exerted by the flow. In general, the largest source of error in simulating morphological evolution arises from these empirical formulas used to estimate sediment transport. Consequently, employing a high-resolution method such as LES for hydrodynamics may be unnecessary. At this stage of model development, no feedback of the suspended load on the hydrodynamics is considered. A future perspective is to add a Boussinesq term in the momentum equation to take into account the density gradient due to the presence of suspended sediments. This would allow the study of other types of problems such as gravity current [Gadal et al., 2023, Shi et al., 2022].

2.2.1 Turbulence models

As stated previously, in the case of RANS filtering, the tensor $\boldsymbol{\tau_f}$ from equation 2.1 is equal to the specific Reynolds stress tensor $\boldsymbol{\tau_f} = -\left\langle \boldsymbol{u'}^T \boldsymbol{u'} \right\rangle$. As already described in the state of the art review (chapter 1), the use of the Reynolds stress tensor introduces 6 additional unknowns (the velocity fluctuation correlations) in the system of equations. The system as such is undetermined, and the classical Boussinesq assumption is used as a closure. It expresses the Reynolds stress tensor as a function of the eddy viscosity (see eq. 1.14). A turbulence model is used to compute ν_t.

OpenFOAM offers multiple turbulence models (see Table 2.1) to the user, many of which are two-equation models based on the turbulent kinetic energy k and either ϵ or ω. A transport equation is then solved for each variable. In river or estuarine environment, most of the numerical studies found in the literature make use of one of the three following turbulence models: $k-\epsilon$ [Fang and Rodi, 2003, Liu and García, 2008], $k-\omega$ [van der Sande et al., 2025, Xu et al., 2022, Baykal et al., 2015] and $k-\omega$ SST [Sattar et al., 2017] which is a combination of the two others. The following section provides a description of those three turbulence models as they are implemented in *OpenFOAM*.

$k-\epsilon$ model

The standard $k-\epsilon$ model was introduced in the work of Launder and Spalding [1983]. It is a two-equation model based on the turbulent kinetic energy k and the dissipation rate of turbulent kinetic energy ϵ. The eddy viscosity is given by the following expression:

$$\nu_t = \beta_* \frac{k^2}{\epsilon} \,. \tag{2.2}$$

models	number of equation	references
Spalart-Allmaras	1	Spalart and Allmaras [1992]
$k-\epsilon$	2	Launder and Spalding [1983]
RNG $k-\epsilon$	2	Yakhot et al. [1992]
realizable $k-\epsilon$	2	Shih et al. [1995]
Lien-Leschziner	2	Lien and Leschziner [1993]
$k-\omega$	2	Wilcox et al. [1998]
$k-\omega$ SST	2	Menter [1994]
$q-\zeta$	2	Gibson and Dafa'Alla [1995]
$k-\epsilon-v^2$	3	Durbin [1991]
$k-\epsilon-v^2-f$	3	Laurence et al. [2005]
$k-k_l-\omega$	3	Walters and Cokljat [2008]
$\gamma-R_{e_\theta}$	4	Langtry and Menter [2009]

Table 2.1: Various turbulence models in *OpenFOAM*.

where β_* is a model constant. Two transport equations describe the temporal evolution of k and ϵ:

$$\frac{\partial k}{\partial t}+\nabla.(\boldsymbol{u}k)=\nabla.\left(\left(\frac{\nu_t}{\sigma_k}+\nu\right)\nabla k\right)+P-\epsilon\,, \tag{2.3}$$

$$\frac{\partial \epsilon}{\partial t}+\nabla.(\boldsymbol{u}\epsilon)=\nabla.\left(\left(\frac{\nu_t}{\sigma_\epsilon}+\nu\right)\nabla \epsilon\right)-C_1P\beta_*k-C_2\frac{\epsilon^2}{k}\,, \tag{2.4}$$

where P is the turbulent kinetic energy production rate defined as:

$$P=\nu_t\boldsymbol{S}:\nabla\boldsymbol{u}=\nu_t\mathrm{tr}\left(\boldsymbol{S}(\nabla\boldsymbol{u})^T\right)=\nu_t\sum_{i=1}^{3}\sum_{j=1}^{3}S_{ij}(\nabla\boldsymbol{u})_{ij}\,. \tag{2.5}$$

where : is the double inner product which can be defined using the trace operator tr. The different constants of the model are summarized in Table 2.2 and can be modified in the file *turbulenceProperties*.

$k-\omega$ model

The $k-\omega$ model is with $k-\epsilon$ the other classical turbulence model. It was introduced by Wilcox et al. [1998] and makes use of the specific dissipation rate of turbulent kinetic energy ω instead of ϵ. The eddy viscosity is defined as follows:

$$\nu_t=\frac{k}{\omega}\,. \tag{2.6}$$

Once again, two transport equations describe the behavior of k and ω:

$$\frac{\partial k}{\partial t}+\nabla.(\boldsymbol{u}k)=\nabla.\left((\alpha_k\nu_t+\nu)\nabla k\right)+P-\beta\omega k\,, \tag{2.7}$$

		$k-\epsilon$									
β_*	C_1	C_2	σ_k	σ_ϵ							
0.09	1.44	1.92	1	1.3							
		$k-\omega$									
β_*	β	α_k	α_ω	γ							
0.09	0.072	0.5	0.5	0.52							
				$k-\omega$ SST							
β_*	α_{k1}	α_{k2}	$\alpha_{\omega1}$	$\alpha_{\omega2}$	β_1	β_2	γ_1	γ_2	a_1	b_1	c_1
0.09	0.85	1	0.5	0.856	0.075	0.0828	5/9	0.44	0.31	1	10

Table 2.2: From top to bottom, default coefficients for $k-\epsilon$, $k-\omega$ and $k-\omega$ SST turbulence models as they are implemented in *OpenFOAM*.

$$\frac{\partial \omega}{\partial t} + \nabla.(\boldsymbol{u}\omega) = \nabla.\left((\alpha_\omega \nu_t + \nu)\nabla\omega\right) + P - \beta\omega^2\,. \tag{2.8}$$

Equation 2.7 is almost identical to equation 2.3, the only difference being the coefficient α_k in the diffusion term and the expression of the dissipative term, which are written different but equivalent: $\epsilon = \beta_* k\omega$. Once again, the different constants of the model are detailed in Table 2.2 and can be modified by the user in the *turbulenceProperties* file.

$k-\omega$ SST model

The $k-\omega$ SST turbulence model was first introduced by Menter [1994] and was initially derived for aerodynamics studies. It consists of a combination of the two previously described turbulence models, the $k-\epsilon$ and the $k-\omega$. The aim of this model is to take the best out of those two models. Indeed, the $k-\epsilon$ is known to work well for free shear flows, but it performs poorly in the presence of adverse pressure gradients and is therefore not suitable for flows with boundary layer detachment. Conversely, the $k-\omega$ model is more effective in describing these types of flows but is less efficient than the $k-\epsilon$ in describing free shear flows in regions outside the range of influence of the solid boundaries (e.g., rigid walls, sediment bed). The $k-\omega$ SST model transitions between the two models using blending functions that take the distance to the nearest wall as an input. The eddy viscosity ν_t is expressed as:

$$\nu_t = \frac{a_1 k}{\max(a_1\omega, b_1 F_{23}\left\|\boldsymbol{S}\right\|)}\,, \tag{2.9}$$

where $\|\boldsymbol{S}\| = \sqrt{\boldsymbol{S} : \boldsymbol{S}}$ is the norm of the strain rate tensor defined with the double inner product : introduced in equation 2.5. F_{23} is a blending function. The temporal evolutions of k and ω are described by two transport equations:

$$\frac{\partial k}{\partial t} + \nabla.(\boldsymbol{u}k) = \tilde{P} - \beta^* k\omega + \nabla.\left((\alpha_k \nu_t + \nu)\nabla k)\right)\,, \tag{2.10}$$

$$\frac{\partial \omega}{\partial t} + \nabla.(\boldsymbol{u}\,\omega) = \frac{\gamma}{\nu_t}P - \beta\omega^2 + \nabla.((\alpha_\omega \nu_t + \nu)\nabla\omega) + 2(1-F_1)\alpha_{\omega 2}\frac{1}{\omega}\nabla k.\nabla\omega\,, \tag{2.11}$$

where F_1 is another blending function. In the equation for k, a limiter is applied to the production rate P:

$$\tilde{P} = \min\left(P, c_1\beta_* k\omega\right) . \tag{2.12}$$

The last term in the ω equation is called the cross-diffusion term. It appears during the derivation of the ω equation from the ϵ equation of the $k-\epsilon$ model (eq. 2.4) using the relation $\epsilon \propto k\omega$. The model constants α_k and α_ω are obtained from other constants using the blending function F_1 as:

$$\alpha_k = F_1(\alpha_{k1} - \alpha_{k2}) + \alpha_{k2} , \tag{2.13}$$

and the same applies for α_ω with the constants $\alpha_{\omega 1}$ and $\alpha_{\omega 1}$, but also for β and γ. It means that α_k, α_ω, β, and γ are not really constants because the values they take vary in space. The constants α_{k1}, α_{k2}, $\alpha_{\omega 1}$, and $\alpha_{\omega 2}$ are issued from the turbulence models $k-\omega$ and $k-\epsilon$ and detailed in Table 2.2.

The first blending function F_1 has undergone modifications since the initial work of Menter [1994], it is defined as follows:

$$F_1 = \tanh\left[\min\left(\min\left(\max\left(\frac{\sqrt{k}}{\beta_*\omega l_w}, \frac{500\nu}{\omega l_w^2}\right), \frac{4\alpha_{\omega 2}k}{CD^+_{k\omega} l_w^2}\right), 10\right)^4\right] , \tag{2.14}$$

where l_w is the distance to the nearest wall. F_1 tends toward 1 when l_w decreases and is equal to 0 far from any wall which deactivates the cross-diffusion term. $CD^+_{k\omega}$ stands for the positive portion of the cross-diffusion term and is defined as:

$$CD^+_{k\omega} = \max\left(2\alpha_{\omega 2}\nabla k.\frac{\nabla\omega}{\omega}, 10^{-10}\right) . \tag{2.15}$$

Two other blending functions have yet to be defined. The blending function appearing in the eddy viscosity definition (eq. 2.9) is defined as $F_{23} = F_2F_3$ where F_2 is defined as follows:

$$F_2 = \tanh\left[\min\left(\max\left(\frac{2\sqrt{k}}{\beta_*\omega l_w}, \frac{500\nu}{\omega l_w^2}\right), 100\right)^2\right] . \tag{2.16}$$

Just as the function F_1, F_2 tend toward 1 close to walls. This formulation was developed by Menter [1994] after he observed that the classical eddy viscosity formulation $\nu_t = k/\omega$ yields an overestimation of the eddy viscosity in the presence of adverse pressure gradients. F_2 acts as a limiter for the eddy viscosity. This is the main feature, which makes the $k-\omega$ SST model effective in the presence of adverse pressure-gradient boundary layers, and to predict flow detachment.

Finally, the function F_3 aims at preventing the limitation of the eddy viscosity for rough wall flows. This extension was developed by Hellsten et al. [1997] and is written as:

$$F_3 = 1 - \tanh\left[\min\left(\frac{150\nu}{\omega l_w^2}, 10\right)^4\right] . \tag{2.17}$$

keyword	blending
stepwise	$\omega = \omega_{\text{vis}}$ for $z_1^+ \leq z_{\text{lam}}^+$ and $\omega = \omega_{\log}$ for $z_1^+ > z_{\text{lam}}^+$
max	$\max(\omega_{\text{vis}}, \omega_{\log})$
binomial	$\left(\omega_{\text{vis}}^n + \omega_{\log}^n\right)^{1/n}$
exponential	$\omega_{\text{vis}} e^{-\Gamma} + \omega_{\log} e^{-1/\Gamma}, \quad \Gamma = \frac{0.01(z_1^+)^4}{1+5z_1^+}$
tanh	$\tanh((\frac{z_1^+}{10})^4)(\omega_{\text{vis}} + \omega_{\log}) + (1 - \tanh((\frac{z_1^+}{10})^4)) \left(\omega_{\text{vis}}^1.2 + \omega_{\log}^1.2\right)^{1/1.2}$

Table 2.3: Different blending functions available for ω smooth wall boundary condition.

By default, F_3 is deactivated and equal to 1.

The different model constants are detailed in Table 2.2 and can be modified by the user in the file *turbulenceProperties*.

2.2.2 Wall boundary condition for turbulent quantities

In sediment transport models based on the Exner equation, the quantity of sediments transported as bedload or eroded from the bed and put into suspension is computed empirically from the shear stress exerted by the flow on the sediment bed considered as a wall boundary. Using RANS modeling, the shear stress exerted on the bed is defined as:

$$u_*^2 = (\nu + \nu_t) \left. \frac{\partial u_=}{\partial z} \right|_{z=z_b} \tag{2.18}$$

where u_* is the friction velocity defined as the square root of the specific shear stress, $u_=$ is the velocity component tangential to the bed, and z_b is the position of the bed boundary, here assumed to be 0 to simplify the notations. Specific boundary conditions are needed for k and ω to obtain a good estimation of the shear stress. In the state-of-the-art review, a description of wall functions k and ω was provided. For the following, the wall treatment for smooth and rough wall boundaries available in *sedExnerFoam* is detailed.

Smooth wall treatment

For a smooth wall boundary, a thin viscous sub-layer exists at the wall in which the turbulence vanishes so that $k = 0$ at the wall surface. The boundary condition for ω is applied at the center of the first cell next to the wall. Depending on the distance z_1 separating the first cell center from the wall boundary, two different conditions can be applied. If the first cell is within the viscous sub-layer ($z_1^+ < 5$), then the viscous condition is used (see eq. 1.30). If the first cell center is located at a distance $z_1^+ > 30$, then the log layer solution holds (see eq. 1.29).

The resulting boundary condition is a blend between the viscous and the log conditions. *OpenFOAM* offers various possibilities of blending functions, which are detailed in Table 2.3. By default, the blending is the following:

$$\omega|_{z=z_1} = \sqrt{\omega_{\text{vis}}^2 + \omega_{\text{log}}^2}\,. \tag{2.19}$$

It corresponds to a binomial blending with a coefficient $n = 2$. Some of the blending functions use a value z_{lam}^+ to switch from the viscous to the log solution. This threshold value is an estimation of the intersection of the viscous and log layers. It is obtained by solving the following equation:

$$z_{\text{lam}}^+ = \frac{\ln\left(\max(9.8 z_{\text{lam}}^+, 1)\right)}{\kappa}\,. \tag{2.20}$$

Rough wall treatment

In the state-of-the-art review, four different boundary condition for representing surface roughness were examined. These different wall functions have all been implemented in *OpenFOAM* for the purpose of this work. Each approach provides an expression for ω at the wall surface, and in some cases also for k, as a function of the friction velocity and the equivalent wall roughness length (k_s). These different boundary conditions are summarized in Table 2.4.

The wall function *wilcoxOmegaWallFunction* for ω corresponds to the initial formulation of the boundary condition from Wilcox et al. [1998] from the first edition of his book in 1993 whereas the *fuhrmanOmegaWallFunction* is the revision he proposed in later versions. It was implemented in *OpenFOAM* with the name Fuhrman because of the work Fuhrman et al. [2010], through which it was first discovered by the author of the code. The two other boundary conditions are the ones proposed by Knopp et al. [2009] and Lee [2018] respectively.

2.3 bedload transport

With the Exner approach, the dense part of the granular flow is outside of the computational domain and the sediment bed interface is one of its boundaries. Thus, the sediment movement happening along this boundary or below it is entirely modeled through empirical formulas relating the bedload flux to both the shear stress exerted by the fluid and the gravity. These formulas were developed during the last century from sediment transport experiments in channels.

The particles start to move when the Shields number $\theta = \frac{u_*^2}{\left(\rho_s/\rho_f - 1\right) g d}$ exceeds a critical value θ_c, where u_* is the friction velocity, ρ_s and ρ_f are the densities of the sediment and the fluid, respectively. A section of the state-of-the-art review focuses on the description of the bedload transport and the threshold of motion. In *sedExnerFoam*, all the formulations to compute the critical Shields number are based on the dimensionless sediment particle diameter D_* (see eq. 1.46). The various formulas available in the model are summarized in Table 2.5 and represented in Figure 2.1. The user can choose between one of those models or manually set a value for θ_c^0, which corresponds to the critical Shields number for a flat bed.

keyword	k	ω
smooth wall		
omegaWallFunction	$k = 0$ or $\nabla k = 0$	$\omega_{\text{vis}} = \frac{6\nu}{\beta_1 z_1^2}\,, \quad \omega_{\log} = \frac{\sqrt{k}}{\beta_* \kappa z_1}$
rough wall		
wilcoxOmegaWallFunction	$\nabla k = 0$	$\omega = \frac{u_*^2}{\nu} S_R\,, \quad S_R = \begin{cases} \left(\frac{50}{k_s^+}\right)^2 & \text{if } k_s^+ < 25\,, \\ \frac{100}{k_s^+} & \text{if } k_s^+ \geq 25 \end{cases}$
fuhrmanOmegaWallFunction	$\nabla k = 0$	$\omega = \frac{u_*^2}{\nu} S_R\,, \quad \begin{cases} \left(\frac{200}{k_n^+}\right)^2 & \text{if } k_n^+ < 5 \\ \frac{K_r}{k_n^+} + \left[\left(\frac{200}{k_n^+}\right)^2 - \frac{K_r}{k_n^+}\right] e^{k_n^+ - 5} & \text{if } k_n^+ \geq 5 \end{cases}$
knoppkWallFunction knoppOmegaWallFunction	$\frac{u_*^2}{\beta_*^{1/2}} \min\left(1, \frac{k_s^+}{90}\right)$	$\min\left(\frac{u_*}{\beta_*^{1/2} \kappa \tilde{d}_0}, \frac{60\nu}{\beta_1 z_1^2}\right)$
knoppkWallFunction leeOmegaWallFunction	$\frac{u_*^2}{\beta_*^{1/2}} \min\left(1, \frac{k_s^+}{90}\right)$	$\min\left(\frac{u_*}{\ln\left(\frac{z_1 + d_0}{d_0}\right) \beta_*^{1/2} \kappa \tilde{d}_0}, \frac{60\nu}{\beta_1 z_1^2}\right)$

Table 2.4: Different wall boundary conditions available for k and ω fields.

keyword	formula	references
	critical Shields number	
Brownlie	$\theta_c^0 = \frac{0.22}{D_*^{0.9}} + 0.06\,10^{-7.7D_*^{-0.9}}$	Brownlie [1983]
Miedema	$\theta_c^0 = \frac{0.2285}{D_*^{1.02}} + 0.0575(1 - e^{-0.0225D_*})$	Miedema [2008]
Soulsby	$\theta_c^0 = \frac{0.3}{1+1.2D_*} + 0.055\,(1 - e^{-0.02D_*})$	Soulsby and Whitehouse [1997]
Zanke	$\theta_c^0 = \frac{0.145}{D_*^{0.5}} + 0.04510^{-1100D_*^{-2.25}}$	Zanke [2003]
	bedload transport formulas	
Camenen	$\phi_b = 12\,\theta^{1.5} e^{-4.5\theta_c/\theta}$	Camenen and Larson [2005]
MeyerPeter	$\phi_b = 8\,\varpi(\theta - \theta_c)^{3/2}$	Meyer-Peter and Müller [1948]
Nielsen	$\phi_b = 12\,\theta^{1/2}\varpi(\theta - \theta_c)$	Nielsen [1992]
vanRijn	$\phi_b = 0.053\frac{\varpi(\theta/\theta_c - 1)^{2.1}}{D_*^{0.3}}$	van Rijn [1984a]
custom	$\phi_b = \eta_b \theta^a \varpi(\theta - \theta_c)^b$	

Table 2.5: Available formulas to compute the critical Shields number from the fluid and sediments physical properties and formulas to compute the bedload flux from the Shields number. The bedload flux is rendered dimensionless by the Einstein number. Those formulas are selected in the file *bedloadProperties* using the entries *criticalShieldsModel* and *bedloadModel*.

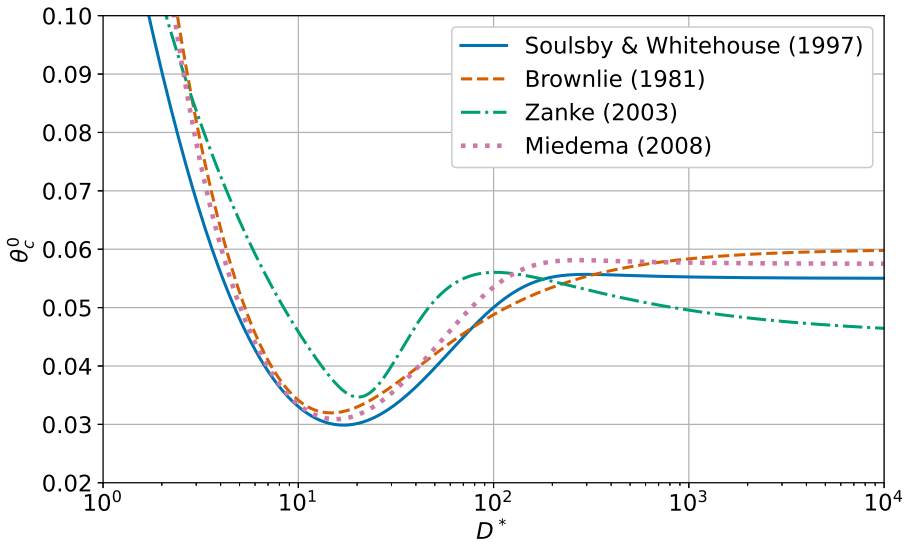

Figure 2.1: Critical Shields number as a function of the dimensionless sediment diameter D_* for different formulas available in *sedExnerFoam*.

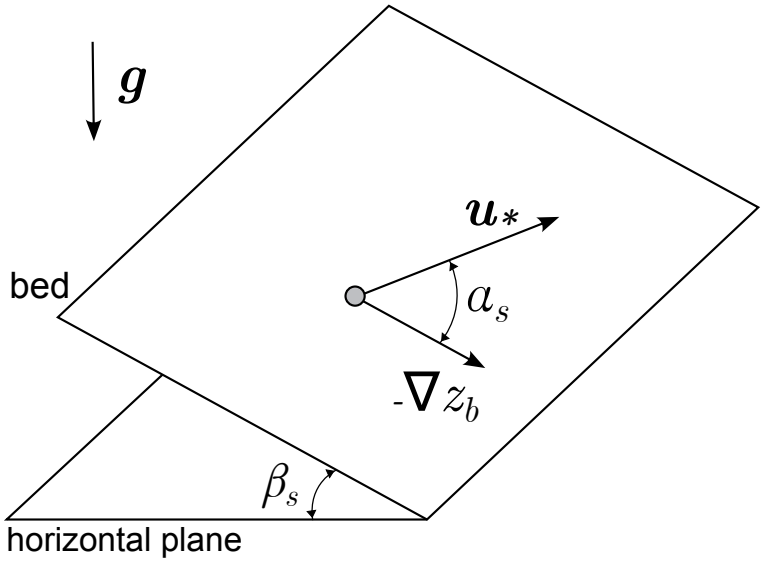

Figure 2.2: Representation of the two angle β_s and α_s. β_s is the bed slope angle and α_s the angle between the steepest slope direction and the direction of the shear. The steepest slope direction is represented by $-\nabla z_b$.

Accurately measuring the threshold of motion is a difficult task, mainly because of the absence of a universal definition of the motion threshold. Some particles can indeed be seen moving even for subcritical values of θ. Furthermore, corrections need to be applied to the value of θ_c to account for bed slope effects. In the following, the base critical Shields number, which is the critical Shields number on a flat bed, is noted θ_c^0. The critical Shields number after slope correction is denoted by θ_c. Following Fredsoe and Deigaard [1992], a correction to account for the local bed slope is applied to the critical Shields number:

$$\frac{\theta_c}{\theta_c^0} = \cos(\beta_s)\sqrt{1 - \frac{\sin(\alpha_s)^2 \tan(\beta_s)^2}{\mu_s^2}} - \frac{\cos(\alpha_s)\sin(\beta_s)}{\mu_s}\,, \tag{2.21}$$

where β_s is the angle of the bed slope and α_s the angle between the steepest slope direction and the direction of the shear. These angles are represented on the schematic in Figure 2.2. The coefficient of static friction μ_s is linked to the angle of repose of the granular material β_r through $\tan(\beta_r) = \mu_s$. The slope correction can be activated/deactivated in the file *bedloadProperties* using the entry *slopeCorrection*.

Various studies have focused on trying to find relationships between the Shields number and $\phi_b = \|\boldsymbol{q_b}\| / \sqrt{(s-1)gd^3}$ [Einstein, 1942, Meyer-Peter and Müller, 1948, van Rijn, 1984a], the dimensionless bedload flux leading to the development of numerous empirical relations. A lot of those formulas are of the form:

$$\phi_b \propto \theta^a \, \varpi(\theta - \theta_c)^b\,, \tag{2.22}$$

with a and b, two real positive coefficients, and ϖ is the threshold function which is defined according to $\varpi(\theta - \theta_c) = \theta - \theta_c$ for $\theta > \theta_c$, and $\varpi(\theta - \theta_c) = 0$ if $\theta \leq \theta_c$. The

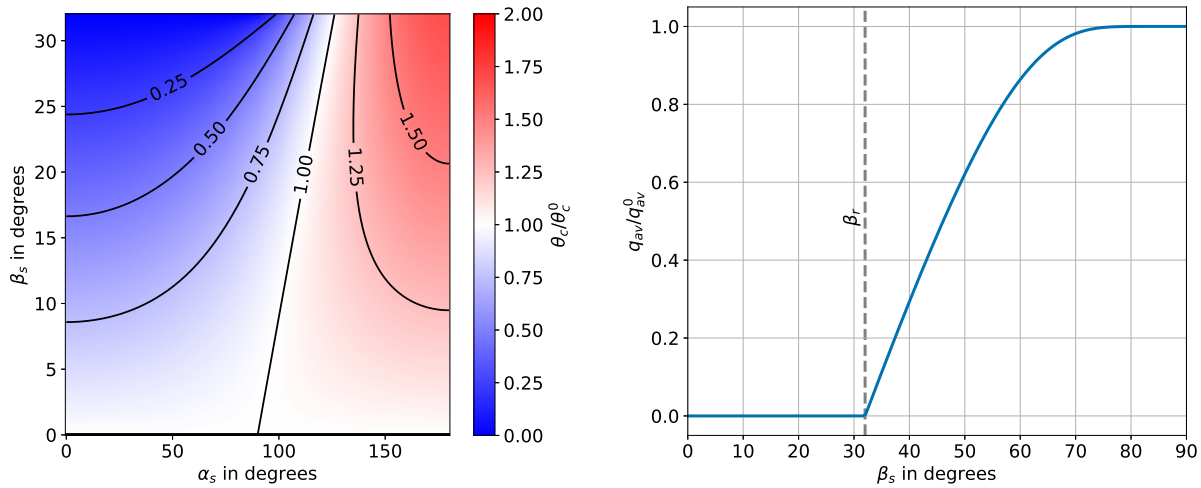

Figure 2.3: On the left, slope correction for the critical Shields number θ_c/θ_c^0 as a function of β_s and α_s (see eq. 2.21). On the right, normalized avalanche bedload flux q_{av}/q_{av}^0 from the formulation of Duran Vinent et al. [2019] as a function of the bed slope (see eq. 2.23). The repose angle was taken equal to $\beta_r = 32$ degrees.

formulas available for the user to compute the bedload are summarized in Table 2.5 and represented in Figure 2.4. The user also has the possibility to define a custom bedload formula by manually setting the prefactor and the coefficients a and b in equation 2.22.

Another phenomenon that needs to be considered when solving the Exner equation is the sediment avalanches occurring when the bed slope exceeds the angle of repose of the granular material. If not taken into account, unrealistic slopes could appear in the numerical solution or even shock situations, which could trigger numerical instabilities in the model. Marieu et al. [2008] proposed a model based on an iterative procedure to redistribute the excess of sediment locally until the bed slope does not exceed the granular material angle of repose. Such a procedure has been successfully tested in other works [Zhou, 2017]. In *sedExnerFoam*, however, the avalanche is modeled with an additional bedload term $\boldsymbol{q_{av}}$ modified from Duran Vinent et al. [2019]:

$$\|\boldsymbol{q_{av}}\| = q_{av}^0 \frac{\varpi[\tanh(\tan(\beta_s)) - \tanh(\tan(\beta_r))]}{1 - \tanh(\tan(\beta_r))}\,, \tag{2.23}$$

with β_s and β_r, respectively the angle of the slope and the repose angle of the granular material. q_{av}^0 is a positive constant which can be set by the user. It corresponds to the maximum possible additional bedload flux due to the avalanche. This avalanche flux is oriented toward the steepest slope direction. One benefit of this formulation is that it enables slopes to exceed the angle of repose in the event of a competition between the bedload flux due to bed shear stress and the one due to the avalanche.

One last aspect that is often overlooked when modeling sediment transport in water, but which is widely used in aeolian transport, is the bedload flux saturation. As described

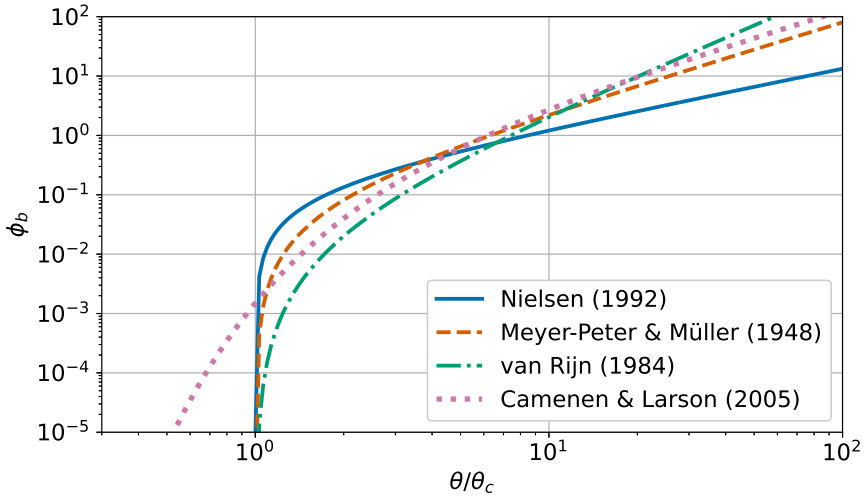

Figure 2.4: The adimensioned bedload flux as a function of the relative Shields number θ/θ_c from the empirical formulas detailed in Table 2.5.

in the state-of-the-art review (chapter 1), the saturation is an approximation of the inertia effect of the sediments transported in the bedload layer. When the bed shear stress varies over time, the bedload flux does not respond instantaneously, but rather over a period of time called the saturation time T_{sat}. Similarly, the bedload flux adapts to spatial variations in bed shear stress over a length called the saturation length L_{sat}. The saturated bedload flux $\boldsymbol{q_{sat}}$ corresponds the the bedload flux at equilibrium and is computed empirically from the formulas presented in Table 2.5. According to references [Charru, 2006, Charru et al., 2013], the equation for saturation can be expressed in a coordinates system aligned with the shear stress as:

$$T_{sat}\frac{\partial q_b}{\partial t} + L_{sat}\frac{\partial q_b}{\partial x} = q_{sat} - q_b\,, \tag{1.54}$$

where x is the coordinate in the direction of the shear stress. It has been argued that the temporal term can be neglected in the case of ripples and dunes formation and migration as the saturation time is typically way smaller than the characteristic time of the bedforms [Charru et al., 2013]. Equation 1.54 being only one-dimensional, a multidimensional expression for the bedload saturation is proposed with the following equation:

$$T_{sat}\frac{\partial q_b}{\partial t} + L_{sat}\nabla.\left(\frac{\boldsymbol{q_b}}{\|\boldsymbol{q_b}\|}\otimes\boldsymbol{q_b}\right) = \boldsymbol{q_{sat}} - \boldsymbol{q_b}\,. \tag{2.24}$$

From the file *bedloadProperties*, the user can activate the saturation and provide values for L_{sat} and T_{sat}. The saturated flux $\boldsymbol{q_{sat}}$ is then computed from the bed shear stress, using one of the formulas from Table 2.5.

2.4 Suspended transport

In *sedExnerFoam*, the suspended load is described by the suspended sediment volume fraction $c_s = V_s/(V_s + V_f)$, where V_s and V_f stand for the volume of sediment and the volume of fluid, respectively. The evolution of c_s in space and time is governed by the advection diffusion equation already presented in the state of the art review:

$$\frac{\partial c_s}{\partial t} + \nabla.[(\boldsymbol{u} + \boldsymbol{w_s})c_s] = \nabla.(\epsilon_s \nabla c_s) \tag{1.53}$$

where $\boldsymbol{w_s}$ is the sediment settling velocity, and ϵ_s is the turbulent diffusivity for the suspended sediment. It is expressed as the ratio of the turbulent eddy viscosity and the Schmidt number σ_c. The possibility of using an additional diffusivity ϵ_w in the near bed area is discussed later on. The suspended sediment concentration is supposed to behave has a passive scalar being transported with the flow and settling due to the effect of gravity. The settling velocity is computed as follows:

$$\boldsymbol{w_s} = w_s^0 . F_h(c_s)\, \boldsymbol{e_g}\,, \tag{2.25}$$

where $\boldsymbol{w_s^0}$ is the terminal sediment settling velocity of a single particle in a quiescent fluid, $\boldsymbol{e_g} = \boldsymbol{g}/\left\|\boldsymbol{g}\right\|$ is a unit vector oriented with gravity, and F_h is a hindrance function that takes values between 0 and 1 and is a decreasing function of c_s. It represents the effect of particles hindering each other as they fall, leading to a drop of their settling velocity as c_s increases [Richardson and Zaki, 1954]. The different models available to compute the terminal falling velocity $\boldsymbol{w_s^0}$ and the hindrance function F_h are summarized in Table 2.6. The different formulas available to estimate the terminal settling velocity $\boldsymbol{w_s^0}$ are represented in Figure 2.5, and the formulas for hindrance effect in Figure 2.6.

The values taken by the Schmidt number σ_c has been a hot topic up to today without a consensus being reached. van Rijn [1984b] proposed a formula to estimate σ_c from the settling velocity and the friction velocity u_*:

$$\sigma_c = \frac{1}{1 + 2\left(\frac{w_s}{u_*}\right)^2}, \quad \text{for} \quad 0.1 < \frac{w_s}{u_*} < 1\,. \tag{2.26}$$

This yields a Schmidt number smaller than unity, which corresponds to sediment diffusion being more intense than the turbulent diffusion for the fluid. Others tried to experimentally estimate σ_c, and highlighted the non-uniformity of the Schmidt number [Amoudry et al., 2005]. However, this issue has yet to be solved, and the Schmidt number is assumed constant in the present model with its value being set by the user.

The final key aspect of this approach is how to enforce the bed boundary condition, which is the exchange of mass between the sediment bed and the suspended load. This is covered in the following section.

keyword	formula (for C_d or w_s^0)	references
	terminal fall models	
Stokes	$w_s^0 = \frac{1}{18\nu}(s-1)gd^2$	Stokes [1901]
Fredsoe	$C_d = 1.4 + \frac{36}{R_{ep}}$	Fredsoe and Deigaard [1992]
Soulsby	$w_s^0 = \frac{\nu}{d}\sqrt{10.36^2 + 1.049D_*^3}$	Soulsby and Whitehouse [1997]
Rubey	$w_s^0 = \left(\sqrt{2/3 + 36D_*^{-3}} - \sqrt{36D_*^{-3}}\right)\sqrt{(s-1)gd}$	Rubey [1933]
fixedValue	value given by user	
	hindrance models	
Zaki	$F_h(C_s) = (1-c_s)^n$	Richardson and Zaki [1954]
ZakiModified	$F_h(c_s) = (1-c_s)^{n-1}(1-c_s/c_s^{max})$	Camenen [2008]
fixedValue	value given by user	

Table 2.6: Different available options in *sedExnerFoam* to compute the terminal falling velocity w_s^0 and the hindrance function F_h. Models are selected in the file *suspensionProperties* using the entries *fallModel* and *hindranceModel*.

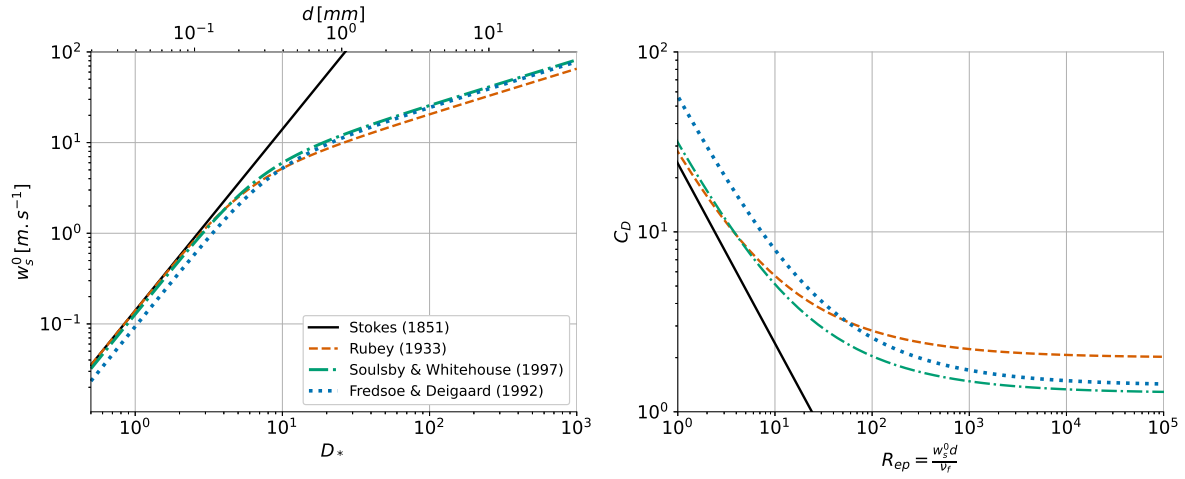

Figure 2.5: On the left, different formulas to estimate the terminal settling velocity from the dimensionless diameter. Considering that the fluid is water ($\rho_f = 1000\,kg.m^{-3}$, $\nu = 1\,10^{-6}$), and that the particles have a density $\rho_s = 2650\,kg.m^{-3}$. The corresponding diameter is shown at the top of the plot. On the right graph, is represented the drag coefficient as a function of the particle Reynolds number, considering the same fluid and particles.

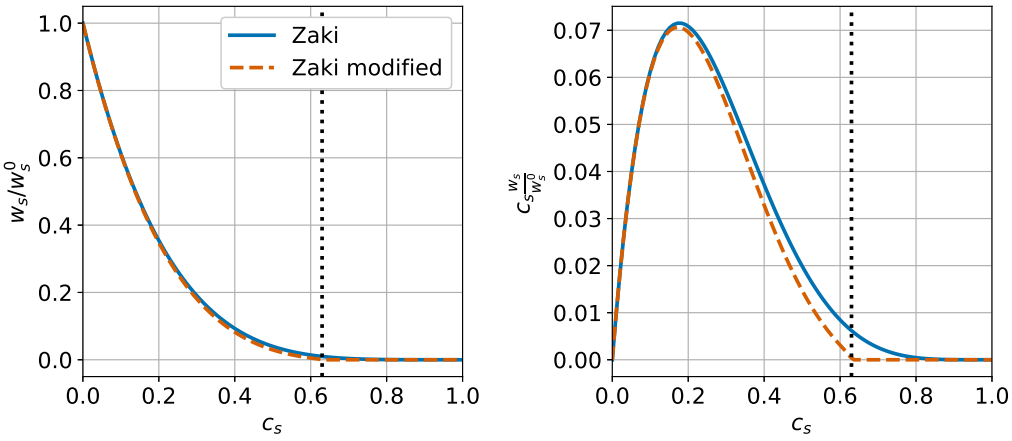

Figure 2.6: Zaki and Zaki modified formulas to compute hindered settling velocity. On the left and right graphs are represented the velocity decrease and the settling flux, respectively, both being functions of the sediment volume fraction.

2.4.1 Erosion/Deposition condition

As said previously, the modeling of the erosion and deposition fluxes is a hard point of classical sediment transport models. Many sediment transport experiments in straight flumes have been conducted to study the relation between the flow and the rate at which particles are eroded from the bed to the water column. van Rijn [1984b] studied the case of sediment transport in a straight channel under equilibrium condition and proposed an empirical formula to compute a reference concentration c_b^* at a certain reference distance from the bed, the so-called reference level δz_b^*:

$$c_b^* = 0.015 \frac{d}{\delta z_b^*} \frac{(\theta/\theta_c - 1)^{3/2}}{(D_*)^{0.3}} . \tag{2.27}$$

The reference concentration corresponds to the concentration observed at a distance δz_b^* from the bed under equilibrium condition (see Figure 2.7).

Since then, a lot of sediment transport models used van Rijn empirical formula and assumed an equilibrium situation at the reference level to impose the boundary condition $c_s(z = \delta z_b^*) = c_b^*$. However, this boundary condition is not appropriate for a lot of situations where a local equilibrium cannot be assumed at the reference level. Celik and Rodi [1988] adapted this boundary condition to handle out of equilibrium situation. The erosion flux is written $E = w_s c_b^*$, and the deposition flux $D = w_s c_b$ with c_b, a sediment concentration value computed from the values in the neighboring cells, which is detailed later on. The idea is that the rate of erosion is always the same as the one under equilibrium condition, and the deposition depends only on the concentration value in the first few cells above the bed. If $c_b > c_b^*$, then suspended sediment get deposited on the bed, and when $c_b < c_b^*$, sediment get eroded from the bed and suspended in the water column. The equilibrium occurs when $c_b = c_b^*$.

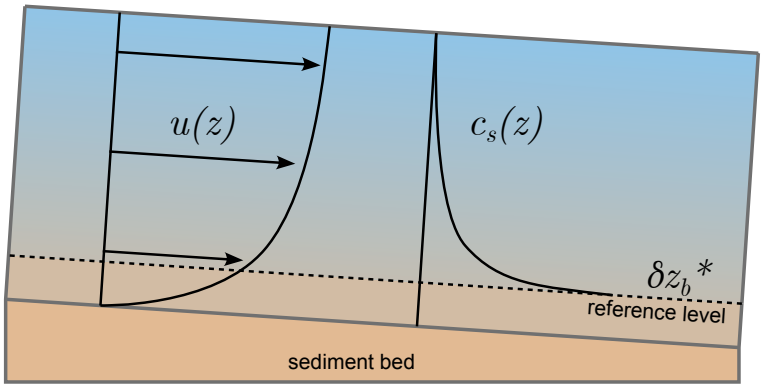

Figure 2.7: Schematic of a channel flow with entrainment of sediment into suspension. The suspended sediment concentration at the reference level is the reference concentration. As the distance from the bed increases, the quantity of suspended material decreases exponentially.

One difficulty is how to impose this reference concentration at the reference level, which is above the bed boundary. Large scale sediment transport models avoid this difficulty by not meshing the region located between the sediment bed and the reference level. The downfall of this method being that the flow near the bed is not solved and needs to be modeled, typically leading to a bad hydrodynamics in highly non uniform flow regions, such as near obstacles. In order to maintain a good hydrodynamics resolution, Jacobsen [2011] developed a model relying on a different mesh for the hydrodynamics and for the suspended load. The bottom boundary of the mesh for the suspended load is located at the reference level, whereas the mesh for the hydrodynamics presented cells in between the sediment bed and the reference level. In *sedExnerFoam*, it was chosen to avoid the use of two different meshes, and to solve both the hydrodynamics and the suspended load on the same mesh.

As stated previously, the deposition and erosion fluxes are computed as suggested by Celik and Rodi [1988]. The erosion E is computed at the reference level $\delta z_b^* = k_s$, the Nikuradse equivalent roughness height ($k_s = 2.5d$), using equation 2.27 and a limiter, so that c_b^* is not exceeding a value $c_{b,max}^*$, typically equal to half the maximum possible sediment volume fraction. This limiter is needed to avoid c_b^* taking non physical values when the bed shear stress becomes important (see eq. 2.27). In their work, Amoudry et al. [2005] use a maximum possible reference concentration $c_{b,max}^* = 0.3$ which is close to the value of 0.32 suggested by Engelund and Fredsøe [1976]. The computed reference concentration is then extrapolated at the height of the first cell center above the sediment bed z_1, using the formula suggested by Fang and Rodi [2003]:

$$c_{b1}^* = min\left(c_b^* e^{-\frac{w_{s1}}{\epsilon_{s1}}\left(z_1 - \delta z_b^*\right)}, c_{b,max}^*\right), \tag{2.28}$$

where c_{b1}^* is the reference concentration extrapolated at the height z_1. w_{s1} and ϵ_{s1} stand for the settling velocity and the sediment turbulent diffusivity values at the center of the first cell above the sediment bed, located at a height z_1. The expression of c_{b1}^* is obtained

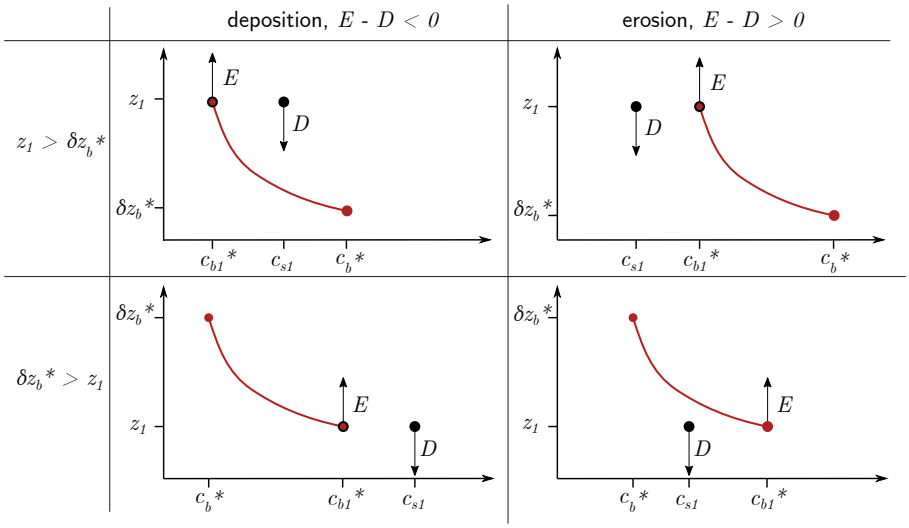

Figure 2.8: Extrapolation of the reference concentration depending on the reference level and the position of the first cell center.

by considering a local equilibrium in a small region above the bed and assuming ϵ_s and $\boldsymbol{w_s}$ to be uniform between the reference level δz_b^* and the center of the first cell above the bed. The deposition and erosion are then computed at the first cell center and not on the bed boundary, leading to $D = w_s c_{s1}$. The total erosion/deposition flux is then estimated as:

$$D - E = w_{s1}(c_{s1} - c_{b1}^*)\,. \tag{2.29}$$

This flux is imposed as a boundary condition for the suspended-load transport (equation 1.53). A schematic representing the situations leading to erosion or deposition depending on the reference concentration, and the positions of the reference level and the first cell center, is represented in Figure 2.8. With this method, the same mesh can be used for both the suspended load and the hydrodynamics with a fine resolution near the sediment bed. It is to be remembered that the various formulas for c_b^* existing in the literature are all empirical and are based on measurements made in straight channel flow experiments. Their validity out of this configuration, let alone in the vicinity of an obstacle disturbing the flow, is subject to caution.

The possibility to use an additional diffusivity near the bed for suspended sediments has been introduced in the model after experimenting difficulties to suspend material from the bed to the water column in the case of fine grid resolution and low to medium dimensionless roughness $k_s^+ = \frac{k_s u_*}{\nu}$. The eddy viscosity being very low on the first cells above the bed, the eroded sediments stay stuck in the first layer of cells, without rising up in the water column. To solve this issue an additional artificial diffusivity is introduced in the near bed region:

$$\frac{\epsilon_w}{\nu} = \frac{\epsilon_w^0}{2}\left(1 - \tanh\left(\xi_w \frac{z - k_s}{k_s}\right)\right)\,. \tag{2.30}$$

It can be interpreted as a saltation effect. In the presence of a viscous sublayer above the bed, the particles need to reach a certain elevation in order to get caught by turbulent eddies and rise in the water column. If the flow is rough however ($k_s^+ \gg 1$), the turbulence reaches the bed, and the use of ϵ_w is not needed. The coefficients ϵ_w^0 and ξ_w are both set to 5 by default, but can be modified in the file *bedloadProperties*.

2.5 Morphology evolution

As already stated in the state-of-the-art review, the morphology evolution is described by the Exner equation. It was first proposed by Exner [1920], an Austrian meteorologist and geophysicist. In their article, Paola and Voller mention that Felix Exner initially suggested that the bed elevation was evolving proportionally with the divergence of the mean flow velocity, but made clear that the mean flow acted as a proxy for the sediment flux. This led to the standard formulation, which is written as follows:

$$(1 - \lambda_s)\frac{\partial z_b}{\partial t} + \nabla_H . \boldsymbol{q_b} = D - E \,, \tag{1.4}$$

where z_b is the bed elevation, λ_s is the porosity of the granular material, which is linked to the maximum possible sediment volume fraction $c_s^{max} = 1 - \lambda_s$. The Exner equation describes the mass conservation of the sediment making up the bed. The bed elevation varies depending on the bedload flux and the exchange of sediments with the suspended load, D and E. Contrarily to the other partial differential equations solved in the model, the Exner equation is a 2D equation, and is thus solved after applying a 2 dimensional plane projection on all variables. The operator ∇_H stands for the divergence operator on this projected plane. The specific treatment needed to handle this equation is described in the following part, dedicated to the model numerical aspects.

2.6 Numerical methods

Following the mathematical description of the model, this section aims to clarify certain significant numerical aspects. These include the numerical methods used, the PIMPLE pressure-velocity coupling algorithm employed by the model, and the specific treatment of the Exner equation and mesh movement. A flow chart of the model is shown in Figure 2.9 and summarizes the sequence of operations performed during a time iteration. After solving the hydrodynamics (eq. 2.1), the shear stress exerted on the bed is computed, and used to estimate the bedload flux $\boldsymbol{q_b}$ (see Table 2.5), and the erosion E (eq: 2.27). Then, the transport equation for suspended sediments is solved with E acting as a source term. From this, the deposition D is known, and a new bed elevation is computed with the Exner equation (eq. 1.4). At the beginning of the next time iteration, the mesh is deformed so that the bed boundary geometry always matches the bed elevation.

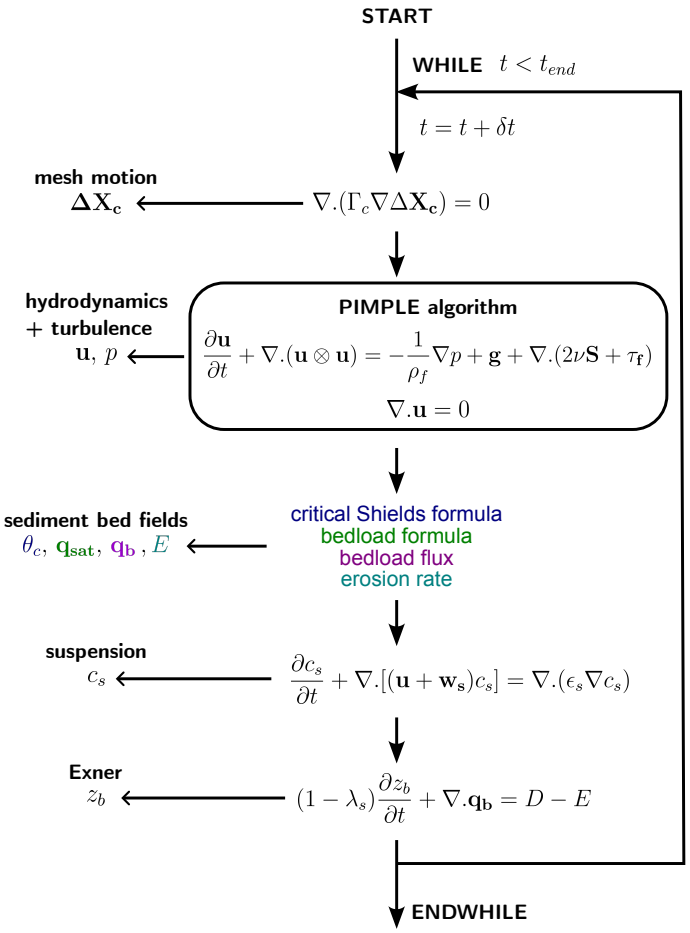

Figure 2.9: Flow chart of *sedExnerFoam*, illustrating the operations performed by the model during each time iteration.

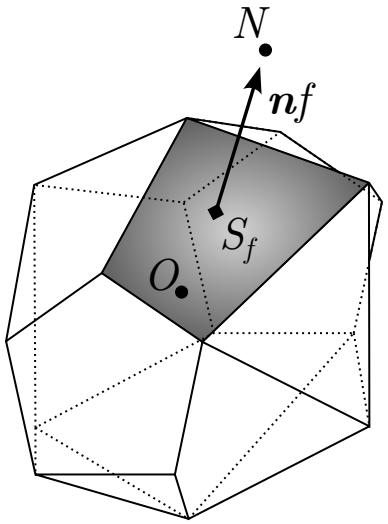

Figure 2.10: Polyhedral control volume. O is the center of the cell owning face f, and N the center of the neighbouring cell sharing face f with O. Modified from Jasak et al. [1999].

2.6.1 Finite Volume Method

OpenFOAM is an object-oriented *C++* library used to solve partial differential equations [Jasak et al., 2007], primarily for computational fluid dynamics applications (CFD). It relies on the finite volume method (FVM) to solve equations on unstructured meshes made of polyhedral cells, such as shown in Figure 2.10. The computational domain is split into a multitude of polyhedral cells over which the partial differential equations to solve are integrated. Using the flux-divergence theorem, the divergence of a field over a cell volume is computed as the flux of the field through the faces at the interfaces between the neighboring volumes. Because the flux of a quantity leaving a volume is equal to the flux of that same quantity entering the neighboring volume, the FVM is mass conservative. The different fields are stored at the cell centers.

Generally, the integral form of the conservation equation of a quantity a (scalar, vector, or tensor field) over the volume V_c of a cell c, delimited by a closed surface S_c has the following form:

$$\underbrace{\frac{\partial}{\partial t}\int_{V_c} a dV}_{①} + \underbrace{\oint_{S_c} \left[(\boldsymbol{u}-\boldsymbol{v_m}).\boldsymbol{n}\right] a dS}_{②} - \underbrace{\int_{V_c} \nabla.(\gamma_a \nabla a) dV}_{③} = \underbrace{\int_{V_c} S_o(a) dV}_{④}, \tag{2.31}$$

where $\boldsymbol{n}$ is the outward pointing unit vector on the cell surface, $\boldsymbol{v_m}$ is the velocity of the mesh, γ_a is the diffusivity, and S_o is a volume source term. The term ① represents the temporal evolution of a in the volume V_c, ② is the advection of the quantity a by a velocity field $\boldsymbol{u}$. In the presence of a moving mesh, the mesh faces velocity $\boldsymbol{v_m}$ appears in the advection term; indeed, the advective flux of a through a face f is proportional to

the relative velocity flux $\boldsymbol{u} - \boldsymbol{v_m}$ at the face. (3) represents the diffusion of the quantity a with a diffusivity γ_a, which could be a scalar field or a tensor. And lastly, (4) is a source/sink term. The way each one of these terms is discretized is detailed, except for (4) as it can take many forms, and thus, no general way to discretize this term can be provided.

Temporal term discretization

In FVM, the different fields are assumed to be uniform within a cell, so that the temporal term (1) in equation 2.31 can be written as follows:

$$\frac{\partial}{\partial t}\int_{V_c} a dV = \frac{\partial a_c V_c}{\partial t}\,, \tag{2.32}$$

where a_c is the value of a at cell c center, and V_c is the volume of the cell. Let us note t^i the time at which the temporal derivative (eq. 2.32) is evaluated. The indices $i-1$ and $i-2$ refer to the two previous time iterations.

The simplest scheme to discretize the temporal derivative term is the first-order Euler scheme:

$$\left.\frac{\partial a_c V_c}{\partial t}\right|^i = \frac{a_c^i V_c^i - a_c^{i-1} V_c^{i-1}}{t^i - t^{i-1}}\,. \tag{2.33}$$

With the Euler scheme, the derivative is straightforwardly evaluated as the slope between two successive values of $a_c V_c$.

Another possibility is the use of the second order Crank-Nicholson time scheme. It estimates the temporal derivative using a blending between the Euler time scheme (eq. 2.33) and the temporal derivative value at the previous time iteration. This blending is done through a coefficient λ_{oc} called the off-centering coefficient, which takes values between 0 and 1 and is set by the user. The scheme is written as follows:

$$\left.\frac{\partial a_c V_c}{\partial t}\right|^i = (1+\lambda_{oc})\frac{a_c^i V_c^i - a_c^{i-1} V_c^{i-1}}{t^i - t^{i-1}} + \lambda_{oc}\left.\frac{\partial a_c V_c}{\partial t}\right|^{i-1}\,. \tag{2.34}$$

At the first time step of the simulation, λ_{oc} is set equal to 0, as the previous time step derivative cannot be evaluated. This is equivalent to the use of a first-order Euler time scheme 2.33). At each time step, the value of $\partial a_c V_c/\partial t$ is stored to be used at the next time iteration. As a result, the time derivative expression (eq. 2.34) contains the history of all previous time derivatives. It must be noted that this definition of the Crank-Nicolson scheme is very different from the original method from Crank and Nicolson [1947], and it is not understood why the *OpenFOAM* developers gave it this name.

Finally, another second-order time scheme available is the *backward* scheme. The idea of this scheme is to estimate the temporal derivative of the quantity $a_c V_c$ on the interval $t \in [t_{i-2}, t_i]$ using a second-order Lagrange interpolating polynomial:

$$(a_c V_c)(t) = \sum_{j=0}^{2} a_c^{i-j} V_c^{i-j} \prod_{\substack{k=0 \\ k\neq j}}^{2} \frac{t - t^{i-k}}{t^{i-j} - t^{i-k}}\,. \tag{2.35}$$

Defining the time steps as $t^i = t^{i-1} + \delta t^i$ and $t^{i-1} = t^{i-2} + \delta t^{i-1}$, and then derivating this function and evaluating it in $t = t^i$, the *backward* scheme is obtained:

$$\left.\frac{\partial a_c V_c}{\partial t}\right|^i = a_c^i V_c^i \frac{2\delta t^i + \delta t^{i-1}}{\delta t^i(\delta t^i + \delta t^{i-1})} - a_c^{i-1} V_c^{i-1} \frac{\delta t^i + \delta t^{i-1}}{\delta t^i \delta t^{i-1}} + a_c^{i-2} V_c^{i-2} \frac{\delta t^i}{(\delta t^i + \delta t^{i-1})\delta t^{i-1}} \,. \quad (2.36)$$

If a uniform time stepping is applied ($\delta t = \delta$ is constant $\forall i \in N$), the following expression is obtained:

$$\left.\frac{\partial a_c V_c}{\partial t}\right|^i = \frac{3a_c^i V_c^i - 4a_c^{i-1} V_c^{i-1} + a_c^{i-2} V_c^{i-2}}{2\delta t} \,. \quad (2.37)$$

It can be noted that, if a first-order Lagrange polynomial is used instead of a second-order one to estimate $a_c V_c$, the first-order Euler time scheme is retrieved.

Advection term discretization

The advection term (2) corresponds to the advection of the field a by a velocity field $\boldsymbol{u}$, which in the general case, depends on a.

$$\oint_{S_c} [(\boldsymbol{u} - \boldsymbol{v_m}).\boldsymbol{n}]\, a dS = \sum_f a_f (\boldsymbol{u}_f - \boldsymbol{v}_{\boldsymbol{m}}^f).\boldsymbol{n}_f S_f \,, \quad (2.38)$$

where $\boldsymbol{u}_f$ and a_f are respectively the value of $\boldsymbol{u}$ and a at face f, $\boldsymbol{v}_{\boldsymbol{m}}^f$ is face f velocity, $\boldsymbol{n}_f$ the unit vector normal to face f, and S_f, the area of face f. $\boldsymbol{u}_f$ is obtained with an interpolation between the two neighboring cells, called *owner* and *neighbor*, and respectively showcased by the indices o and n. Usually, a linear interpolation is used to estimate $\boldsymbol{u}_f$, but the user could select another interpolation method. The linear interpolation is written as follows:

$$\boldsymbol{u}_f = \frac{d_{N-f}\boldsymbol{u}_O + d_{O-f}\boldsymbol{u}_N}{d_{N-f} + d_{O-f}} \,, \quad (2.39)$$

where d_{O-f} and d_{N-f} are the respective distances between the face center f and the *owner* and neighbor cell centers, O and N. $\boldsymbol{u}_O$ and $\boldsymbol{u}_N$ are the values of $\boldsymbol{u}$ at the center of the owner and neighbor cells. The advection term is non-linear if the velocity field depends on a. In order to linearize this term and allow an implicit resolution of the equation, the value of $\boldsymbol{u}_f$ at the previous time step is used. In *OpenFOAM*, the quantity $\phi_f = \boldsymbol{u}_f.\boldsymbol{n}_f S_f$ is computed at the previous time iteration $i-1$. The advective term then becomes:

$$\sum_f a_f^i \left(\phi_f^{i-1} - \boldsymbol{v}_{\boldsymbol{m}}^{fi}.\boldsymbol{n}_f S_f\right) = \sum_f a_f^i \left(\boldsymbol{u}_f^{i-1}.\boldsymbol{n}_f^{i-1} S_f^{i-1} - \boldsymbol{v}_{\boldsymbol{m}}^{fi}.\boldsymbol{n}_f^i S_f^i\right) \,. \quad (2.40)$$

In fluid mechanics problem, the momentum equation (see eq. 2.1) has a non-linear advective term representing the advection of the fluid momentum by its own velocity field. As previously done for a scalar field, it is integrated on a cell volume:

$$\int_{V_c} \nabla.(\boldsymbol{u} \otimes \boldsymbol{u}) dV = \oint_{S_c} \boldsymbol{u}(\boldsymbol{u}.\boldsymbol{n}) dS = \sum_f \boldsymbol{u}_f (\boldsymbol{u}_f.\boldsymbol{n}_f) S_f \,. \quad (2.41)$$

In order to linearize this term and build a matrix system, one of the two velocities is computed explicitly.

$$\int_{V_c} \nabla.(\boldsymbol{u} \otimes \boldsymbol{u}) dV = \sum_f \boldsymbol{u}_f^i (\boldsymbol{u}_f^{i-1}.\boldsymbol{n}_f) S_f \,. \tag{2.42}$$

In *OpenFOAM*, the quantity $\boldsymbol{u}_f^{i-1}.\boldsymbol{n}_f S_f$ which corresponds to the flux of velocity through the face f is noted ϕ and is computed explicitly. The value of $\boldsymbol{u}_f^{i-1}$ is obtained by interpolation from the value $\boldsymbol{u}_O^{i-1}$ et $\boldsymbol{u}_N^{i-1}$, the velocity at the center of the *owner* and *neighbor* cells, respectively. A linear interpolation is generally employed, but the user could consider another interpolation scheme.

Diffusion term discretization

The diffusive term (3):

$$\int_{V_c} \nabla.(\gamma_a \nabla a) dV = \oint_{S_c} \gamma_a \nabla a.\boldsymbol{n} dS = \sum_f \gamma_a^f \nabla a|_f.\boldsymbol{n}_f S_f \,, \tag{2.43}$$

where γ_a^f is the diffusivity evaluated at the face f, obtained with an interpolation between γ_a value in the two cells sharing the face f. Generally a linear interpolation is used. $\nabla a|_f$ is the surface normal gradient of a evaluated directly as follows:

$$\nabla a|_f = \frac{a_O - a_N}{\boldsymbol{X}_O - \boldsymbol{X}_N} \tag{2.44}$$

where a_O and a_N are the values of a at the center of the owner and neighbor cells, respectively. $\boldsymbol{X}_O$ and $\boldsymbol{X}_N$ are the position of the owner and neighbor cell centers. If the non-orthogonality of the mesh is high, that is if the angle between the vector $\boldsymbol{X}_O - \boldsymbol{X}_N$ and the face normal vector $\boldsymbol{n}_f$ is important, an explicit non orthogonal correction can be added for better accuracy in the numerical discretization.

2.6.2 Advection schemes

When performing numerical simulation of fluid mechanics problems, the system behavior is in most cases way more sensitive to the advection term (2) discretization than the other terms. For that reason, *OpenFOAM* provides many different numerical schemes for the advective term. In this section are described the basic advection schemes available as more complex schemes are derived from them. The most basic scheme is the linear scheme, where the value of the field at a face f is an interpolation between the values of the same field at the two cells sharing the face f:

$$u_{f,lin} = \frac{d_{N-f} a_O + d_{O-f} a_N}{d_{N-f} + d_{O-f}} \,, \tag{2.45}$$

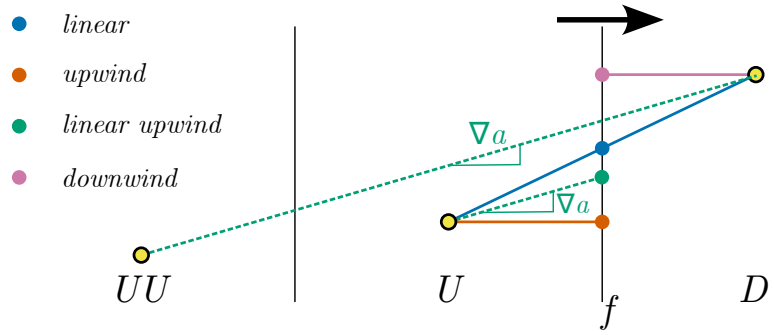

Figure 2.11: Schematic of basic advection schemes, value on face f from downwind cell D, upwind cell U and upwind-upwind cell UU.

where d_{O-f} and d_{N-f} are respectively the distance between the face f and the cell centers of the owner cell O and neighbor cell N. The *linear* scheme is accurate but unstable.

U is the upwind cell D the downwind cell and UU is the upwind-upwind cell (see Figure 2.11). The *upwind* scheme use the value of the field at the upwind cell of face f:

$$u_{f,up} = a_U \,. \tag{2.46}$$

Another useful second order scheme is the *linear-upwind* scheme, which adds an explicit correction to the *upwind* scheme. This correction is based on the gradient of the field at the upwind cell center $\nabla a|_U$. It is written as follows:

$$u_{f,up} = a_U + (\boldsymbol{X}_f - \boldsymbol{X}_U).\nabla a|_U \,, \tag{2.47}$$

where $\boldsymbol{X}_f - \boldsymbol{X}_U$ is the vector going from the upwind cell center to the center of face f. One particularity of this scheme is that the upwind part is added implicitly in the matrix system and the gradient-based correction is added explicitly. The gradient of a field at the center of a cell C is computed from the values of this same field at the faces delimiting the cell:

$$\nabla a|_U = \frac{1}{V_c} \sum_f a_f S_f \boldsymbol{n}_f \,. \tag{2.48}$$

2.6.3 Pressure-velocity coupling

When dealing with compressible flows, a state equation usually allows to compute the pressure from other quantities, like the temperature and the density. On the other hand, when the fluid is considered incompressible, there is no equation describing the pressure field. The pressure needs to be adjusted so that the solution of the momentum equation also verifies the continuity equation. To achieve that, a pressure equation is derived from the momentum and continuity equation. The equation for the fluid and the pressure can be solved simultaneously using one big matrix [Uroić et al., 2019]. The other strategy is to rely on a pressure-velocity coupling algorithm to solve these equations iteratively

until convergence of the system. For instance, the *SIMPLE* algorithm was developed by Patankar and Spalding [1983] to solve stationary flows. As stated previously, *sedExnerFoam* is based on the *PIMPLE* algorithm, which is a combination of two algorithms, *SIMPLE* and *PISO*, introduced by Issa [1986] for transient flow solution. In the following, the *PISO* and *PIMPLE* algorithms are detailed.

Discretizing equation 2.1 on a mesh made up of n cells, the following linear system is obtained:

$$\boldsymbol{\mathcal{M}}\boldsymbol{u} = \boldsymbol{\mathcal{B}} - \nabla p\,, \tag{2.49}$$

where $\boldsymbol{\mathcal{M}}$ is a matrix and $\boldsymbol{\mathcal{M}}\boldsymbol{u}$ corresponds to the implicit part of the system. $\boldsymbol{\mathcal{B}}$ is a vector of dimension n, which encompasses all the explicit terms. Equation 2.49 is first solved using the pressure at the previous time step p^{i-1}. It gives a first predictor value $\boldsymbol{u}_{\text{pred}}$ for $\boldsymbol{u}$. This first estimate of the velocity field does not verify the continuity equation. A correction on the pressure field and on the velocity field is needed in order to verify both the momentum and the continuity equations. Starting from equation 2.49, the matrix $\boldsymbol{\mathcal{M}}$ is decomposed into the sum of a diagonal matrix and an off-diagonal matrix:

$$\boldsymbol{\mathcal{M}} = \boldsymbol{\mathcal{A}} + (\boldsymbol{\mathcal{M}} - \boldsymbol{\mathcal{A}})\,, \tag{2.50}$$

where $\boldsymbol{\mathcal{A}}$ is the diagonal part of $\boldsymbol{\mathcal{M}}$, and $\boldsymbol{\mathcal{M}} - \boldsymbol{\mathcal{A}}$ the off-diagonal part. Using this decomposition, equation 2.49 can be written as:

$$\boldsymbol{\mathcal{A}}\boldsymbol{u} = \boldsymbol{\mathcal{B}} - (\boldsymbol{\mathcal{M}} - \boldsymbol{\mathcal{A}})\boldsymbol{u} - \frac{1}{\rho_f}\nabla p\,. \tag{2.51}$$

A vector $\boldsymbol{\mathcal{H}}$ is defined as $\boldsymbol{\mathcal{H}} = \boldsymbol{\mathcal{B}} - (\boldsymbol{\mathcal{M}} - \boldsymbol{\mathcal{A}})\boldsymbol{u}^{\text{pred}}$. Then using $\boldsymbol{u}^{\text{pred}}$ as an estimate for $\boldsymbol{u}$ in the off-diagonal part of the system $(\boldsymbol{\mathcal{M}} - \boldsymbol{\mathcal{A}})\boldsymbol{u}$, the following equation is obtained:

$$\boldsymbol{\mathcal{A}}\boldsymbol{u} = \boldsymbol{\mathcal{H}} - \frac{1}{\rho_f}\nabla p\,. \tag{2.52}$$

Since $\boldsymbol{\mathcal{A}}$, is diagonal $\boldsymbol{\mathcal{A}}^{-1}$ is directly computed as:

$$\boldsymbol{\mathcal{A}}^{-1}_{ij} = \begin{cases} 1/\boldsymbol{\mathcal{A}}_{ij} & \text{if } i = j\,, \\ 0 & \text{else}\,, \end{cases} \tag{2.53}$$

and equation 2.52 becomes:

$$\boldsymbol{u} = \boldsymbol{\mathcal{A}}^{-1}\boldsymbol{\mathcal{H}} - \boldsymbol{\mathcal{A}}^{-1}\left(\frac{1}{\rho_f}\nabla p\right)\,. \tag{2.54}$$

Applying a divergence operator to the previous equation, and using the mass conservation equation (eq. 2.49) to suppress the velocity term $\nabla.\boldsymbol{u} = 0$, the correction equation for the pressure is obtained.

$$\nabla.(\boldsymbol{\mathcal{A}}^{-1}\boldsymbol{\mathcal{H}}) = \nabla.\left(\frac{1}{\rho_f}\boldsymbol{\mathcal{A}}^{-1}\nabla p\right)\,. \tag{2.55}$$

The corrected pressure p^{corr} is obtained by solving this equation. Then the corrected velocity $\boldsymbol{u}^{\text{corr}}$ is directly computed by replacing p by p^{corr} in equation 2.54. Multiple corrector steps can be made. For that the computed corrected velocity field $\boldsymbol{u}^{\text{corr}}$ is used to update the value of $\boldsymbol{\mathcal{H}} = \boldsymbol{\mathcal{B}} - (\boldsymbol{\mathcal{M}} - \boldsymbol{\mathcal{A}})\boldsymbol{u}^{\text{corr}}$. Then equation 2.55 is solved once again with the new value of $\boldsymbol{\mathcal{H}}$ and a new corrected pressure and velocity fields are obtained from equation 2.55 and 2.54. The different operations of the *PISO* algorithm are detailed in Algorithm 1.

Algorithm 1: *PISO* algorithm

assemble system for $\boldsymbol{u}$: $\boldsymbol{\mathcal{M}}\boldsymbol{u} = \boldsymbol{\mathcal{B}}$;
$\boldsymbol{u}^{\text{pred}} \leftarrow$ solution of eq. 2.49 : $\boldsymbol{\mathcal{M}}\boldsymbol{u} = \boldsymbol{\mathcal{B}} - \nabla p$;
$\boldsymbol{\mathcal{A}} \leftarrow \boldsymbol{\mathcal{M}}\boldsymbol{\mathcal{I}}_n$;
while *PISO loop* **do**
  $\boldsymbol{\mathcal{H}} \leftarrow \boldsymbol{\mathcal{B}} - (\boldsymbol{\mathcal{M}} - \boldsymbol{\mathcal{A}})\boldsymbol{u}^{\text{pred}}$;
  $p^{\text{corr}} \leftarrow$ solution of eq. 2.55: $\nabla.(\boldsymbol{\mathcal{A}}^{-1}\boldsymbol{\mathcal{H}}) = \nabla.\left(\frac{1}{\rho_f}\boldsymbol{\mathcal{A}}^{-1}\nabla p\right)$;
  $\boldsymbol{u}^{\text{corr}} \leftarrow \boldsymbol{\mathcal{A}}^{-1}\boldsymbol{\mathcal{H}} - \boldsymbol{\mathcal{A}}^{-1}\left(\frac{1}{\rho_f}\nabla p^{\text{corr}}\right)$;
  $\boldsymbol{u}^{\text{pred}} \leftarrow \boldsymbol{u}^{\text{corr}}$;
  $p \leftarrow p^{\text{corr}}$;
end
$\boldsymbol{u} \leftarrow \boldsymbol{u}^{\text{pred}}$;

It should be noted that the different matrix involved in the algorithm ($\boldsymbol{\mathcal{M}}$, $\boldsymbol{\mathcal{A}}$) need to be stored only once before the *PISO* loop and are not modified afterward.

The *PIMPLE* algorithm is very similar but possess a second loop encompassing the *PISO* algorithm. After every *PISO* loop, the matrix system described by equation 2.49 is assembled once again to obtain new values of $\boldsymbol{\mathcal{M}}$ and $\boldsymbol{\mathcal{B}}$. If only one *PIMPLE* loop is used, the algorithm is equivalent to the *PISO* algorithm. Using multiple *PIMPLE* iterations allows to solve the fluid equations even for Courant number higher than unity without triggering instabilities.

The algorithm also offers the possibility to under-relax equations 2.49 and 2.55. Under-relaxing a linear system means that only a fraction of the solution of the system is used to update the field values. For instance, if $\boldsymbol{u}^{\text{sol}}$ is the solution of equation 2.49 and $\boldsymbol{u}^{\text{old}}$ the old field, then using a relaxation factor $0 < \alpha_u \leq 1$ the solution of the under-relaxed system is $\boldsymbol{u} = \alpha_u\boldsymbol{u}^{\text{sol}} + (1 - \alpha_u)\boldsymbol{u}^{\text{old}}$. This is equivalent to dividing all the diagonal coefficients of matrix $\boldsymbol{\mathcal{M}}$ by α_u, so that $\boldsymbol{\mathcal{A}}$ becomes $\boldsymbol{\mathcal{A}}/\alpha_u$, and to update the vector $\boldsymbol{\mathcal{B}}$ to $\boldsymbol{\mathcal{B}}(1/\alpha_u - 1)\boldsymbol{\mathcal{A}}\boldsymbol{u}^{\text{old}}$. Under-relaxation is a mean to reinforce the diagonal dominance of a matrix system and help the convergence of the iterative method used to solve the system. The *PIMPLE* algorithm is summarized in Algorithm 2.

Algorithm 2: *PIMPLE* algorithm

$p^{\text{pred}} \leftarrow p$;
while *PIMPLE loop* **do**
  assemble system for $\boldsymbol{u}$: $\boldsymbol{\mathcal{M}u} = \boldsymbol{\mathcal{B}}$;
  under-relaxa system, $\boldsymbol{\mathcal{A}} \leftarrow \boldsymbol{\mathcal{A}}/\alpha_u$, $\boldsymbol{\mathcal{B}} \leftarrow \boldsymbol{\mathcal{B}}(1/\alpha_u - 1)\boldsymbol{\mathcal{A}u}$;
  $\boldsymbol{u}^{\text{pred}} \leftarrow$ solution of eq. 2.49 : $\boldsymbol{\mathcal{M}u} = \boldsymbol{\mathcal{B}} - \nabla p$;
  while *PISO loop* **do**
    $\boldsymbol{\mathcal{H}} \leftarrow \boldsymbol{\mathcal{B}} - (\boldsymbol{\mathcal{M}} - \boldsymbol{\mathcal{A}})\boldsymbol{u}^{\text{pred}}$;
    assemble system for p: $\nabla.(\boldsymbol{\mathcal{A}}^{-1}\boldsymbol{\mathcal{H}}) = \nabla.\left(\frac{1}{\rho_f}\boldsymbol{\mathcal{A}}^{-1}\nabla p\right)$;
    $p^{\text{corr}} \leftarrow$ solution of eq. 2.55: $\nabla.(\boldsymbol{\mathcal{A}}^{-1}\boldsymbol{\mathcal{H}}) = \nabla.\left(\frac{1}{\rho_f}\boldsymbol{\mathcal{A}}^{-1}\nabla p\right)$;
    under-relax: $p^{\text{corr}} \leftarrow \alpha_p p^{\text{corr}} + (1-\alpha_p)p^{\text{pred}}$: ;
    $\boldsymbol{u}^{\text{corr}} \leftarrow \boldsymbol{\mathcal{A}}^{-1}\boldsymbol{\mathcal{H}} - \boldsymbol{\mathcal{A}}^{-1}\left(\frac{1}{\rho_f}\nabla p^{\text{corr}}\right)$;
    $\boldsymbol{u}^{\text{pred}} \leftarrow \boldsymbol{u}^{\text{corr}}$;
    $p^{\text{pred}} \leftarrow p^{\text{corr}}$;
  end
  $p \leftarrow p^{\text{pred}}$;
  $\boldsymbol{u} \leftarrow \boldsymbol{u}^{\text{pred}}$;
end

2.6.4 Exner equation and finite-area

Projection of the finite-area mesh

Unlike equations for fluid and suspension transport, the Exner equation is a surface equation and is therefore treated separately on a finite-area mesh. The finite-area method was introduced in *OpenFOAM* by Tukovic and Jasak [2008], initially to study the surfactant at the interface between two fluids. It is used to solve partial differential equations on a surface curved in the 3D space. This is done by splitting the surface over a finite number of polygonal control areas (see Figure 2.12) over which the equations are integrated. The surface's curvature is considered when dealing with differential operators, including gradient, divergence, and Laplacian.

In *sedExnerFoam*, the finite-area method is used to solve the Exner equation (eq. 1.4) on the bed surface. Thus, the finite-area mesh is the bed boundary of the finite-volume mesh. The Exner equation is not solved directly on the finite-area mesh, but on a horizontal projection (see Figure 2.13), so that the curvature of the bed does not play any role in the solution.

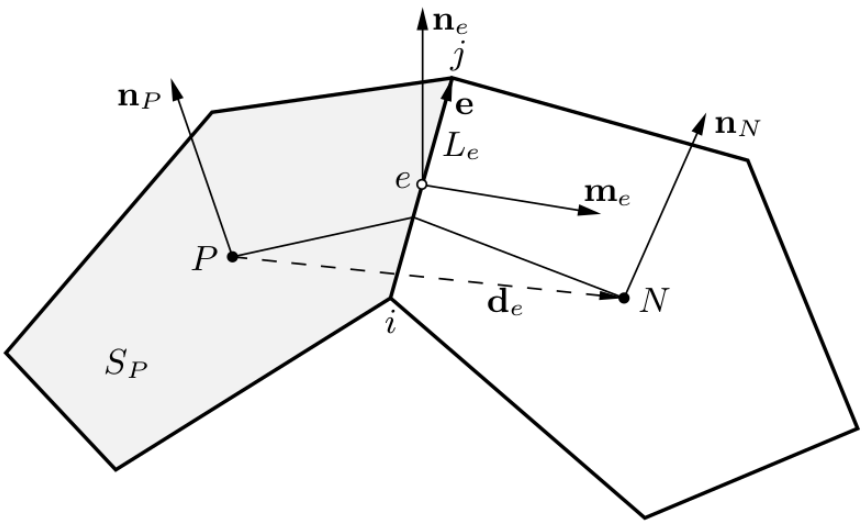

Figure 2.12: Polygonal control area. Image from Tukovic and Jasak [2008].

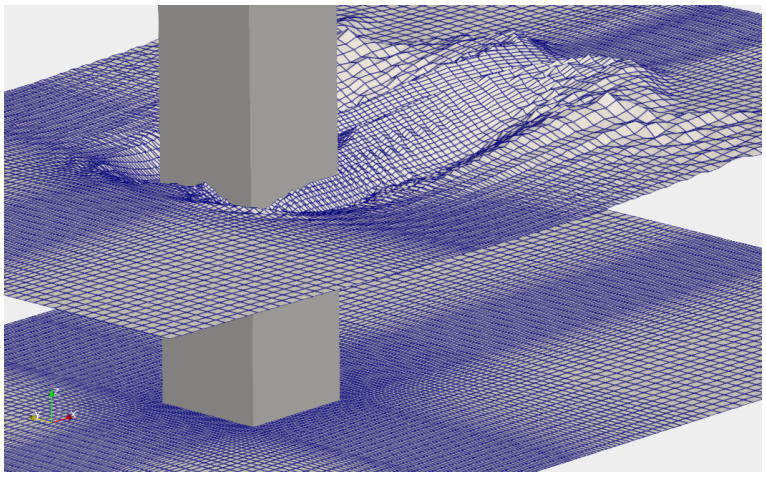

Figure 2.13: Projection of the finite-area mesh on a horizontal plane.

Resolution of the Exner equation

Integrating the Exner equation (eq. 1.4) over the projection of a face f of the finite-area mesh yields:

$$(1-\lambda_s)S_{fp}\frac{\partial z_b}{\partial t}\bigg|_f = -\sum_e (\boldsymbol{q_{b,ep}}.\boldsymbol{n_{ep}})l_{ep} + (D-E)_f S_{fp}\,, \tag{2.56}$$

where $S_{fp} = S_f(\boldsymbol{n_f}.\boldsymbol{e_g})$ is the projected area of face f and S_f is face f area, $\boldsymbol{n_f}$ is the face normal unit vector oriented outward of the computational domain and $\boldsymbol{e_g}$ is a unit vector oriented along the gravity vector. l_{ep} is the length of the projected edge and $\boldsymbol{n_{ep}}$ the projected normal edge vector which is oriented toward the outside of f. To discretize the temporal term in equation 2.56, an Adams-Bashforth scheme is used. The users can select the order of the scheme (1 or 2), the first order Adams-Bashforth being equivalent to a first order Euler explicit scheme. The right hand side of equation 2.56 corresponds to the volume variation of sediment contained under face f. Integrating equation 2.56 between the previous time iteration t^{i-1} and the current time iteration t^i, for which z_b value is still not known, the following equation is obtained:

$$\int_{t^{i-1}}^{t^i} \frac{\partial z_b}{\partial t} dt = \int_{t^{i-1}}^{t^i} F(t,\boldsymbol{x}) dt\,. \tag{2.57}$$

The second order Adams-Bashforth scheme is obtained by integrating this relation assuming a linear evolution of F between t^{i-1} and t^i so that:

$$z_b^{i+1} = z_b^i + \frac{1}{t^i - t^{i-1}} \int_{t^{i-1}}^{t^i} \left(F^{i-1}(\boldsymbol{x}) + \frac{F^i(\boldsymbol{x}) - F^{i-1}(\boldsymbol{x})}{t^i - t^{i-1}} (t - t^{i-1}) \right) dt\,. \tag{2.58}$$

From equation 2.56, at each time step, an increment of bed elevation δz_b is computed for each face centers. In *OpenFOAM*, the mesh geometry is defined by the vertices coordinates. Thus, to impose a mesh motion, the vertical displacements computed at face centers need to be interpolated from faces to vertices. Particular caution must be given to the interpolation scheme to ensure mass conservation. A naive approach would be to linearly interpolate δz_b, which would be mass conservative for cases limited to one horizontal dimension and structured mesh, but would fail to preserve the mass in the general case of an unstructured mesh. Jacobsen [2015] made a detailed review of the different possible methods to solve the Exner equation and analyzed their benefits and shortcomings. He proposed a mass conservative interpolation scheme, which is the one implemented in the current model.

A dual mesh is constructed as depicted in Figure 2.14. Each vertex v belonging to the primary mesh is the center of a face of the dual mesh. The vertices delimiting this dual face are the neighboring primary faces f_i sharing the vertex v as well as the centers of the edges whose one end is vertex v. The mass increment of the sediments contained under a face f is $m_f = \rho_s S_{fp} \delta z_b|_f$, where $\delta z_b|_f$ is the face elevation increment. To ensure mass conservation during the interpolation process, the sum of the mass contained under

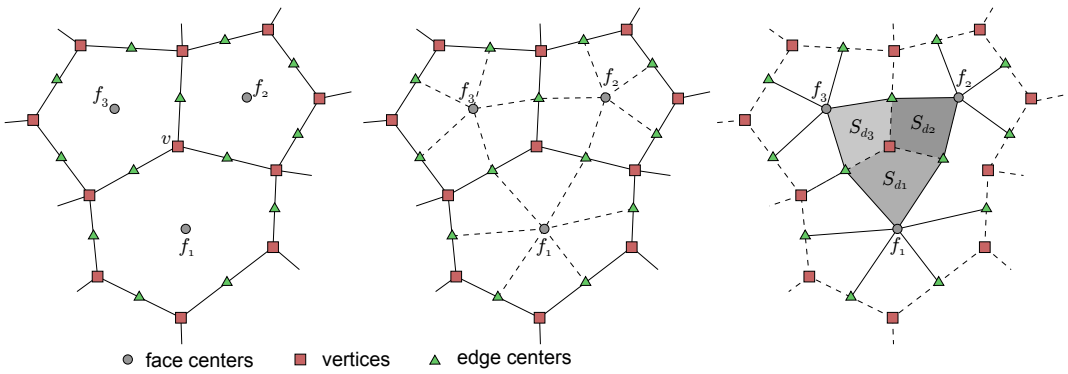

Figure 2.14: Decomposition of the horizontal projection of the finite area mesh into a dual mesh.

every face must be the same when computing this sum for the initial mesh and for the dual mesh. The vertical displacement of each vertex $\delta z_b|_v$ is then a linear combination of the displacements of the faces sharing this vertex. The weight associated with each face is proportional to the area of the quadrilateral defined by the face center, the vertex and the centers of the two edges belonging to the face and sharing the vertex (see Figure 2.14). Let us note the area of this quadrilateral S_{df}, the value of the elevation increment $\delta z_b|_v$ associated to a vertex v is computed:

$$\delta z_b|_v = \frac{1}{S_v} \sum_f S_{df} \delta z_b|_f \,, \tag{2.59}$$

where S_v is the area of the dual face whose center is the vertex v. It is equal to the sum of the area of each face associated quadrilateral: $S_v = \sum_f S_{df}$. Thus, the sum of the interpolation weights is equal to 1. This interpolation method is mass conservative and also has the advantage of acting as a filter on the vertical bed displacement and helps to keep the numerical solution of the Exner equation stable.

At each time step, the Exner equation provides the rate of bed level change, which is then imposed as a vertical displacement at the mesh vertices located on the sediment–fluid interface. These displacements then serve as boundary conditions for a mesh motion solver based on the Laplace equation:

$$\nabla.(\Gamma_c \nabla \boldsymbol{\Delta X_c}) = 0 \,, \tag{2.60}$$

where Γ_c is the mesh diffusivity and $\nabla \boldsymbol{\Delta X_c}$) is the displacements of the cell centers. Solving equation 2.60 yields a new position for the center of each cell. Once again, the mesh geometry being defined by the vertices, the displacements must be interpolated from cell centers to the vertices to obtain the new mesh geometry. The mesh diffusivity Γ_c must be specified by the user. In order to maintain a good mesh quality over time, a good practice is to set Γ_c as proportional to the inverse of the distance to the sediment $\Gamma_c \propto 1/l_w$ or to the inverse of the square of the distance $\Gamma_c \propto 1/l_w^2$.

2.7 Conclusion

This chapter has provided a detailed presentation of *sedExnerFoam*, encompassing both its mathematical formulation and numerical implementation. The first part focused on establishing the physical foundations of the model, including the hydrodynamic equations, turbulence modeling through the RANS approach, and appropriate wall treatments for near bed flows. The sediment transport component was also described in depth, with emphasis on motion thresholds, empirical transport formulas for both bedload and suspended load, and the incorporation of bedload flux saturation to capture sediment flow interactions more accurately.

The second part of the chapter addressed the numerical methods used to implement the model. The finite volume and finite area approaches were introduced, followed by a discussion of critical numerical procedures such as the pressure–velocity coupling algorithm. Special attention was given to the numerical resolution of the Exner equation, which governs morphological evolution and is central to simulating scour and bedforms development.

Together, these components provide a framework for simulating sediment transport and bed morphology evolution in various situations. The next chapters will focus on the application and validation of this model through case studies and comparisons with experimental or reference data.

Chapter 3

Model validation

Following an exhaustive description of the model, this chapter presents the various benchmarks that ensure its proper functioning. These benchmarks were selected to evaluate each component of the model separately. The goal is to demonstrate the model's capabilities and ensure its correct implementation and behavior. During development, the Exner equation was implemented independently of the hydrodynamics and suspended load. A simplified model is used to drive morphological changes without solving the hydrodynamics. This model is presented at the beginning of the chapter and is applied to an idealized dune migration case. Three benchmarks not associated with bed-level changes illustrate the implementation of the suspended load without coupling with the morphology. These benchmarks range from the sedimentation of a mixture of silicon oil and polystyrene particles, to sediments suspension in a channel under equilibrium conditions, that is when turbulent diffusion and buoyancy cancel each other out, and out of equilibrium when a flow encounter a transition between a non-erodible bed to an erodible one. Finally, the mass conservation property of the model is verified through different benchmarks involving the fully coupled model.

3.1 Idealized dune transport

The main contribution of this work is certainly the implementation of the Exner equation in *OpenFOAM*. When studying the morphological formation or evolution of bedforms driven by the shear stress exerted on the sediment bed by the flow, different sources of error are to be considered such as the resolution of the flow itself and the accurate prediction of eventual boundary layer detachments and recirculation cells above bedforms, or the uncertainty associated with empirical bedload formulas. In order to isolate and test the Exner equation separately, the sediment bed morphological evolution was first implemented as a standalone model, and driven by a very simplified flow and an idealized relation linking the flow and the bedload flux. With this simplified model presented later on, an analytical solution can be derived to describe the bed level evolution over time and used to verify the numerical implementation of the Exner equation. Such a model has already been used [Johnson and Zyserman, 2002] to study spatial oscillations generated

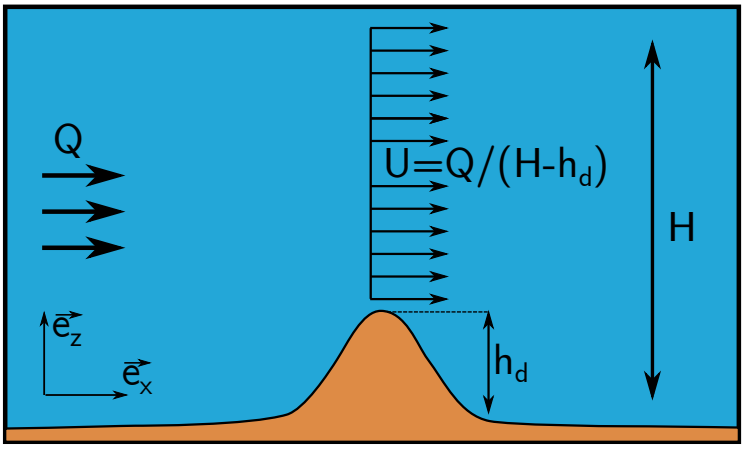

Figure 3.1: Schematic of the idealized dune transport case.

by the Exner equation and its filtering.

The dimensional idealized migration of a dune is considered. A dune of height h_d is immersed in a channel with uniform water depth H ($H > h_d$). The flow is considered uniform in the vertical direction and the discharge per unit width is Q. The fluid velocity field is supposed vertically uniform and in the stream wise direction, the velocity changes is obtained by conservation of mass:

$$u = \frac{Q}{H - z_b}\,, \tag{3.1}$$

where z_b is the bed level, so that u is an increasing function of the bed level. A schematic of the problem is illustrated in Figure 3.1. In this simplified case, only bedload transport is considered. To be able to derive an analytical solution of the Exner equation, the bedload q_b must be expressed as a function of the bed elevation z_b. This is done by assuming that the bedload is a power law of the velocity u:

$$q_b = \alpha_d u^{\beta_d}\,, \tag{3.2}$$

where α_d and β_d are two positive constants. Using the chain rule of calculus, the Exner equation can be written as a wave equation:

$$\frac{\partial z_b}{\partial t} + c(z_b)\frac{\partial z_b}{\partial x} = 0\,, \tag{3.3}$$

$$c(z_b) = \frac{\partial q_b}{\partial z_b} = \frac{\alpha_d \beta_d Q^{\beta_d}}{(H - z_b)^{\beta_d + 1}}\,, \tag{3.4}$$

where $c(z_b)$, is the celerity of the bedform.

Starting with a given initial bed level $z_b(x, t = 0) = F_0(x)$, the solution to equation (3.3) is obtained with the method of characteristics, leading to $z_b(x, t) = F_0(x - ct)$. Depending on F_0, shocks can occur as the dune migrates. A shock occurs if, at least on

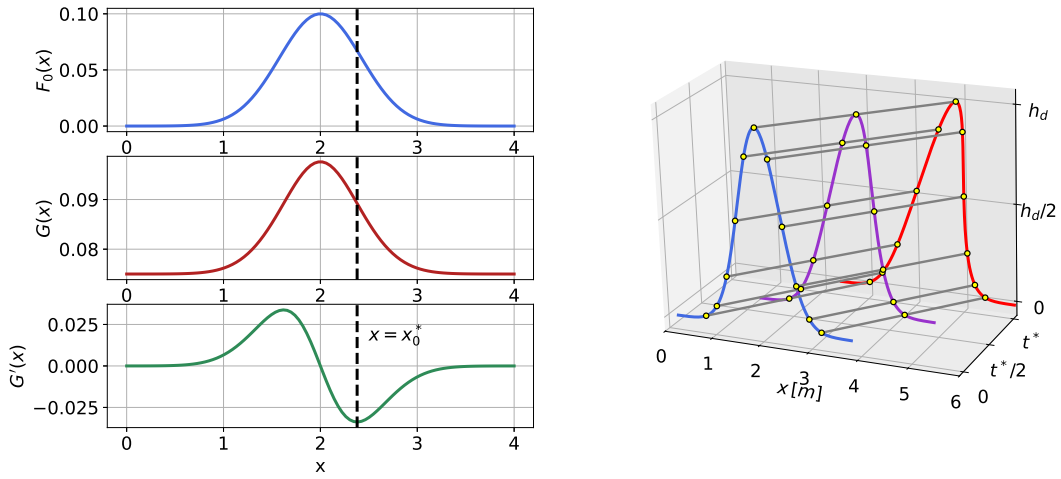

Figure 3.2: On the left, representation of the initial condition $F_0(x)$, the slope of the characteristic lines $G(x)$, and the derivative of G. On the right, representation of the advection of the initial Gaussian dune along the characteristic lines.

some interval $\mathcal{I} \in \mathbb{R}$, the function $G : x \to c(F_0(x))$, which is the slope of the characteristic lines, is decreasing. This is because a decrease of G means that the characteristic lines are intersecting. The dune celerity c being an increasing function of z_b, shocks will occur if the initial bedform F_0 presents at least one negative slope. In this idealized dune transport case, the initial dune profile is Gaussian:

$$F_0(x,t) = h_d\, e^{-\left(\frac{x - x_d^0}{\sigma_d}\right)^2}, \tag{3.5}$$

with h_d the height of the dune, x_d^0 the initial position of the top of the dune and σ_d a parameter linked to the dune width such that $F_0(x_d \pm \sqrt{\ln(2)}\sigma_d) = 0.5h_d$. This initial condition leads to the following expression for the slope of the characteristic lines:

$$G(x) = \frac{\beta_d \alpha_d Q^{\beta_d}}{(H - h_d e^{\left(\frac{x-x_d^0}{\sigma_d}\right)^2})^{\beta_d+1}}. \tag{3.6}$$

For more clarity, the functions F_0, G and G' are represented in Figure 3.2.

With this initial dune profile, a shock will appear somewhere at the downstream side of the dune. In order to know the position and time of the shock, it is needed to find the position x_0^* defined as follows, $G'(x_0^*) = min_{x\in\mathcal{R}}\,(G(x))$. It corresponds to the initial position of the point belonging to the characteristic line on which the first shock occurs. The breaking time is then obtained as $t^* = -1/G'(x_0^*)$, and the shock position x^* as well by advection of x_0^* along its characteristic line, $x^* = x_0^* + G(x_0^*)t^*$.

The following parameters are chosen:

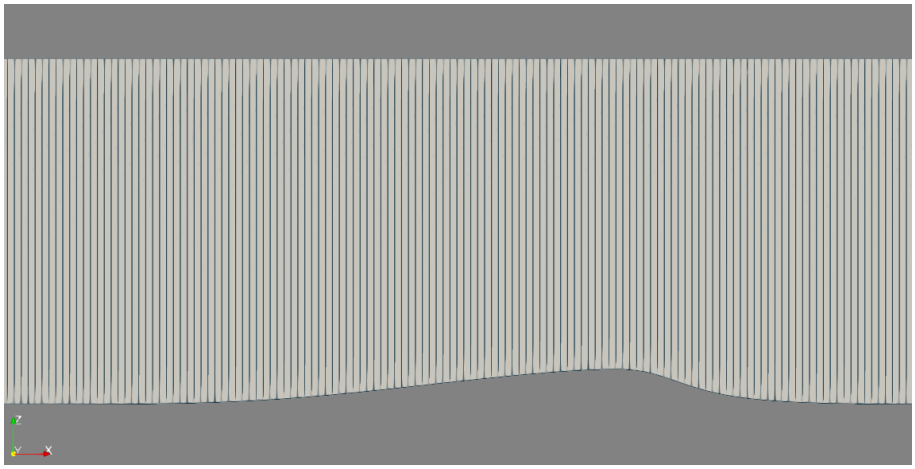

Figure 3.3: Visualization of the mesh during the migration of the dune.

- flow properties, $H = 1\,m$ and $Q = 1\,m^2/s$
- bedload flux, $\alpha_d = 0.05$ and $\beta_d = 1.5$ (eq. 3.2)
- dune properties, $h_d = 10\,cm$, $\sigma_d = 0.6\,m$

For this configuration, the breaking time is $t^* = 24.67\,s$ and the shock position $x^* = 4.51\,m$. The domain is 6 meters long and the initial position of the dune is $x_0 = 2\,m$. The mesh is made of a single row of 600 cells uniformly spaced in the stream wise direction. The shape of the domain changes over time with the bottom boundary matching with z_b. A visualization of the mesh is presented in Figure 3.3. A solution to equation 3.3 is looked for between time $t = 0$ and the breaking time t^*. A second *Adams-Bashforth* scheme is used for time discretization and a linear upwind scheme for the advective term. The simulation is run until the braking time has been reached. A comparison between the model results and the analytical solution is presented in Figure 3.4.

Overall, the model fits well with the analytical solution, except when the time gets close to the breaking time, where a small instability starts to develop at the top of the dune. Upstream of the dune's crest, the derivative of z_b with respect to x is positive, which implies $G'(x) > 0$ in this area. This means that the characteristic lines move away from each other in this area and that the bed slope decreases. On the downstream side of the dune, $G'(x) < 0$, and consequently, the slope increases until a shock occurs represented by a red dotted line in Figure 3.4.

As stated in the previous chapter, the interpolation from faces to vertices needed to enforce mesh motion acts as a filter on the bed elevation increment. However, depending on the case, it may not be sufficient to suppress the appearance of numerical instabilities, in particular in regions presenting steep slopes. The use of an avalanche model (eq. 2.23) brings more stability by limiting the maximum bed slopes and preventing shocks. However, no analytical solution can be derived for this problem if the avalanche mechanism is taken into account. This is illustrated in Figure 3.5 where the bed level at different times during the migration process, obtained with the avalanche model, is presented. The

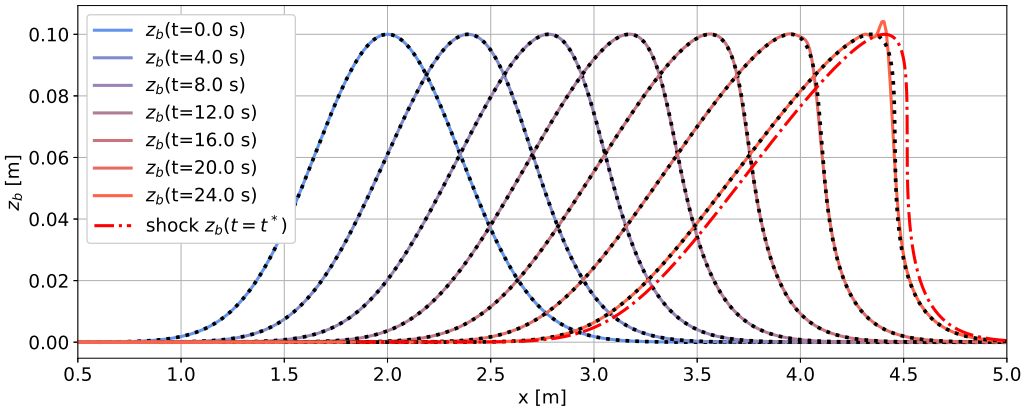

Figure 3.4: Idealized migration of an initially Gaussian dune, comparison between the numerical model results (solid lines) and the analytical solution (black dotted lines) at different times.

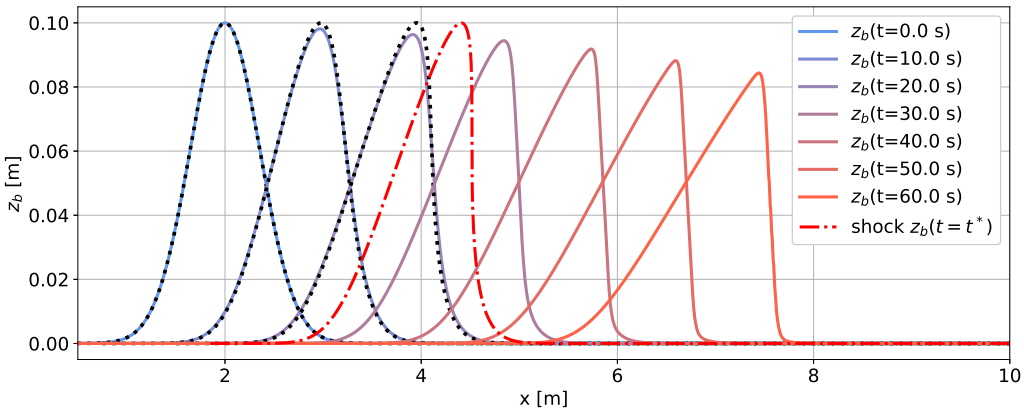

Figure 3.5: Idealized migration of an initially Gaussian dune with avalanche mechanism taken into account. Comparison between the numerical model results (solid lines) and the analytical solution (black dotted lines) at different times.

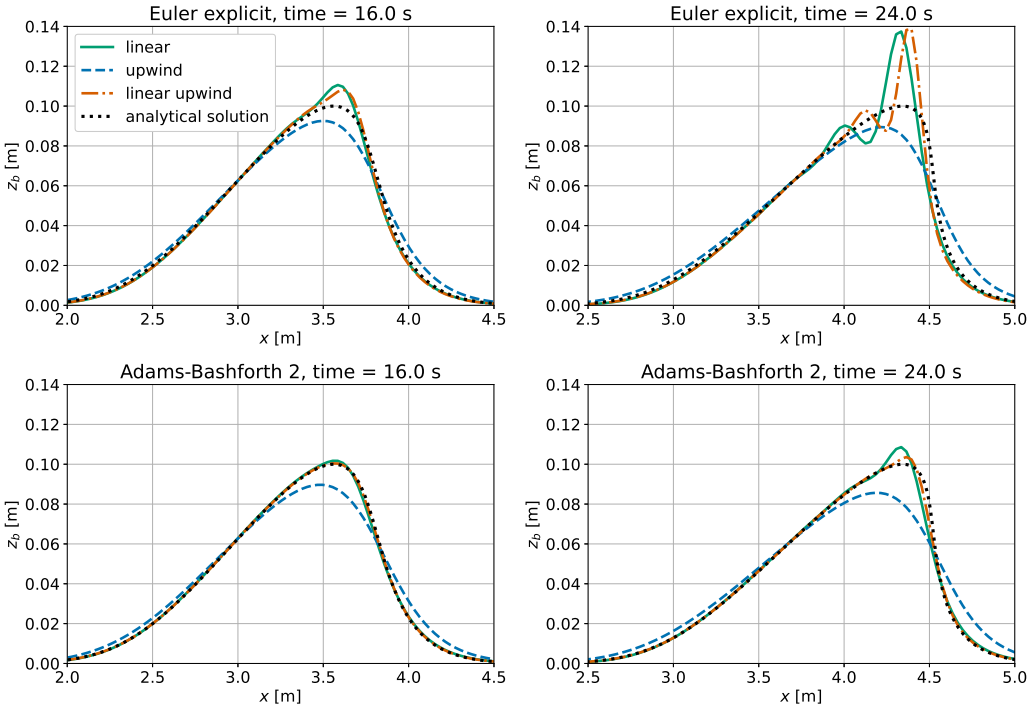

Figure 3.6: Comparison of the bed level issued from numerical simulations at two different times during the migration process, and obtained with the three different numerical schemes available for the advective term, and the two schemes for temporal integration (*Euler explicit* on top plots and *Adams-Bashforth 2* on bottom plots). The comparison is made at two different times, one intermediate time (left plots) and one time close to the breaking time (right plots).

dune continues its migration even after the breaking time and spreads, its length increases and its height decreases.

When solving the Exner equation, two different explicit schemes can be used to discretize the temporal evolution term (*backward*, *Euler explicit*) and three for the bedload term (*upwind*, *linear* and *linear-upwind*). Figure 3.6 illustrates how the chosen numerical schemes affect the solution stability and precision by comparing the bed evolution obtained at two different times for every possible schemes combination.

At the dune front, the gradient of z_b becomes important and consequently the gradient of q_b as well. Depending on the numerical schemes used, this can trigger oscillations. Using the Euler explicit scheme for time integration, the use of a second order scheme for advection leads to instabilities appearing on the dune's crest. On the other hand, the low order upwind scheme brings up numerical diffusion, and thus a poor prediction, but ensures numerical stability. A better match between the numerical results and the analytical solution is achieved using a second order scheme for the temporal term (*Adams Bashforth 2*) and the numerical solution no longer presents oscillations.

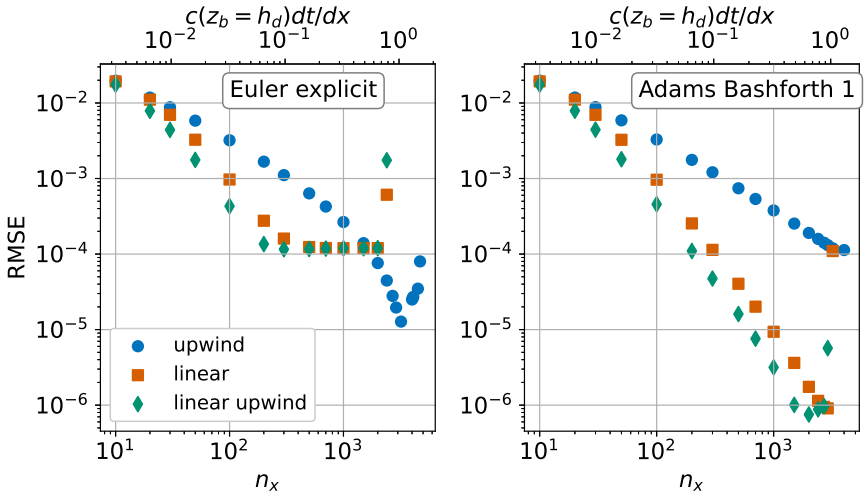

Figure 3.7: Root Mean Square Error for different combinations of schemes and mesh refinements. The time step is constant $\delta t = 0.05\,s$ for all simulations.

From the results presented in Figure 3.6, the combination of an *Adams-Bashforth 2* scheme for the time discretization and a *linear* or *linear-upwind* scheme for the bedload flux, both being second order schemes, seems to offer the best compromise between stability and accuracy. Choosing an *Euler-explicit* time scheme tends to trigger instabilities while the use of an order 1 *upwind* scheme leads to more stability at the cost of accuracy. To further illustrate the different behaviors of the possible scheme combinations and for different mesh refinements, multiple simulations are performed and the results are compared with the analytical solution.

The stability of the numerical solution is related to the mesh refinement through the maximum Courant number, whose evaluation is straightforward as the celerity of bedforms c is known (eq. 3.3). The maximum Courant number is: $\max(C_o) = c(z_b = h_d)\delta t/\delta x$, where δt is the time step value and δx the width of the mesh faces in the x-direction, the mesh being uniform. The accuracy of the numerical solution is evaluated using the Root Mean Square Error (RMSE):

$$\text{RMSE} = \sqrt{\frac{1}{N_F}\sum_f (z_b^n|_f - z_b^s|_f)^2}\,, \tag{3.7}$$

where the index f stands for the finite area mesh faces, N_F the number of faces of the mesh, $z_b^n|_f$ is the elevation of face f center (numerical solution), and $z_b^s|_f$ is the analytical bed elevation at face f center. To further study the impact of mesh resolution and numerical scheme on the numerical solution, many simulations are run with varying number of cells and different numerical schemes combination. The time step is constant and equal to $\delta t = 0.05\,s$. Each simulation is represented by a point in Figure 3.7.

For low Courant numbers (poor mesh quality), all simulations are stable and present

similar errors. As the mesh quality increases, the RMSE decreases but at a faster rate for second order schemes for bedload advection, until the solution becomes unstable when the maximum Courant number gets close to 1. The sudden rise of RMSE values for high mesh resolution is the sign of those instabilities. An *upwind* scheme allows to use a higher Courant number without the simulation failing. This is due to the numerical diffusion that this first order scheme involves. When using an *Euler explicit* time scheme along with one of the second order schemes for advection, it is observed that the RMSE does not depends anymore on the mesh resolution for values of maximum Courant number of 0.1 and higher until the appearance of instabilities. It shall be recalled here that a filtering process is applied on the numerical solution at each time step as the bed elevation increment is interpolated from faces to vertices (discussed in the previous chapter). The results presented support the use of a combination of an *Adams-Bashforth 2* scheme along with a *linear* or *linear-upwind* scheme to ensure both stability and accuracy.

During the development of an Exner morphodynamics model coupled with a CFD approach for the hydrodynamics, it can be difficult to identify the precise cause of model instability during the development phase. For this reason, the Exner equation was initially developed as a standalone model and the presented idealized dune migration case was chosen to test the model behavior, and validate its implementation. A simple power law was used to express the bedload flux as a function of the depth averaged velocity, which itself depends solely on the local bed level by mass conservation consideration. With this idealized model, the relation between the bedload flux and the bed level is known and the Exner equation can be written as a wave equation, with the wave celerity being a continuous function of the bed level. Using the method of characteristics, this wave equation can be solved analytically and the solution is compared to the model results. The migration of an initially Gaussian dune was presented and the numerical solution sensitivity to numerical schemes and mesh resolution was studied. When coupling the hydrodynamics resolution to the Exner equation, the dune migration process becomes much more complex. Depending on the flow velocity and the dune's characteristics, the flow detachment can occur and a recirculation forms downstream of the dune's crest. The morphological evolution of a lone dune under steady flow conditions is presented in detail in chapter 4.

3.2 Settling of particles in a quiescent fluid

As a first benchmark for the suspended load, the settling of non-cohesive particles in a quiescent fluid is studied. As no feedback of the suspended load on the hydrodynamics is considered in the present model, the fluid stays still as the particles settle ($\boldsymbol{u} = 0$). Using the coordinates z as the vertical, and considering a horizontally uniform concentration, the equation 1.53 becomes:

$$\frac{\partial c_s}{\partial t} - w_s^0 \frac{\partial F_h c_s}{\partial z} = 0 \tag{3.8}$$

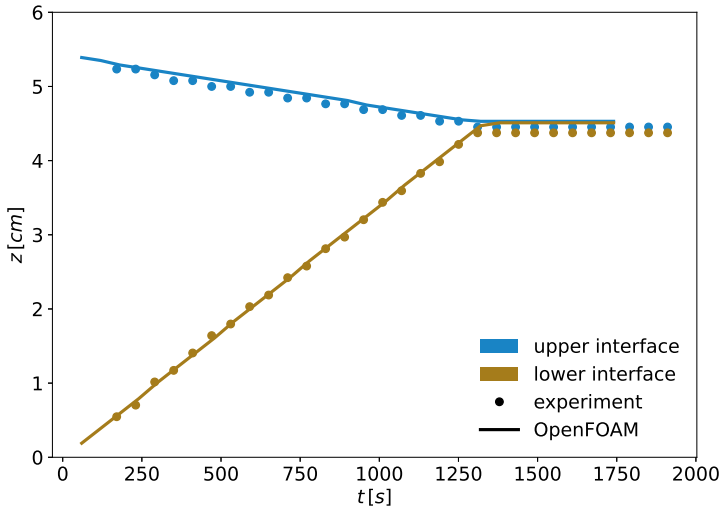

Figure 3.8: Position of the upper and lower interfaces over time. Comparison between numerical results and experimental measurements from Pham Van Bang et al. [2008].

where F_h is the hindrance function defined in 2.25 depending only on c_s. Using the chain rule of calculus to write the advection term of equation 3.8 as a function of c_s times the derivative c_s with respect to z, the equation can be written as a wave equation according to the Kynch theory of sedimentation. [Kynch, 1952]:

$$\frac{\partial c_s}{\partial t} - \underbrace{w_s^0 \left(F_h + c_s \frac{dF_h}{dc_s} \right)}_{\text{wave celerity}} \frac{c_s}{\partial z} = 0 \,. \tag{3.9}$$

The experimental data from Pham Van Bang et al. [2008] is used for validation. The experiment consists in the settling of a mixture of spherical polystyrene beads of density $\rho_s = 1050\, kg.m^{-3}$ and diameter $d = 0.29\, mm$ in Rhodorsil silicon oil of density $\rho_f = 950\, kg.m^{-3}$ and kinematic viscosity $\nu = 2.105\, 10^{-5}\, m^2.s^{-1}$. The mixture was prepared in a cylindrical container of diameter $50\, mm$ and height $100\, mm$. The mixture is initially well mixed in the vertical direction with a solid volume fraction $c_s^0 = 0.48$. The container is placed into a Magnetic Resonance Imaging (MRI) device which automatically measures vertical profiles of particles concentration. At $t = 0$, the solid volume fraction is uniform in the mixture so that all particles start to fall at the same velocity. In the lower part of the mixture, the beads immediately come into contact with the bottom wall of the container and settle on it. The particles at the top then fall onto the first layer, and so on, until the entire mixture has settled. On the concentration profile, this corresponds to an interface of solid volume fraction $c_s = 0$ rising from the bottom wall. On the other extremity of the mixture, another interface of solid volume fraction $c_s = 0$ is going down. When the two interfaces meet, all the particles have settled (see Figure 3.8).

The computational domain is 1 dimensional and consists in a vertical column of 300 cells uniformly spaced over a height of $6\, cm$. The mixture is initially spread over a distance

of $5.4\,cm$ above a rigid wall located at the coordinates $z = 0$. This initial concentration profile is described in the numerical simulation with a hyperbolic tangent function as follows:

$$c_s(t=0) = \frac{c_s^0}{2}\left(1 + \tanh\left(10\frac{z-0.054}{0.049-z}\right)\right), \tag{3.10}$$

with $c_s^0 = 0.5$, the initial suspension volume fraction. Contrary to the other simulations presented in this work, the sediments are not allowed to go through the bottom boundary and must stay in the domain. This is done by imposing a zero settling velocity at the wall, $w_s|_{z=0} = 0$. For c_s, a zero gradient boundary condition is applied. At the top boundary, a Dirichlet condition $c_s = 0$ is applied on the solid volume fraction, and zero gradient condition for the settling velocity.

To represent the dependency of the settling velocity on the solid volume fraction, one of the available hindrance functions presented in Table 2.6 has to be chosen. For this case, the settling velocity must vanish when the suspended particles volume fraction reaches the value $c_s^{max} = 0.6$. This behavior is not reproduced by the initial hindrance correction from Richardson and Zaki [1954]. The modified Zaki hindrance model proposed by Camenen [2008] is used instead (see Table 2.6). With this model the settling velocity vanishes when $c_s = c_s^{max}$. After adjusting the empirical parameter n of the hindrance model to match the experimental data, the results obtained with $n = 3.65$ are presented in Figures 3.8 and 3.9. The velocities of the lower and upper interfaces match well with the experiment, but the predicted lower interface is really sharp compared to what was observed with the MRI device.

For this simple case of settling particles, an empirical formula for hindrance effects seems sufficient for predicting the reduction in settling velocity, which is due to complex physical processes, such as interactions between solid particles, or an increase in drag due to interstitial fluid leakage.

3.3 Suspension under equilibrium conditions

A classical test is the suspension of sediment in a straight flume under equilibrium condition, which has been extensively studied [van Rijn, 1984b, Lyn, 1988, Muste et al., 2005]. The situation is the following, a fully developed flow in a channel is considered. The channel is supposed to be long enough, so that the vertical profiles of velocity and turbulent eddy viscosity are stationary. Under equilibrium conditions, the vertical profile of suspended sediment concentration is the results of a balance between the gravity, which makes the particles to settle at a velocity $\boldsymbol{w_s}$, and the mixing induced by turbulence. Taking z as the vertical direction, the transport equation for the suspended load (eq. 1.53) then reduces to:

$$\frac{d}{dz}\left(w_s c_s + \epsilon_s \frac{dc_s}{dz}\right) = 0\,, \tag{3.11}$$

where $w_s = |\boldsymbol{w_s}|$.

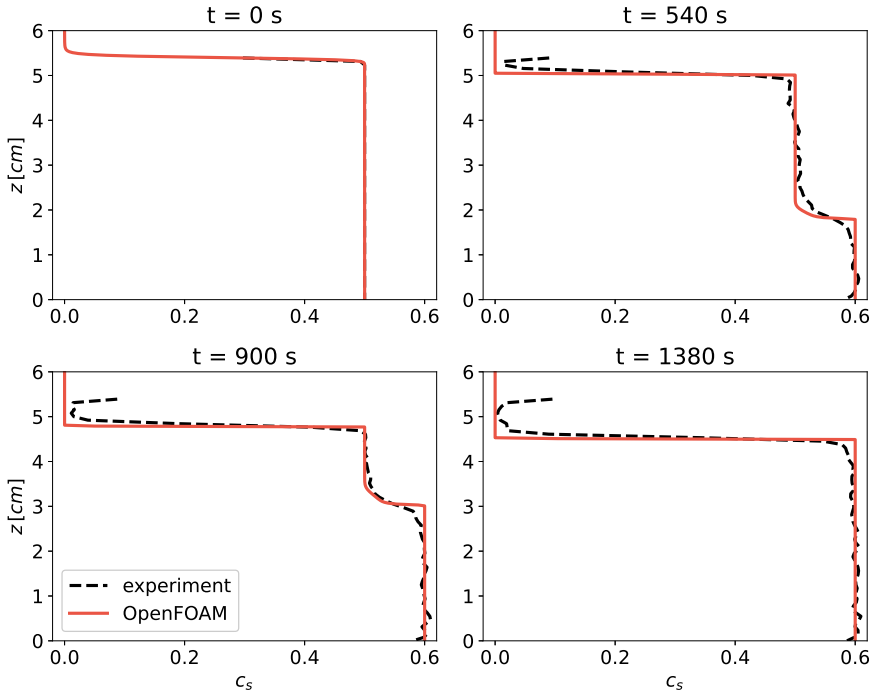

Figure 3.9: Suspended sediment volume fraction profiles at different times during deposition. Comparison between numerical results and experiment from Pham Van Bang et al. [2008].

Depending on the shear stress exerted on the bed, granular material is eroded and suspended in the water column. Then, the turbulent diffusion uplifts the particles until an equilibrium is reached. Assuming a parabolic turbulent viscosity profile, $\nu_t(z) = u_*\kappa z(H - z)$, the solution of equation 3.11 between the reference level δz_b^*, where the concentration is the reference concentration c_b^*, and the top of the water column H is the so-called Rouse profile:

$$c_s(z) = c_b^* \left(\frac{H - z}{z} \frac{\delta z_b^*}{H - \delta z_b^*} \right)^{R_o}, \tag{3.12}$$

where $R_o = \sigma_c w_s / \kappa u_*$ is the Rouse number and κ is the von Kármán constant. In the case of channel flow with a free surface, the eddy viscosity follows a parabolic distribution only in the lower part of the channel where the wall influence dominates. In his study van Rijn [1984b] used a parabolic-constant distribution, that is parabolic in the lower half and constant in the upper half, for the eddy viscosity in order to derive suspended sediment concentration profiles arguing that it would lead to more realistic results than a classic parabolic distribution. In the same work, he proposed his well-known formula to compute the reference concentration from the bed shear stress, the chosen reference level and the fluid and sediments characteristics (see eq. 2.27). He suggested the value of $\delta z_b^* = 0.05H$ for the reference level.

In order to illustrate the difference between the classical boundary condition $c_s(z = \delta z_b^*) = c_b^*$ and the boundary condition used in *sedExnerFoam* described by equation 2.29, two set of simulations of suspension under equilibrium condition in a channel are presented. For the first ones the hydrodynamics is first solved separately, then equation 3.11 is integrated on a second mesh starting at the reference level using the eddy viscosity profile previously computed. At the reference level, the reference concentration formulation from van Rijn [1984b] is applied as a Dirichlet condition. For the second set of simulations, the same mesh spreading from the sediment bed to the water surface is used to solve both the hydrodynamics and the suspended sediment concentration using the method from Celik and Rodi [1988] to extrapolate the reference concentration boundary condition to the center of the first cell above the bed.

To validate the model, numerical results are compared with experimental data from Lyn [1988]. The experiments were conducted in a 13 meters long and 26.7 centimeters wide flume with a bottom covered by a layer of sand. Flow and suspended sediments concentration measurements were made approximately 9 meters downstream of the channel entrance. The experiment parameters are summarized in Table 3.1. For the four experiments, measurements of the velocity field, the velocity correlations and the suspended sediment concentration profiles are available.

The four equilibrium bed experiments are reproduced numerically. The mesh used is 1 dimensional. It consists of a column of 100 to 120 cells oriented in the vertical z-direction and with cyclic boundary conditions in the x-direction. As a result, only the x-component u of the velocity field is not null. For the 4 simulations, the $k - \omega\, SST$ turbulence model is used and the mesh resolution near the bed is kept to $z^+ \approx 1$ to ensure a good resolution and a correct estimation of the shear stress exerted on the bed. The free surface is not

experiments	1565	1965	2565	1957
$d\,(mm)$	0.15	0.19	0.24	0.19
$w_s^0\,(cm.s^{-1})$	1.6	2.3	3.1	2.3
$\overline{u}\,(m.s^{-1})$	0.649	0.671	0.744	0.672
$u_*\,(cm.s^{-1})$	3.58	3.75	4.25	3.95
R_o	1.09	1.24	1.38	1.17

Table 3.1: Parameters of Lyn [1988] experiments. Particles diameter ϵ_s, terminal settling velocity $\boldsymbol{w_s^0}$, mean water velocity $\overline{u}$, friction velocity u_* and Rouse number R_o.

considered, instead a rigid lid is applied at the top, with zero gradient condition for the turbulent kinetic energy k, a Dirichlet condition for ω and a slip boundary condition for the velocity $\boldsymbol{u}$. The sediments bed motion is deactivated, so that the bed level does not decrease as sediments is eroded and put into suspension. To take into account the bed roughness effect on the hydrodynamics, the modification of the boundary condition for ω proposed by Wilcox et al. [1998] and referred in this work as Fuhrman condition is used (eq. 1.34). The flow is forced by means of a uniform volume source term imposing a targeted mean velocity. The transient problem is solved and the simulations are run until a steady state is reached.

For the first set of simulation, the eddy viscosity vertical profiles obtained with *sedExnerFoam* are extracted. Then a uniform mesh made up of 50 cells is used to integrate 3.11 from the reference level $\delta z_b^* = 0.05H$ where the reference concentration formulation from van Rijn [1984b] is applied as a Dirichlet condition. The equation is solved separately using a FVM python code. A linear scheme is used to discretize the settling term. The profiles of velocity, eddy viscosity and suspended sediment volume fraction are plotted in Figure 3.10 for the four cases alongside the experimental data from Lyn [1988]. Overall, the predicted suspended sediment concentration profiles match well with the experiment. The fact that a different mesh is used to compute the hydrodynamics and the suspended load can be seen from the ordinate limits of the different curves. They span from $z = 0$ to $z = H$ for the velocity and the eddy viscosity and from $z = \delta z_b^*$ to $z = H$ for the suspended sediment volume fraction.

For the second set of simulations, equation 3.11 is solved by *sedExnerFoam* together with hydrodynamics and the method from Celik and Rodi [1988] is used to impose the erosion/deposition boundary condition (see eq. 2.29). The numerical results and the experimental data are represented in Figure 3.11. The match on the hydrodynamics with the experimental data is really good for both the velocity and the Reynolds stress $\tau_{xz} = \langle u'w' \rangle$. However, the model predicts almost no suspension of sediments for every case. To be more exact, there is suspension but only in the first cell above the bed where the erosion boundary condition is imposed, but there is not enough turbulent diffusion in the near bed area to uplift the eroded material in the water column. The turbulent eddy viscosity profiles are also represented with a zoom on the near bed area. In the numerical simulation, the eddy viscosity vanishes as z tends toward 0 faster than the black dotted line, which represents the relation $\nu_t(z) = \kappa u_*(z + d_0)$, where $d_0 = 0.03 * k_s$

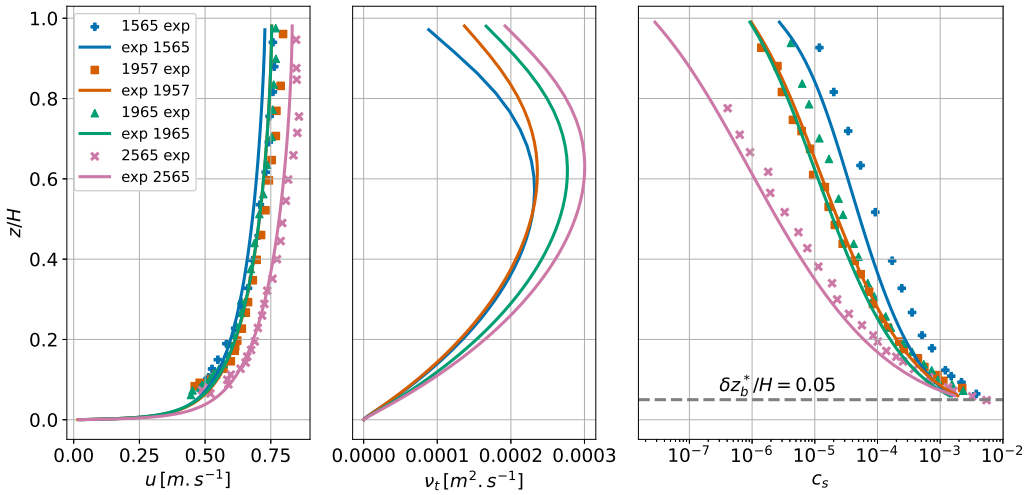

Figure 3.10: Stream-wise velocity, eddy viscosity and suspended sediment concentration profiles obtained with the reference concentration imposed at $\delta z_b^* = 0.05H$. Comparison with experimental data from Lyn [1988].

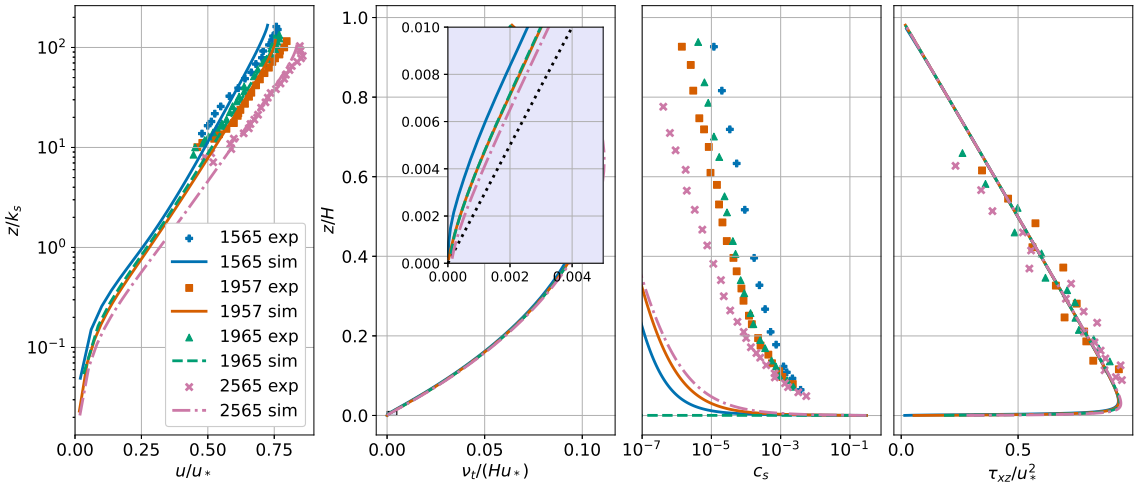

Figure 3.11: Comparison between numerical and experimental results obtained for the 4 different cases from Lyn [1988]. Vertical profiles of velocity, eddy viscosity, suspended sediment volume fraction and specific Reynolds shear stress.

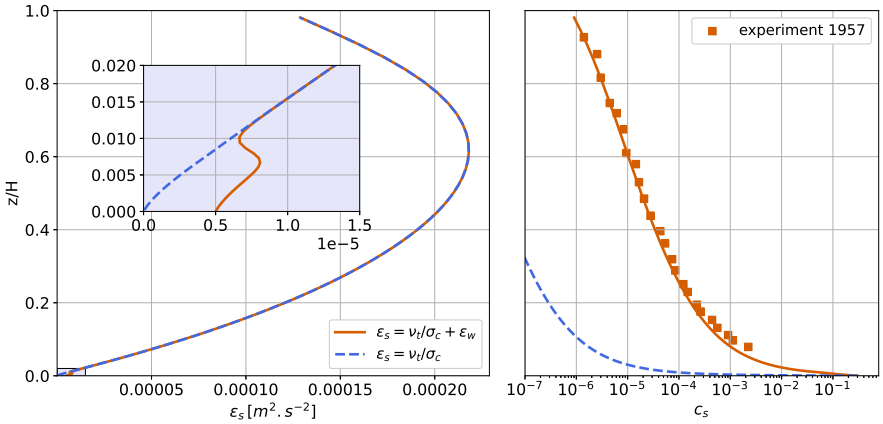

Figure 3.12: Illustration of the effect of the additional near bed diffusivity on the suspended sediments volume fraction profiles. A simulation using $\epsilon_w = 0$ is plotted for comparison.

is the hydrodynamical roughness. This equation was proposed by Aupoix and Spalart [2003], Durbin et al. [2000] to take into account the wall roughness in the log layer. To summarize, the erosion boundary condition is working as intended. Sediment is uplifted from the bed to the center of the first cell above the bed where the volume fraction of suspended sediments reaches values of $c_s > 0.1$. However, there is locally no turbulence diffusion. For all the experimental cases, the flow is smooth or intermediately rough with value of the roughness Reynolds number $k_s^+ = k_s u_*/\nu$ taking values between 13 to 26 depending on the case. For low roughness Reynolds number, the viscous sub-layer close to the bed is only partially disturbed and the turbulence diffusion vanishes. Without any turbulence to uplift the sediments, they stay stuck in a very fine layer above the bed. This behavior is not observed when performing simulations of fully rough flows because turbulence diffusion is then not negligible in the near-bed area.

To avoid this behavior of the suspension, an additional near bed diffusivity ϵ_w was implemented in *sedExnerFoam* (see eq. 2.30). It takes the form of a hyperbolic tangent centered around the roughness height k_s and therefore contributes to the total diffusion for the suspended sediments only in the area $z < k_s$. In Figure 3.12 is represented the vertical profiles of diffusivity for the suspended sediments as well as the suspended sediments volume fraction for two different simulations of the case 1957 from Lyn [1988]. The first simulation was already presented in Figure 3.11 and no additional near bed diffusivity is used so that $\epsilon_s = \nu_t/\sigma_c$ with a Schmidt number $\sigma_c = 1$. For the second one the additional near bed diffusivity $\epsilon_s = \nu_t/\sigma_c + \epsilon_w$ is used with the default coefficient values $\epsilon_w^0 s = 5$ and $\xi_w = 5$. A zoom on the near bed area allow to visualize the difference between the two diffusivity profiles. This localized increase in diffusivity allows the suspended material to rise higher in the water column. Once the sediments reach a height $z = k_s$, the turbulent diffusion takes over. This results in a concentration profile that aligns with the experimental data.

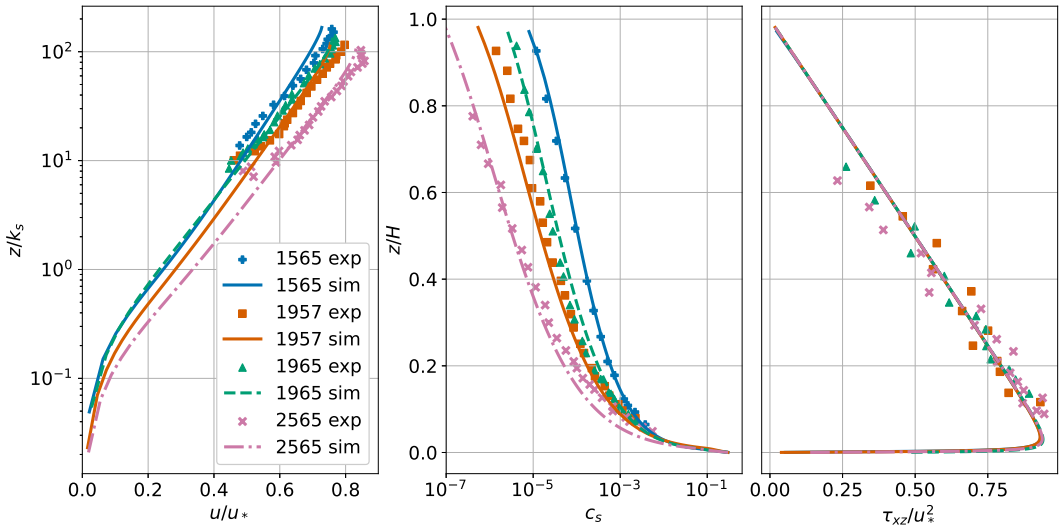

Figure 3.13: Velocity and suspended sediment concentration profiles from simulations and comparison with experimental data from Lyn [1988].

The 4 experimental cases are reproduced numerically with the additional near bed diffusivity ϵ_w activated. The results are plotted alongside the experimental data in Figure 3.13. For all 4 simulations, the turbulent Schmidt number was set to values slightly above 1, $\sigma_c \in [1.1, 1.2]$, meaning that the turbulent diffusivity for sediment concentration is lower than the turbulent diffusivity for the fluid. In general, the numerical results show good agreement with the experiments. For the suspension profiles, it is observed that for the case 2565, not enough sediment is suspended in the lower part of the water column compared with the experiment. A better fit could be obtained by further adjusting the parameters ϵ_w^0 and ξ_w in equation 2.30 which are both set to 5. Other adjustment parameters are the turbulent Schmidt number and the bed roughness height k_s considered in the boundary condition for ω.

The suspension of sediments under equilibrium conditions is a classical benchmark almost systematically used to validate sediment transport models [Lesser et al., 2004, Warner et al., 2008]. The classical way of imposing the erosion/deposition boundary condition as suggested by van Rijn [1984b] was first illustrated. Coupled with a fine near bed resolution for the hydrodynamics all the way to the bed boundary, this boundary condition is difficult to apply as it is imposed at a distance from the bed boundary called the reference level. After illustrating this method by using a different mesh for the suspended sediments, simulations performed with the boundary from Celik and Rodi [1988] were presented. For smooth flow and intermediate roughness regimes, it was found that the sediments eroded tends to stay stuck in the first cell above the bed due to the absence of turbulence to uplift this particles near the bed. An additional near bed diffusivity was introduced to mimic the saltation of particles and other particle-particle interaction which make the sediments rise just high enough to get caught by eddies. This additional diffusivity is totally empirical and was implemented to correct an undesired

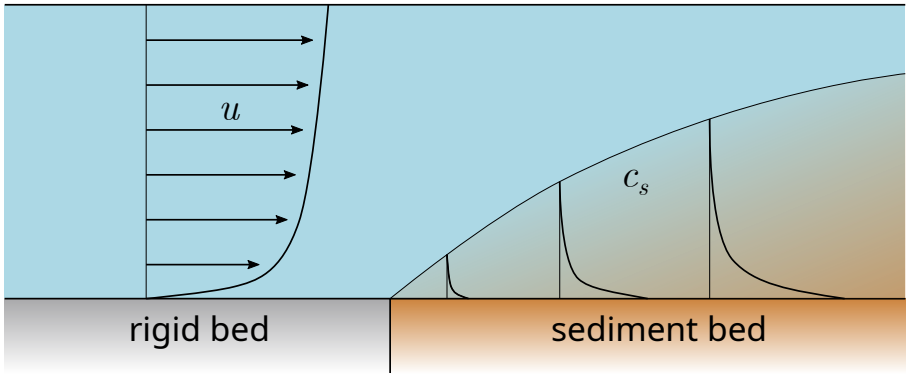

Figure 3.14: Schematic of the development of a suspension downstream of a transition between a rigid bed and an erodible sediment bed.

behavior in the model. In the future, it would be interesting to develop closure based on the granular processes at work.

3.4 Development of the suspension

After studying the suspension of sediments in a channel under equilibrium conditions in the previous validation case. Another problem of suspension in a channel is presented. The channel is composed of two distinct parts. The first one has a rigid bottom and is supposed to be long enough so that the flow is already fully developed by the time it reaches the end. The bottom of the second part of the channel is an erodible sediment bed. The initially clear water flow passes over the transition between rigid bed to erodible bed and starts to uplift sediments from the bottom. The quantity of suspended sediments gradually increases downstream of the transition until equilibrium is reached, when turbulent diffusion and particle settling due to gravity cancel each other out and $D - E = 0$. A schematic of the situation is represented in Figure 3.14 As in the previous validation case, no hindrance model is used and the particles fall at the terminal settling velocity w_s^0. The bed level evolution is not considered.

For this problem, a pseudo-analytical solution derived by Hjelmfelt and Lenau [1970] is used for comparison. The derivation of the analytical solution is based on some hypotheses detailed hereafter.

1. The sediments are transported uniformly in the stream-wise direction by the mean velocity $\overline{u}$.
2. The turbulent viscosity vertical profile is assumed parabolic, $\nu_t = \kappa u_* z(1 - z/H)$ for $z \in [\delta z_b^*, H]$ where δz_b^* is the reference level and H, the water depth.
3. The concentration at $z = \delta z_b^*$ is supposed to be constant along the flume and equal to c_b^*, the reference concentration.
4. The horizontal turbulent diffusion is neglected.

Based on those hypotheses, Hjelmfelt and Lenau [1970] simplified the transport equation for the suspended-load to obtain the following dimensionless equation:

$$\frac{\partial C}{\partial X} = R_o \frac{\partial C}{\partial Z} + \frac{\partial C}{\partial Z}\left(Z(1-Z)\frac{\partial C}{\partial Z}\right), \tag{3.13}$$

where R_o is the Rouse number, C is the ratio of the suspended sediments volume fraction to the reference concentration and X and Z are the dimensionless horizontal and vertical coordinates of this 2D problem defined as follows:

$$R_o = \frac{\sigma_c w_s^0}{\kappa u_*} \quad C = \frac{c_s}{c_b^*}, \quad X = \frac{\kappa u_*}{\sigma_c \overline{u}} fracxH, \quad Z = z/H. \tag{3.14}$$

Hjelmfelt and Lenau performed a separation of variables and used the Sturm Liouville theory to obtain a pseudo analytical solution for equation 3.13 which only depends on the Rouse number. The form of the solution they obtained is complex and is not fully detailed in the present work. The full derivation of the solution can be found in Hjelmfelt and Lenau [1970]. The pseudo analytical solution of equation 3.13 takes the following form:

$$C(X,Z) = \left(\frac{\delta z_b^*/H}{1-\delta z_b^*/H}\right)^{R_o} + \sum_k^{\infty} a_k e^{-X(\alpha_k - 1/4)} P(Z,\alpha_k). \tag{3.15}$$

The α_k coefficients are roots of the following equation:

$$F_{\text{hyper}}\left(\frac{1}{2}+R_o+\alpha, \frac{1}{2}+R_o-\alpha, 1+R_o, 1-\frac{\delta z_b^*}{H}\right) = 0, \tag{3.16}$$

where F_{hyper} is the hypergeometric function, which is the solution of a second-order ordinary differential equation known as Euler's hypergeometric differential equation. It is defined by the following power series:

$$F_{\text{hyper}}(a,b,c,Z) = \sum_{n=0}^{\infty} \frac{(a)_n (b)_n}{(c)_n} \frac{z^n}{n!}, \tag{3.17}$$

in which $(a)_n = a(a+1)(a+2)\ldots(a+n-1)$ for $n \geq 1$ and $(a)_0 = 1$ is the rising factorial also called the Pochhammer symbol.

The roots α_k of equation 3.16 cannot be found analytically and an iterative root algorithm is used to compute them. P is a function also defined from the hypergeometric function as follows:

$$P(Z,\alpha) = (1-Z)^{R_o} F_{\text{hyper}}\left(\frac{1}{2}+R_o+\alpha, \frac{1}{2}+R_o-\alpha, 1+R_o, 1-Z\right). \tag{3.18}$$

The a_k coefficients are computed from the derivative of P and the α_k coefficients. The main difficulty lies in the finding of the roots α_k and the entire process is detailed in the work of Hjelmfelt and Lenau [1970].

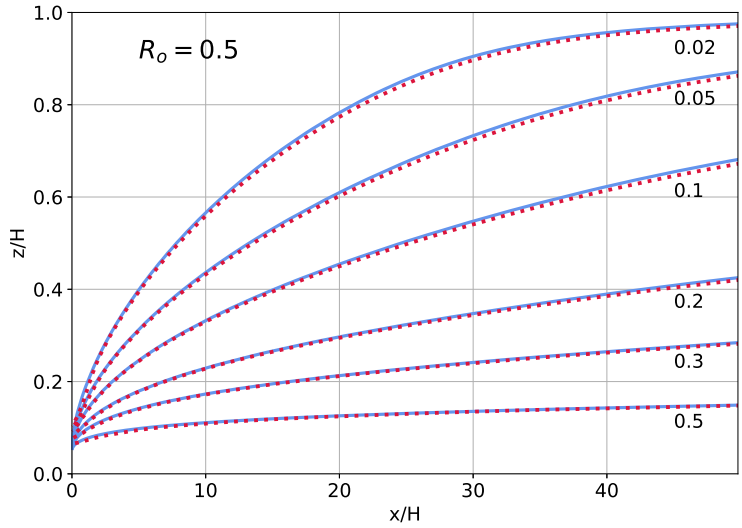

Figure 3.15: Isolines of c_s/c_b^* for a Rouse number of 0.5 with hypothesis from Hjelmfelt and Lenau [1970] enforced except the null horizontal turbulent diffusion. Solid blue curves represent the model results and the dotted red ones the pseudo analytical solution.

For this benchmark two simulations are presented. For the first one, all the hypothesis presented above are enforced except for the fourth one. That is, the horizontal turbulent diffusion is not neglected. In the second simulation, none of the hypotheses are enforced. The flow velocity and the turbulent eddy viscosity are the results of a RANS simulation using a $k-\omega\,SST$ model. The erosion/deposition boundary condition described by equation 2.29 is applied instead of imposing the reference concentration at $z = \delta z_b^*$, and an additional near bed diffusivity is used as illustrated in the previous validation case. For both simulations, the water height in the channel is $H = 0.1\,m$ and the mean velocity is $\overline{u} = 0.9\,m.s^{-1}$. The properties of the sediments were chosen to obtain a Rouse number of $R_o = 0.5$ corresponding to a highly suspended regime. The sediment diameter is $d = 0.12\,mm$ and the terminal settling velocity is $w_s^0 = 0.773\,cm.s^{-1}$.

For the first simulation, the computational domain begins at the end of the rigid bed and spreads over a distance of 6 meters downstream of the transition. The hydrodynamics is fully determined by the hypothesis, that is, a uniform velocity field $u = \overline{u} = 0.9\,m.s^{-1}$ and the eddy viscosity follows a parabolic distribution. Only the transport equation for the suspended load needs to be solved. The domain bottom boundary is located at the reference level set as $\delta z_b^* = 0.05H$ where a Dirichlet condition $c_s(\delta z_b^*) = c_b^*$ is imposed. The problem is solved on a structured 2D rectangular mesh made of 650 cells uniformly spaced in the stream wise direction and 100 cells in the vertical direction with a better refinement near the bottom and top boundaries. The transport equation for the the suspended load is discretized with an *Euler implicit* scheme for the temporal term and a *linear-upwind* scheme for the advection term. Some isolines of c_s/c_b^* are represented in Figure 3.15. The match of the numerical results with the pseudo-analytical solution is almost exact, suggesting that the stream-wise turbulent diffusivity (hypothesis 4) is

indeed negligible. All the isolines of concentration develop from the inlet at the reference level and slowly become horizontal as an equilibrium situation is approached.

However, some of the hypotheses from Hjelmfelt and Lenau [1970] are normally not verified. The vertical velocity profile is not uniform, the concentration at the reference level may vary in space and reach an equilibrium after some distance from the inlet and last the turbulent eddy-viscosity profile is not exactly parabolic. A series of particle diameter values was selected to vary the Rouse number but here only the case $R_o = 0.5$, obtained for a The same mean flow velocity $\overline{u} = 0.9\,m.s^{-1}$ is taken and the resulting shear stress exerted on the bed corresponds to a friction velocity $u_* = 3.77\,cm.s^{-1}$. The $k - \omega\,SST$ turbulence model is used and the rough wall boundary from Wilcox et al. [1998] (eq. 1.34) condition is used for ω with a roughness height $k_s = 2.5\,d$.

A first 1D simulation is performed without sediment to obtain vertical profiles for $\boldsymbol{u}$, k and ω corresponding to a fully developed channel flow. For that, a mesh made of a column of 120 cells more refined near the bottom and top boundaries is used. To obtain an eddy viscosity profile close to a parabolic distribution, a smooth wall condition is applied at the top. The bed being rough, the obtained eddy viscosity profile is not exactly symmetrical. The fields $\boldsymbol{u}$, k and ω are extracted from this first simulation and used as the inlet boundary condition for the second simulation for which suspension is activated. The flow entering the domain being already fully developed, only c_s vary with the x-position. The mesh consists in a 2-dimensional structured mesh more refined close to the bed to ensure the condition $z^+ \approx 1$ ($n_x = 2000$, $n_z = 100$). Isolines of c_s/c_b^* values from the model and the pseudo-analytical solution are presented in Figure 3.16. To compute the pseudo-analytical solution, the reference level was chosen equal to $\delta z_b = 0.05H$ as in the work of Hjelmfelt and Lenau [1970] and the reference concentration is taken equal to $c_b^* = 0.025$ and applied as a boundary condition at the elevation $z = \delta z_b$.

Compared with the situation where the hypotheses on the flow are enforced (see Figure 3.15), the model results do not match the pseudo analytical solution but the global behavior remains the same. Starting from no suspension, the suspended sediment quantity gradually increases with the distance to the inlet until reaching an equilibrium situation where the settling and the turbulent diffusion cancel each other out. Figure 3.17 shows the vertical suspended sediment volume fraction c_s profiles at different positions along the channel and shows the convergence toward an equilibrium solution close to a Rouse profile (black dashed line).

As stated previously, the difference with the pseudo-analytical solution comes from the unrealistic hypothesis made to derive it. A better agreement could yet be found, for instance by playing with the boundary conditions for ω at the top and bottom boundaries which would affect the shape of ν_t profile. Another adjustment parameter is the reference concentration at the reference level which is the bottom boundary condition of the pseudo analytical solution.

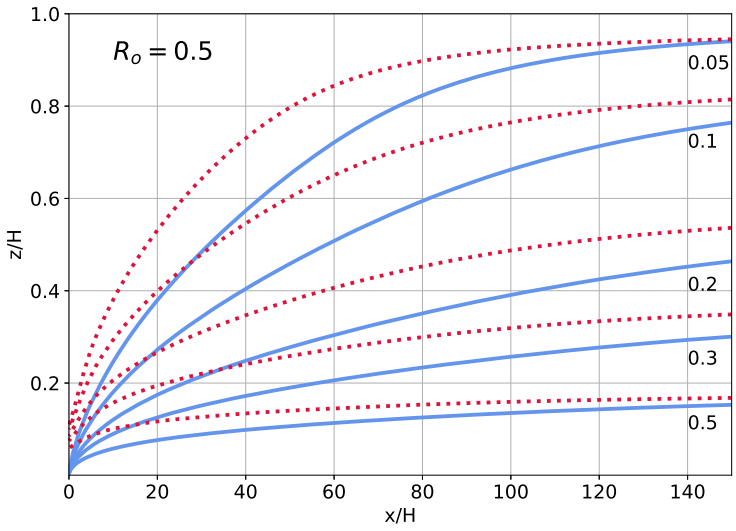

Figure 3.16: Isolines of c_s/c_b^*. Comparison between pseudo-analytical solution from Hjelmfelt and Lenau [1970] (red dotted lines) and the model solution (solid blue lines) without enforcement of the hypothesis used to derive the pseudo-analytical solution.

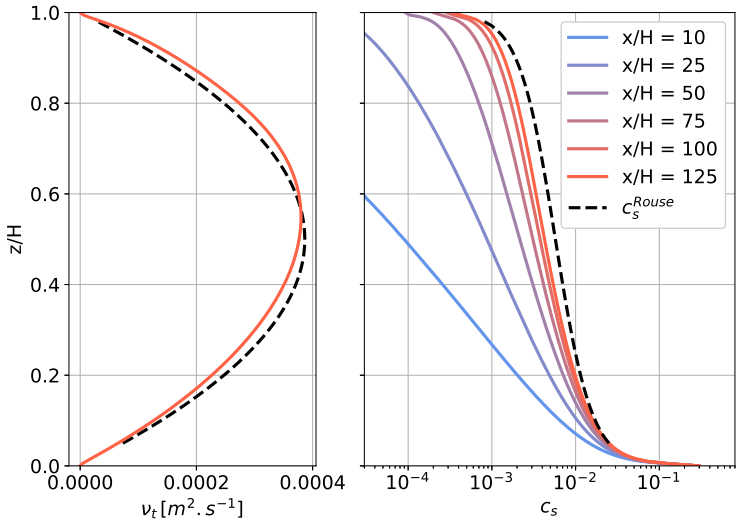

Figure 3.17: On the left hand side, the turbulent eddy viscosity obtained with the model (solid line) and the theoretical parabolic profile (black dashed line). On the right hand side, vertical profiles of c_s at different x-positions in the channel. For comparison, the Rouse profile corresponding to the pseudo analytical solution in Figure 3.16 is also plotted (black dashed line).

3.5 Deposition and mass conservation

The next cases are mass conservation tests ensuring the correct coupling between the suspension and the sediment bed morphology evolution. Two sedimentation cases are presented. A one dimensional case of uniform settling of particles in a still basin, and a 2D case of sedimentation in an hourglass.

Uniform settling

A still basin of depth $H = 1\,m$ is initially uniformly loaded with a volume fraction $c_s^0 = 0.05$ of suspended sediment of diameter $d = 0.29\,mm$ and density $\rho_s = 2650\,kg.m^{-3}$ corresponding to a mass concentration of $132\,kg.m^{-3}$. No hindrance effect is considered so that the particles settle at the terminal settling velocity $w_s^0 = 3.6\,cm.s^{-1}$ estimated with the formula from Fredsoe and Deigaard [1992] (see Table 2.6). At the end of the simulation, all sediments have deposited so that the final bed elevation is:

$$z_b = \frac{c_s^0}{c_s^{\max}} H \,, \tag{3.19}$$

where c_s^{max} is the deposited sediments volume fraction. If the fluid motion is neglected, the bed evolution in time during the sedimentation process can be described by the following equation:

$$c_s^{\max} \frac{\partial z_b}{\partial t} = c_s^0 \left(w_s^0 + \frac{\partial z_b}{\partial t} \right) . \tag{3.20}$$

where $w_s^0 + \frac{\partial z_b}{\partial t}$ is the settling velocity of particles relative to the bed motion. Knowing the final bed position, the previous equation can be integrated to obtain T_{sedim}, the end time of the sedimentation process:

$$T_{\text{sedim}} = \frac{c_s^{\max} - c_s^0}{c_s^{\max}} \frac{H}{w_s^0} \,. \tag{3.21}$$

The numerical application yields $T_{\text{sedim}} = 24.84\,s$.

Now if the bed action on the fluid is not neglected, that is the bed motion push the fluid upward so that $\boldsymbol{u}(z = z_b) = \frac{\partial z_b}{\partial t} \boldsymbol{e_z}$, then by conservation of mass the fluid motion equates to the one of the bed boundary everywhere in the water column. By taking into account the advection by the fluid in equation 3.20, the term of bed motion in the right hand side vanishes so that the time it takes for all sediments to settle is now:

$$T_{\text{sedim}} = \frac{H}{w_s^0} \,, \tag{3.22}$$

which corresponds to the time a single particle needs to fall from the top of the water column to the bed, $T_{\text{sedim}} = 27.1\,s$.

The problem is solved on a 1D mesh made of 100 cells uniformly spaced in the vertical direction. The suspended sediment volume fraction at the top boundary is set to 0 so that

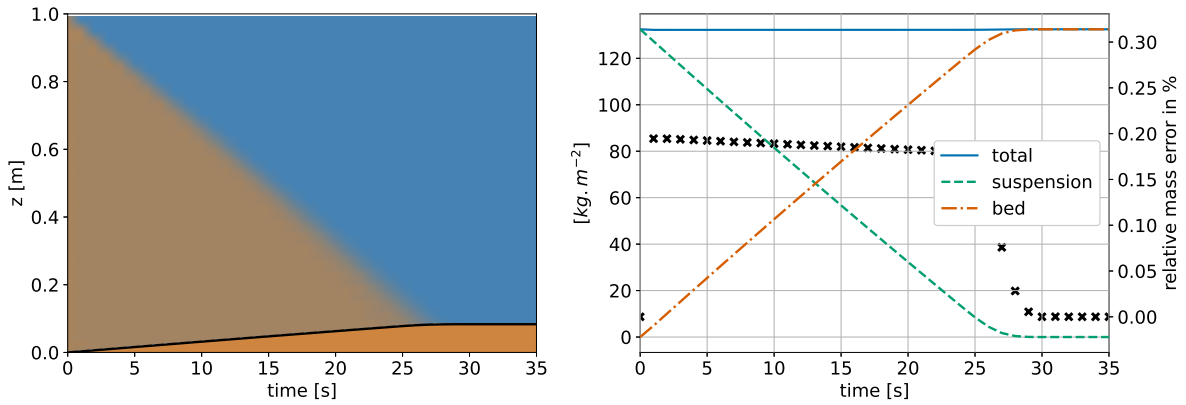

Figure 3.18: Variation over time of the sediment mass per unit area divided into suspended and deposited sediments. The relative error on the total mass in percentage is represented by black crosses.

no sediments enter the computational domain from the top. The water is initially still, so that there is no turbulent diffusion and the diffusive term in the transport equation for the suspended load vanishes (eq. 1.53). However, since a moving wall boundary is applied at the bed, as soon as the simulation starts the fluid move upward with the same velocity as the bed. The temporal term is discretized with an implicit Euler time scheme (eq. 2.33) and the advective term with a *linear-upwind* scheme.

The variation over time of the sediment mass distribution between suspension and deposited sediments is represented in Figure 3.18. Initially, all the mass is suspended. As the sediments deposit, the suspended mass linearly decreases until the end of the sedimentation process at 27 seconds. The total mass of the domain stays constant over time.

When looking at the total mass error which is the sum of the suspended and deposited masses per unit area divided by the initial mass of sediments in the domain $\rho_s c_s^0 H$, it can be seen in Figure 3.18 that the total mass is not exactly conserved during the simulation. In reality is mass is indeed conserved but there is a one time step delay in the bed response leading to this error. During a time iteration, the equation for the concentration of suspended sediments is solved and the erosion/deposition flux is computed and leads to a new elevation of the sediment bed boundary after resolution of the Exner equation (see Figure 2.9). But the mesh motion being solved at the beginning of the time iteration, the bed level increment computed at a given time will only affect the mesh geometry at the next time step. As a result, there is a one-time step delay in the morphological response of the bed, which leads to an error in the total mass. However, this error returns to zero once all the suspended sediments have settled.

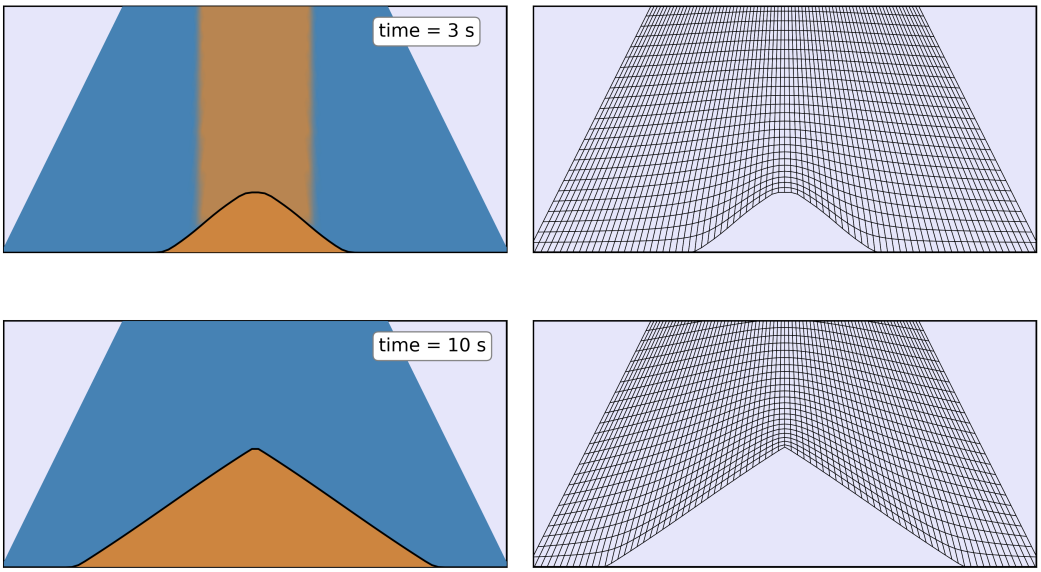

Figure 3.19: Representation of the sediment in the domain at two different times. At 3 seconds where a deposition mound is being formed as suspended sediment deposit and 10 seconds where all the sediments have settled. On the right part of the graph is shown the corresponding mesh to highlight the model mesh deformation capability.

Deposition in an hourglass

Another settling case is presented, this time a 2D non uniform settling case. The computational domain is conic shaped, wider at the bottom (5cm) and narrower at the top (1cm) with a height of 4 cm. Initially, only water is present in the domain and sediments are injected at the top boundary condition with a constant concentration. The sediments settle under the action of gravity and deposit on the bed. As the settling is non-uniform spatially, the sediment bed slopes get important on the extremity of the deposition mound and the avalanche mechanism takes over leading to the formation of a conic shape similar to the one observed in an hourglass. The repose angle is taken equal to $\beta_r = 32°$. The sediments diameter is $d = 0.29\,mm$ and their density $\rho_s = 2600\,kg.m^{-3}$. The sediment settling velocity $w_s^0 = 3.5\,cm.s^{-1}$ is computed using the formula from Fredsoe and Deigaard [1992] (see Table 2.6) and is considered uniform as the hindrance effect is not taken into account. A constant flux of sediment is injected during 7 seconds by imposing a constant suspended sediment volume fraction at the top boundary $c_s = 0.05$. The simulation then runs for 3 more seconds so that all sediments have settled by the end of the simulation (see Figure 3.19). The 2D mesh is uniform and made of 80 cells in the horizontal direction and 40 in the vertical. An *Euler explicit* time scheme and *linear-upwind* schemes are used to discretize the transport equation for the suspended sediments. At the bottom a moving

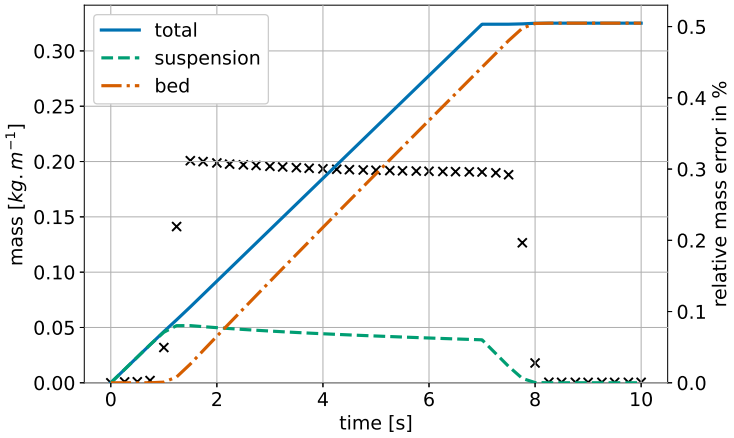

Figure 3.20: Variation over time of the sediment mass per unit width divided into suspended and deposited sediments. The relative error on the total mass in percentage is represented by black crosses. Suspended sediments is injected during the 7 first seconds and all deposit before the simulation ends.

wall velocity condition is used so that $\boldsymbol{u}(z = z_b) = \frac{\partial z_b}{\partial t}\boldsymbol{e_z}$.

The mass repartition of sediments between suspension and deposition is represented in Figure 3.20. At the beginning of the simulation, all the sediments are suspended and their quantity increases linearly over time until $t = 1.14s$ where the sediments start to deposit on the bed. As the domain bottom boundary rises, the space occupied by suspended sediments shrinks leading to a diminution of the mass of suspended sediments. At 7 seconds, sediments stop being injected into the domain and approximately one second later, all the sediments have settled. Once again, the mass error is evaluated by comparing the mass of sediment which has been injected into the domain to the sum of the suspended mass and the bed mass. Just as in the 1 dimensional case, the one time step delay in the bed morphology response induces an error on the total mass in the domain (see Figure 3.20). This error then vanishes at the end of the sedimentation process so that the mass conservation is verified.

Through these two sedimentation cases, the mass conservation properties of the solver during deposition has been demonstrated which validates the coupling of the suspended load and the Exner equation for pure sedimentation cases. To fully validate the coupling, the mass conservation of the model must also be verified during an erosion process.

3.6 Erosion in a channel

Previously, two sedimentation tests have been used to verify *sedExnerFoam* mass conservation property during deposition. To fully validate the coupling between the suspended load and the Exner equation, a last benchmark of erosion in a channel with initial water depth $H = 10\,cm$ is presented. The computational domain is the same as in the 1D

channel flow simulations previously studied. The domain is made up of one column of 80 cells more refined in the near bed area. In the flow direction, cyclic boundary conditions are used so that the situation is that of a channel of infinite length.

To force the flow, two methods are usally considered. The first is to impose a constant pressure gradient in the x-direction. The flow is then accelerated until the friction exerted by the bed on the fluid compensates the pressure gradient. Noting dx the width of the cells and dp the pressure difference between the upstream and downstream faces of the cells, the flow verify the following equality once it has reached equilibrium:

$$dpH = \rho_f u_*^2 dx \,. \tag{3.23}$$

However, in a erosion case, that is if the friction velocity is higher than the threshold oh motion, particles are eroded from the bed and put into suspension. As a result the bed level decreases and the water depth H increases which in turn cause the friction velocity at equilibrium (see eq. 3.23) to increase, causing even more erosion. This leads to an unstable situation where the bed level never stops decreasing and the equilibrium $E = D$ is never reached. Another method available in *OpenFOAM* is to set momentum source which accelerates the flow until the mean flow velocity reaches the desired value. As sediment is eroded from the bed, the water depth H increases but the mean velocity remains the same. Sediments are put into suspension until erosion and deposition cancel each other out.

A mean velocity $\overline{u} = 0.6\, m.s^{-1}$ is imposed. The sediments have a diameter $d = 0.19\, mm$, a density $\rho_s = 2650\, kg.m^{-3}$ and the maximum volume fraction is set to $c_s^{\max} = 0.6$. Initially the fluid is still but the mean velocity momentum force rapidly accelerates the flow. The simulation is run for 40 seconds, enough for an equilibrium to be reached. The results are presented in Figure 3.21. As the flow accelerates, the shear stress rapidly increases and exceeds the motion threshold before stabilizing at a value corresponding to the Shields number $\theta = 0.3$. The erosion process begins as soon as the threshold of motion is attained. The mass of sediments eroded from the bed is represented by the ref area in Figure 3.21. It can be observed that an excess of sediments is eroded during the flow acceleration phase. During a second phase characterized by an almost constant shear stress, the excess of suspended sediments deposit until the system the equilibrium $E - D = 0$ is reached. The mass of suspended sediments settling on the bed during this phase is represented by the blue area, and the mass still in suspension at equilibrium is the difference between the red and blue area. The mass of sediments in the bed is calculated relatively to the bed initial position $z_b = 0\, m$ and therefore takes negative values during the erosion process. The bed mass and the suspended mass perfectly balance each other so that the total mass of sediments is conserved. Once again, a small error on the total mass is observed but is only due to the one step delay in the bed response. The relative mass error represented in Figure 3.21 is computed as the ratio between the total mass to the suspended mass at the end of the simulation.

This last benchmark is complementary to the sedimentation cases presented previously and validate that no mass loss or gain comes from the coupling between the Exner equation and the suspended load.

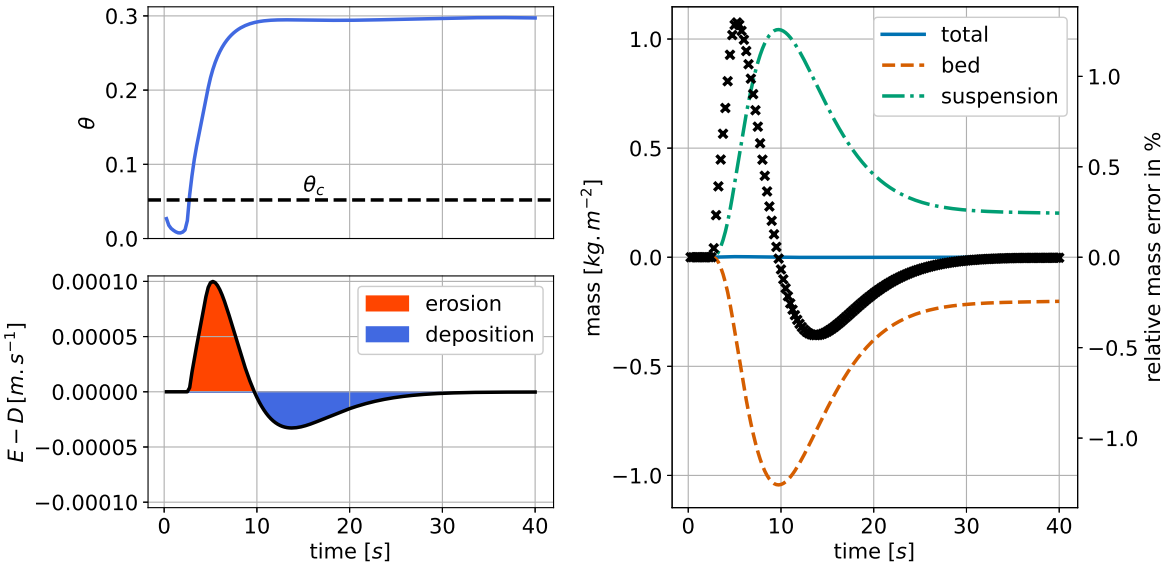

Figure 3.21: On the top left, variation over time of the Shields number. The black dashed line represents the threshold of motion. On the bottom left, the mass transfer between the bed and the suspension is represented by the evolution of $E - D$. On the right, the variation over time of the sediment mass per unit area divided into suspended and deposited sediments. The relative error on the total mass in percentage is represented by black crosses.

3.7 Conclusion

This chapter is dedicated to validating the different components of *sedExnerFoam* and illustrating its behavior through a series of benchmarks. These different validation cases reflect the model's development history. They were designed at the same time and have been continuously used to test the model's implementation, stability, and sensitivity to different closures, mesh resolutions, and numerical schemes. As mentioned previously, these tests are simple as they were chosen with the objective to isolate the different physical process and validate them separately. In a complex fully coupled morphodynamics study, identifying the source of a strange behavior in the model results can prove difficult due to the multiple potential sources of error and the interactions between the hydrodynamics, the suspension and the Exner equation. In addition to the simulation presented in this chapter, the continuous integration procedure includes more minimalist tests to track the introduction of bugs in the model. This reduces the risk of introducing errors into the code as it is developed further and increases the confidence of potential users of the model, making them more likely to use it.

Chapter 4

Dune migration

Many sediment transport problems involve bedforms of various sizes, ranging from ripples to mega dunes. These form, grow and migrate under the influence of the flow. Ripples are the smallest pattern that can be observed underwater. Under certain conditions, a coupling instability between the flow and the morphological response of the bed can lead to their formation on an initially flat bed. As they grow, they can merge to form larger structures. After studying and validating the behavior of the model's different components in the previous chapter, the first application of the fully coupled model is now examined. In this chapter, the model's ability to predict bedforms migration is tested and the different parameters of the model having a significant impact of the morphology are identified and discussed. It is divided into two parts. The first one is dedicated to the numerical study of a lone 2D dune made up of glass beads migrating in a flume under the influence of an unidirectional flow. This topic has been studied experimentally by Kiki Sandoungout who observed different migration regimes depending on the dune mass and the flow velocity. In a second part, an attempt to simulate the morphological of an initial conic deposit of sediments into a crescent-shaped dune known as barchan is presented.

4.1 2D dune migration in a straight flume

This study presents the migration and evolution of a lone dune under the influence of a steady flow. The subject was studied experimentally by Kiki Sandoungout [2019], who worked on the identification of the different dune migration regimes. At the beginning of each experiment, the fluid is still and the initial shape of the dune is conic before it changes during the migration. The migration regime depends on the mean flow velocity and on the initial mass of the dune. In his work, Kiki Sandoungout [2019] identified a total of three different regimes. A stationary regime, for which two stages are observed. During the first one, the dune morphology rapidly changes from an initial conic shape obtained by deposition of sediments in still water. After some time, the dune reaches a stationary state and moves at a constant velocity in the flow direction. A second regime is the spread regime, in which the dune's length decreases indefinitely. The third and final regime is the mass loss regime, in which the dune is quickly washed away by the flow.

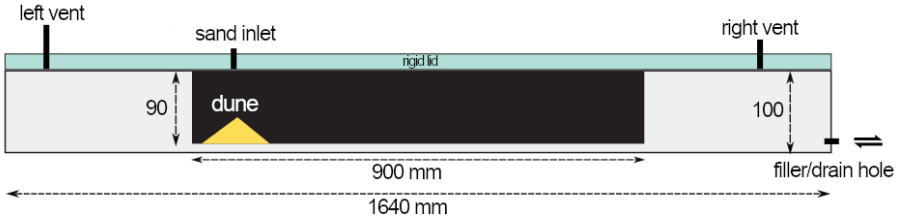

Figure 4.1: Front view of the experimental setup from Kiki Sandoungout [2019].

$d\,(mm)$	$\rho_s\,(kg.m^{-3})$	$w_s^0\,(cm.s^{-1})$	θ_c^0	sphericity	β_r
0.4	2500	7.67	0.079	> 0.89	28

Table 4.1: Characteristics of the glass beads used in the work Kiki Sandoungout for the study of dune migration in a flume.

4.1.1 Experimental configuration

The experimental facility consists of a hydraulic tunnel operating in a closed circuit. The experimental area comprises a straight channel with a length $L_c = 900\,mm$, a height $H = 90\,mm$ and a thickness $W_c = 6.03\,mm$. The flume is completely filled with water and closed at the top by a rigid lid. Directly above the experimental zone, a hole located $200\,mm$ from the left edge is used to introduce sediment into the channel. Two motors located on each side of the experimental are used to drive the flow. They can operate in both directions of rotation, which allows identical flows to be generated in both flow directions. A schematic of the flume used by Kiki Sandoungout to conduct the experiments is shown in Figure 4.1.

The granular material used in the experiments consists of spherical glass beads. The author used two different classes of particles having the same density $\rho_s = 2500\,kg.m^{-3}$ but different median diameter, $d = 1\,mm$ and $d = 0.4\,mm$ respectively. In the present study, only the particles of diameter $d = 0.4\,mm$ are used. The particles terminal fall velocity in water has been measured experimentally to: $w_s^0 = 7.67\,cm.s^{-1}$ which differs slightly from values obtained with the models presented in table 2.5 ($w_s^0 \approx 5\,cm.s^{-1}$). The critical Shields number ($\theta_c^0 = 0.079$) obtained experimentally is large compared to what is expected from the formulas in table 2.5. This could be due to the confinement of the particles in the flume, the ratio of the channel width to the particle diameter being only equal to $W_c/d = 16$. The sphericity of the particles, which is the ratio of a particle area to the area of a sphere having the same volume is superior to 0.89, indicating that the particles are close to spheres. The different characteristics of the glass bead used by Kiki Sandoungout are summarized in table 4.1.

The experimental data available consist of bed levels at different times during the migration as well as the temporal evolution of different characteristics which are the dune position, height and length. When the dune does not have a sharp crest, it was found difficult experimentally to identify the precise x-location corresponding to the top of the dune. Instead, the author chose to track the dune migration using the coordinate x_h,

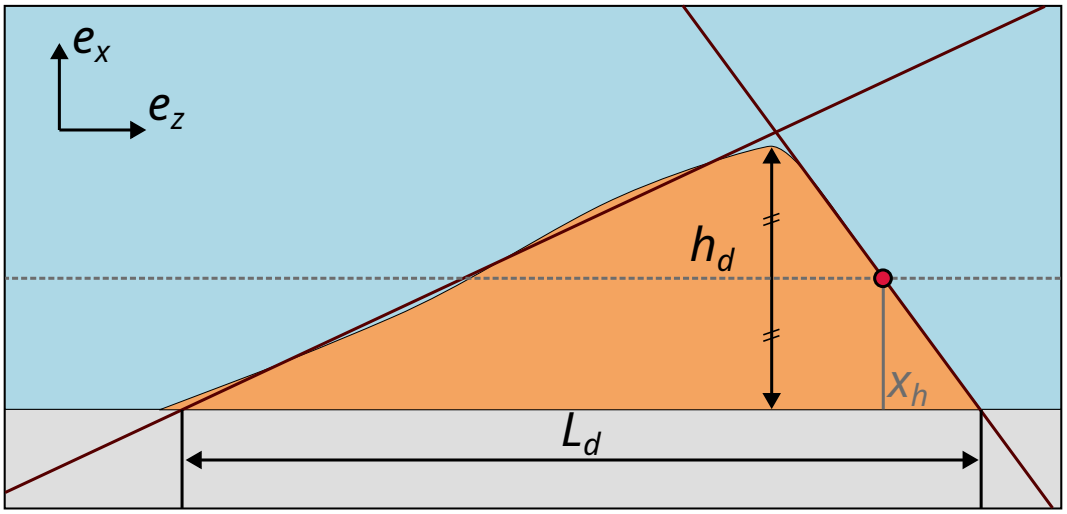

Figure 4.2: Schematic showing how the dune's characteristics are defined. The dune's position is tracked using the coordinate x_h corresponding to the abscissa of the mid-height of the downstream side of the dune. The dune's length L_d is the base of the triangle formed by the lines approximating the downstream and upstream slopes and the rigid bed.

defined from the abscissa of the mid-height of the downstream face. For the length of the dune L_d, it was chosen to estimate it from the base of the triangle formed by the two lines approximating the downstream and upstream faces. This method allows to avoid artifacts in the profile that can occur at the foot of the upstream or downstream face. The definitions of x_h, h_d and L_d are summarized in the schematic shown in Figure 4.2.

Two experiments are considered in this work. The first one is a stationary regime configuration. A mass $m_0 = 10\,g$ of sediments is introduced through a hole drilled in the channel cover. It deposits under the influence of gravity and form a conic shaped mound with slope angles equal to the angle of repose of the granular material. Once the initial pile has formed, a motor is activated to create a left-to-right flow in the experimental zone with a bulk velocity $\overline{u} = 0.43\,m.s^{-1}$. A representation of the experiment is shown in Figure 4.3. In this stationary dune migration case, the initial mound is conic-shaped. During a first transient phase, the dune rapidly changes before reaching a steady state characterized by a time-invariant equilibrium shape which migrates at a constant speed. The time it takes for the dune to reach this stationary state is relatively short and lasts less than 10 seconds. In the example shown, the equilibrium profile of the dune exhibits a clear asymmetry with a straight downstream face.

The second experiment correspond to a mass loos scenario. This regime is observed in situations involving small dune mass and high mean flow velocity. Side views of the dune at times 0, 4 and 8 seconds during the mass loss experiment are shown in Figure 4.4. In the mass loss experiment considered, the mass of the initial heap is $m_0 = 2\,g$ and the bulk flow velocity is $\overline{u} = 0.54\,m.s^{-1}$. The two configurations are summarized in Table 4.2.

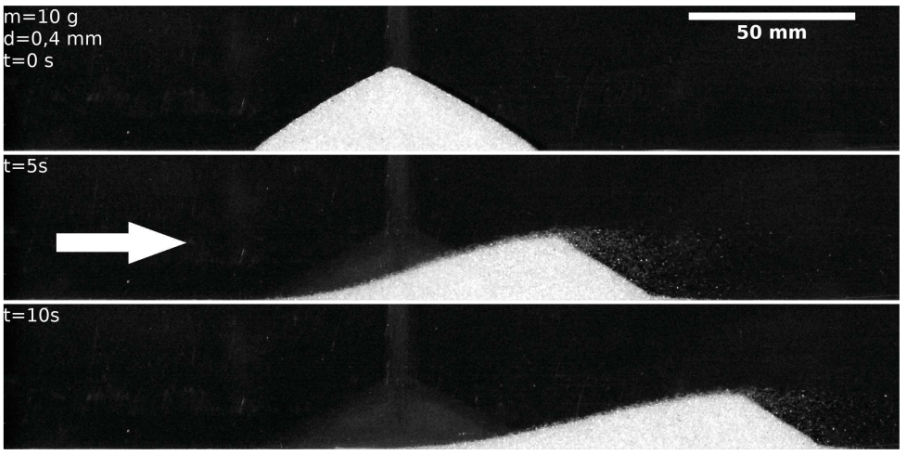

Figure 4.3: Sequence of images showing an initial mound of mass of $m_0 = 10\,g$ quickly deforming to reach a stationary shape. The initial velocity is $\overline{u} = 0.43\,m.s^{-1}$, and the particles diameter is $d = 0.4\,mm$. Image taken from Kiki Sandoungout [2019].

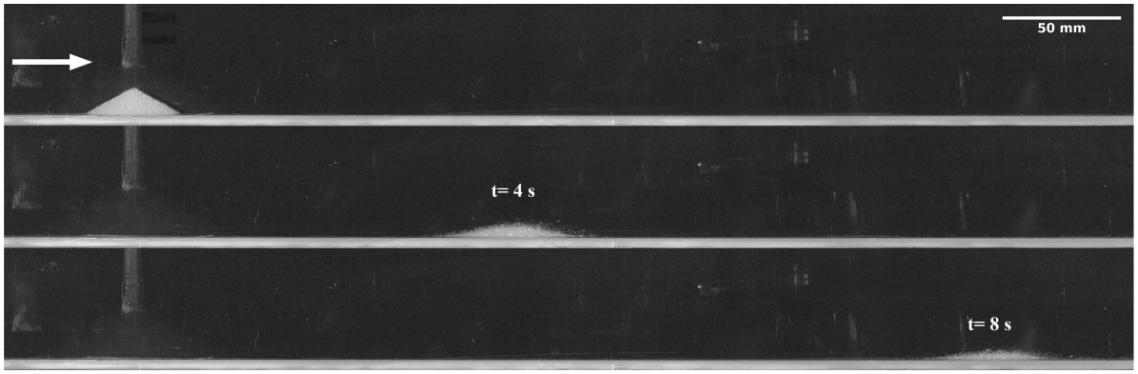

Figure 4.4: Mass loss scenario with complete disappearance of the dune. Evolution of an initial mass $m_0 = 2\,g$ subjected to a flow velocity $\overline{u} = 0.54\,m.s^{-1}$. Images are taken at three different instant during the migration process. From top to bottom, 0, 4, and 8 seconds.

regime	bulk flow velocity $\overline{u}\,[m.s^{-1}]$	mass of dune $m_0\,[g]$
stationary	0.43	10
mass loss	0.54	2

Table 4.2: Initial dune mass and bulk flow velocity for the two migration regimes studied.

4.1.2 Numerical configuration

An important aspect of this experiment is the narrowness of the channel, which makes friction on the side walls significant. The straightforward way to take into account lateral walls friction would be to run three dimensional simulations. To avoid the computational cost associated with this method it was chosen instead to neglect the lateral variation of the flow and to compute the specific shear stress on the lateral walls $\boldsymbol{\tau_{wall}}$ with the Darcy-Weissbach equation:

$$\boldsymbol{\tau_{wall}} = f\frac{|\boldsymbol{u}|\boldsymbol{u}}{8}\,, \tag{4.1}$$

where f is the Darcy-Weissbach friction factor which can be computed explicitly with the equation from Swamee and Jain [1976]:

$$f = \frac{0.25}{\left[\log_{10}\left(\frac{k_w/D_h}{3.7} - \frac{5.74}{Re_W^{0.9}}\right)\right]^2}\,, \tag{4.2}$$

where k_w is the roughness height corresponding to the roughness of the lateral walls and $Re_W = uW_c/\nu$ is the Reynolds number defined with the flume width. The hydraulic diameter D_h, is defined as four times the ratio of the wet area to the wet perimeter of the flume:

$$D_h = 2\frac{HW_c}{H + W_c}\,. \tag{4.3}$$

Integrating the momentum conservation equation (eq. 2.1) over the flume width, a new explicit source term $\boldsymbol{F_{walls}}$ corresponding to the effect of the lateral wall friction appears in the equation:

$$\boldsymbol{F_{walls}} = -f\frac{|\boldsymbol{u}|\boldsymbol{u}}{4W_c}\,. \tag{4.4}$$

Channel simulations without the presence of a dune have been run to validate the modeling of the lateral walls with the Darcy-Weissbach equation. The velocity profiles in the channel obtained for different water discharges are illustrated in Figure 4.5 and compared to experimental results from Kiki Sandoungout [2019]. For each discharge value, another simulation without lateral friction is also presented for comparison. Lateral friction leads to a more uniform velocity field as the distance to the upper and lower walls increases, as well as to higher velocity gradients near the boundaries. It also results in an increased shear stress exerted on the bottom of the flume for the same bulk velocity. The agreement with experimental data is improved except at the top where the flow is disturbed by the presence of a screw hole, which makes the experimental data noisy and unreliable in this area.

As explained previously, the advantage of taking into account lateral friction as a source term is that it enables the use of a two-dimensional mesh to study these dune migration problems, which significantly reduces the computational cost of the simulations. The computational domain thus consists of a 2D uniform rectangular mesh with uniform spacing in the x-direction (flow direction) and more refined at the top and bottom boundaries in the z-direction. After being initially generated with a flat bottom, the mesh is

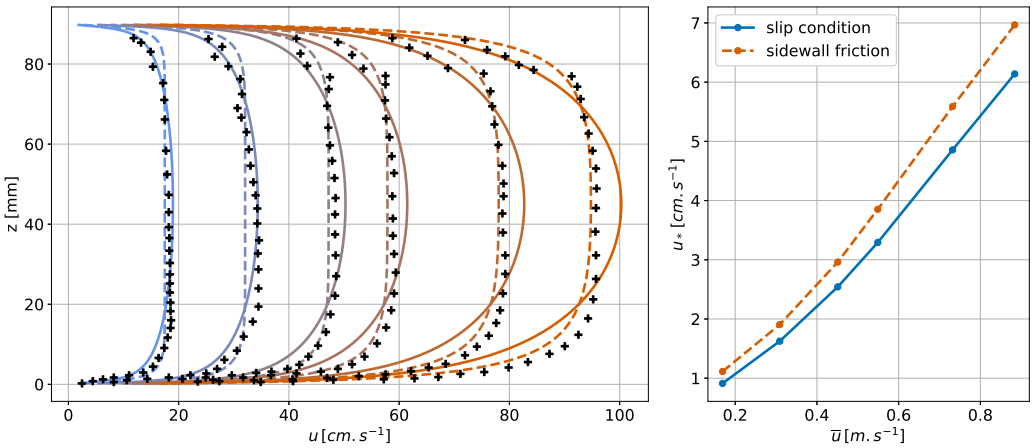

Figure 4.5: On the left graph, velocity profiles obtained for different bulk velocities ($16.9\,cm.s^{-1}$, $30.9\,cm.s^{-1}$, $45.1\,cm.s^{-1}$, $54.9\,cm.s^{-1}$ and $73.2\,cm.s^{-1}$). The solid lines represent profiles obtained without friction on the lateral walls and the dashed line to the one obtained taking into account the lateral friction. The black crosses are experimental results from Kiki Sandoungout [2019]. On the right graph, the friction velocity on the smooth bottom wall of the flume as a function of the bulk velocity with and without lateral friction is represented.

meshes	M0	M1	M2	M3
n_x number of cells in x-direction	300	500	1000	1100
n_z number of cells in z-direction	30	50	70	80
z_1 distance from first cell center to wall boundary in mm	1.037	0.359	0.257	0.142

Table 4.3: Characteristics of the four mesh used in the numerical study of dune migration. Ranging from coarse mesh M0 to fine mesh M3. The domain length is 800 mm and domain height is 90 mm for all meshes.

deformed so that the bottom boundary matches with the initial dune shape (see Figure 4.6). Throughout this numerical study, four different meshes will be used ranging from coarse to fine resolution. Their characteristics are summarized in Table 4.3. As explained in the description of the experimental setup of Kiki Sandoungout [2019], the initial dune is formed by the settling of particles injected through a hole drilled in the rigid lid covering the top of the channel. As they settle, the particles form a conic shaped mound with slopes having a constant angle whose value is not the same in all the experiments but is equal or smaller than the angle of repose of the granular material ($\beta_r = 28$ degrees). The top of the dune is round and approximated with a second order polynomial. Initially the sediments are loosely packed with a volume fraction of $c_s^{max} \approx 0.54$. As the dune migrates under the influence of the flow, the sediments get compacted and the sediment volume fraction in the bed increases resulting in the dune volume decreasing over time until the volume fraction reaches a constant value. This variation of the sediment volume

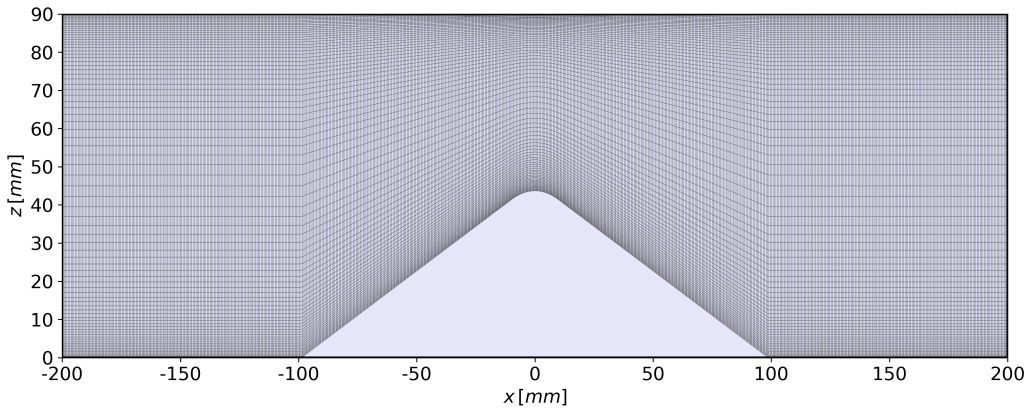

Figure 4.6: Example of a mesh used in the numerical study of a stationary dune migration regime. The bottom boundary matches with the initial dune geometry.

fraction in the bed cannot be reproduced by the present model in which the bed porosity is considered constant over space and time. Therefore, it was chosen to initialize the dune with a volume corresponding to the one at the end of the experiment and not the initial one. The initial mass of the sediments injected into the flume being known, and assuming that the dune is not losing mass over time, the final volume of the dune after it has compacted can be used to define an alternative initial condition, with the right mass of sediments but a different compaction of the granular material (see Figure 4.7). In the numerical simulations, this results in a dune initially smaller than the experimental one. However, after some time, the volume of the experimental dune has decreased and matches the volume of the numerical dune.

All the simulations presented here are RANS simulations using a $k-\omega\ SST$ turbulence model. To set up the inlet conditions, 1D channel simulations were run until a steady state is reached. The obtained vertical profiles of $\boldsymbol{u}$, k and ω were then extracted and imposed as Dirichlet conditions at the inlet of the 2D simulation domain. A no-slip condition is applied at the top and bottom boundaries so that the velocity is zero at the top and equal to the motion of the bed at the bottom, $\boldsymbol{u}|_{z=z_b} = \partial z_b/\partial t \boldsymbol{e_z}$ (movingWallVelocity in *OpenFOAM*). Still for those boundaries, a zero gradient condition is used for the pressure p. At the outlet, the pressure is fixed at a zero value and a zero-gradient condition is applied for the other fields. A smooth surface treatment is applied at the top boundary, which is a zero gradient condition for k and ω is set according to equations 1.30 and 1.29. Regarding the consideration of bed roughness in the simulations, a difficulty arises as the dune surface is rough and the bottom of the flume is smooth. The correct way to handle this boundary would be to switch from rough to smooth surface treatment depending on the position of the dune in the flume. Applying a rough treatment on the dune but switching to smooth wall condition in area where there is no sediment. Unfortunately, this is not possible yet at this stage of model development. Simulations with different bed roughness treatment will thus be presented and compared. Moreover, the bedload and

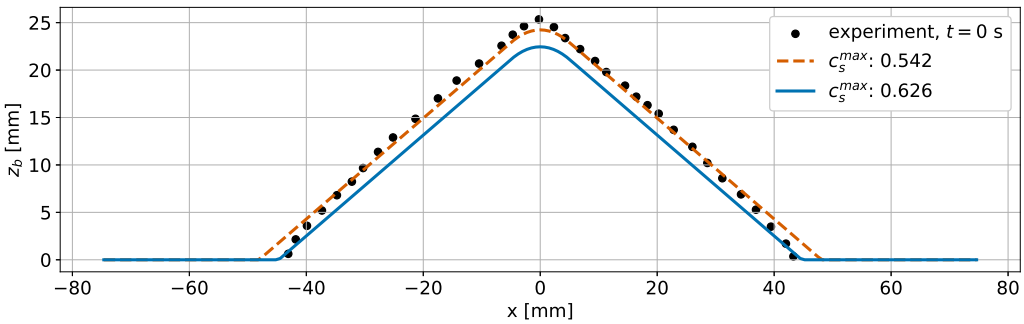

Figure 4.7: The black dots represent the experimental initial bed level. The orange dashed line is an initial condition fitted on the experimental bed level and the solid blue line is the initial condition designed based on the final volume of the dune. Assuming that the dune is not losing mass over time, this shows the compaction of the granular experiment as the dune migrates. The solid blue line is used as the initial condition for the numerical simulations.

erosion fluxes must be corrected to take the rigid wall into account, such that the bedload and the erosion vanish when the width of the sediment layer becomes null. Without this correction, the model would be able to dig into the rigid bottom of the flume.

A second order backward scheme is used for all simulations (eq. 2.36). The advective term of the Navier-Stokes equation was discretized using a *linear-upwind* (eq. 2.47) and a *limited linear* scheme was used for the advective terms in the transport equations for k and ω.

4.1.3 Hydrodynamics

This study first focuses on the stationary regime case but before running any dune migration simulation, a study on the hydrodynamics of the flow passing above the initial dune geometry is presented. The goal is to study the effect of mesh resolution and the impact of the bed boundary condition on the flow and on the friction velocity as it is what drives the sediments transport.

Channel flow without dune

The flow in the channel without the presence of a dune is first studied. To that end, channel flow simulations using different bottom roughness boundary conditions were run. These simulations consist of a 1D mesh made up of a vertical column of cells. In the x-direction, a cyclic boundary condition is applied which corresponds to a channel of infinite length. A uniform source term accelerates the fluid from an initial still condition to a flow of mean velocity $\overline{u} = 0.451\, m.s^{-1}$. The choice of a slightly different velocity than in the dune migration experiment ($\overline{u} = 0.43\, m.s^{-1}$) is motivated by the existence of experimental velocity measurements of the flow in the experimental area of the flume

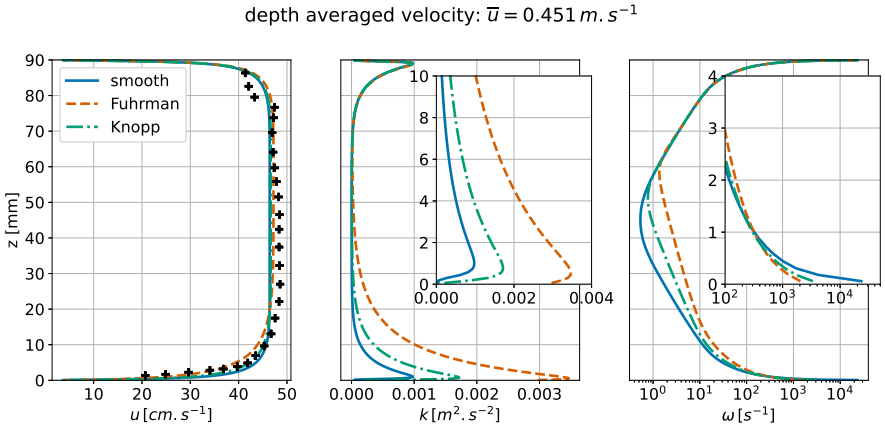

Figure 4.8: Vertical profiles of $\boldsymbol{u}$, k and ω obtained in channel simulations with 3 different bottom wall treatments. Smooth boundary condition (solid blue line), Fuhrman rough boundary condition described by equation 1.34 (green dashed line) and Knopp et al. rough boundary condition (dashed-dotted red line).

without the presence of a dune. A fine mesh made up of 120 cells is used for 3 different cases for which different bottom roughness conditions are considered. A smooth bottom, a rough bottom using the modified Wilcox formulation referred as Fuhrman and another rough bottom case using the formulation from Knopp et al. [2009]. The vertical profiles for $\boldsymbol{u}$, k and ω are represented in Figure 4.8. In the smooth case, the profiles are symmetrical as the top and bottom boundary conditions are identical. Using a rough bottom condition, the boundary layer width, that is, the distance that the velocity needs to pass from zero velocity at the wall to the uniform velocity at the channel's center, is increased. The Fuhrman condition predicts a hydraulically rougher flow as the turbulent kinetic energy does not vanish near the wall, which coincides with a lower value of ω involving lower dissipation of turbulent kinetic energy. These channel simulations were run with meshes of different resolutions. The friction velocity on the flume bottom wall obtained for each simulation is represented in Figure 4.9. The other rough boundary conditions [Wilcox et al., 1998, Lee, 2018] were not represented in Figures 4.8 and 4.9 as in this case, the Wilcox boundary (eq. 1.33) gives the same results as the Fuhrman condition, and the one from Lee [2018] results identical to the one obtained with the condition from Knopp et al. [2009].

Flow over a rigid dune

The same channel simulations are run again, this time with a bulk velocity $\overline{u} = 0.43\, m.s^{-1}$, corresponding to the velocity of the stationary regime (see Table 4.2) and the obtained vertical profiles are imposed as Dirichlet conditions at the inlet of the 2D computational domain and a 10 grams dune is introduced at its center. The simulations are run without morphological evolution until the flow reaches a steady state is reached. As in the case of channel flow without dune, different roughness boundary conditions are used and

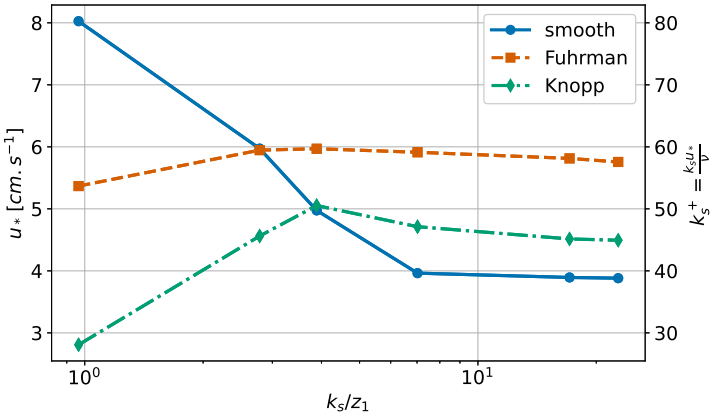

Figure 4.9: Effect of mesh resolution on friction velocity at bottom wall of the flume obtained for 3 different wall boundary conditions. z_1 stands for the distance from the first cell center to the wall.

compared (smooth bed, Fuhrman and Knopp). For each bottom boundary condition, 4 simulations are run, each one using a different mesh (see Table 4.3). A representation of the flow streamlines is presented in Figure 4.10. The dune is partially obstructing the channel, causing the flow to accelerate as it moves up the dune's upstream slope. Downstream of the dune crest, the flow gradually gets more space to develop, which causes it to decelerate. This configuration generates an adverse pressure gradient leading to the detachment of the flow near the crest of the dune. The associated recirculation cell is clearly visible in Figure 4.10 both on the streamlines representation and on the velocity profile for every bottom boundary condition. At the end of the recirculation area, the flow reattaches to the bottom of the flume. It can be observed that the two rough conditions used are predicting a larger recirculation cell. On Figure 4.10, there are still negative stream wise velocities $100\,mm$ downstream of the dune crest whereas the flow as already reattached to the wall in the case of a rough wall condition. This can be further observed in Figure 4.11 in which are represented the x-component of friction velocity for each wall boundary condition and different mesh resolutions. Negative friction velocity values indicate the presence of the recirculation cell, which spread up to 130 mm downstream of the dune's crest for a smooth bed and only up to 100 mm when a Fuhrman condition is used. In the case of the Knopp condition, the length of the recirculation cell exhibits a strong dependency to grid resolution, so a specific value cannot be retained. The recirculation cell also exhibits a greater height in the case of a smooth wall boundary. The flow detachment position can also be located from this same Figure by the rapid drop in u_* after it has reached a maximum value close to the dune's crest. The position of the maximum friction velocity always appears a bit upstream of the crest. In the case of a smooth condition, the point of maximum friction velocity is affected by the mesh resolution and is positioned further upstream from the crest as the mesh is refined. However, it appears to be insensitive in the case of a rough bottom. Using a fine mesh reveals details

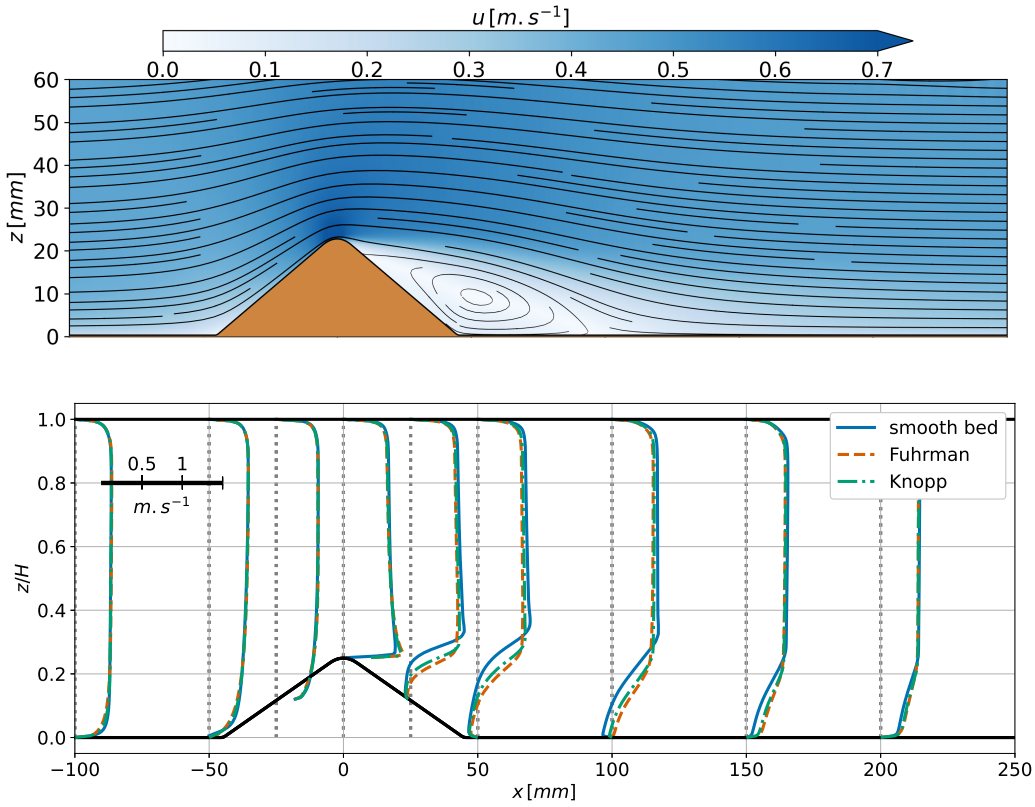

Figure 4.10: On the top, velocity fields and streamlines at stationary state. On the bottom graph, vertical profiles of the stream wise velocity component for 3 simulations with different bottom boundary conditions. The solid gray line indicates the bed level. The Mesh M3 was used for all simulations.

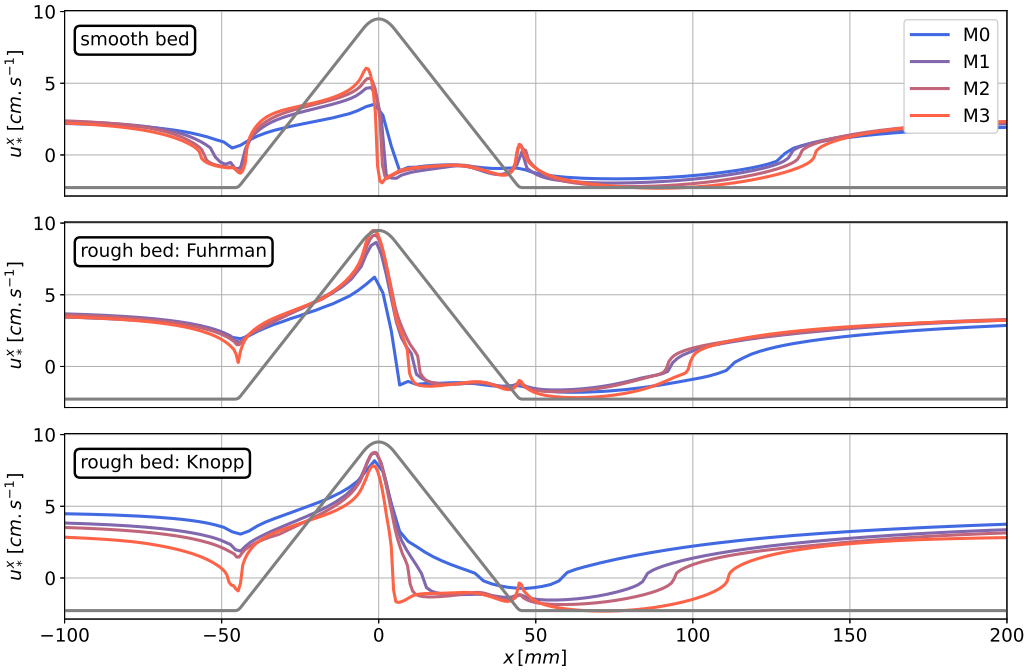

Figure 4.11: Comparison of stream wise component of friction velocity obtained for 3 different bottom boundary conditions (smooth bed, Fuhrman and Knopp) and 4 different mesh resolutions (M0, M1, M2 and M3).

about the flow at the ends of the dune. For instance, a small recirculation occurs at the upstream foot of the dune (smooth bed, Fuhrman), and the friction velocity decreases at the transition between the downstream slope and the flat bottom.

In conclusion of this sensitivity analysis, it shall be kept in mind that the details of the flow around the dune is sensitive to the roughness of the bottom and to the grid resolution. As already explained, the spatial variation of the roughness can not be simulated by the *sedExnerFOAM* model yet but this may have an influence on the hydrodynamics and subsequently on sediment transport predictions and the underlying predicted morphological evolution. Nevertheless, this morphological evolution will be studied in the next section.

4.1.4 Morphological evolution

After describing the main features of the flow around the initial dune geometry, as well as the impact of the mesh resolution and bed roughness on the hydrodynamics, morphological evolution simulations are now presented. The simulations are set up as follows. First, a simulation without morphological evolution is run until the flow reaches a stationary state. The achieved state then serves as the initial condition for the morphological evolution simulation and the dune start its migration under the influence of an already fully developed flow. Experimentally, the fluid is initially still and the pump starts to operate at $t = 0\,s$ accelerating the flow to the selected velocity setpoint. This inconsistency in the initial condition can lead to a different morphological response in the first few seconds of the simulation. The different adjustment parameters of the model were thus tuned to match the experimental results beyond the first seconds of simulation.

If not stated otherwise, the base critical Shields number is set to $\theta_c^0 = 0.05$ and the slope correction is activated (eq. 2.21). The bedload flux is computed with the formula from Meyer-Peter and Müller [1948] and the avalanche coefficient q_{av}^0 in equation 2.23 is taken equal to $3\,10^{-4}\,m^2.s^{-2}$. For the suspended load, the terminal settling velocity of the particles is computed using the formula from Fredsoe and Deigaard [1992] (see table 2.6) resulting in $w_s^0 = 4.9\,cm.s^{-1}$, the Schmidt number is taken equal to $\sigma_c = 1$ and the additional wall diffusivity introduced in equation 2.30 is used.

To evaluate the numerical results and tune the different adjustment parameters of the model, bed level data at different times during the experiment as well as the temporal evolution of the dune position, its length and height.

First attempts, no saturation

Usually, when running morphodynamics simulations, the simulations are stable if the time step ensure that the Courant number is smaller than one everywhere in the computational domain. In *OpenFOAM*, the Courant number can be estimated at the mesh face centers that delimit the mesh cells:

$$C_o = \frac{\boldsymbol{u}_f.\boldsymbol{n}_f}{d_{O-N}}\delta t\,, \tag{4.5}$$

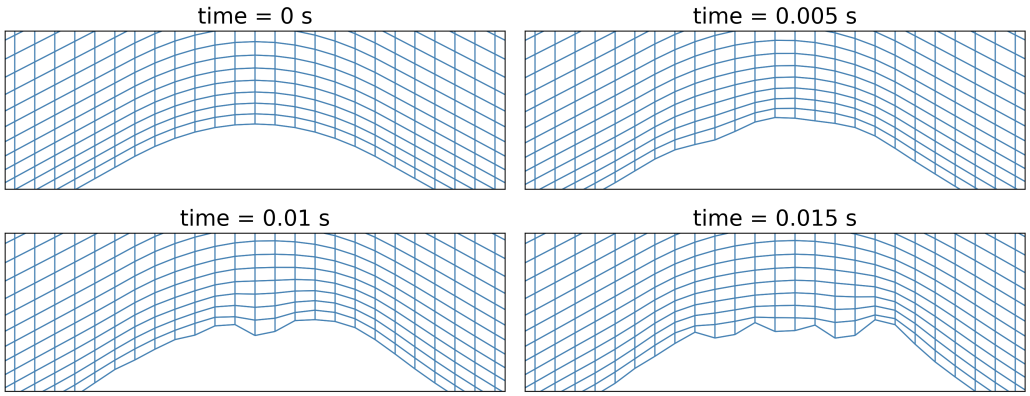

Figure 4.12: Exner instabilities occurring at the top of the dune. Representation of the mesh at different times before the simulation failure.

where δt is the time step, $\boldsymbol{n}_f$ is normal vector of face f, $\boldsymbol{u}_f$ is the fluid velocity at the face and d_{O-N} is the distance between the centers of the owner and neighbor cells sharing the face f. There is also a stability condition to respect to avoid triggering instabilities in the Exner equation but it is almost always less restrictive than the stability condition for the hydrodynamics, and there is thus no need to consider it. However, in situation like the present one, when a morphological evolution simulation is initiated with an already fully developed flow with an important bed shear stress, it can prove necessary to reduce the time step value, at least during the initial phase, in order to avoid the emergence of bed level instabilities which easily lead to the failure of the simulation by severely distorting the mesh. An example of such instabilities is shown in Figure 4.12.

Following the study of the bed roughness condition on the hydrodynamics above the initial dune geometry, the same simulations are run, this time with the morphology evolution activated. As a reminder, three different boundary conditions are used at the bed, the smooth wall condition and two rough wall boundary conditions, Fuhrman and Knopp (see Table 2.4). Using the the finest mesh M3, the bed levels obtained after 10 seconds of simulations are shown in Figure 4.13. The shape of the dune at 10 seconds differs strongly from the experiment results (see Figure 4.3). First, the experiment suggests that the upstream slope should be significantly less steep (12°) than the downstream one (33°) which is not observed. Secondly, the upstream slope is not uniform and becomes steeper close to the crest. Last, for all simulations, a mound of sediments formed downstream of the dune, right at its base. To further illustrate the difference in behavior between the numerical dunes and the experiment, the time evolution of their morphological parameters (position, height and length) is represented in Figure 4.14 . Regardless of the selected bottom boundary condition, the predicted migration velocity is a lot smaller than the experimental one. The experiment indicates a migration velocity of $8.61\,mm.s^{-1}$ but numerically, the maximum predicted migration velocity is $3.13\,mm.s^{-1}$ for the rough bed case with a Fuhrman boundary condition. In addition, the dune's shape evolution is not following the same trend as in the experiment. Its height is reducing over time but not

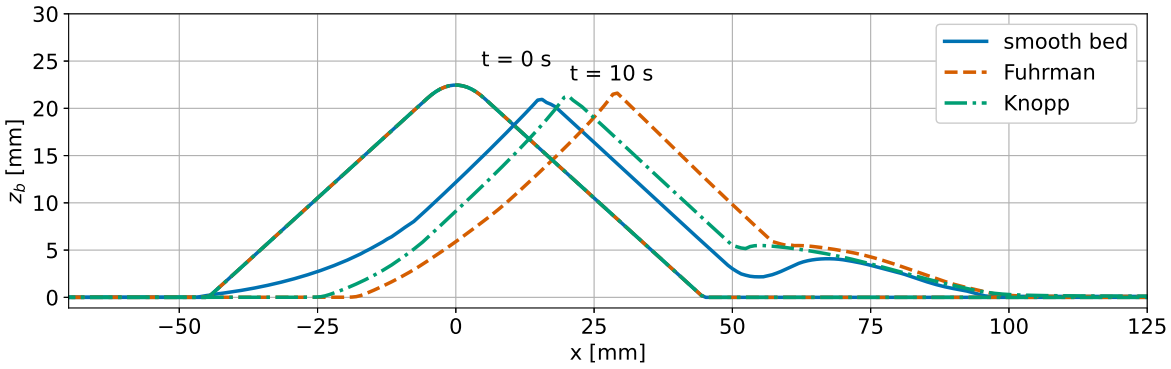

Figure 4.13: Bed level position at the initial time and after 10 seconds for 3 different roughness boundary conditions.

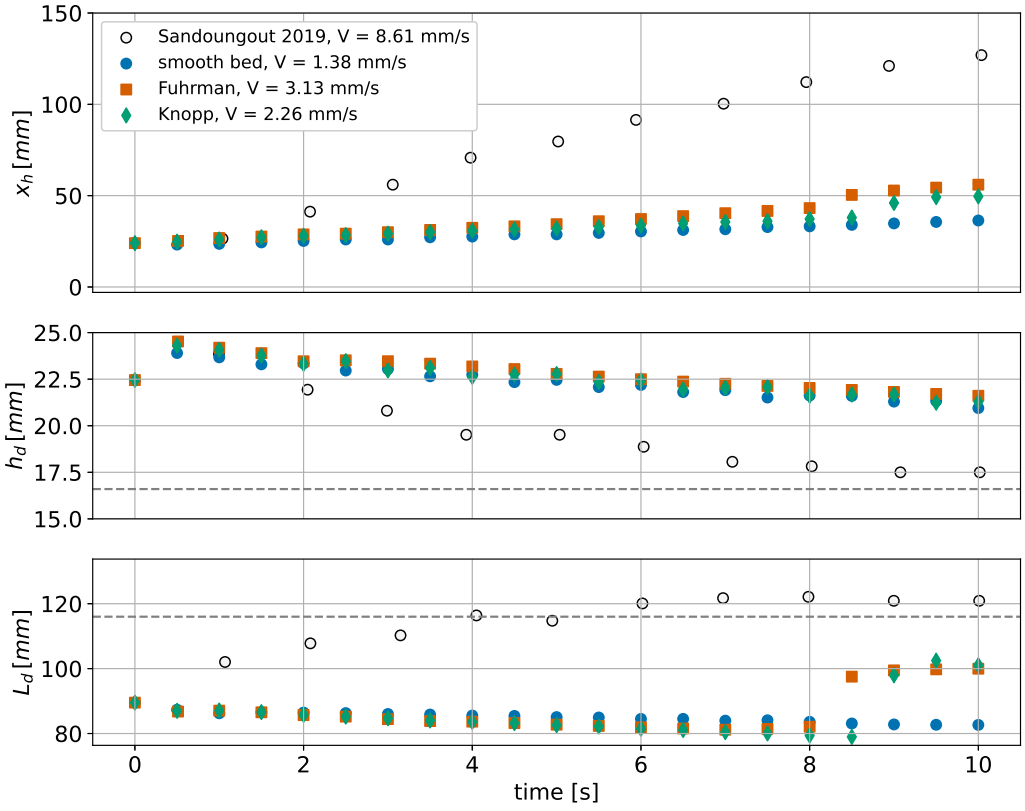

Figure 4.14: Dune morphological parameters evolution in time. From top to bottom are plotted the dune position represented by the coordinates x_h, which is located halfway up the downstream face of the dune, as well as the dune height h_d and the dune length L_d. Comparison between numerical simulation results obtained with different roughness bottom boundary conditions and experimental data from Kiki Sandoungout [2019].

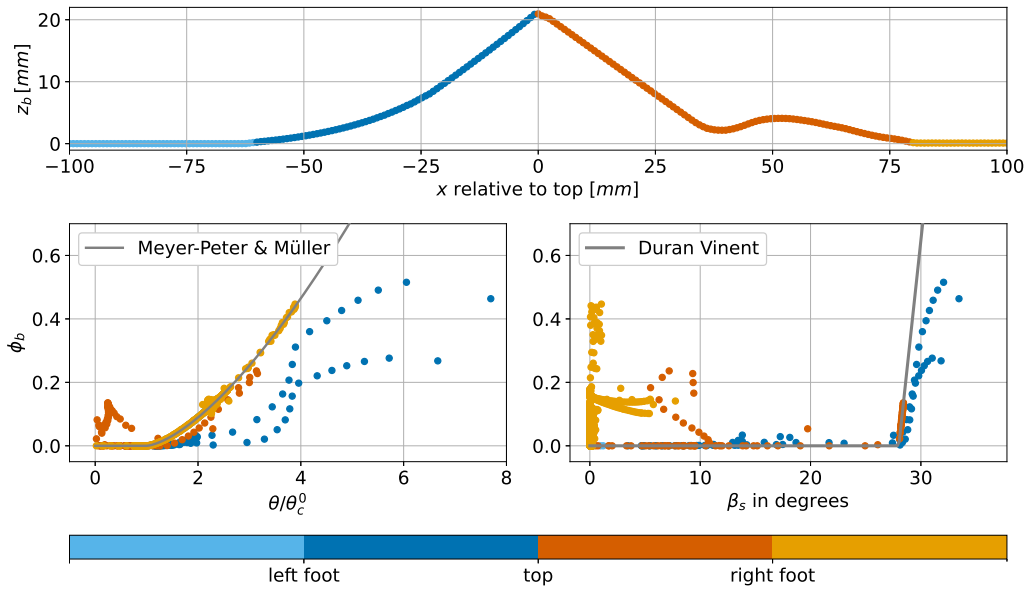

Figure 4.15: On the top, position of the bed, on the bottom from left to right, the dimensionless bedload as a function of the shields number, and as a function of the local slope. The colors divide the domain into four parts, the flat bed upstream of the dune (light blue), the upstream slope (dark blue), the downstream slope of the dune (orange), and the flat bed downstream of the dune (yellow). The results were extracted 10 seconds after the start of the migration.

fast enough and its length is slowly decreasing when it should increase. To investigate this strange dune migration behavior, a focus is made on the smooth bed case and the dimensionless bedload ϕ_b is represented in Figure 4.15 as a function of the Shields number θ and as a function of the local bed slope β_s. The bedload formula from Meyer-Peter and Müller [1948] and the avalanche formula from Duran Vinent et al. [2019] are plotted alongside the simulation results. The correlation between the data points and the formulas for shear induced bedload or for avalanche, indicate what phenomenon is driving the bedload flux locally. As expected, the points on the flat bed (light blue and yellow) match with the Meyer-Peter formula. On the upstream slope of the dune (dark blue points), slopes steeper than the angle of repose is encountered and the points match pretty well with the avalanche formula. From this, it can be seen that avalanche are occurring even on the upstream slope of the dune, where the steepest local slope are found. In the experiment however, the upstream slope is mild and the bedload flux is this area is only due to bed shear stress. On the downstream slope of the dune (orange), some points coincide with the bedload formula and others with the avalanche model when the avalanche is expected to be the main driving mechanism in this area. Overall, the behavior of the dune during its migration largely differs from the one observed experimentally and does not seem physical.

To further dig into this problem and understand what is the cause of this unexpected

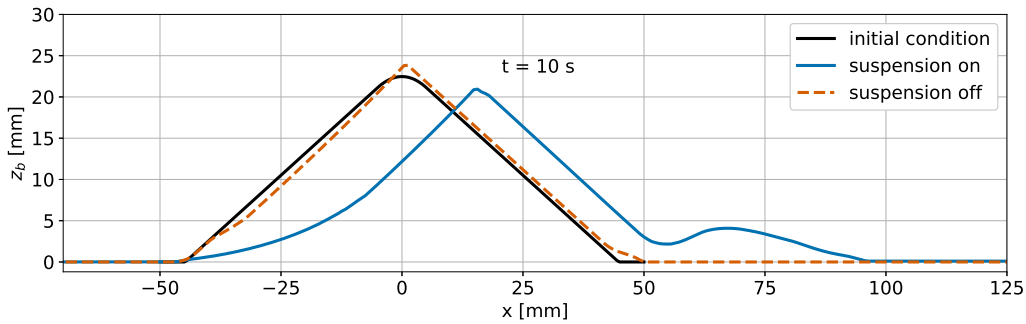

Figure 4.16: Bed level after 10 seconds with and without taking suspension into account. The simulations were run using the mesh M3 and smooth bed boundary conditions.

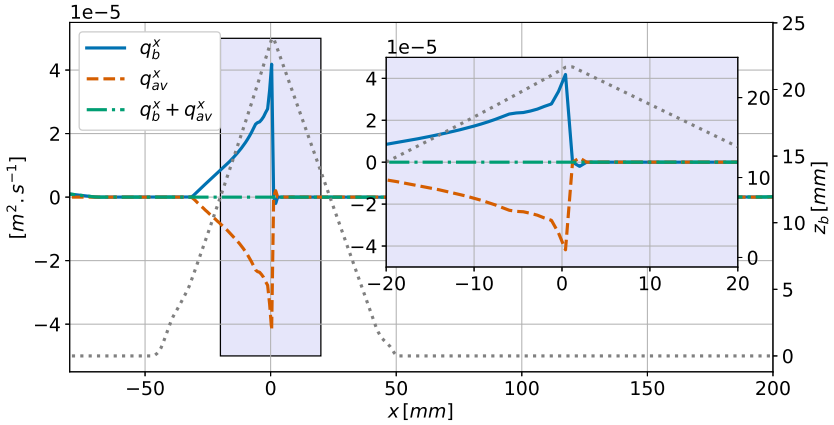

Figure 4.17: Representation of the x-component of the bedload flux around the dune. The bedload flux is divided into two contributions. One from the bed shear stress and the other to the avalanche mechanism.

behavior, another smooth bed simulation is run, this time without taking into account the suspended load. The bed levels obtained from two simulations, with and without suspension respectively, after 10 seconds of simulations are presented in Figure 4.16. Without suspension, the dune appears to be stuck at its initial position, only the shape of the dune's crest has changed and has become steeper. In the simulations already presented, the migration is driven exclusively by the suspended load explaining the strange shape of the dune and the appearance of a small mound at the right foot of the dune corresponding to the deposition of suspended sediments trapped in the recirculation cell. As shown in Figure 4.17, the total bedload flux, that is the sum of the bedload resulting from shear stress and the one due avalanche activity is null. The dune remains in a non-physical equilibrium state, where avalanches cancels out the bedload flux due to shear stress. At the top of the dune, the bedload due to shear stress abruptly falls from a maximum value to zero because of the flow detachment occurring at the dune's crest. Thus, there is no bedload flux passing over the crest of the dune, which stops its migration.

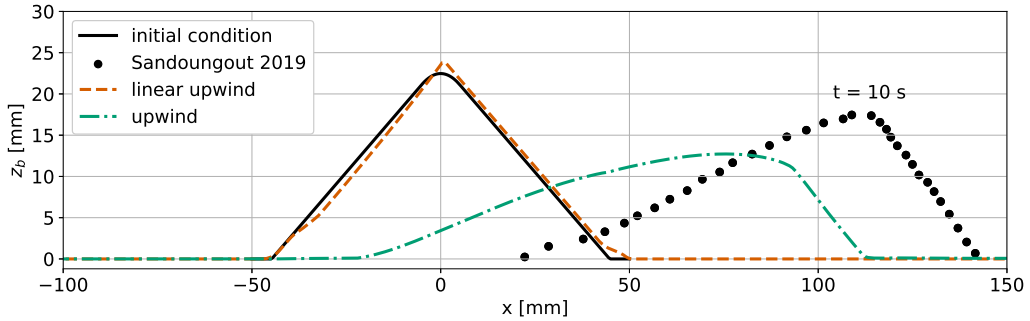

Figure 4.18: Bed level after 10 seconds for two different advection schemes, *upwind* and *linear-upwind*. Suspension is switched off. Smooth bed conditions were applied and the finest mesh M3 is used.

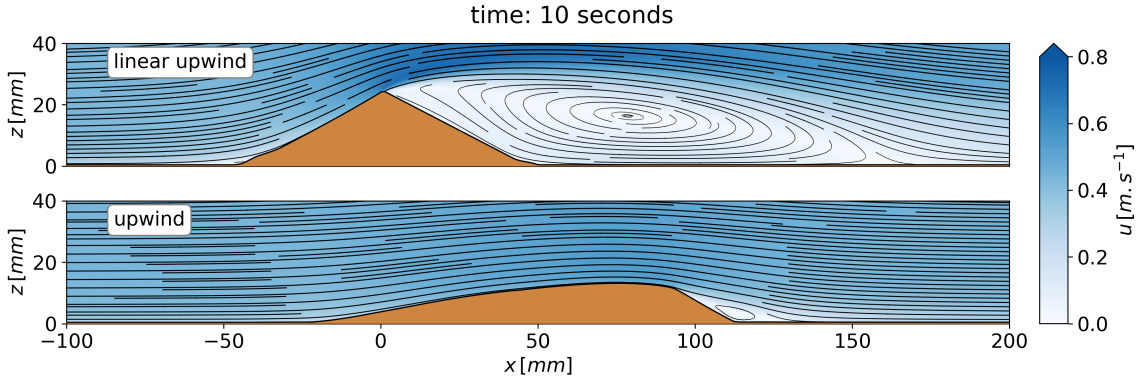

Figure 4.19: Representation of the dune and the flow streamlines, 10 seconds after the beginning migration process. From top to bottom, results obtained with a *linear-upwind* scheme and *upwind* schemes respectively.

To further illustrate the problem, a smooth bed simulation using an *upwind* scheme to discretize the advection term in the fluid momentum equation (eq. 2.1) is run and compared with the smooth bed case without suspension already presented in Figure 4.16 for which a *linear-upwind* scheme was used. For comparison the bed levels obtained after 10 seconds of simulations are shown in Figure 4.18. Using a low order *upwind* scheme to discretize the advection term of equation 2.1 brings numerical diffusion in the simulation and changes the behavior of the recirculation cell. The flow detachment position is not predicted at the dune's crest but somewhere on the downstream slope. Therefore, bed shear stress remains significant at the top of the dune and for a short distance downstream. This allows for sediments to be transported as bedload on the downstream side of the dune and then being caught in the avalanche process. As a result, the previous situation, where the avalanche and the bedload flux on the upstream side of the dune cancel each other out, is no longer observed.

The different simulations presented have highlighted the importance of the flow de-

tachment in the dune migration process, associated with a drop in the shear stress exerted on the bed. In the cases presented, the suspended load is the only transport mechanism driving the dune motion. Sediments are eroded from the upstream side and deposit downstream of the dune creating a small mound which is not observed experimentally. When the suspension is not taken into account in the simulation, the migration is stopped by an equilibrium between the flow pushing the sediments towards the dune's crest and avalanches, so that the total bedload flux ($\boldsymbol{q_{av}} + \boldsymbol{q_b}$) becomes null.

Saturation of the bedload flux

The importance of the flow detachment in the dune migration process has been highlighted in the previous section. On the upstream slope of the dune, the flow is accelerated and the bed shear stress increases. At the position where the flow detaches, the shear stress value suddenly drops. Then the sediments accumulate at the crest and the dune height increases. At some points the upstream slope becomes steeper than the angle of repose and the avalanche bedload compensates the shear induced bedload. The dune then stops moving and stays stuck in a non physical state.

A closer look at Figure 4.3 helps to understand what is missing in the numerical simulation. On the upstream slope of the dune the particles in motion form a thin layer called the bedload layer. They roll and slide on the below particles. These particles arrive at the top of the dune with a certain velocity and their inertia make them continue their motion even after having reached the flow detachment position. It takes a certain distance and time for them to react to the sudden change of bed shear stress and consequently, they continue their motion on some distance after the flow detachment position. Moreover, the slope changes abruptly at the top of the dune and the glass beads lose contact with the bed. The suspended particles downstream of the crest are observed in the photos of the experiment in Figure 4.3.

In the simulations already presented, the bedload flux reacts instantaneously to the Shields number. Because of that, the bedload transport becomes null at the detachment point, where the shear stress values drop after passing through a maximum value. The dune's morphological response depending on the position of the maximum bedload flux is illustrated by the schematic in Figure 4.20. If the position of maximum shear stress, and consequently the location of maximum bedload flux, is located downstream of the crest, then the dune migrates in the flow direction and also decreases in height [Duran Vinent et al., 2019]. However, if it is located upstream of the crest, the dune's height increases, making the upstream slope steeper. When the local slope β_s exceeds the angle of repose an avalanche is triggered and the slope reach a value verifying the equality $q_{av}(\beta_s) = \sqrt{(s-1)gd^3}\theta(\theta - \theta_c)^{3/2}$, where q_{av} is the additional bedload due to avalanche computed using the formula from Duran Vinent et al. [2019] (see eq. 2.23).

As a means to control the position of the maximum bedload flux [Andreotti et al., 2002b, Charru et al., 2013], a formulation for bedload saturation was implemented in *sedExnerFoam*. It is a first order approximation of inertia of the particles transported as bedload. Previously, the effect of the bed roughness condition used was studied without

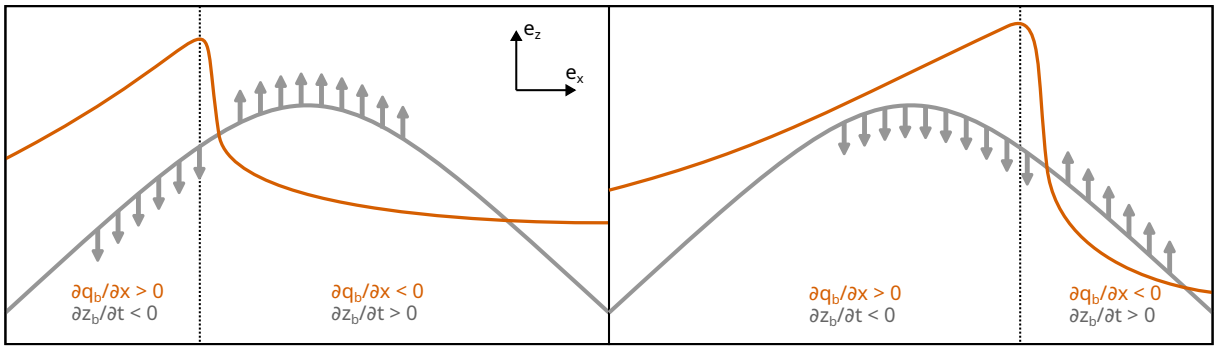

Figure 4.20: Schematic of the bed level morphological response to the position of the maximum bedload flux, upstream or downstream of the dune's crest. The grey arrows indicates if the bed level rises or decreases locally.

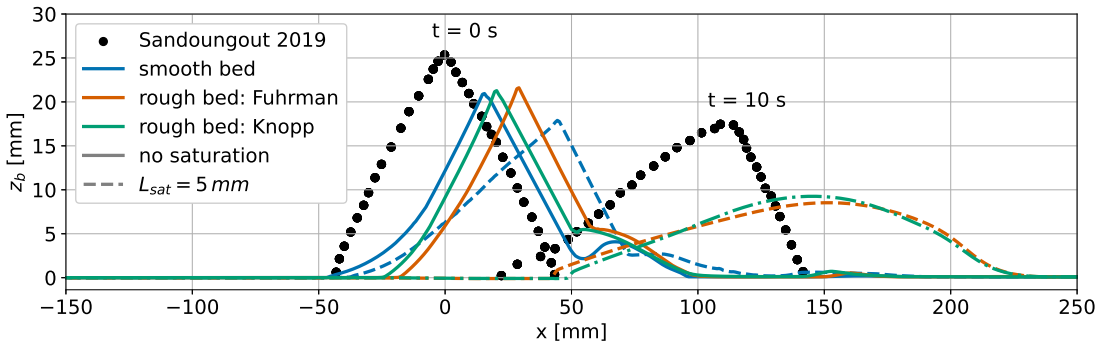

Figure 4.21: Bed level after 10 seconds for 3 different bottom roughness conditions. The solid lines are results obtained without saturation of the bedload flux and the dashed lines, simulations with $L_{sat} = 5\,mm$.

saturation and the results were presented in Figure 4.13. The same simulations are run again, this time using a saturation length $L_{sat} = 5\,mm$. The bed elevations after 10 seconds of migration are presented in Figure 4.21. For all cases, the results show an increase of dune migration velocities even when the saturation smooths the bedload flux and thus lower the maximum bedload value. The migration velocity is controlled by the quantity of sediments passing over the crest to join the slip face (downstream) of the dune controlled by avalanche. For the same value of saturation length, two different behaviors for smooth and rough bed are observed. For the smooth bed case, the dune's crest remains sharp whereas for both Fuhrman and Knopp bottom conditions, the dune spread and takes a round shape similar to the one previously observed when a low order *upwind* scheme was used to discretize the advection term of the fluid momentum equation (see Figure 4.18 and 4.19). An explanation of the shape difference observed for the same saturation length value is the flow detachment position dependency on bed roughness. It was observed that taking into account bed roughness shifts downstream the position of flow detachment compared to the one predicted with a smooth bed condition. It is clearly

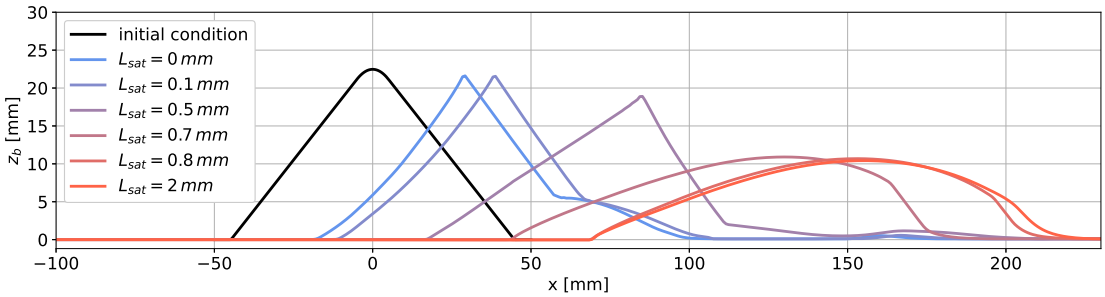

Figure 4.22: Bed elevation obtained with a rough bed treatment and different saturation length values, ranging from $L_{sat} = 0\,mm$ (no saturation) to $L_{sat} = 2\,mm$.

visible in Figure 4.11 that, with a fine near bed resolution, the position of maximum friction velocity for a smooth bed is located upstream of the one obtained with a rough bed treatment. For particles to pass over the top of the dune, a larger value of L_{sat} is required if the roughness of the bed is neglected. In the results presented, the round dune obtained with a rough bed is due to an overly large value of saturation length.

The sensitivity of the dune to the value of L_{sat} is studied for a rough bed using Fuhrman condition. The saturation length varies between 0 and 2 millimeters and the bed level after 10 seconds of migration are presented in Figure 4.22. For $L_{sat} = 0.1\,mm$, the dune's upstream side remains concave as in the case without saturation. This is a sign of an accumulation of sediments at the top of the dune and is due to the position of maximum bedload located upstream of the crest. For $L_{sat} = 7\,mm$, the upstream slope becomes uniform as in the experiment. As the saturation length is further increased, a critical point has been reached and the migration velocity significantly increases. The shape of the dune changes, its peak is no longer sharp and it takes the round shape previously observed using an *upwind* scheme (see Figure 4.18).

For the smooth bed case, the saturation also increases the migration velocity of the dune. However since the flow detachment is located further upstream of the crest than in the rough bed case, larger values of L_{sat} are necessary for the bedload flux to pass on the downstream face of the dune. The results presented in Figure 4.23 show the bed level after 10 seconds of migration using a smooth bed condition for values of L_{sat} varying from $1\,mm$ to $20\,mm$. Contrarily to what was observed for the rough bed case, the dune never takes a round shape even for large values of L_{sat}. It is also observed that using an excessively large value of $L_{sat} = 20\,mm$ slows down the migration. Saturation acts as a spatial filter and smooths out the maximum of $\boldsymbol{q_{sat}}$. For very large value of L_{sat} this results in an underestimation of $\boldsymbol{q_b}$ and the migration velocity is reduced. The bedload and saturated bedload fluxed obtained using values of $L_{sat} = 1\,mm$ and $L_{sat} = 5\,mm$ are presented in Figure 4.24 allowing to directly visualize the spatial relaxation of $\boldsymbol{q_b}$ and the effect of L_{sat} on the reduction of the maximum bedload flux.

When the numerical study of dune migration using *sedExnerFoam* began, saturation was not implemented, nor was it planned to be implemented. To obtain dune migration

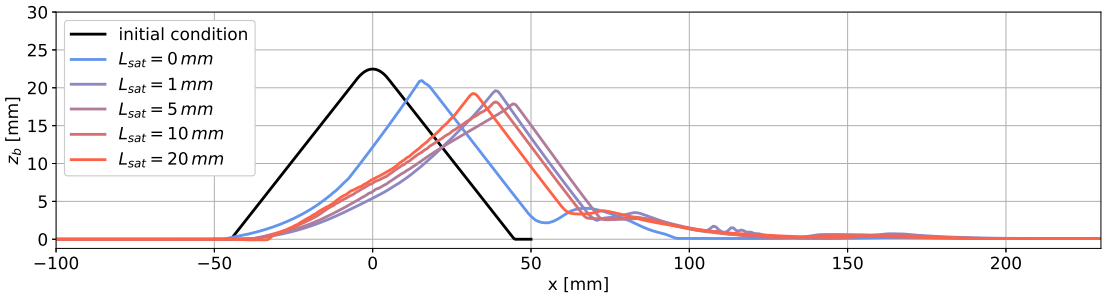

Figure 4.23: Bed elevation obtained with a smooth bed treatment and different saturation length values, ranging from $L_{sat} = 1\,mm$ (no saturation) to $L_{sat} = 20\,cm$.

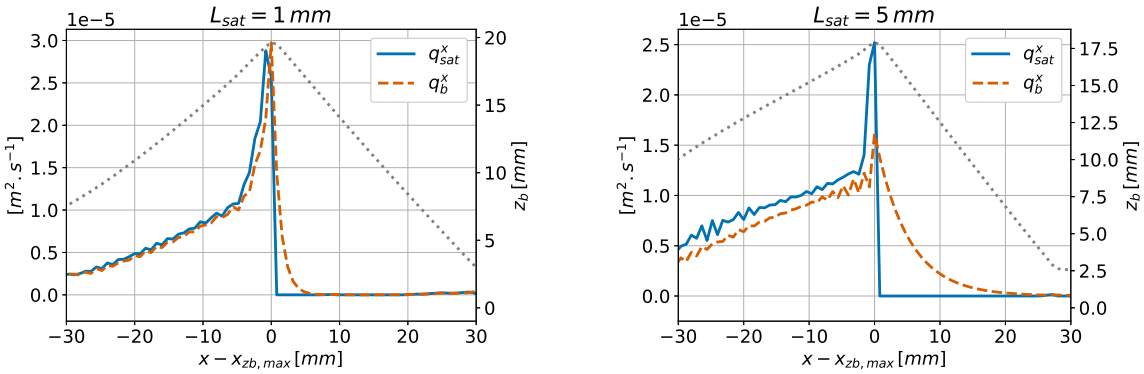

Figure 4.24: Representation of the x-component of $\boldsymbol{q_{sat}}$ and $\boldsymbol{q_b}$ for two values of saturation length, $L_{sat} = 1\,mm$ and $L_{sat} = 5\,mm$ respectively, obtained after 10 seconds of migration. A smooth bed boundary condition was used for both simulations. The x-coordinates is taken relative to the position of the dune's crest and the gray dotted line represents the bed elevation.

that matched the experiment, many parameters were varied, including the effects of mesh resolution, numerical schemes, bedload formulas, slope correction of the critical Shields number, etc. Even though it was possible to obtain agreement with certain experimental characteristics, it was not possible to match them all at the same time, i.e., speed, height, length, and overall shape. After multiple trials and errors, saturation was implemented in the model which is not commonly done in numerical models for sediment transport under water [Lesser et al., 2004, Liu and García, 2008, Baykal et al., 2015, Song et al., 2022]. Taking into account the saturation length allows sediments to continue moving for a certain distance after the sudden drop in stress associated with the detachment of the flow. Without it, the sediments accumulate just before the dune's crest and never pass to the on the downstream side of the dune which stops the migration process.

4.1.5 Other relevant fitting parameters

Even though the saturation length has been identified as a key feature controlling the morphological response of the dune, other parameters of the model need to be adjusted to obtain a good fit with the experiments, in term of migration velocity and dune shape. Experimentally, the fluid is initially still and the pump starts to operate at $t = 0\,s$ accelerating the flow to the selected velocity setpoint. As the time it takes for the flow to accelerate and reach a mean velocity $u = 0.43\,m.s^{-1}$ is unknown, the simulations are initiated with an already fully developed flow. This inconsistency in the initial condition leads to a different morphological response in the first few seconds of the simulation. Another difference already mentioned but reminded here is that the initial mound is initially quite loose and get compacted during the migration. As a result, the dune volume changes during the experiment but the compaction of the sediments in the bed is constant in *sedExnerFoam*. Therefore, the initial dune geometry was generated with a volume corresponding to the final compaction. For the same initial mass, the numerical dune is smaller than the experimental one but their volumes end up match after some time. For these two reasons, the different adjustment parameters of the model were tuned to match the experimental results beyond the first 5 seconds of simulation.

An example of a simulation obtained after multiple attempts and fitted on the experimental results is shown in Figure 4.25 which represents the dune and the flow of water at three different times, 0, 15 and 30 seconds after the beginning of the migration process. After around 10 seconds, the dune has reached a stationary state, and qualitatively the dune shape at 15 and 30 seconds looks the same. The recirculation downstream of the initial geometry is a bit wider than the one at the end of the simulation. Some artefacts are observed on the bed downstream of the dune. They are small deposits of suspended sediments trapped by the recirculation cell.

For quantitative comparison, the bed elevation at different times is compared to the ones measured experimentally in Figure 4.26 together with another identical simulation except for the fact that the suspended load was not taken into account. Overall, the dune fits really well with the experimental results except for the crest of the dune which is too sharp in the simulations. In this case, the suspended load accelerates a little the

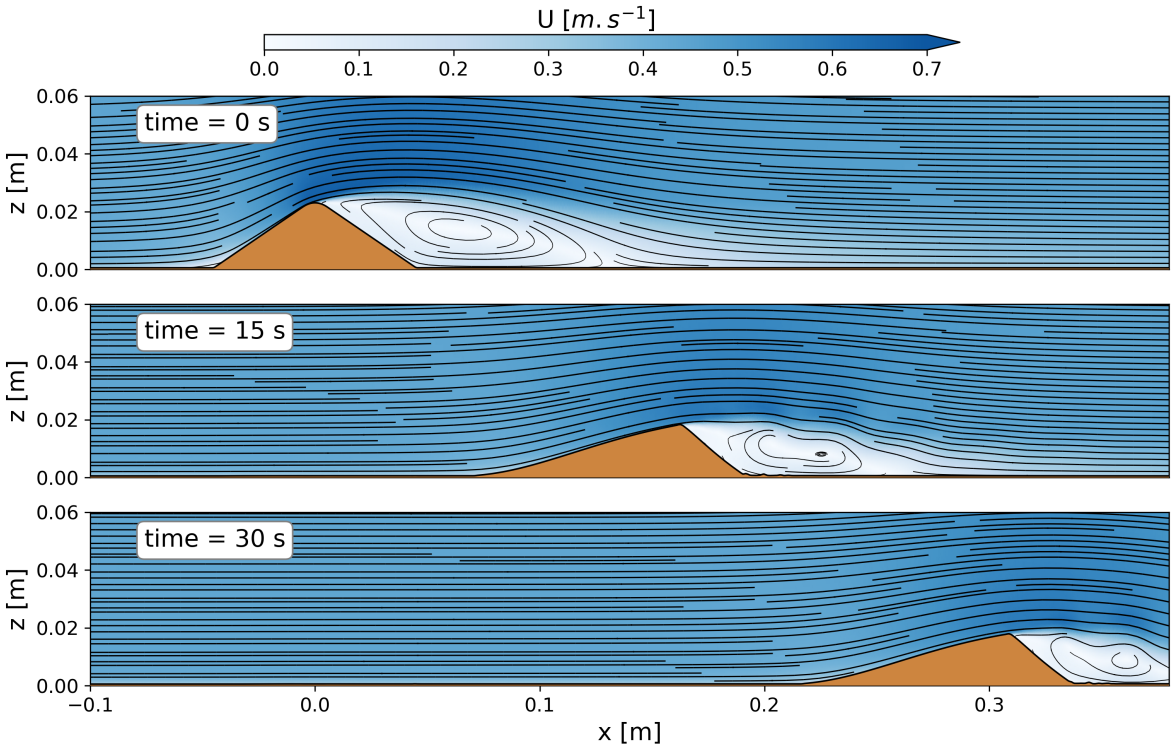

Figure 4.25: Representation of the dune and the flow streamlines at different times (0, 15 and 30 seconds) during the migration process.

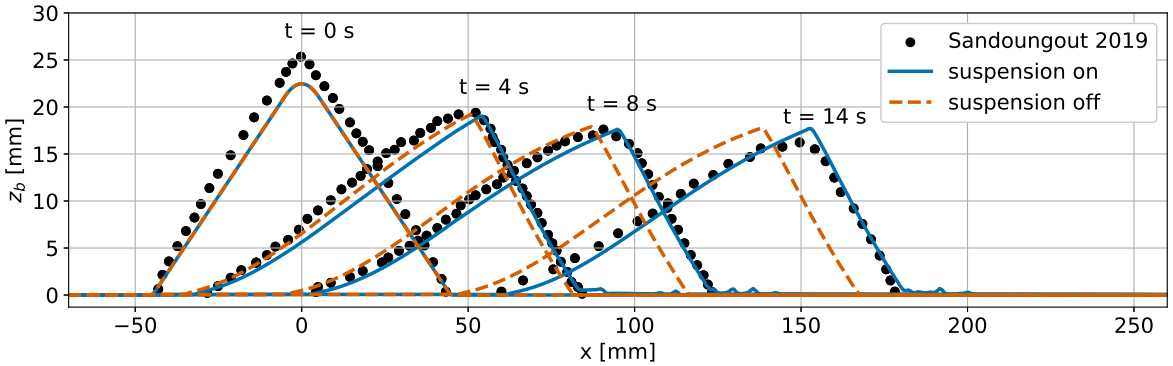

Figure 4.26: Sediment bed elevation at different times, 0, 4, 8 and 14 seconds. Comparison between results from two simulations and experimental results. The simulations use the same mesh, same parameters but for one, the suspended load is not taken into account.

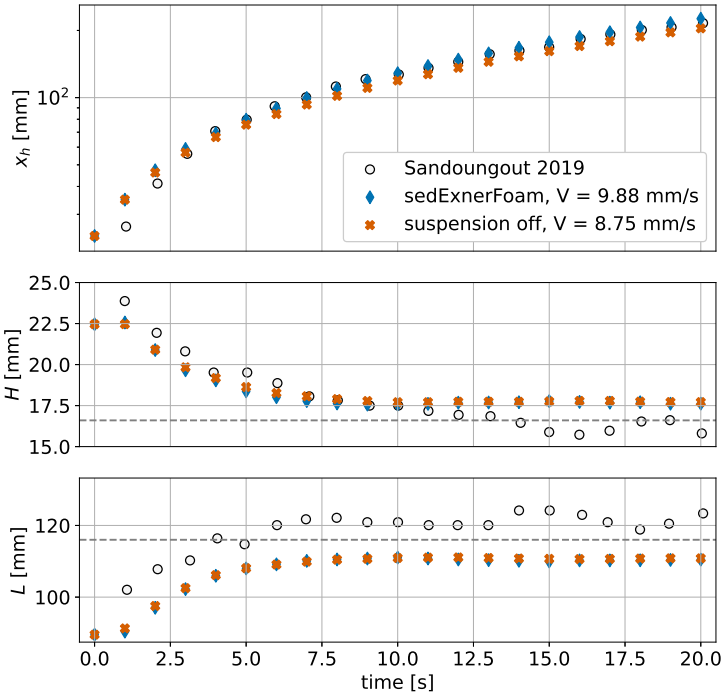

Figure 4.27: Dune morphological parameters evolution in time. From top to bottom are plotted the dune position represented by the coordinates x_h, which is located halfway up the downstream face of the dune, as well as the dune height and the dune length.

migration but the form of the dune seems unaffected showing that the shape is due to bedload transport only.

The dune morphological parameters over time which are the dune position, height and length are represented in Figure 4.27. Regarding the migration velocity only a small difference is observed, $9.88\,mm.s^{-1}$ and $8.75\,mm.s^{-1}$ for simulations with and without considering the suspended load respectively. The height of the dune is slightly overestimated. At the same time the length of the dune seems to be underestimated but it could also be a consequence of the method used to estimate the dune length (see Figure 4.2). The two stages of the dune migration are clearly observed. During the first 10 seconds, the dune shape changes rapidly, its height decreases and its length increases. At 10 seconds, the dune has already reached a stationary stage and its shape remains unchanged as it migrates at a constant velocity.This difference is better observed in Figure 4.25 which shows the bed elevation profiles at different times.

A first element that significantly affects the results is the resolution of the mesh and in particular the near bed resolution in the areas where the flow is highly non uniform. In this case study, it corresponds to the upstream slope of the dune where the flow is contracted and accelerated until the top of the dune where the flow detaches and generates a recirculation cell illustrated in Figure 4.25. As illustrated in the description of the hydrodynamics around the initial geometry, a poor near bed mesh quality leads to

an under estimate of the bed shear stress (see Figures 4.8 and 4.11) and as a consequence to a slower dune migration. With the M3 mesh used to obtain the results presented, the distance in wall unit between the cell centers making up the first layer of cells above the bed boundary and the bed boundary is kept between $z^+ = 1$ and $z^+ = 5$. Not surprisingly the numerical scheme used to discretize the advective term in the momentum equation (eq. 2.1) also affects the dune morphological response as illustrated in Figure 4.18. This is mainly because of its effect on the recirculation cell characteristics and the position of the detachment region which is located upstream of the dune crest with high order schemes but downstream with a low order *upwind* scheme. When the flow detachment appears downstream of the dune crest, the dune shape was found to take a rounder shape not matching the experimental results.

Another parameter of importance in this case is the critical Shields number θ_c^0 which is evaluated in the range $0.033 - 0.046$ by the different models presented in table 2.5 but was experimentally estimated at a higher value of 0.079. Increasing the value of θ_c^0 not only slows down the dune but also reduces its height and length in the stationary regime. An intermediate value of $\theta_c^0 = 0.05$ was found to yield good results. In addition, the critical Shields number was corrected with the local slope according to the formula from Fredsoe and Deigaard [1992] (eq. 2.21). A last key parameter is the formula chosen to calculate the bedload transport. It was found that the formulas presented in table 2.5 were all predicting dune velocity at least two times slower than the one observed experimentally. Therefore, a custom bedload formula $\phi_b = 32\theta^{1/2}\varpi(\theta - \theta_c)$ was used. It corresponds to an intensified version of the formula from Nielsen [1992] and can be considered reasonable in view of the significant scatter associated with bedload measurements [Recking, 2010]. Indeed, even if these formulations are commonly used to model sediment transport in a variety of flow conditions, they are empirical relations derived from data obtained for uniform flows in a straight channel. Therefore, they may not precisely describe sediment transport in accelerated flow regions, recirculation cells and other non uniform flows features.

4.1.6 Mass loss scenario

In the present study, the focus was made on the stationary dune migration regime characterized by a stationary shape and a constant velocity. Depending on the flow condition and the initial mass of the heap, Kiki Sandoungout [2019] observed other regimes, one of them is the mass lost scenario. The disappearance of the dune after some time is a characteristic of this regime, which is observed for small dunes with an initial mass of $m_0 < 3\,g$. In this regime, the recirculation cell downstream of the dune is nonexistent or too small to trap the suspended sediments which are washed away by the flow.

The mass loss experiment presented in Figure 4.4 is reproduced numerically. A 1D channel flow simulation with mean velocity $\overline{u} = 0.54\,m.s^{-1}$ is run and the vertical profiles imposed at the inlet of the 2D domain. The finest mesh M3 (see table 4.3) is used. First, a simulation is run without morphological evolution until the hydrodynamics reach a steady state. The steady state then serves as the initial condition for a second simulation that includes morphological evolution. For this case, a rough bed Fuhrman condition was

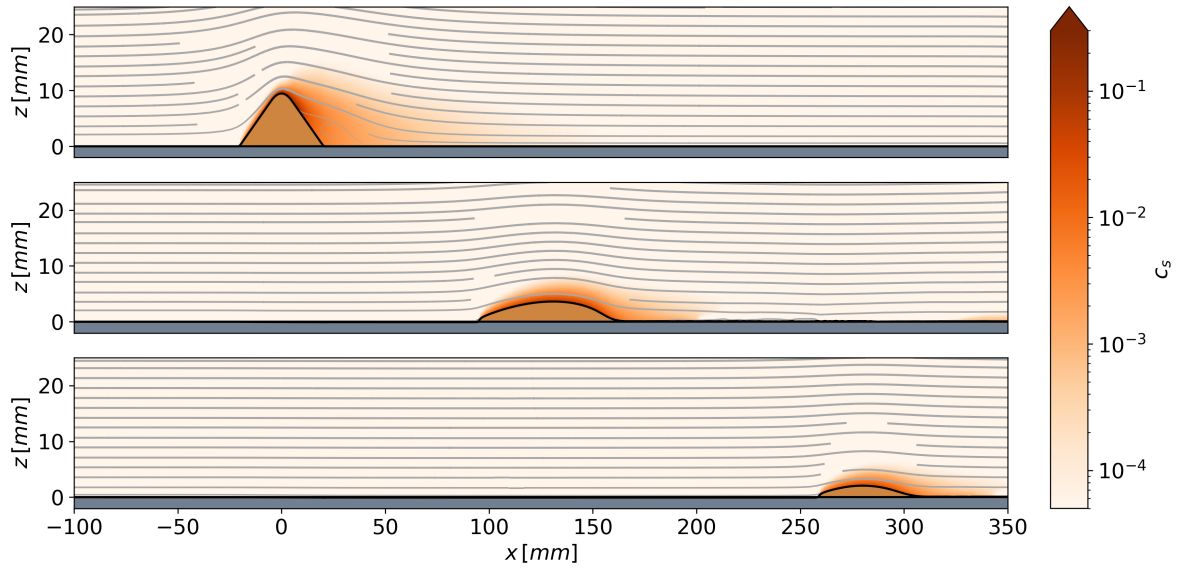

Figure 4.28: Migration of a dune in a mass loss configuration ($m_0 = 2\,g$). The dune, the flow streamlines as well as the suspended sediments volume fraction are represented for three different times, 0, 4 and 8 seconds respectively.

used with a saturation length of $1\,mm$. Using a smooth bed condition was also tested but resulted in a mass loss process slower than what was observed experimentally. The bed level, flow streamlines and suspended sediments volumes fraction at three different times (0, 4 and 8 seconds) are shown in Figure 4.28. At $t = 0\,s$, a small recirculation cell exists downstream of the dune but it is not visible anymore at latter times. During the migration, the dune takes a round shape characteristics of situation where the maximum bedload position is located downstream of the dune's crest. The suspended sediments that were initially part of the dune are seen being carried away by the flow. Over time the area occupied by the dune in Figure 4.28 gets lower as observed experimentally (see Figure 4.4). To look precisely at the mass loss rate, the dune mass is computed as follows:

$$m = c_s^{\max} \rho_s W_c \sum_f z_b|_f \delta_x \,, \tag{4.6}$$

where $z_b|_f$ is the elevation of the face f center, δx is the length of the faces, W_c the width of the channel and c_s^{max} is the volume fraction of sediments in the dune. The evolution of the dune mass over time is represented in Figure 4.29.

In the numerical simulation, two stages can be identified from the evolution of the dune's mass in time. During a first phase lasting around 3.5 seconds, the mass of the dune is conserved. This is how long it takes for the dune to change to a round shape preventing flow detachment and the formation of a recirculation cell that traps sediments. The mass loss happens only in a second phase, during which the mass of the dune decreases at a constant rate of $0.28\,g.s^{-1}$. At the end of the simulation ($t = 10\,s$), the dune has totally

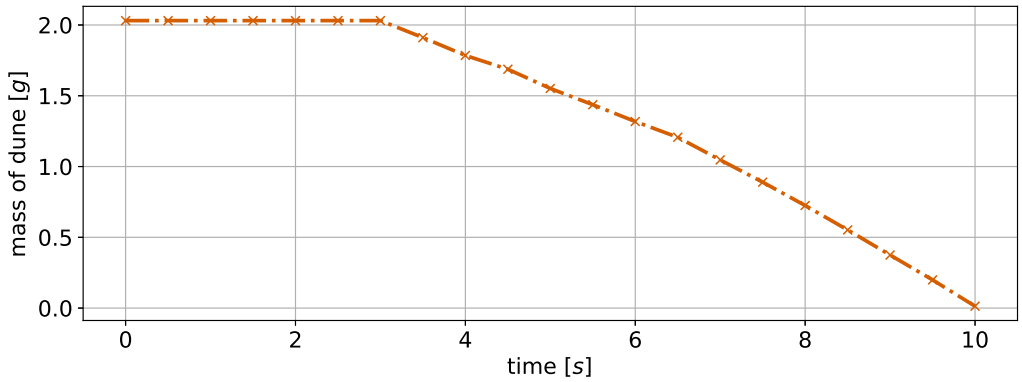

Figure 4.29: Mass of the dune as a function of time in a mass loss scenario ($m_0 = 2\,g$).

disappeared.

The results presented in this section have demonstrated the capability of *sedExnerFOAM* to simulate the migration of a lone dune over a starved bed. The many simulations and tests that have been performed have illustrated the sensitivity of the model results to the grid resolution and to the bottom boundary conditions as well as to the suspended load and bedload flux saturation. In order to demonstrate the 3D capabilities of the model, the formation and migration of a 3D Barchan dune is prensted in the next section.

4.2 Formation and migration of a subaqueous barchan

When the flow is not confined in a thin channel as in the previous dune migration study, various forms can emerge depending on the sediments and flow characteristics. In their work, Du Pont et al. [2024] created a comprehensive classification system for the various types of dunes found in nature, organized by morphology. One of them and maybe the simplest is the barchan dune (see Figure 4.30). It is a crescentic dune characterized by two horns pointing downstream. The back of the dune is exposed to the wind which erodes the sand and then deposit on the brink sliding down on the lee side through an avalanche process [Andreotti et al., 2002a]. Barchans are found in various deserts around the world but their distribution, detailed in the work of Goudie [2020], is uneven. For example, they are rarely observed in Australia, even though deserts occupy most of the country.

The specific conditions required for the morphogenesis of barchans are the reason for this uneven distribution. The wind must be dominant in one direction because barchans form oriented dunes. The different location where barchans have been observed have an index of directional variability of the wind between 0.7 and 0.97 [Goudie, 2020]. Another important parameter is the sand availability, which, when low, facilitates their appearance. Observing barchans is accessible to anyone with an access to internet. In Figure 4.31

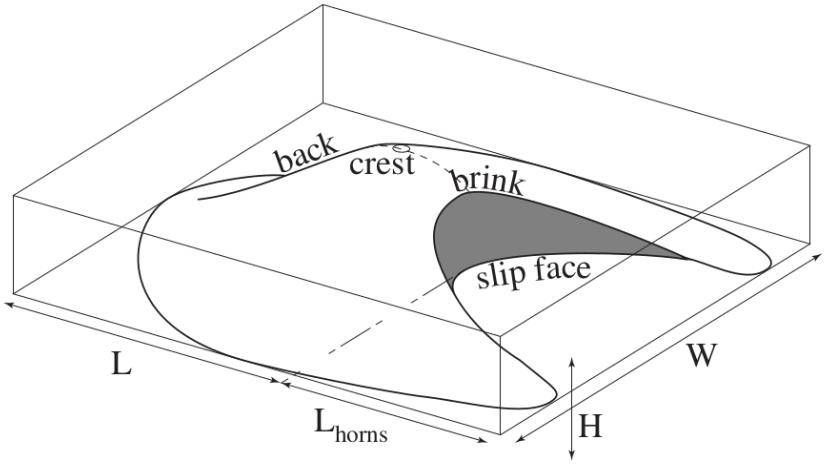

Figure 4.30: Sketch of a barchan dune taken from Andreotti et al. [2002a].

is shown a compilation of barchans found at 4 different sites using google earth satellite images. They are for instance easy to observe in the Namid desert, which spans both South Africa and Namibia [Bourke and Goudie, 2009] or in the Gobi desert [Dong et al., 2013]. Barchans were also observed on Mars surface [Bourke, 2010] or on Titan [Radebaugh et al., 2010], the second largest moon of Jupiter after Ganymede. While most field studies have historically focused on aeolian barchans, the advent of sonar technology has opened the door to the study of submarine barchans [Wynn et al., 2002]. Like their subaerial counterpart, a condition to their existence is flow persistent in a specific direction. For that reason, they are observed in specific sites as in the study of Todd [2005] where barchans are observed in an area where a persistent flow of mean velocity $10\,cm.s^{-1}$ associated with a permanent anticyclonic gyre. Their area of study is located in the Scotian Shelf south of Nova Scotia (south-east of Canada).

In their work, Alvarez and Franklin [2017] investigated experimentally the formation of a barchan from an initial conic heap on a rigid bottom under water.

4.2.1 Experimental setup

The experimental setup of Alvarez and Franklin [2017] consists in a channel with rectangular cross section working in closed circuit and covered at its top by a rigid lid. The channel has a width of $160\,mm$ and is filled with water up to the rigid lid located at $H = 50\,mm$ away from the bottom. The channel is 5 meters long and the initial heap was placed 3 meters downstream of the inlet which corresponds to 40 hydraulic diameter ensuring the full development of the flow by the time it reaches the dune. A flow straightener was placed at the inlet to homogenize the flow.

Alvarez and Franklin studied 13 different configurations in total. The experiments were conducted with 3 different set of particles, glass beads of density $\rho_s = 2500\,kg.m^{-3}$ and mean diameter $d = 0.5\,mm$ and $0.25\,mm$ respectively, and zirconium particles of

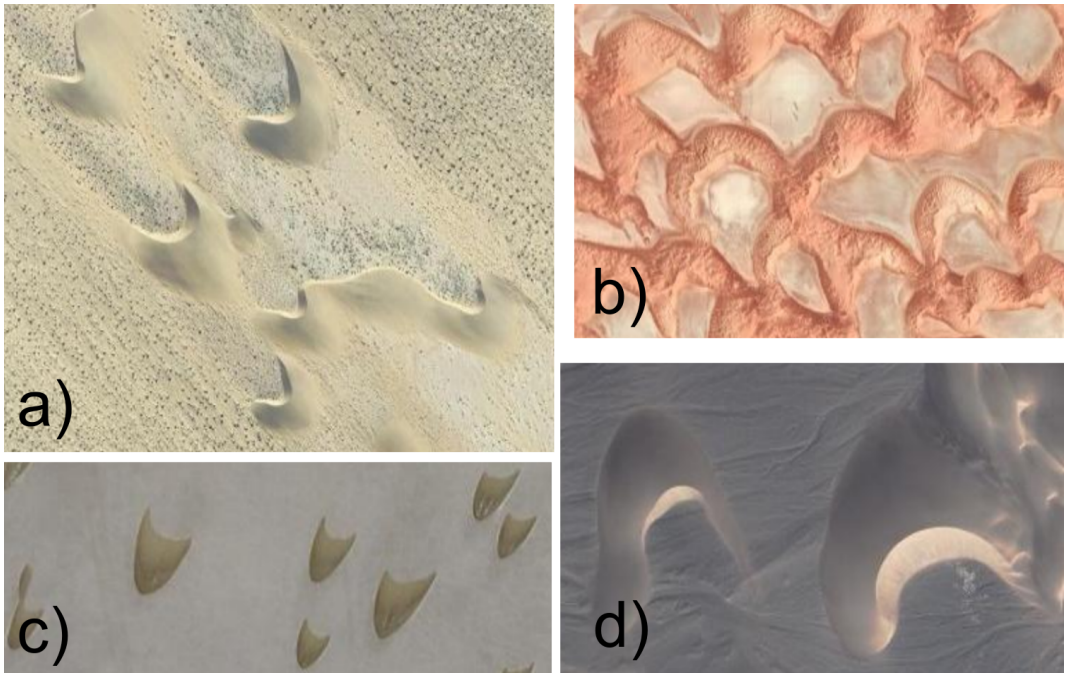

Figure 4.31: Satellite view of barchans found in Google earth. a) Namid desert, South Africa, Namibia; b) barchanoid ridge in the Arabian Desert, Saudi Arabia; c) Moçâmedes desert, Angola d) Dasht-e Lut, Iran.

density $\rho_s = 4100\,kg.m^{-3}$ and mean diameter $d = 0.5\,mm$. The cross-section velocity $\overline{u}$ was varied between three different values of $\overline{u} = 0.234\,m.s^{-1}$, $\overline{u} = 0.293\,m.s^{-1}$ and $\overline{u} = 0.333\,m.s^{-1}$ corresponding to Reynolds numbers $R_e = \overline{u}H/\nu$ of $1.16\,10^4$, $1.47\,10^4$ and $1.67\,10^4$ respectively. For the glass beads experiments, the initial heap mass was $10.5\,g$ and for the zirconium experiments two different initial mass of $16.5\,g$ and $10.5\,g$ were used. For three of those experiments, with glass beads and two with zirconium particles, top views of the dune at different times during the migration is shown in Figure 4.32. These images show the progressive formation of the horns and the difference of behaviors obtained depending on the particles used and the Reynolds number. Because the flow conditions are similar, the time it takes for the horns to develop is larger for zirconium particles which are denser as the Shields number is lower.

4.2.2 Numerical configuration

Because it takes a shorter time for the barchan only the first experiment of Alvarez and Franklin [2017] is reproduced numerically. The computational domain consists of a cuboid hexahedral mesh made up of $220 \times 160 \times 32$ cells. The cells are uniform in the horizontal directions but ten times smaller in the vertical near the bottom and top boundaries than in the middle of the channel. The mesh is then distorted so that the bottom boundary matches the initial heap. A representation of the computational domain is shown in Figure 4.33.

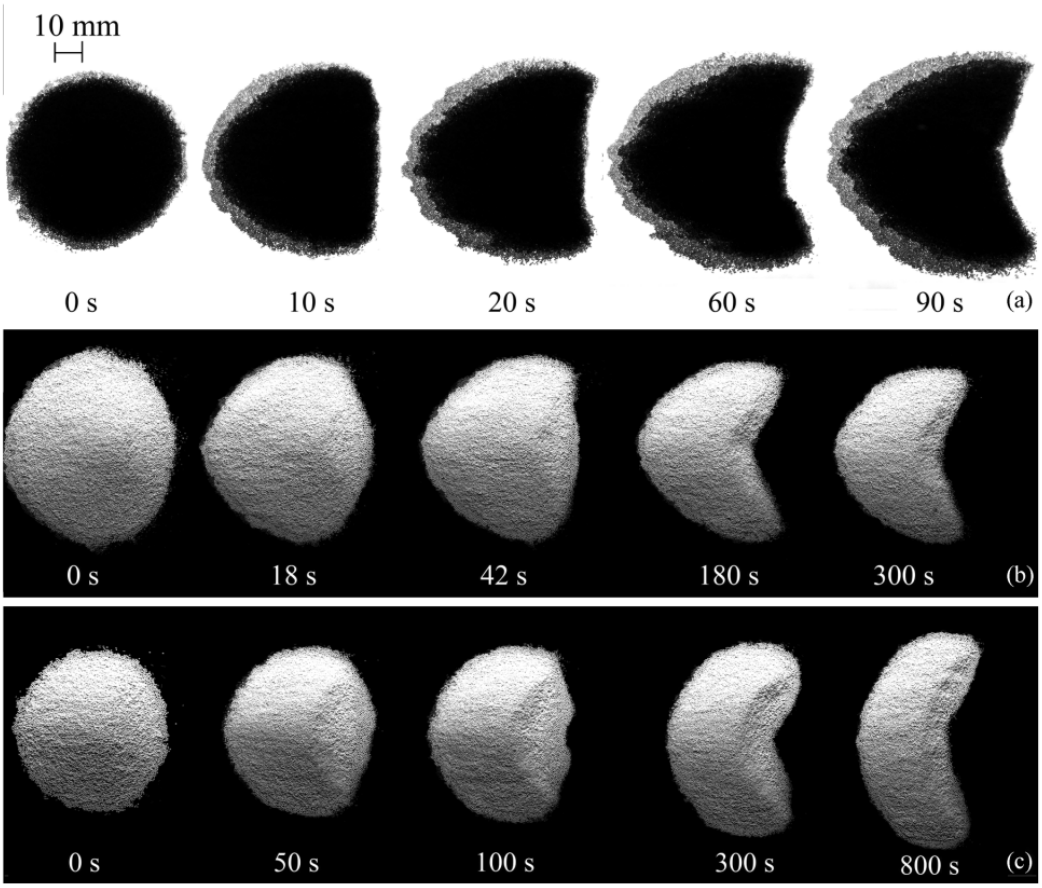

Figure 4.32: Top views of initially conical heaps migrating under the influence of a steady flow. From top to bottom are represented one experiment with glass beads ($\rho_s = 2500\,kg.m^{-3}$) and two with zirconium particles ($\rho_s = 4100\,kg.m^{-3}$). The corresponding Reynolds number are $1.47\,10^4$, $1.67\,10^4$ and $1.47\,10^4$ respectively.

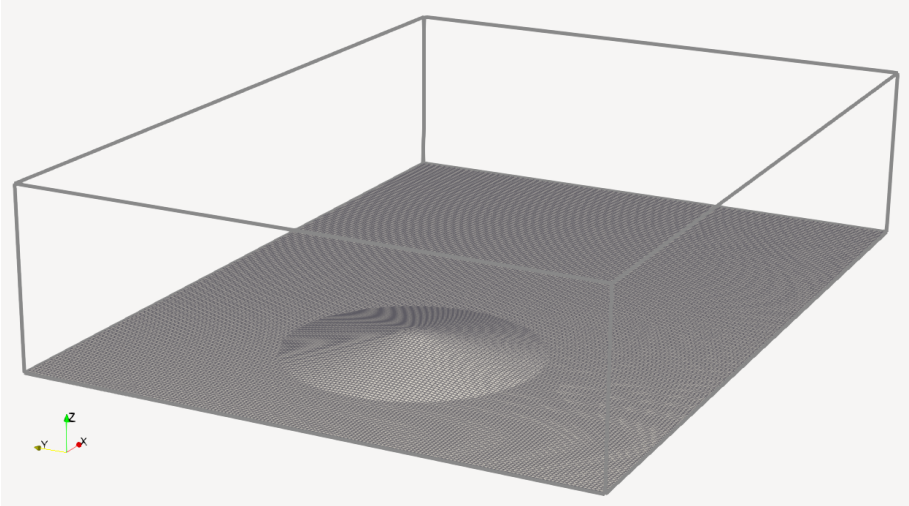

Figure 4.33: Representation of the computational domain with the initial heap geometry. The faces of the cell forming the first layer above the bed are shown and the thick gray lines delimits the domain.

At the top and bottom boundaries as well as the lateral sides, a smooth wall treatment is applied. As in the study of a dune migrating in a thin channel previously presented, there is at the moment no possibility to take into account wall roughness in only the area of the bottom boundary where the dune is present. Because of that a choice as to be made, either to use a rough bed condition even in the part of the channel free of particles or neglect the roughness of the dune. It was chosen to neglect the effect of roughness and use a smooth bed condition. The bedload flux is computed using the formula from Meyer-Peter and Müller [1948]. A zero gradient condition is applied at the outlet for the fluid velocity and the turbulent quantities k and ω. The dynamic pressure is set to 0 at the outlet. In order for the flow to be fully developed when it reaches the dune, a one-dimensional simulation of steady-state channel flow without the dune was performed. The 1D mesh consists in a column of 120 cells 20 times more refined at the top and bottom boundaries than in the middle of the domain. The flow is forced with a uniform volume force accelerating the fluid to a selected mean velocity $\overline{u} = 0.294\, m.s^{-1}$. The resulting velocity, k, and ω profiles are shown in Figure 4.34. They are imposed at the inlet of the 3D domain as a Dirichlet condition and zero gradient condition is used for the pressure. Two simulation were run, one with only bedload transport being taken into account and the other one with both bedload and suspended load.

4.2.3 Results and discussion

The bed elevation z_b at different times if shown in Figure 4.35. Symmetric horns growing at each side of the dune are observed leading to the expected crescentic shape of the dune. Qualitatively, the barchan formation from an initial conic heap is similar to the first experiment presented in Figure 4.32 but some differences are observed. Contrary to

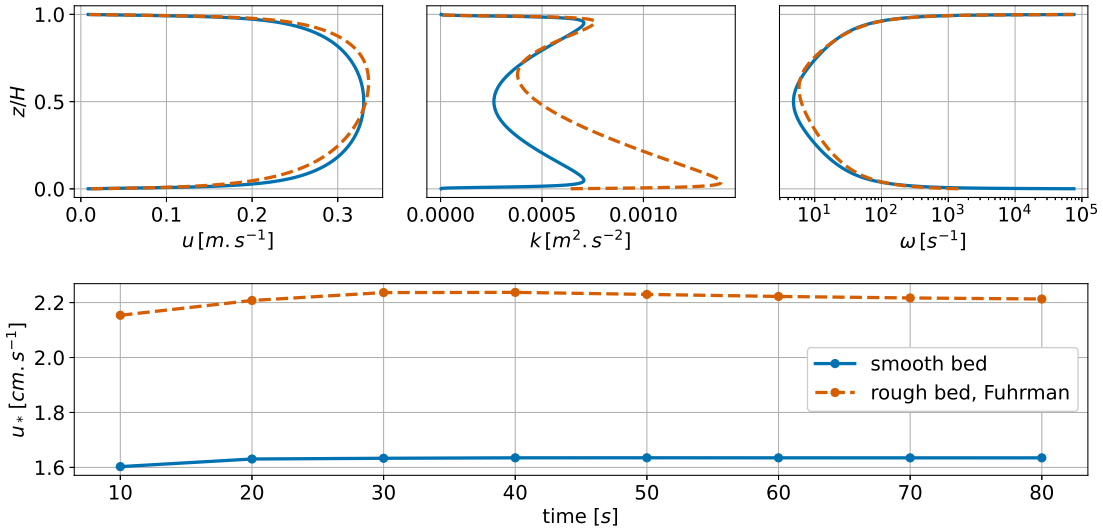

Figure 4.34: On the top from left to right, vertical profiles of stream wise velocity component, specific turbulent kinetic energy and specific dissipation of turbulent kinetic energy. On the bottom, temporal evolution of the friction velocity on the bottom boundary. The results obtained with a rough bottom boundary condition are also plotted for comparison.

the experiment, the width of the barchan increases over time, and the slip face takes on a smooth, circular shape after 90 seconds of migration, whereas it appears angular in the experiment. This is probably due to the fact that no saturation was taken into account. The equation 1.54 for saturation effect being a 1D equation, it is not possible to apply it to this 3D problem. An attempt to implement was made (see eq. 2.24) but its application to 3D problems does not yield good results. This makes the stable implementation of saturation for multidimensional case one of the issues to address in the future.

4.3 Conclusion

The highlight of this chapter was dune migration. A lone dune migrating in a thin channel was studied extensively and used to identify important model parameters that could reproduce the observed morphological evolution. The stationary regime, which corresponds to an unchanged shape and constant migration velocity, was examined in detail. Using the saturated bedload flux, which neglects the inertia of particles transported as bedload, was found to lead to unexpected behavior in cases of flow detachment occurring upstream of the dune's crest. In such situations, sediments accumulate at the top of the dune, causing the upstream slope to steepen until an avalanche is triggered, canceling out the bedload flux driven by shear stress. To address this issue, saturation of the bedload flux was implemented in the model. This concept is widely used in aeolian contexts but generally neglected in subaqueous studies. The saturation length was found to be a crucial parameter that controls both the migration velocity and the shape of the dune

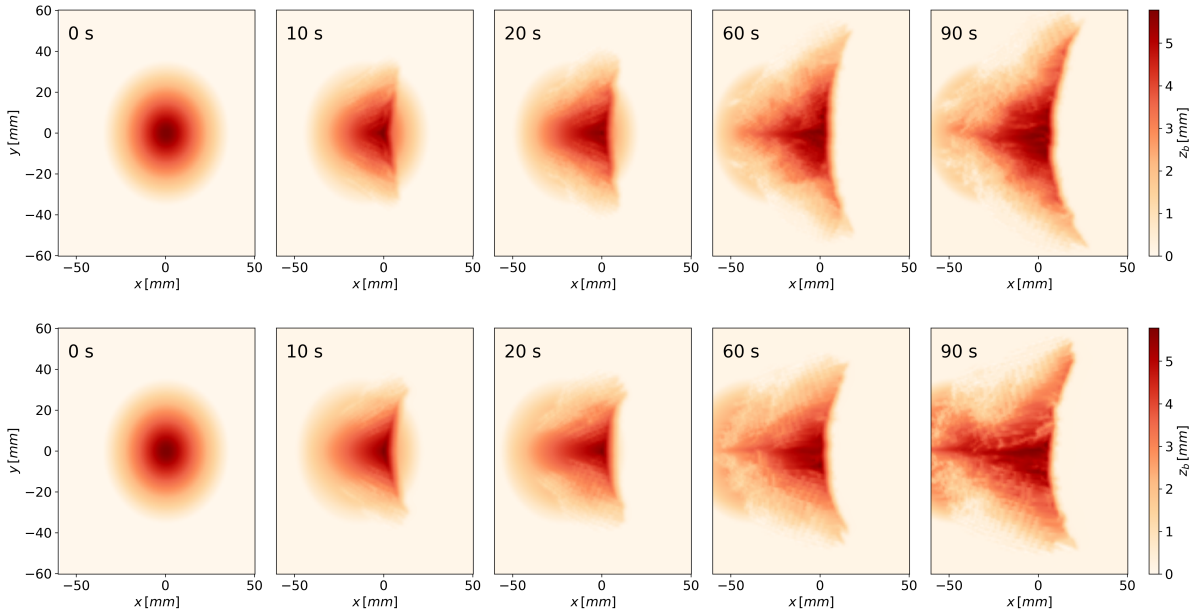

Figure 4.35: Bed level elevation at different times showing the development of a barchan from an initial conic heap. On top are results obtained taking into account bedload transport and only and at the results presented at the bottom were obtained with both bedload and suspended laod transport. The x-coordinate is taken relative to the position of maximum bed elevation.

but also acts as a filter for the bedload. In the presence of flow detachment, the shear stress drops and the saturated bedload flux vanishes. With saturation effect taken into account, the bedload does not react instantaneously to the sudden change of shear stress and allows sediments to be transported downstream of the dune on the slip face where they are caught in the avalanche process.

Another migration regime called the mass loss regime was also reproduced numerically. In this regime observed only for small dunes, there is no flow detachment and thus no recirculation trapping the suspended sediments. As it migrates, the dune is eroded by the flow and progressively looses mass until it totally disappears. The fact that the model can capture this two migration regimes with the same set of parameters gives credit to the model fomulation and implementation.

To conclude the chapter, an application of the model to a 3D barchan formation and migration case was presented. Qualitatively, the model is able to reproduce the formation and growing of the horns which give the barchan its crescentic shape. However, the lack of a functional 3D saturation model alters the migration and the dune tends to spread in the lateral direction.

Chapter 5

Scour around a cylinder

In the previous chapter, a comprehensive numerical investigation of dune migration under steady flow conditions was presented. The formation and movement of bedforms are fundamental processes encountered in nearly all scenarios involving morphological evolution. In the context of scour, the presence of an obstacle within the natural flow path of a river disrupts the flow, generating turbulent structures and localized flow acceleration. This leads to increased bed shear stress, which in turn causes the erosion of granular material and the development of a scour hole. The eroded sediments are transported downstream, forming migrating dunes. This chapter focuses on the three-dimensional scour that develops around a cylindrical pile subjected to steady flow. As a preliminary step, sediment transport is excluded in order to evaluate the solver's ability to reproduce the coherent flow structures characteristic of such configurations. To this end, two experimental setups involving flow around a wall-mounted cylinder are simulated numerically. These setups differ in the nature of the rigid bottom boundary—smooth in one case and rough in the other. Following the validation of hydrodynamic results against experimental data, and an analysis of the influence of mesh resolution and bed roughness, the study proceeds to assess the model's capability to simulate scour. This case study highlights the model's potential for addressing scour-related problems, while also identifying the key technical challenges that must be addressed to enable its application to real-world engineering scenarios.

5.1 Description of the experimental and numerical configurations

Since the primary objective of this thesis is the numerical investigation of scour around hydraulic structures, it is appropriate to apply the developed model to a case study related to scour. This section presents the classical problem of scour around a cylindrical pile—a well-established benchmark in morphological evolution studies [Liu and García, 2008, Baykal et al., 2015, Nagel et al., 2020] which has also been extensively examined through experimental approaches [Breusers et al., 1977, Chiew and Melville, 1987]. Despite this extensive body of work, few studies provide comprehensive datasets encompassing both

parameters	smooth bed	rough bed
Mean velocity $\overline{u}\,(cm.s^{-1})$	32.6	32.6
Cylinder diameter $D_{\text{cyl}}\,(cm)$	53.6	53.6
Water depth $H\,(cm)$	54	54
Reynolds number $Re_D = \overline{u}D_{\text{cyl}}/\nu$	$1.7\,10^5$	$1.7\,10^5$
Froude number $F_r = \overline{u}/\sqrt{gH}$	0.14	0.14
Friction velocity $u_*\,(cm.s^{-1})$	1.3 - 1.5	2.3
Nikuradse equivalent roughness length $k_s\,(mm)$	-	10

Table 5.1: Experimental conditions for the rigid bed experiments.

the scour process and the associated hydrodynamics. For this reason, the experiment conducted by Roulund et al. [2005] is selected for comparison. In addition to a scour experiment, the authors carried out two rigid-bed experiments and provided detailed measurements of mean flow velocity and bed shear stress. This allows for the validation of the hydrodynamic model independently from sediment transport processes—one of the original goals of their study, which also included a numerical component. The only distinction between the two rigid-bed configurations lies in the nature of the flume's bottom surface: one is smooth, while the other is rough. This section provides detailed descriptions of rigid-bed experiments and the scour experiment, alongside thorough explanations of the numerical setups used to replicate each scenario.

5.1.1 Rigid bed experiments

The rigid-bed experiments were made using a cylinder of diameter $D_{\text{cyl}} = 53.6\,cm$. These experiments have been performed in two different flumes. A first one was conducted in a flume of length $35\,m$ and of width $3\,m$. The bottom surface of the flume was smooth and henceforth this experiment is referred to as smooth bed case. For the second experiment referred as rough bed case, the flume used was $28\,m$ long and $4\,m$ wide and contrarily to the former experiments, the bottom surface was made rough by adding a single layer of crushed stones. The resulting equivalent roughness height of the rigid-bed is $k_s = 10\,mm$. For both experiments, the mean flow velocity in the channel was $\overline{u} = 0.326\,m.s^{-1}$ and the water height was $54\,cm$ which is approximately equal to the cylinder diameter. The conditions for these experiments are summarized in Table 5.1.

In their numerical simulations, Roulund et al. [2005] neglected the free surface, arguing that its influence on the hydrodynamics would be of secondary importance due to the relatively low Froude number. The Froude number, defined as the ratio of flow inertia to gravitational forces, is given by:

$$F_r = \frac{\overline{u}}{\sqrt{gH}}\,. \tag{5.1}$$

where $\overline{u}$ is the bulk flow velocity. A low Froude number (typically $F_r < 0.3$) indicates subcritical flow, where gravitational effects dominate over inertial forces, justifying the assumption of a rigid lid or neglect of free surface deformation in the simulations. The

presence of the cylinder causes the water level to increase upstream as the flow approaches it, reaching a maximum value at the point of contact. On the side edges of the cylinder, the flow accelerates and the water level decreases to a minimum. The presence of the cylinder induces a local increase in the water surface elevation upstream, with the maximum occurring at the front stagnation point where the flow directly impinges on the cylinder. Along the sides, the flow accelerates around the obstacle, leading to a corresponding decrease in water level, reaching a local minimum. In both rigid-bed experiments, the Froude number was $F_r = 0.14$, indicating subcritical flow conditions. For the configurations investigated, Roulund et al. [2005] observed that the variations in water surface elevation were less than 2% of the mean water depth and concluded that these variations have a negligible influence on the overall flow field.

Two types of measurements were conducted: velocity and shear stress. These were obtained using a two-component Laser Doppler Anemometer (LDA) and a single-component hot-film probe. Measurements were taken in the symmetry plane of the flow, both upstream and downstream of the cylinder. Experimental data on the mean velocity field were collected along horizontal lines at various distances from the bed. For the smooth bed case, velocity measurements were taken at heights of 0.5, 1, 2, 5, 10, and 20 centimeters above the bed. In the rough bed case, measurements were recorded at 0.3, 1.3, 2.3, 4.3, 9.3, 19.3, 29.3, 39.3, and 49.3 centimeters. These vertical profiles allow for a detailed characterization of the flow structure and bed-induced effects under different roughness conditions.

5.1.2 Numerical setup, rigid bed simulations

As depicted in Figure 5.1, the computational domain consists in a cuboid with a cylindrical hole. It has a length of $12\,D_{\text{cyl}}$ and a width $8\,D_{\text{cyl}}$. The center of the cylinder is placed at the origin of the coordinates system $4\,D_{\text{cyl}}$ downstream of the inlet and $8\,D_{\text{cyl}}$ upstream of the outlet. The height of the domain is equal to $1\,D_{\text{cyl}}$

The $k-\omega\,SST$ turbulence model is used for all simulations. Regarding the boundary conditions no free surface is considered, instead a rigid lid is applied at the top boundary represented by a no-slip condition for the velocity field and a zero gradient condition for k, ω and p. A smooth wall treatment is applied at the cylinder boundary and for the bed either a smooth or a rough condition is used depending on the case considered. For the rough case, a Fuhrman condition is used (see table 2.4). The flow at the inlet is supposed fully developed. A zero gradient is used for the pressure field. As in almost all the simulations presented in this work, a 1D channel flow simulation is run to obtain the profiles of $\boldsymbol{u}$, k and ω. These profiles are imposed at the inlet of the 3D domain as Dirichlet conditions. At the outlet, a zero gradient condition is used for all fields except the dynamic pressure which is set to 0.

In Figure 5.2 are presented the vertical profiles of $\boldsymbol{u}$ and k for the smooth and rough bed cases. For comparison, results from simulations using the different rough wall conditions available in *sedExnerFoam* are shown. Black dots represent experimental measurements from Roulund et al. [2005] and the dashed line a log law fitted on the data. The

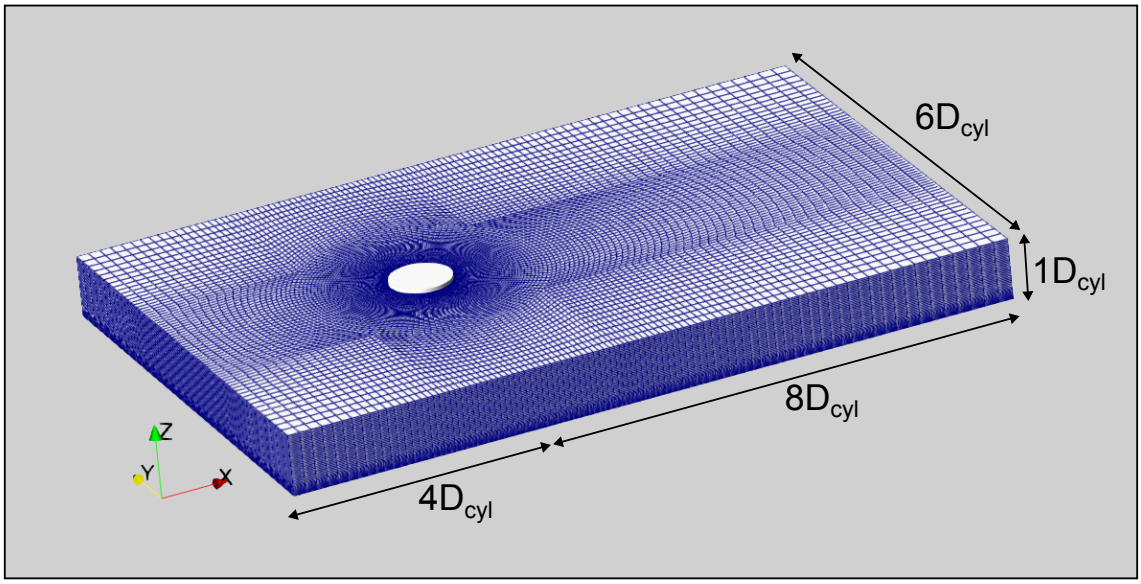

Figure 5.1: Computational domain for rigid bed cases

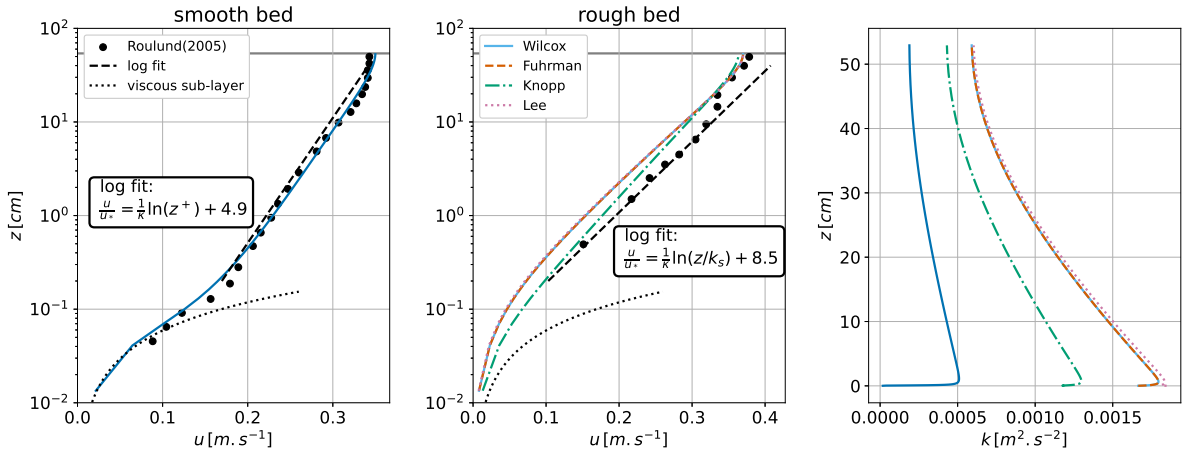

Figure 5.2: From left to right: velocity profile for a smooth bed, velocity profile for a rough bed for different boundary conditions, specific turbulent kinetic energy profiles. The dots are experimental measurements from Roulund et al. [2005]. The black dashed lines are log fits on the experimental data for smooth and rough cases. The black dotted line represents the viscous sub-layer corresponding to the equation $u/u_* = z^+$.

mesh	number of cells	$r_1\,[mm]$	$z_1\,[mm]$
M0	307 580	1	2
M1	780 900	0.5	0.8
M2	1 743 000	0.2	0.5

Table 5.2: Characteristics of the different meshes used for the study of the hydrodynamics around a cylinder. r_1 and z_1 are the distance of the closest cell centers to the wall boundary for the cylinder and the bed boundaries respectively.

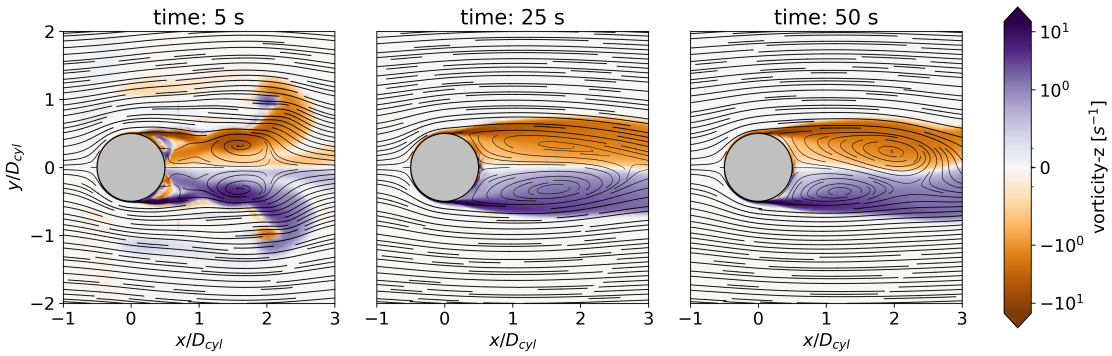

Figure 5.3: Representation of the flow streamlines around a cylinder computed at different times. The simulation is a rough bed case using the finest mesh M3.

black dotted line represents the theoretical velocity in the viscous sub-layer corresponding to the equation $u/u_* = z^+$. In the rough case, the flow is fully rough ($k_s^+ = 250$) meaning the velocity profiles do not match the viscous sublayer equation. It can also be seen that the results obtained with Wilcox, Fuhrman and Lee rough conditions almost perfectly align when the Knopp boundary condition yields lower flow velocity in the lower part of the domain and less turbulent kinetic energy in the water column. Unlike in the smooth bed case, where the velocity profile corresponds perfectly to the experimental data, the velocities in the rough case are slightly below those observed in the lower half of the water column.

The cylinder diameter and the water height being identical for both experimental cases, the same mesh can be used for smooth and rough bottom surfaces. The characteristics of the three different meshes used throughout this study are summarized in table 5.2. The meshes are noted M0, M1, and M2, from the coarser to the finer one.

At the start of the simulation, the flow is at rest and is suddenly set in motion by the inlet condition. The formation of the vortex shedding process takes some time, starting with the development of two symmetrical vortices attached to the cylinder. The formation of the Kármán vortex street is initiated by the oscillation and detachment of this pair of vortices (see Figure 5.3).

As the experimental data are mean velocity measurements, the simulation must be long enough to achieve statistically convergent flow. Each simulation is run for 200 sec-

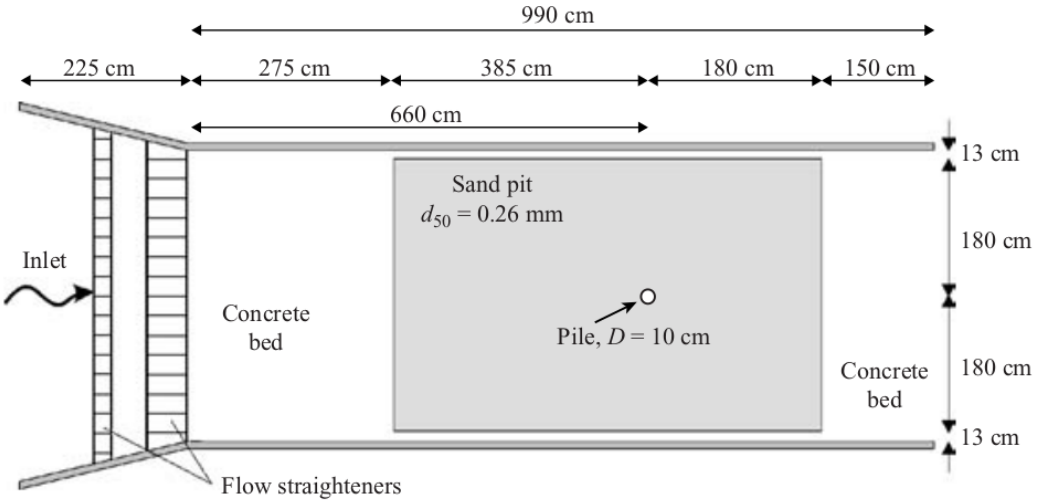

Figure 5.4: Representation of the experimental setup for the scour experiment. Image from Roulund et al. [2005].

onds, and the averaged fields are computed using results from 100 to 200 seconds, which corresponds to approximately 60 bulk time ($D_{cyl}/\overline{u}$), and compared with experimental data from Roulund et al. [2005]. Three simulations are run for each case, smooth and rough bed, corresponding to the three meshes summarized in Table 5.2.

Live-bed experiment

In the scour experiment or live-bed case, the cylinder has a smaller diameter $D_{\text{cyl}} = 10\,cm$ and the mean flow velocity in the channel is higher $\overline{u} = 0.46\,m.s^{-1}$. This corresponds to a pile Reynolds number of $Re_D = 4.6\,10^5$. Just as in the rigid bed cases, the cylinder surface is hydraulically smooth. The experimental setup is represented in Figure 5.4. The channel is 3.86 meters large. The sand pit begins 2.76 meters downstream of the inlet and is 5.65 meters long. The cylinder is placed in the sand pit, 5.6 meters downstream of the inlet, and extends to the pit's bottom. The sand particles had a mean diameter of $d_{50} = 0.26\,mm$ and a geometric standard deviation of $d_{85}/d_{50} = 1.5$. Here, d_{85} and d_{50} correspond to grain sizes for which 85% and 50%, respectively, are finer. The conditions for the scour experiment are summarized in table 5.3.

The presence of ripples even outside the area of influence of the cylinder reveals that the experiment was conducted in the live-bed regime. The observed ripples were $3-4\,cm$ high with a wavelength of $10-15\,cm$ and thus they considerably affect the roughness of the bed surface. Estimating the ripple equivalent roughness length to $k_s = 15\,cm$, the friction velocity outside the area of influence of the cylinder was estimated from a log fit for fully rough flow (eq. 1.24) to $u_* = 4.8\,cm.s^{-1}$. Using the decomposition introduced by Engelund [1966], the part of the shear stress due to skin friction only was estimated to $u'_* = 2.8\,cm.s^{-1}$. Leaving the ripples aside, the roughness Reynolds number can be estimated as $k_s^+ = k'_s u'_*/\nu$ and has a value of 18.2 which corresponds to transitional value

parameters	live bed
Mean velocity $\overline{u}\,(cm.s^{-1})$	46
Cylinder diameter $D_{\text{cyl}}\,(cm)$	10
Water depth $H\,(cm)$	40
Particles diameter $d_{50}\,(mm)$	0.26
Reynolds number $Re_D = \overline{u}D_{\text{cyl}}/\nu$	$4.6\,10^4$
Froude number $F_r = \overline{u}\sqrt{gH}$	0.23
Friction velocity $u_*\,(cm.s^{-1})$	4.8
Friction velocity due to skin friction $u'_*\,(cm.s^{-1})$	2.8
Shields number θ	0.55
Shields number due to skin friction θ	0.19
Nikuradse equivalent roughness length (ripples) $k_s\,(mm)$	150
Nikuradse equivalent roughness length (grain) $k'_s\,(mm)$	0.65
Roughness Reynolds number (ripples)	7200
Roughness Reynolds number (grain)	18.2

Table 5.3: Experimental conditions for the live-bed experiment.

between smooth and rough flows. On the other hand, the roughness Reynolds number taking into account the presence of ripples is $k_s^+ = k_s u_*/\nu$ and yields $k_s^+ = 7200$ which corresponds to a really high roughness value.

5.1.3 Numerical setup, live-bed simulations

Just as for the rigid bed cases, the computational domain consists in a cuboid with a cylindrical hole and the same boundary conditions are applied. An example of a mesh is illustrated in Figure 5.5. The cylinder was placed at the center of the domain which is $12\,D_{\text{cyl}}$, $6\,D_{\text{cyl}}$ wide and $4\,D_{\text{cyl}}$ high. The velocity measurements were taken at the end of the experiment, once sufficient time had passed for the ripples to develop. Two 1D simulations of flow in a channel with and without taking into account the roughness due to the presence of ripples were run and the results are presented in Figure 5.6. In the case where the roughness due to the ripples is considered ($k_s = 150\,mm$), a good match with the experimental velocity profile is obtained. On the other hand, if only the sand roughness is taken into account ($k_s = 0.65\,mm$), the situation is that of a transitionally rough flow regime and the resulting vertical profiles of velocity, k and ω are totally different. The velocity is higher near the bed because the flow is not hindered by the presence of ripples, and there is less turbulent kinetic energy in the water column. Still it was chosen to impose the results of the simulation using sand grain roughness only as an inlet simulation for the 3D scour simulation. The reason for that is that the sediment bed is initially flat and the ripples take some time to form and grow.

As with rigid bed cases, the flow is initially still, but the inlet condition suddenly puts the fluid into motion at the start of the simulation. During the first few iterations, the fluid's rapid acceleration creates significant shear stress on the bed, triggering numerical

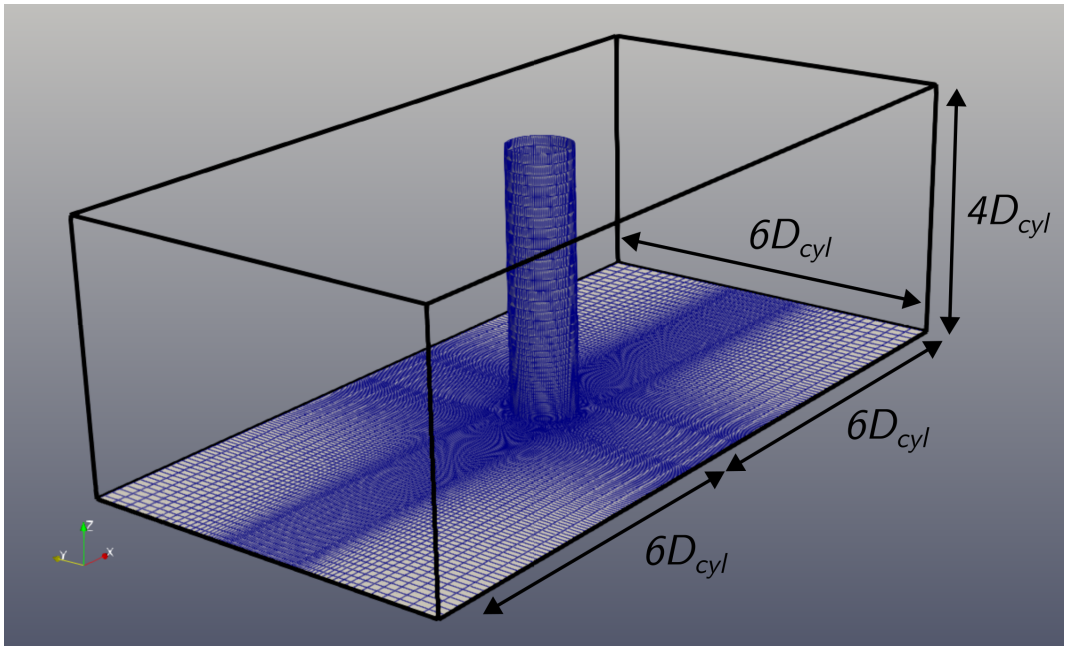

Figure 5.5: Representation of the computational mesh used for live bed simulations.

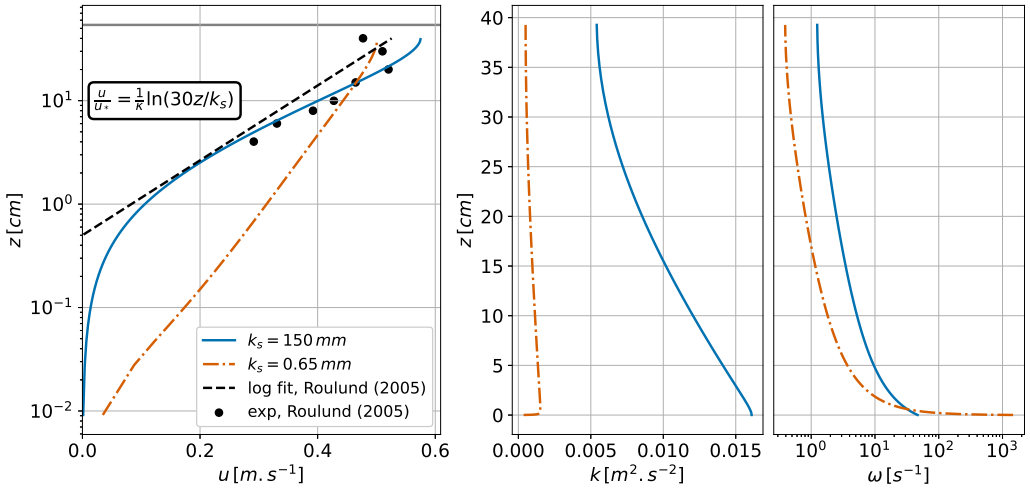

Figure 5.6: From left to right: velocity profiles for obtained with two bed roughness values, $k_s = 150\,mm$ and $k_s = 0.65\,mm$, turbulent kinetic energy profiles k and specific turbulent kinetic energy dissipation ω. The black dots and the black dashed line are the experimental measurements from Roulund et al. [2005] and the associated log fit respectively.

instabilities associated with the bed mobility and the mesh deformation, that cause the simulations to fail. To avoid this problem, the 3D simulations are initially run for 25 seconds without sediment transport. This time is sufficient to reach a statistically converged state. Then, the suspension and bedload are activated and the scour process begins.

5.2 Simulation of the flow around a wall mounted cylinder

This section focuses on the flow around a vertical cylinder mounter on a plane surface. The aim is to validate the ability of the hydrodynamics solver separately from the morphological response and assess through comparison with experimental results of flow velocity measurements and bed shear stress. The effect of bed roughness and mesh resolution is also investigated.

Turbulent structures of the flow

The numerical results are first presented through a qualitative description of the flow, with particular attention given to the identification of coherent structures that develop around the cylinder. These structures are visualized using iso-volumes of the Q-criterion (see Figure 5.7), which is a widely used method for detecting vortices in turbulent flows. The Q-criterion is defined as the second invariant of the velocity gradient tensor and represents the balance between the rotation rate and strain rate of the flow. Regions where the Q-value is positive indicate dominance of rotational motion over strain, thereby highlighting the presence of coherent vortical structures. It is defined as follows:

$$Q\text{crit} = \frac{1}{2}\left[\text{tr}(\nabla \boldsymbol{u})^2 - \text{tr}(\|\nabla \boldsymbol{u}\|^2)\right] , \tag{5.2}$$

where tr is the trace operator. The image clearly reveals the presence of the horseshoe vortex system near the base of the cylinder, as well as the Kármán vortex street in the wake region. These flow structures are examined in greater detail in the following sections.

The presence of the pile in a steady current induces an adverse pressure gradient, which causes the upstream boundary layer to separate before reaching the cylinder, leading to the formation of the horseshoe vortex system. The ends of this vortex are carried downstream by the main flow, resulting in the characteristic U-shaped structure visible in Figure 5.7. From the same figure, it can be observed that the horseshoe vortex in the smooth bed case appears thinner than in the rough bed case. Moreover, it consists of a system of multiple vortices rather than a single coherent structure. To examine the horseshoe vortex more closely, flow streamlines in the symmetry plane upstream of the cylinder are shown in Figure 5.8. In the smooth bed case, a total of four distinct vortices are observed, three of which constitute the horseshoe vortex system. The model successfully reproduces the full horseshoe vortex system, consisting of three vortices, two rotating clockwise and one rotating counterclockwise—along with a small vortex attached near the bottom. In

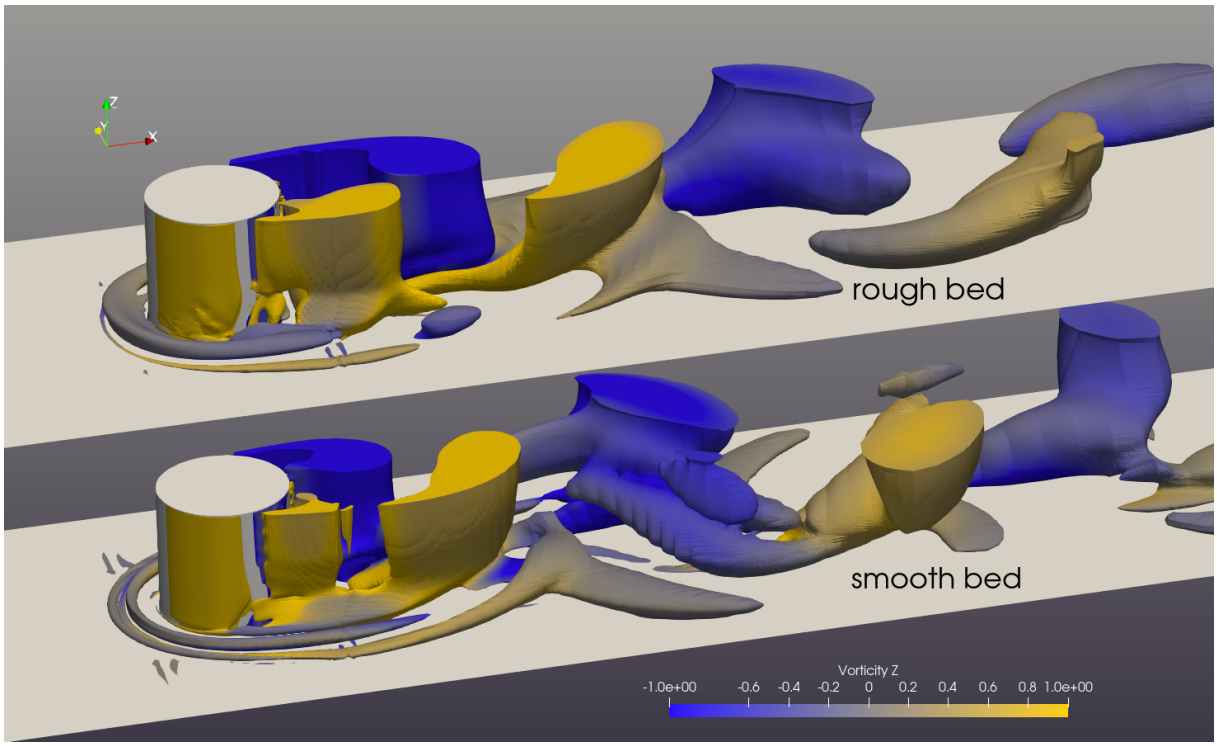

Figure 5.7: Iso-volumes of Q-criterion of values 0.05 and 10. From top to bottom, rough and smooth bed cases. The mesh M3 is used ised for both cases. The volumes are colored with the z-component of the vorticity highlighting the rotation direction.

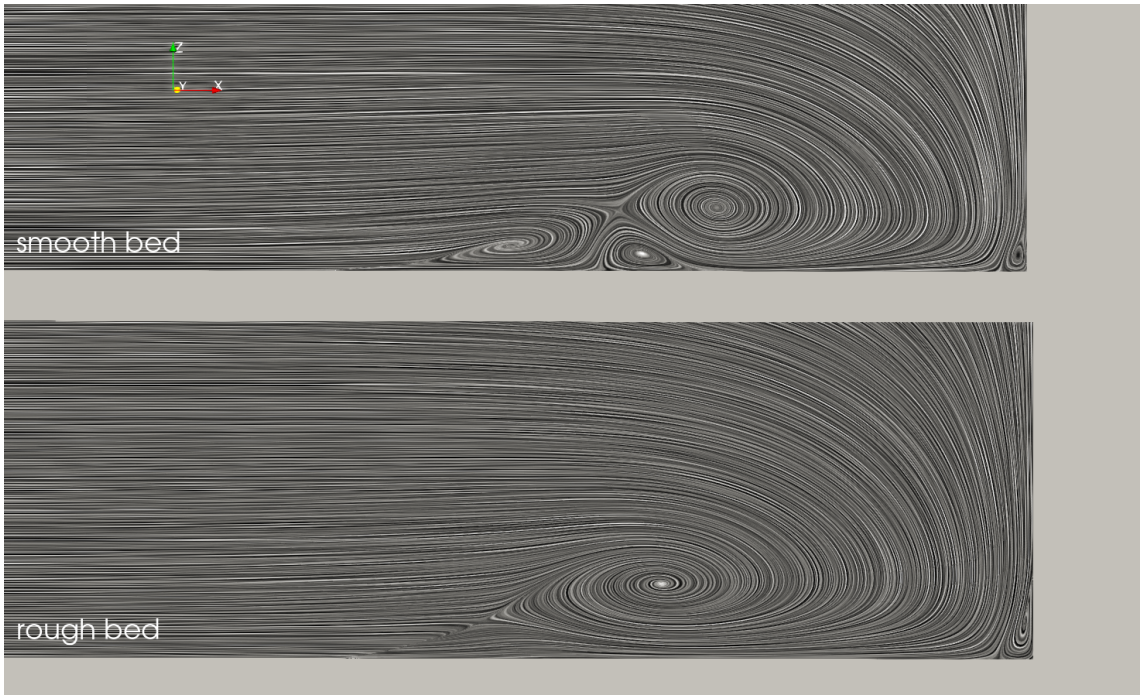

Figure 5.8: Flow streamlines in the symmetry pane of the flow upstream of the cylinder for the smooth bed case on top, and the rough bed case at the bottom.

contrast, the rough bed case exhibits only a single large horseshoe vortex in addition to the bottom-attached vortex.

Velocity fields

In the smooth bed scenario, Figures 5.9 and 5.10 demonstrate good agreement between the numerical results and experimental data in the upstream region. However, the coarsest mesh tends to underpredict the streamwise velocity. The horseshoe vortex can be identified by the change in flow direction close to the bed. As previously discussed, the numerical simulations reveal a system consisting of three vortices, which is particularly noticeable in the measurements taken closest to the bed ($z = 0.5\,cm$). As the flow approaches the cylinder, the streamwise velocity gradually decreases, becomes slightly negative, indicating the first clockwise vortex, increases again due to an anti-clockwise vortex, then drops to another negative value (second clockwise vortex), and finally returns to zero at the stagnation point. This behavior is observed across all three mesh resolutions. However, the size of the vortices varies with mesh refinement, with the coarsest mesh predicting a larger vortex system. In contrast, the experimental measurements captured only a single vortex, as the streamwise velocity component changes sign only once before reaching the cylinder. This discrepancy is likely attributed to the inherently complex and oscillatory behavior of the horseshoe vortex system [Baker, 1991], which cannot be fully resolved using a single hot-film probe.

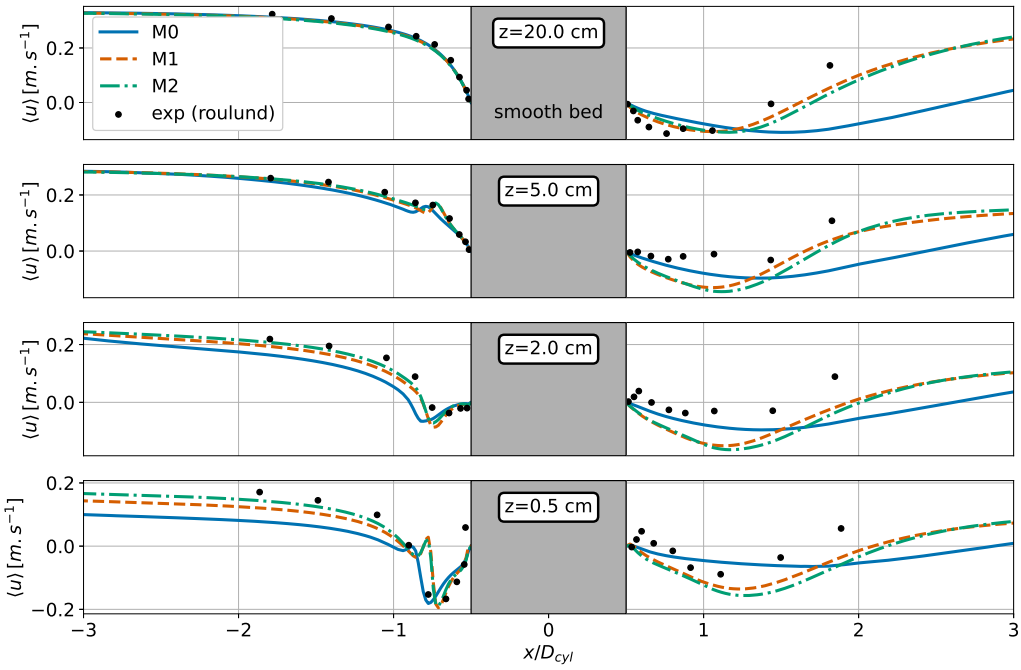

Figure 5.9: Stream-wise velocity for a smooth bed in the flow symmetry plane and at different elevations for three mesh resolutions.

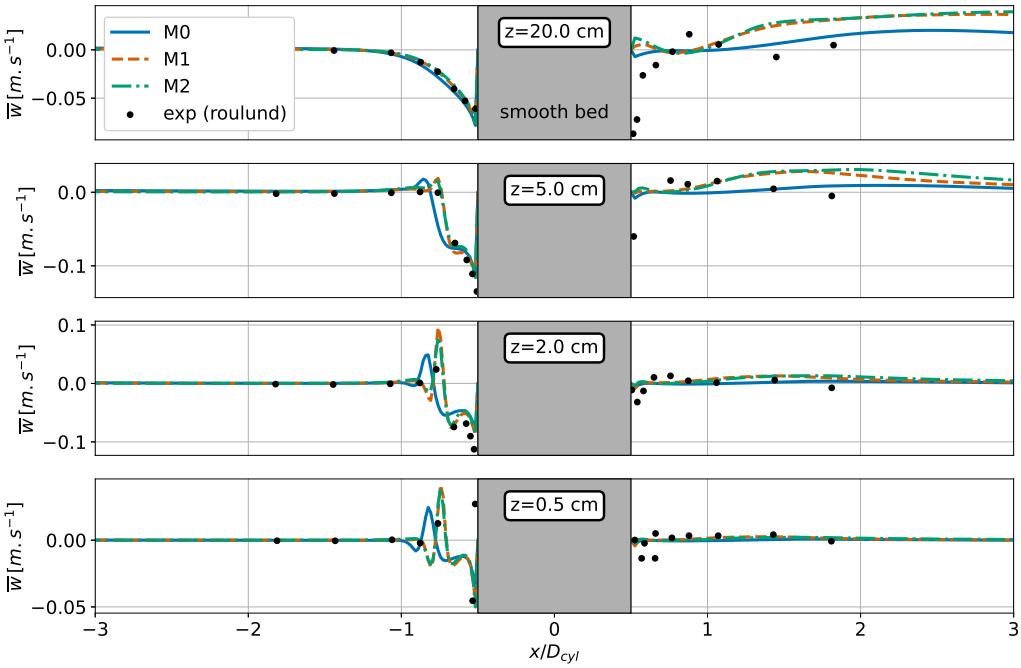

Figure 5.10: Vertical velocity for a smooth bed in the flow symmetry plane and at different elevations for three mesh resolutions.

The downflow induced by the stagnation point is clearly visible in Figure 5.10, where large negative values of the vertical velocity component are observed up to the bed level. At this location, variations associated with the horseshoe vortex become apparent once again. On the downstream side, flow recirculation is also evident, characterized by a negative streamwise velocity component. The extent and intensity of this recirculation are influenced by mesh resolution: the coarsest mesh predicts a larger but weaker recirculation. In contrast, both mesh M1 and M2 show good agreement with the experimental data, except near the bed, where the simulated recirculation is more pronounced than what is observed experimentally.

For the rough bed case (Figures 5.11 and 5.12), the main flow features remain similar to those observed for the smooth bed. As previously noted, only a single large horseshoe vortex is present. On the upstream side of the cylinder, there is good agreement with the experimental data, although the strength of the horseshoe vortex is influenced by mesh resolution the coarser mesh underpredicts the reverse flow velocity. Downstream of the cylinder, the vertical structure of the recirculation region differs from that of the smooth bed case. This variation is not captured by the numerical simulations, which tend to overpredict the extent of the recirculation near the free surface. Near the bed, the measured streamwise velocities are two to three times higher than those predicted numerically. This discrepancy may lead to an underestimation of the sediment transport induced by the wake vortices. Additionally, vertical velocity measurements show significant fluctuations that are not reproduced by the simulations.

Overall, the agreement between the simulations and measurements is good for both the smooth and rough bed cases. This is particularly true on the upstream side of the cylinder, where the counter-current velocity associated with the downflow and the velocity fluctuations induced by the horseshoe vortex system align closely with experimental data. In their study, Roulund et al. [2005] underestimated the counter-current velocity associated with the horseshoe vortex. This discrepancy may stem from the boundary conditions applied at the bed or from an insufficient mesh resolution. Similarly, Nagel et al. [2020] investigated the same problem using RANS simulations and also slightly underestimated the strength of the horseshoe vortex. In the rough bed case, where a Fuhrman boundary condition was applied (see Table 2.4), the RANS model predicts only a single vortex, whereas three stationary vortices are observed in the smooth case. These three vortices were clearly identified by Gilletta et al. [2025] using hybrid RANS-LES and pure LES simulations. Across various studies using RANS approaches [Roulund et al., 2005, Nagel et al., 2020, Gilletta et al., 2025], the presence of only one horseshoe vortex is consistently reported. Downstream of the cylinder, the agreement between simulation and experiment deteriorates. This is not unexpected, as the wake region is dominated by intense turbulence, which a RANS approach is generally inadequate to fully capture due to its limited ability to resolve complex turbulent structures.

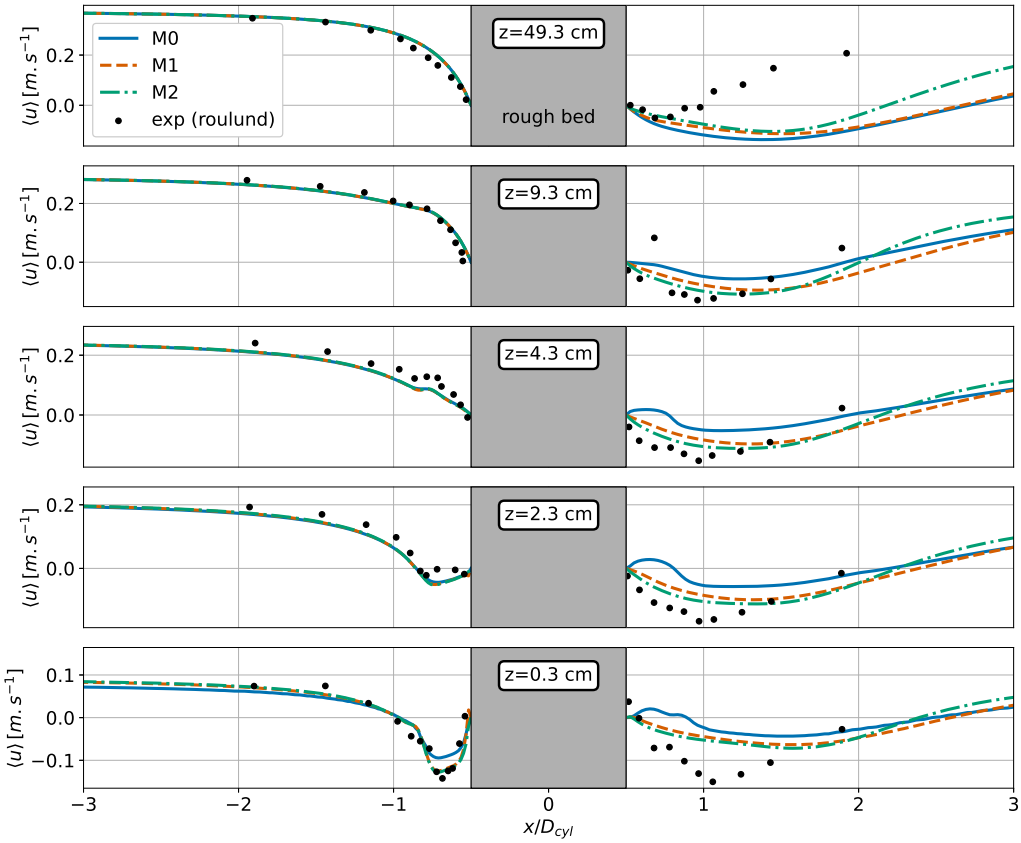

Figure 5.11: Stream-wise velocity for a rough bed in the flow symmetry plane and at different elevations for three mesh resolutions.

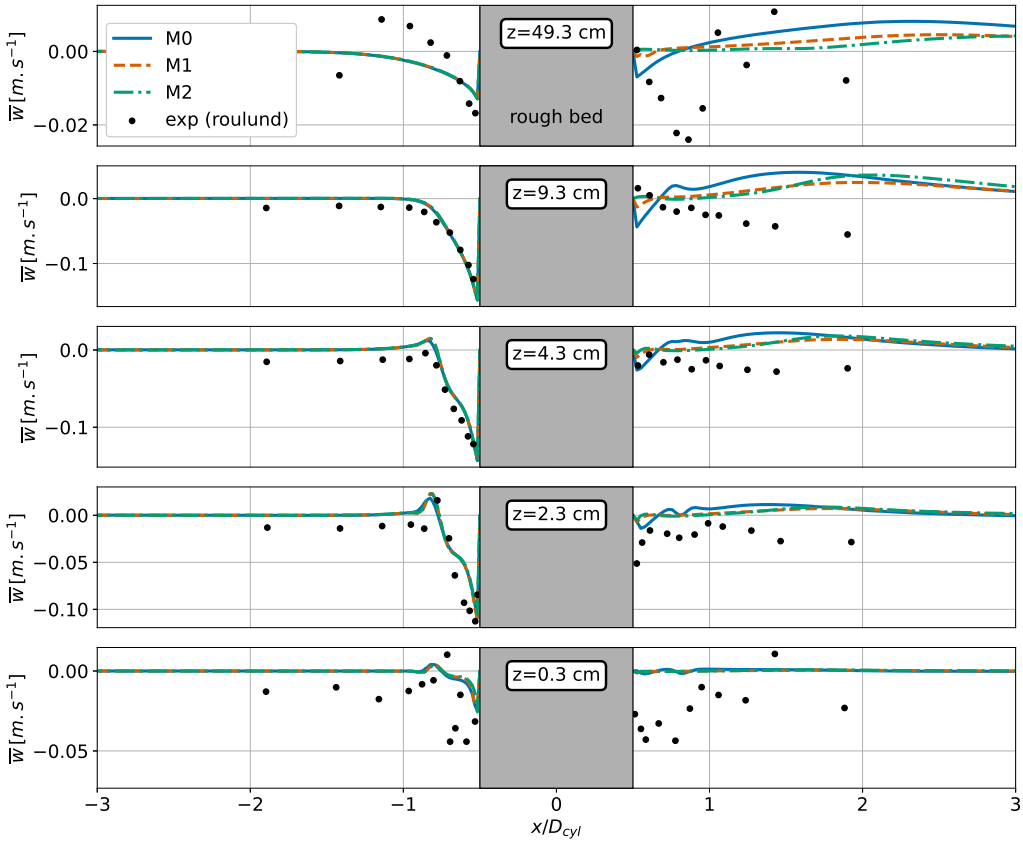

Figure 5.12: Vertical velocity for a rough bed in the flow symmetry plane and at different elevations for three mesh resolutions.

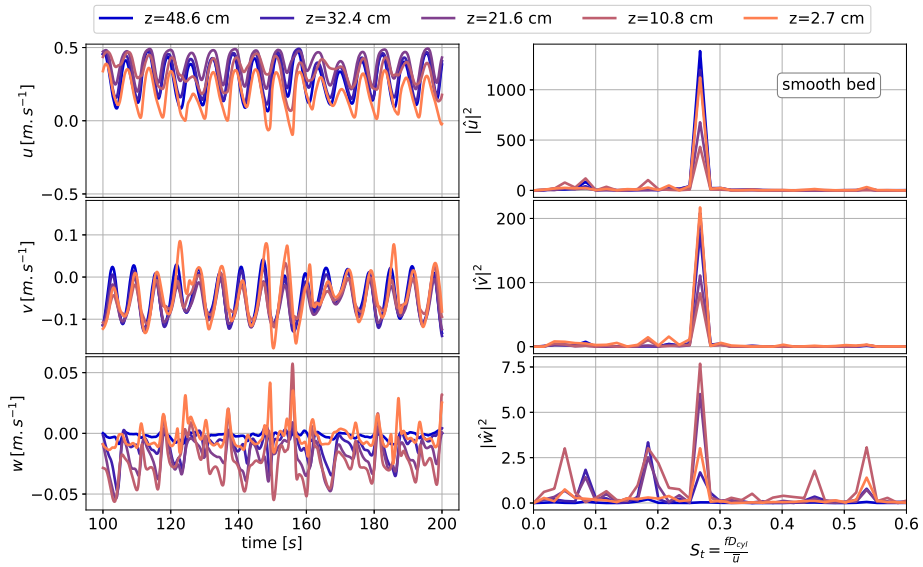

Figure 5.13: Wake vortices for a smooth bed. On the right, temporal evolution of the three components of the velocity fields for each probe. On the left, energy spectral density of each signal.

Vortex shedding

The most prominent flow feature is the vortex shedding phenomenon, which produces a Kármán vortex street downstream of the cylinder (see Figure 5.7). On the upstream side, a boundary layer forms along the cylinder surface but detaches due to the adverse pressure gradient created by the divergent flow geometry at the rear of the cylinder [Sumer et al., 2006]. Qualitatively, the detached vortices appear very similar in both the smooth and rough bed cases. Still in Figure 5.7, a distinct yellow sheet can be observed covering the upstream face of the cylinder, representing the boundary layer. This layer is characterized by a strong gradient in the tangential velocity component, resulting from the no-slip condition at the cylinder surface. The point where this sheet ends along the sides of the cylinder corresponds to the boundary layer detachment location. To analyze the flow variations in more detail, five probes were placed in the domain. All probes share the same x and y coordinates and are located 50 cm downstream of the cylinder. They are deliberately positioned laterally at a distance of $D_{cyl}/2$ from the flow symmetry plane to capture the passage of wake vortices. Vertically, the probes are positioned at 5%, 20%, 40%, 60% and 90% of the total water depth. The temporal evolution of all three velocity components at each probe for the smooth bed case is shown in Figure 5.13.

The energy spectral density of each temporal signal is also plotted. The time series show some degree of irregularity, which is reflected in the spectra. Fourier analysis reveals a dominant vortex shedding frequency of approximately $0.16 \pm 0.01 Hz$, corresponding to a Strouhal number of $S_t \approx 0.27$. This is higher than the typical shedding frequency observed for a free-standing cylinder (i.e., without a wall) at the same Reynolds number

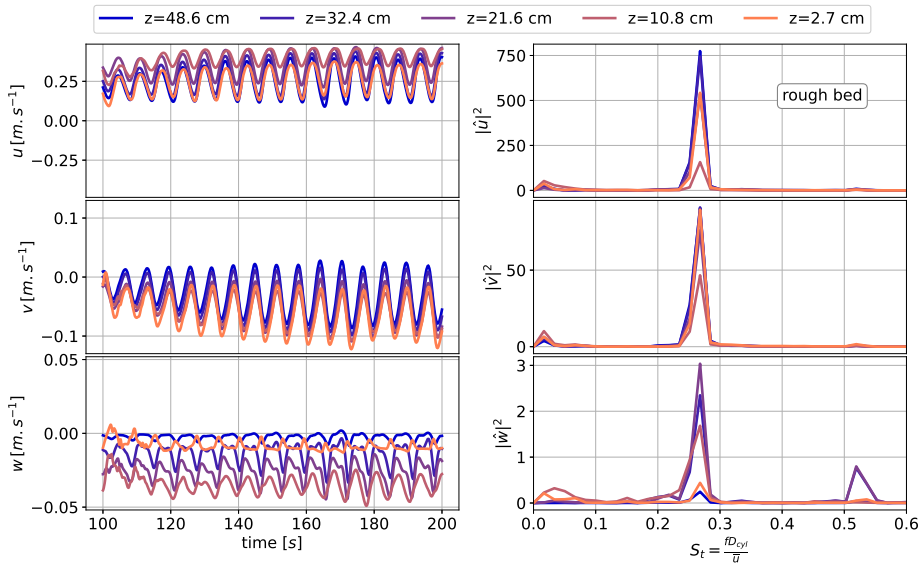

Figure 5.14: Wake vortices for a rough bed. On the right, temporal evolution of the three components of the velocity fields for each probe. On the left, energy spectral density of each signal.

($Re_D = 1.7\,10^5$). In subcritical regimes (e.g., $Re_D \in [300,\ 3\,10^5]$), the shedding frequency is generally associated with a Strouhal number around $S_t \approx 0.2$, as reported by Schewe [1983] and illustrated in Figure 1.5. A similar shedding frequency was reported by Nagel et al. [2020], while a slightly higher Strouhal number of $S_t = 0.3$ was found in the study by Baykal et al. [2015]. Furthermore, the vertical velocity signals display a broader frequency spectrum, indicating a more complex and energetic flow structure in the vertical direction. The Strouhal number is not affected by bed roughness. However, the temporal velocity signals reveal that roughness influences the time required for the flow to stabilize. In the smooth bed case, no clear transient behavior is observed after 100 seconds, indicating that the flow has already stabilized. In contrast, for the rough bed, vortex shedding is still developing at this stage, with eddy-associated velocity fluctuations continuing to intensify.

Shear stress on the bottom surface

Figure 5.15 shows the x-component of the friction velocity field u_*^x upstream of the pile obtained for the smooth bed case with 3 different mesh resolutions (M0, M1 and M2). The simulation results are plotted alongside experimental data. The shear stress gradually decreases and the presence of the three horseshoe vortices is shown by change in the shear direction. Far away from the cylinder, the shear stress is constant and is equal to the undisturbed shear stress. As the distance to the cylinder is reduced, the shear stress progressively decreases and becomes negative at a distance to the cylinder surface inferior to $D_{\text{cyl}}/2$. This reversal of the direction of shear stress is associated with the counter-current flow of the horseshoe vortex. Because the horseshoe vortex system is made of

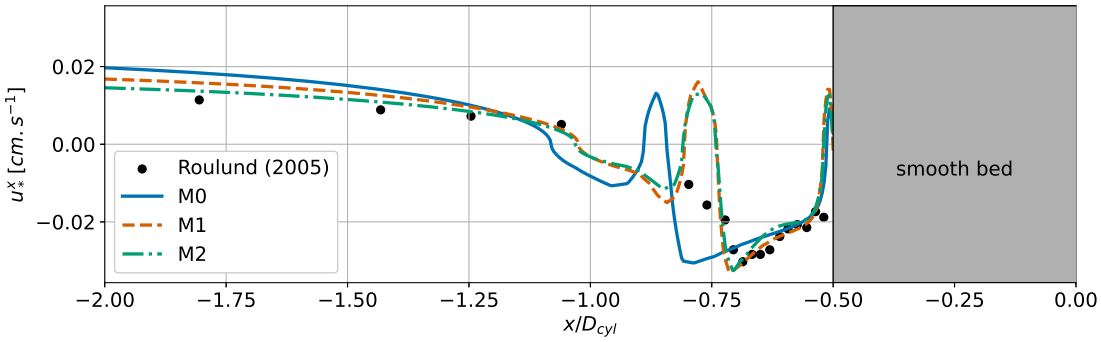

Figure 5.15: Friction velocity upstream of the pile in the symmetry plane of the flow. Results for a smooth bed and with three mesh resolutions M0, M1 and M2.

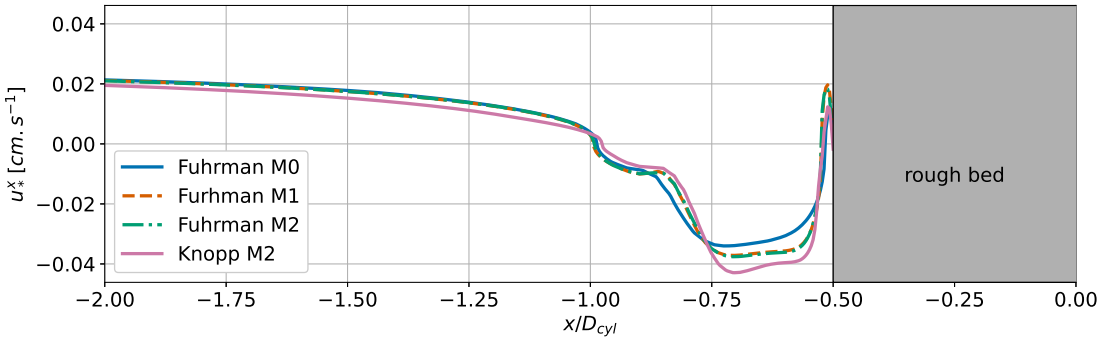

Figure 5.16: Friction velocity upstream of the pile in the symmetry plane of the flow. Results for a rough bed and with three mesh resolutions M0, M1 and M2 using a Fuhrman condition for wall roughness. The results of a simulation made with the finest mesh M2 and a Knopp boundary condition is also represented for comparison.

three vortices, the shear stress direction changes three times before reaching the pile. Really close to the pile, the shear becomes positive again highlighting the presence of the small corner vortex already presented in Figure 5.8 which is also observed in the rough case (see Figure 5.16).

In Figure 5.17 are shown map of the mean shear stress amplification $\|\tau_b\| / \tau_b^{up}$, where τ_b^{up} denotes the undisturbed bed shear stress upstream of the pile, computed by averaging the shear stress in a region unaffected by the presence of the cylinder. In both cases, the maximum bed shear stress occurs near the lateral edges of the cylinder, slightly upstream. The amplification of bed shear stress at the sides is more pronounced in the smooth bed case.

Overall, the model shows a good ability to reproduce the flow around a wall mounted cylinder. It has been found that a poor mesh quality leads to an underestimate of the strength of the horseshoe vortex system and therefore to its erosion capacity in the scour

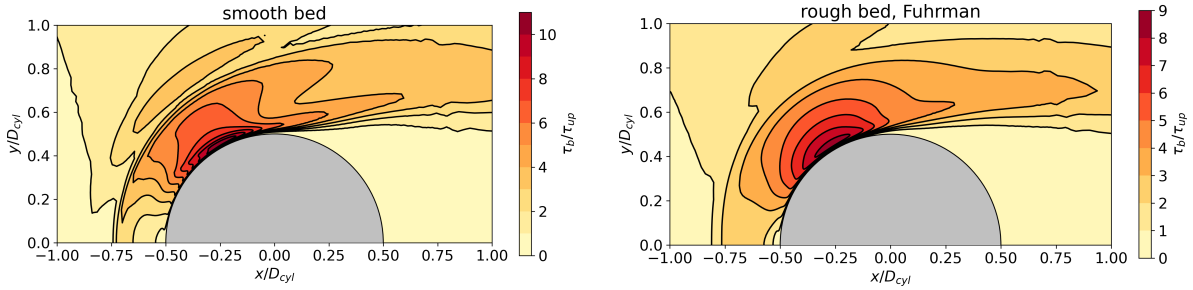

Figure 5.17: Amplification of the mean bed shear stress around a cylindrical pile mounted on a wall. The left plot shows the result obtained with a smooth wall surface and the right plot the results from a rough wall surface.

process. In the results presented, mesh convergence was achieved. Accurate modeling of bed roughness is essential for predicting sediment transport, scour development, and hydrodynamic forces in environmental and engineering applications.

5.3 Simulation of the scour process

In the following section are presented the numerical results obtain for the live bed configuration. The simulation as first run for 25 seconds, which is enough to reach a statistically converged state in this case. Indeed the ratio of the velocity to the cylinder diameter is almost ten times superior to the one in the rigid bed case, so that 25 seconds correspond to more than 100 bulk time ($D_{cyl}/\overline{u}$). After this time, the morphological evolution is switched on and the scour process begins. In figure 5.18 is shown the early development of the scour hole. Initially, the scour hole begins to develop on the sides of the cylinder, at locations where the shear stress is highest due to flow acceleration (see Figure 5.17), rapidly creating a small depression in the bed. Sediment is transported away from these high-stress regions by the swirling motion of the horseshoe vortex and the accelerating flow along the cylinder sides, leading to the formation of small bedforms downstream. A secondary depression forms in the wake region, and by 10 seconds, it appears likely to merge with the main scour hole.

At this stage, it was not possible to run the simulations long enough to reach an equilibrium state. This limitation is due to numerical instabilities in the Exner equation, which eventually cause the simulations to crash. Examples of these instabilities observed prior to failure are illustrated in Figure 5.19. Upstream of the cylinder, where the scour process is dominated by the horseshoe vortex, small bedforms begin to appear in areas of steep bed slopes. Additional instabilities are also visible along the cylinder sides. In previous studies, various authors have employed spatial filtering techniques to suppress such instabilities. For instance, Baykal et al. [2015] applied a least-squares-based spatial filter in the immediate vicinity of the pile. However, the current version of *sedExnerFoam* does not include any spatial filtering. Although the implementation of a spatial filter on the bed elevation increment has been considered at various stages of model development,

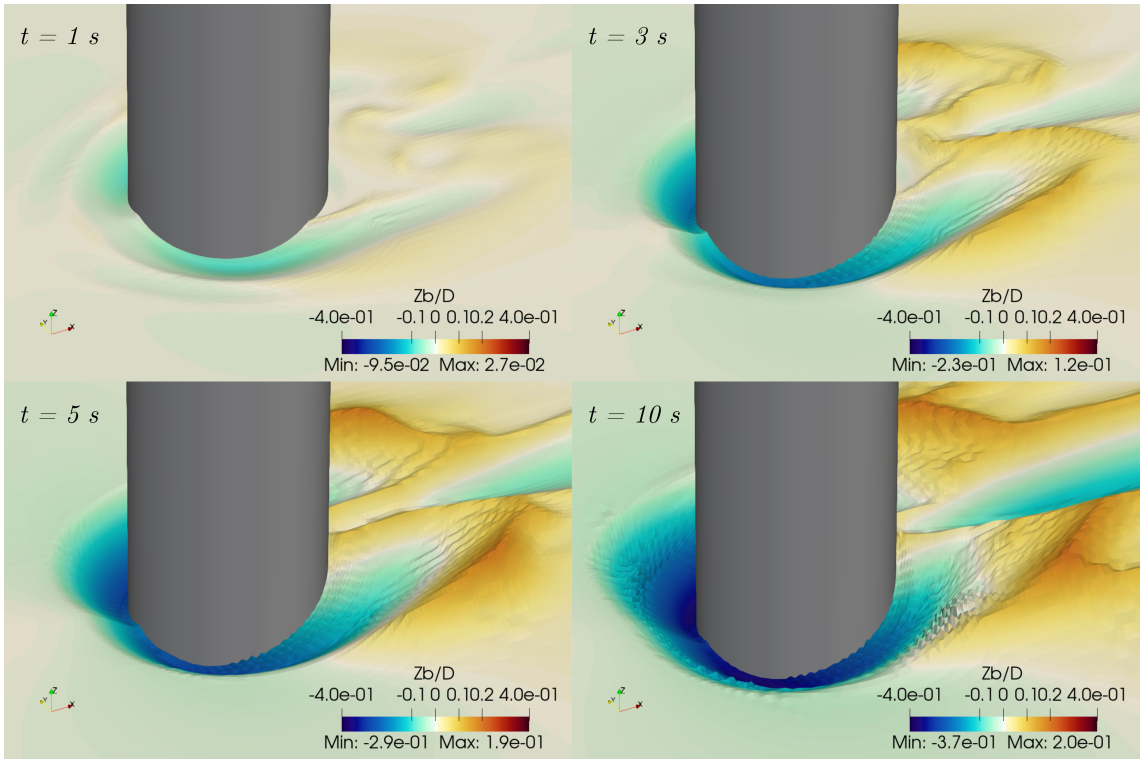

Figure 5.18: Development of the scour hole around a cylinder, 1, 5 and 10 seconds after the beginning of the scour process.

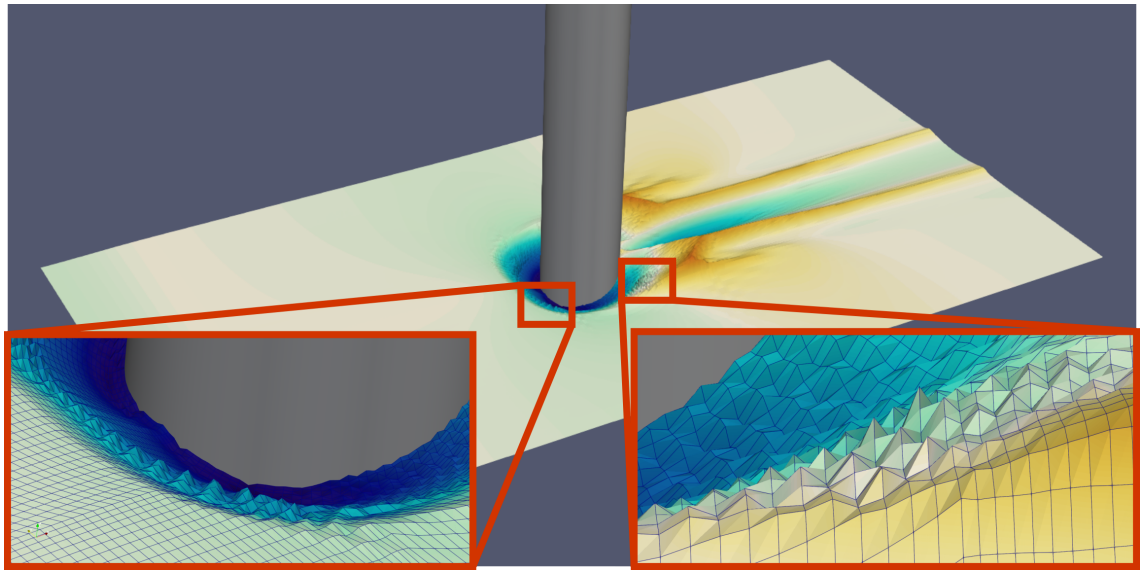

Figure 5.19: Apparition of bed instabilities during the development of the scour hole.

it was ultimately not adopted, as the saturation term is assumed to act as a natural filter. The challenge, however, lies in the absence of a validated 3D formulation for the saturation equation. A new formulation is proposed in the present work (see eq. 2.24), but it has not yet been validated and requires further testing before it can be reliably applied to three-dimensional scour simulations.

Figure 5.20 shows the x-component of the bedload transport due to bed shear stress and avalanching, after 10 seconds of scour development, along the symmetry plane upstream of the cylinder. As the flow regime corresponds to live bed conditions, a bedload flux is present upstream of the scour hole and increases slightly as it approaches the hole. Within the scour region, the bed shear stress reverses direction under the influence of the horseshoe vortex, causing sediment to be dragged upstream. In contrast, avalanching contributes to sediment transport downslope into the scour hole. The avalanche-induced bedload flux appears quite noisy, which can be attributed to the fact that avalanching at each bed face is directly governed by the local slope, indicating small-scale, irregular variations in slope throughout this region. It has not been identified at this point, if the avalanche is responsible for the instabilities observed in Figure 5.19.

Figure 5.21 illustrates the scour development for two simulations: the previously discussed case and another in which bedload transport was neglected. The resulting scour patterns and rates are remarkably similar. The only notable differences are slightly lower bedforms downstream of the cylinder and a less pronounced bed depression in the wake region. This outcome highlights a known limitation of Exner based models, where bedload and suspended load transport are treated independently. There is a concern that part of the bedload flux may already be implicitly accounted for in the suspended load calculations—particularly when using fine near-bed resolution, as in the present study. This redundancy can potentially lead to an overestimation or misrepresentation of total

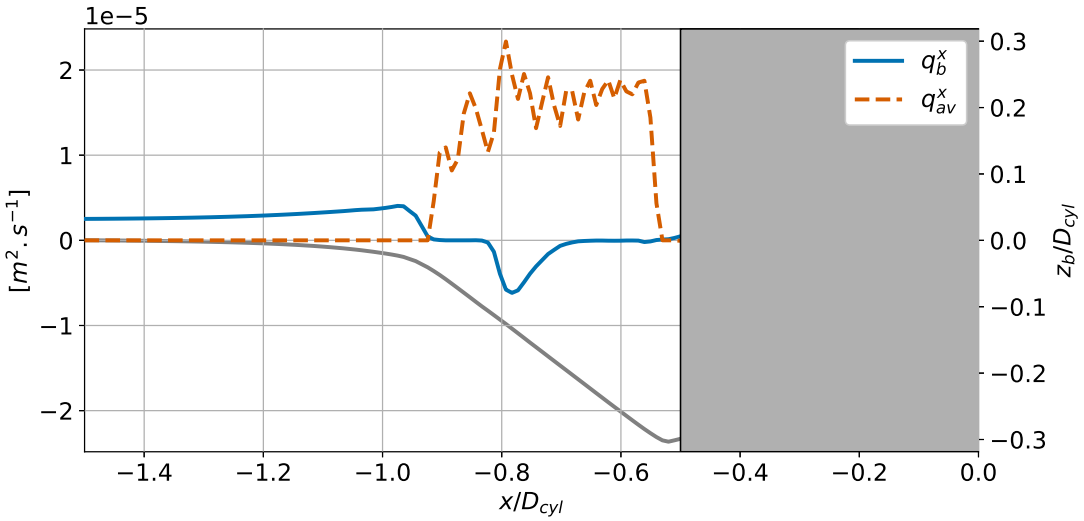

Figure 5.20: Bedload components due to avalanche and to bed shear stress in the symmetry plane of the flow upstream of the cylinder. Results after 10 seconds of scour process. The gray line indicates the bed elevation.

sediment transport if both components are not clearly separated. Nevertheless, given the high level of uncertainty associated with empirical formulations used to compute bedload flux and erosion rates, an overestimation by a factor of two may still fall within an acceptable range of accuracy.

The scour rates from the two simulations are presented in Figure 5.22, alongside experimental measurements. In the experiment, the development of the scour hole follows a logarithmic progression over time. The black dotted line in the figure represents this logarithmic trend and serves as a reference for comparing the numerical results to the experimental data. The predicted initial scour rates align well with this trend, suggesting that bedload transport does not play a dominant role in the early stages of the excavation process.

5.4 Conclusion

This chapter has examined the three-dimensional scour processes developing around a wall-mounted cylindrical pile under steady flow conditions, focusing on the evaluation of the numerical model's capabilities. Initial simulations, conducted without sediment transport, successfully captured key hydrodynamic structures such as the horseshoe vortex and wake vortices, which are commonly observed in experimental studies. The comparison between smooth and rough bed configurations highlighted the significant influence of bed roughness on near-bed turbulence, particularly affecting the number of vortices comprising the horseshoe vortex system when using RANS modeling. Furthermore, near-bed mesh resolution was shown to play a crucial role in accurately estimating the excess bed shear

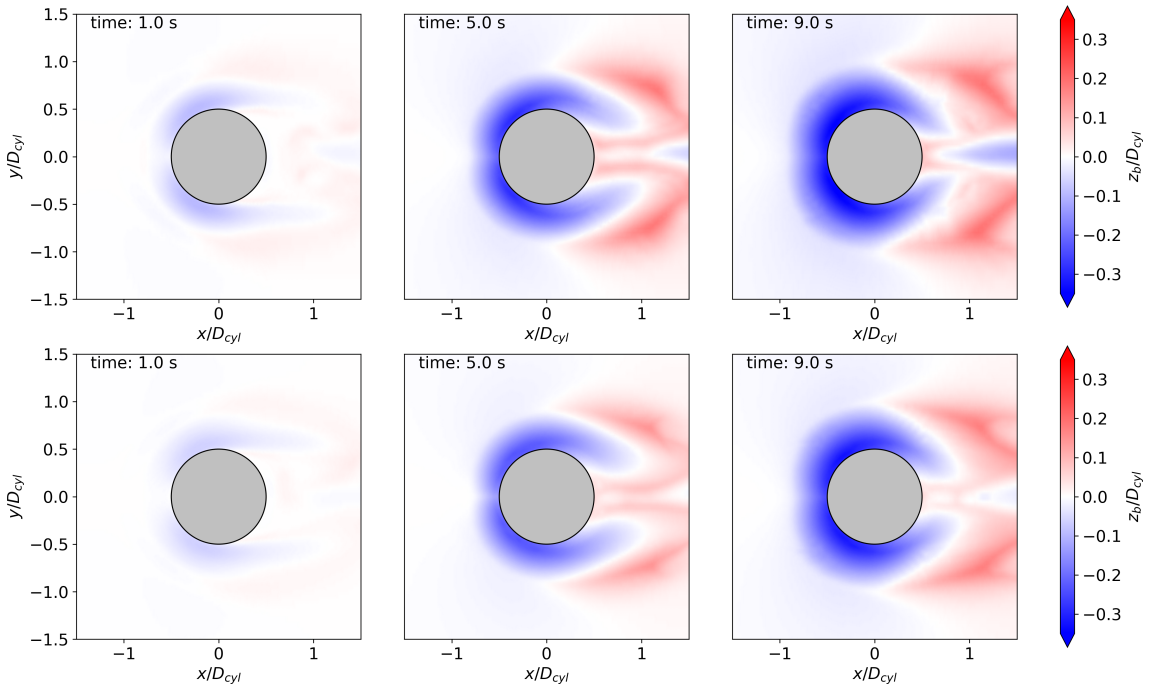

Figure 5.21: Bed level evolution after 1, 3, 5 and 10 seconds of scour process. On top are results obtain considering both bedload and suspended load transport. At the bottom are results obtained with suspended load transport only.

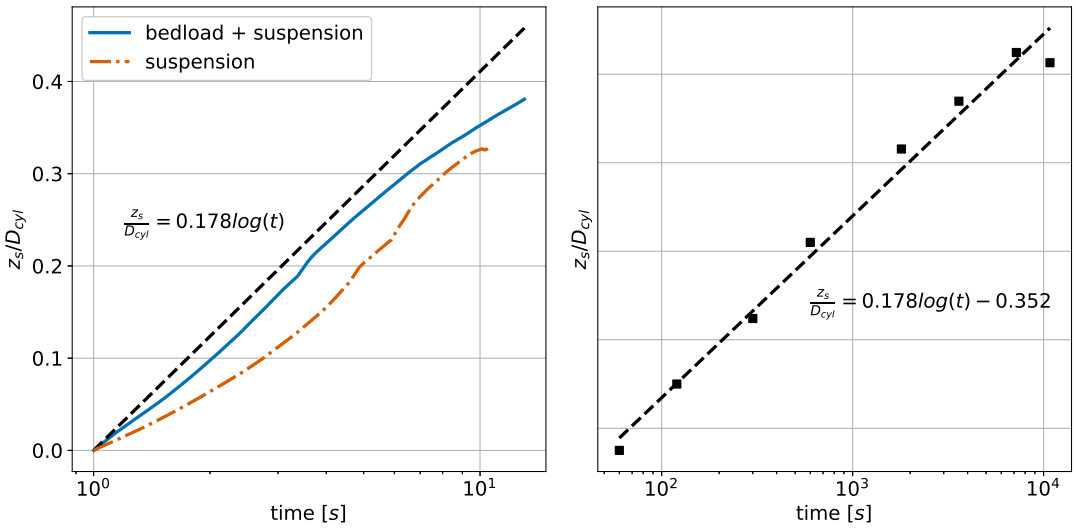

Figure 5.22: Maximum scour depth over time for two simulations, compared with the trend observed in the experimental measurements of Roulund et al. [2005].

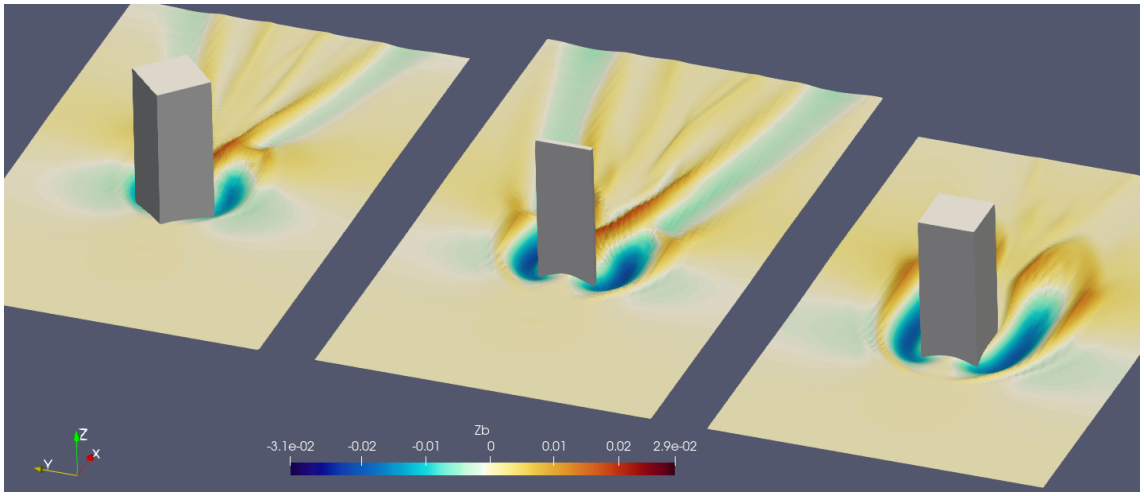

Figure 5.23: 3D view of scour around various geometries.

stress associated with the horseshoe vortex system, an essential factor for the numerical simulation's ability to reliably predict the scour process.

Following hydrodynamic validation, sediment transport was incorporated to evaluate the model's ability to simulate the onset and early development of scour, particularly in regions influenced by the horseshoe vortex. However, numerical instabilities, especially within the Exner equation, limited the duration of the simulations and prevented the attainment of equilibrium scour profiles. In the absence of the filtering effect provided by the saturation model, small bedforms at the scale of the mesh resolution developed in various parts of the computational domain, notably within the scour hole. In three-dimensional simulations, pinpointing the exact cause of simulation failures is often challenging. This is especially true for *sedExnerFoam*, where failures arise from a complex interplay between instabilities in the Exner equation, mesh deformation solvers, and the hydrodynamic response to evolving bed instabilities.

Despite these limitations, the study demonstrates the model's strong potential for simulating scour around cylindrical structures and other geometries (see Figure 5.23) It also identifies key areas for improvement, including the need for better handling of numerical instabilities, potential implementation of spatial filtering techniques, and further validation of proposed saturation formulations for 3D scour modeling. The avalanche model used in the present work is also a potential area of improvement. These findings lay the groundwork for more robust and accurate simulations of complex scour phenomena in real-world engineering applications.

Conclusion and perspectives

The aim of this PhD project was to develop a model of sediment transport and morphological evolution that could be used to study scour phenomena in engineering applications. The model, named *sedExnerFoam*, was made publicly available under an open-source licence, in line with the philosophy of the *OpenFOAM* C++ library in which it was implemented. The code is based on an *OpenFOAM* solver called *pimpleFoam* for transient incompressible flows. Building on this, the model was expanded to include different sediment transport processes. During the initial development phase, bedload transport and the Exner equation were developed in a separate model that did not incorporate hydrodynamics. A simple flow model, assuming mass conservation, coupled with a bedload flux formula that depends directly on the local flow velocity was used to solve the Exner equation. Following the initial phase, the equation for suspended sediment concentration was implemented alongside the flow model. This model includes different closures for settling velocity and hindrance effects, as well as erosion-deposition fluxes. During this development phase, various benchmarks were created to verify the model's performance. These tests now form part of a continuous integration strategy aimed at maintaining code quality over time and avoiding regression.

The development of the model has led to the submission of an article to the scientific journal Geoscientific Model Development [Renaud et al., 2025], which is currently under review. The article has a similar structure to the current PhD thesis, comprising a description of the model, some benchmarks and an application to the migration of a lone dune. However, the present manuscript is more comprehensive, containing additional information, tests and explanations.

General conclusions

The review of the state of the art (chapter 1) begins with a description of the phenomenon being modeled. The main turbulent structures generated by the interaction of a flow with an obstacle are detailed: the horseshoe vortex and the von Kármán vortex street. A review of the various existing modeling options and the scales to which these methods are adapted justifies the development of a model based on the Exner equation. Next, the different physical processes to be modeled are reviewed, beginning with a description

of the RANS equation and turbulence modeling. When using the Exner equation, the amount of sediment transported by the flow is calculated using empirical formulas. Since these formulas use bed shear stress as an input, its correct estimation is crucial. For this reason, the boundary layer flows above smooth and rough surfaces are described in detail, along with the wall functions for turbulence models based on ω, which are necessary to correctly capture the near-wall hydrodynamics and therefore compute the shear stress. Finally, the review concludes with a discussion of the closures for bedload and suspended sediment load transport.

The next two chapters (2 and 3) are considered a single unit. The first chapter provides a detailed description of the model and the various equations that are solved, as well as the different modelling options available to users regarding turbulence and sediment transport (bedload and suspended load). It also provides details of the numerical aspects of the model, such as how the equations are discretised, the pressure-velocity coupling algorithm employed and how mesh deformation is imposed. The second chapter consists of various validation cases designed to test and demonstrate the model's components separately. An idealised dune transport problem, for which an analytical solution can be derived, was used to test the implementation of the Exner equation and the sensitivity of the results to numerical schemes and mesh resolution. For suspended load, the classical case of suspension under equilibrium conditions was studied by comparison with four experiments. It has been shown that, in cases where the flow is hydraulically smooth, using a fine near-bed mesh resolution leads to eroded sediments becoming trapped in the first cell above the bed boundary. This is due to the presence of the viscous sublayer, where turbulence vanishes. Without turbulent diffusion, suspended sediments cannot rise further in the water column. To address this issue, an additional near-bed diffusivity was added to the model to enable suspended sediments to rise by at least a distance equal to the roughness length, at which point turbulent diffusion takes over.

In Chapter 4, the migration of a lone dune in a thin channel was presented as the first application of the model. The aim was to reproduce the experimental configurations from the work of Kiki Sandoungout [2019] and to investigate how the behaviour of the dune is affected by the different model parameters. It was found, in particular, that shifting the position at which the flow detaches from the dune to generate a recirculation cell by a small amount significantly affects the morphological response. Since flow detachment is associated with a sudden decrease in bed shear stress and, consequently, in bedload flux, its occurrence upstream of the dune crest results in sediment accumulation at the top of the dune. This causes the upstream slope of the dune to become steeper until an avalanche is triggered, balancing the bedload flux and stopping the migration process. To avoid this unphysical situation, it was necessary to introduce saturation into the model to take the inertia of sediments in the bedload layer into account. This addition to the model enables sediments to continue moving a certain distance after flow detachment, allowing them to pass over the dune crest. Since morphological responses affect hydrodynamics and vice versa, changes in dune shape induced by saturation can be significant. The boundary conditions applied to turbulent quantities (k, ω) to account for the roughness of the sediment bed interface were also found to influence the flow detachment point,

thereby affecting the resulting morphological response. Additionally, particular attention must be paid to the selection of rough boundary conditions for turbulent quantities, as they significantly influence flow behavior and, consequently, bed evolution.

Finally, the scour around a circular cylinder has been studied numerically (see chapter 5). Three experimental configurations from Roulund et al. [2005] were reproduced, two of which were rigid bed cases with smooth and rough bottoms, respectively. These two cases were used to validate the hydrodynamics and verify the model's ability to reproduce turbulent structures around a pile, such as horseshoe and Kármán vortices. Surprisingly, using a $k-\omega\,SST$ turbulence model was sufficient to simulate a horseshoe vortex system consisting of three static vortices rather than a single vortex in the smooth bed case. To the author's knowledge, this generally requires a more resolved method, such as LES or hybrid RANS-LES modeling [Gilletta et al., 2025]. Although discrepancies with the measurements were observed, particularly downstream of the cylinder where eddy shedding generates highly turbulent structures, the RANS approach was able to capture the main flow structures globally. Following the study of the hydrodynamics, the third configuration, a live bed case, was examined. The model was able to reproduce the initial scour development; however, it was not possible to run the simulations for long enough at this stage to reach equilibrium scour depth. The various limitations of the model are discussed in the 'Perspectives' section that follows. Nevertheless, the trend in the scour process appears consistent with experimental observations, which supports the model's potential for studying scour around obstacles.

Perspectives and future improvements

The scientific and technical insights gained during the course of this PhD work have enabled key areas for improving the model to be identified, along with plans for future developments aimed at encouraging its use in scour studies. These are described in the next section.

Maintaining mesh quality during deformation

The main difficulty with the model is maintaining good mesh quality during the scouring process. The mesh motion procedure is as follows:

1. The Exner equation has been solved, with an increase in bed elevation associated with each face of the bed boundary.
2. As the mesh geometry is defined by the positions of the vertices, the bed elevation increment is interpolated from the faces forming the bed boundary to the vertices.
3. *OpenFOAM* mesh deformation utilities convert bed vertex motion into a boundary condition for the Laplace equation (see eq. 2.60). This equation diffuses the bed boundary displacements to the rest of the computational domain.
4. The Laplace equation is solved to determine the vertical displacement at each cell center.

5. *OpenFOAM* computes the new positions of the vertices based on the displacements of the cell centers.

Two steps in this procedure remain unclear. Firstly, how is the displacement of the bed boundary converted into a boundary condition for the mesh motion equation? Secondly, how does *OpenFOAM* interpolate the cell centre displacements, which are the solution to the Laplace equation, to the vertices? In practice, it has been found that, in the presence of a dune with a sharp crest, cells adjacent to the slope break tend to degenerate, leading to simulation failure. This is because, during the interpolation step, vertices located just above the bed boundary can be displaced underneath it. Currently, the only viable solution to this issue is to avoid using cells with high aspect ratios near the bed. In other words, the horizontal dimensions of a cell near the bed must not be significantly greater than its vertical dimension. If this condition is not met in any part of the computational domain, the simulation will break as soon as sharp bedforms appear or move into that area. One solution to this issue would be to use the mesh deformation method described in [Jasak and Tukovic, 2006], which is implemented in the extend branch of *OpenFOAM*.

In their work, the authors argue that the finite volume method is not well-suited to handling complex mesh deformation, and they propose a method for solving mesh deformation directly at the vertices using a finite element approach. The difficulty lies in the fact that *OpenFOAM* was designed to handle unstructured meshes made up of polyhedra of any dimension. However, to solve mesh motion using the FEM, prior knowledge of the geometry of the mesh elements is required to derive a form function. As there is no known form function for polyhedra of any dimension, the method relies on decomposing the mesh into tetrahedra. This can significantly increase the size of the mesh used to solve the Laplace equation. For example, it increases the number of cells by six for a hexahedral mesh. This, together with the fact that this method is unavailable in the *OpenFOAM* branch in which *sedExnerFoam* was implemented, is the reason why it has not been tested. In May 2025, a week-long event was organised as part of the SEMIES program in Grenoble. The aim was to bring together groups of PhD students in mathematics and provide them with a specific problem to consider. One group of four students was tasked with identifying issues encountered with *sedExnerFoam*, one of which was mesh deformation leading to cell degeneration. An idea that emerged during the week was that, for bed displacements limited to the vertical direction, the Laplace equation for mesh motion has an analytical solution that can be used to directly compute the vertex displacements required to accommodate the bed boundary motion. This approach has two key advantages and appears to be a promising development for the future. Firstly, it eliminates the need for the interpolation step that causes the issue. Secondly, assembling a matrix system to solve the mesh motion is no longer necessary.

Three-dimensional saturation of the bedload

As demonstrated in Chapter 4, the saturation of the bedload flux is a key element in controlling the morphological response of dunes. Although the concept of bedload saturation is fundamental to the aeolian sediment transport community, it is rarely used in

subaqueous sediment transport. The main reason for this is that the saturation length is very small in water, and most models use a resolution that is too large in comparison with the saturation length. However, as this study aims to examine local scour around hydraulic structures, a fine-scale resolution is required to accurately capture the complex hydrodynamics and turbulent features in the vicinity of the obstacle that are responsible for the scour process. At the spatial resolution considered in this study, flow detachment above bedforms is resolved, leading to strong local shear stress gradients. Without saturation, the bedload flux reacts instantaneously to spatial and temporal variations in bed shear stress, resulting in unphysical behaviour. Notably, when flow detachment occurs slightly upstream of a dune's crest, sediments accumulate at the top of the dune instead of rolling over it. This results in an unphysical shape, with the upstream side becoming steeper until an avalanche compensates for the bedload flux.

The current issue is that, to the author's knowledge, there is no three-dimensional formulation of bedload flux saturation. For this reason, all of the 3D simulations presented in this work were performed without saturation. In practice, however, neglecting saturation effects appears to be less critical in 3D cases, since sediments can also move laterally. As discussed in Chapter 4, a barchan dune can migrate even without saturation. However, it has been found that the barchan grows laterally, a behaviour not observed in the experiments reported in Alvarez and Franklin [2017]. The main suspect is, of course, the fact that saturation is not taken into account in this problem, causing the sediments to be transported to the sides of the barchan.

A 3D formulation of saturation has been proposed and implemented in *sedExnerFoam* (see eq. 2.24). This equation is solved explicitly and has not been fully tested against experimental data. The next step for the model is therefore to conduct all the necessary tests to validate the 3D formulation of the saturation, and perhaps, if required, to implement an implicit version. This is of particular interest given the natural filtering effect it has on the Exner equation, as observed in 2D cases; this could address other issues in 3D simulations.

Near bed diffusivity

During the study of suspended sediments under equilibrium conditions, it was found that, for hydraulically smooth flows, using a fine near-bed mesh resolution resulted in the eroded sediments being trapped in the viscous sublayer close to the bed. To address this issue, an additional diffusivity term was added to the transport equation for suspended sediment concentration. This new closure is entirely empirical and enables the suspended sediments to rise high enough in the water column for turbulent diffusivity to take over. Without this additional diffusivity, the equilibrium profile of the volume fraction of suspended sediments depends heavily on the near-bed mesh resolution (see Figure 5.24).

The main criticism of this method is that this formulation is purely empirical. One idea explored during my PhD thesis was to use knowledge from Eulerian–Eulerian modeling to attribute the additional diffusivity to a physical process and derive a more physically based closure. This was the subject of a presentation at the 12th International Conference

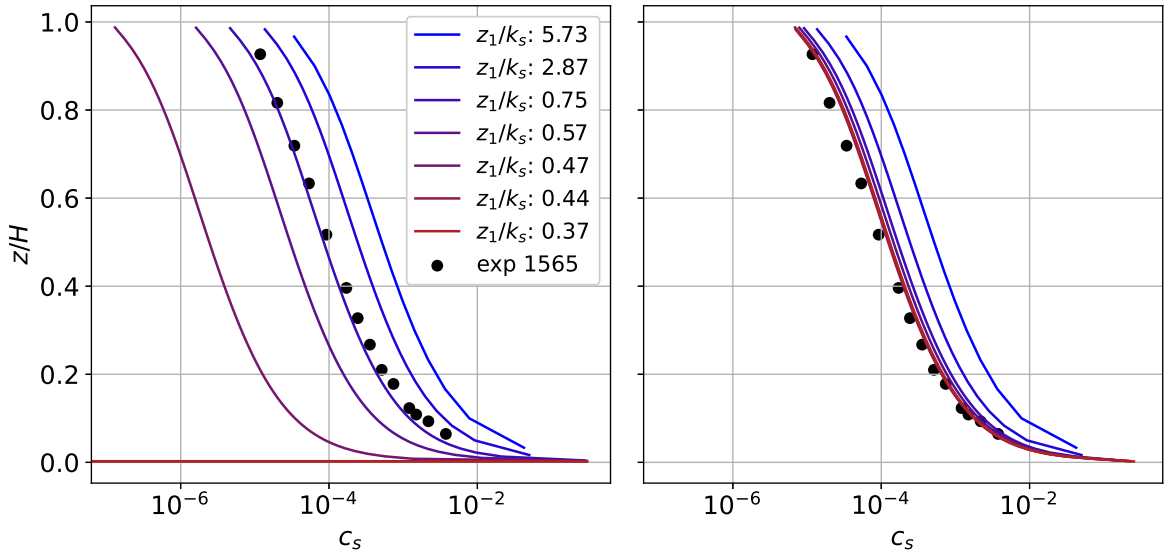

Figure 5.24: Mesh sensitivity of the suspended sediments volume fraction vertical profile under equilibrium condition. Comparison with one of the experiments from Lyn [1988]. From left to right, the additional diffusivity is switched off and on respectively. The values of z_1/k_s indicate the near bed mesh resolution, z_1 being the distance of the first cell center to the bed boundary and k_s the roughness length here equal to $0.375\,mm$.

on Multiphase Flow, held in Toulouse, France, in May 2025. Starting from the equations of the two-phase flow model and performing a number of simplifications, an alternative version of the Rouse equation was obtained in the following form:

$$c_s w_s^0 + \left(\frac{\nu_t}{\sigma_c} + \tau_p T_0 \right) \frac{\partial c_s}{\partial z} = 0\,, \tag{5.3}$$

where τ_p is the particle relaxation time and T_0 the granular temperature. It was found possible to replace the near-bed diffusivity and eliminate the mesh dependence of the solution by expressing the granular temperature as a function of the friction velocity or turbulent kinetic energy using simple expressions. However, this work still needs to be developed further.

Other issues

Another issue with the current model is that the Exner equation is only implemented for sequential simulations. Although parallel simulations can still be conducted, the bed boundary must be kept on a single processor. Figure 5.25 shows a decomposition of a domain for simulating scour around a cylinder. As can be seen, the mesh decomposition is clearly non-optimal, with one processor sharing a large interface with the others. Although no scalability analysis has yet been conducted, for a large computational domain

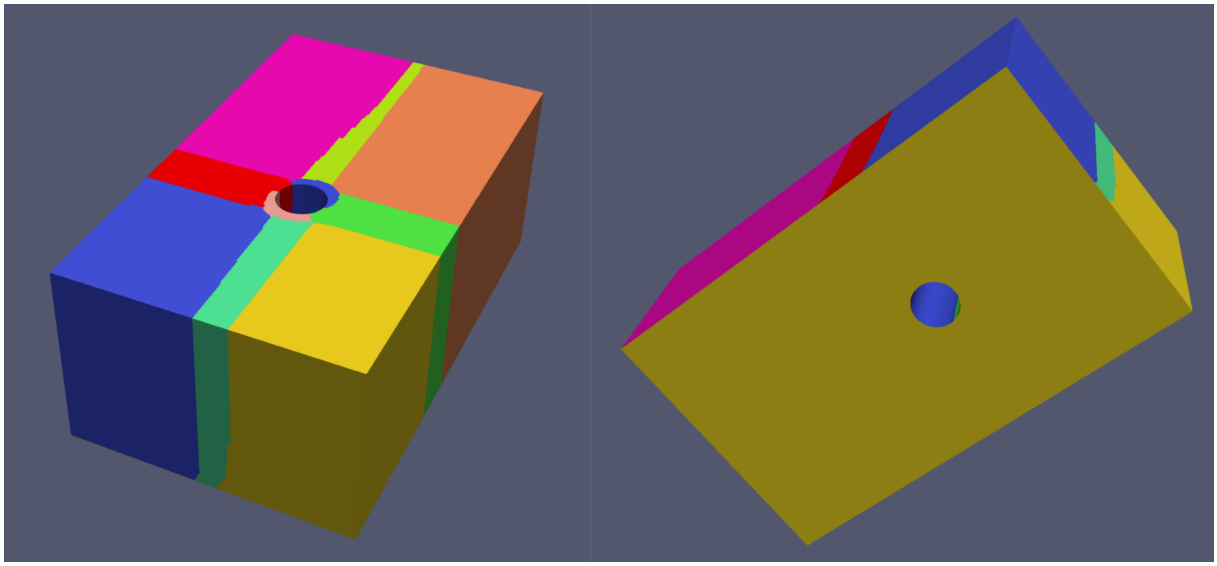

Figure 5.25: Decomposition of a mesh with conservation of the bed boundary on a unique processor. Each color indicates a specific processor.

the decomposition will significantly impact simulation time. To parallelise the sediment bed boundary, two implementations must be modified. Firstly, the bedload flux must be interpolated from face centers to edge centers in order to compute the quantity of sediments entering or leaving each face. Secondly, the bed elevation displacement must be interpolated from faces to vertices.

n some cases that have not yet been identified, the volume fraction of suspended sediments can become negative. While this issue does not appear to significantly affect the evolution of the sediment bed morphology, it should still be investigated and addressed.

In this study, avalanches were considered as an additional form of bedload flux, depending on the local bed slope. This formulation is based on that proposed by Duran Vinent et al. [2019], and the user must specify the prefactor for the avalanche flux. In practice, it has proven difficult to select a value that ensures avalanches are powerful enough to prevent the local bed slope from becoming excessively steep, while also satisfying the numerical stability condition of the Exner equation throughout the simulation. Further work on the avalanche formulation is necessary to improve the robustness of the model. Other formulations, such as the one in Apsley and Stansby [2008], could be implemented and tested. Marieu et al. [2008] also proposed an iterative procedure to redistribute sediments until the angle of repose is not exceeded anywhere in the domain. This method has been successfully implemented in the model of Zhou [2017] who reports that the computational cost associated to avalanches using this iterative method is significant for parallel computation.

Another important aspect of sediment transport simulations, which is highlighted throughout this work, is that the boundary conditions for turbulent quantities (e.g. (k, ω, etc) should be taken into account to reflect the rough nature of the sediment bed.

Currently, there are four different ways to impose rough boundary conditions available in *sedExnerFoam*. These are the two formulations proposed by Wilcox et al. [1998] - the initial formulation and the latter modification - as well as the formulations proposed by Knopp et al. [2009] and Lee [2018]. All these methods require a fine near-bed resolution to correctly estimate the bed shear stress. To handle larger computational domains, more robust formulations are needed to accurately model the scour process in areas of interest while maintaining acceptable predictions at the edge of the domain, where a coarser resolution is used.

Lastly, the model has been updated to include a rigid rockbed functionality, enabling the numerical study of lone dunes migrating over a rigid starved bed, as discussed in Chapter 4. The current implementation is imperfect and not mass-conserving for 3D cases. This involves limiting the sediment flux at the edges that define the faces that form part of the sediment bed boundary, depending on the availability of sediments at those faces (or beneath them). The width of the sediment layer above the rigid bottom determines the availability of sediments. This functionality is useful for real-world applications, where situations in which some parts of the domain cannot be eroded are commonplace, and an implementation that satisfies mass conservation for 3D cases should be provided.

Bibliography

Ferdous Ahmed and Nallamuthu Rajaratnam. Flow around bridge piers. *Journal of Hydraulic Engineering*, 124(3):288–300, 1998.

Carlos A Alvarez and Erick M Franklin. Birth of a subaqueous barchan dune. *Physical Review E*, 96(6):062906, 2017.

LO Amoudry, T-J Hsu, and PL-F Liu. Schmidt number and near-bed boundary condition effects on a two-phase dilute sediment transport model. *J. Geophys. Res.: Oceans*, 110 (C9), 2005.

Bruno Andreotti, Philippe Claudin, and Stéphane Douady. Selection of dune shapes and velocities part 1: Dynamics of sand, wind and barchans. *The European Physical Journal B-Condensed Matter and Complex Systems*, 28(3):321–339, 2002a.

Bruno Andreotti, Philippe Claudin, and Stéphane Douady. Selection of dune shapes and velocities part 2: A two-dimensional modelling. *The European Physical Journal B-Condensed Matter and Complex Systems*, 28(3):341–352, 2002b.

David D Apsley and Peter K Stansby. Bed-load sediment transport on large slopes: model formulation and implementation within a rans solver. *Journal of Hydraulic Engineering*, 134(10):1440–1451, 2008.

B Aupoix and PR Spalart. Extensions of the spalart–allmaras turbulence model to account for wall roughness. *International Journal of Heat and Fluid Flow*, 24(4):454–462, 2003.

Christopher James Baker. *Vortex flow around the bases of obstacles*. PhD thesis, Apollo - University of Cambridge Repository, 1979. URL `https://www.repository.cam.ac.uk/handle/1810/244806`.

CJ Baker. The turbulent horseshoe vortex. *Journal of Wind Engineering and Industrial Aerodynamics*, 6(1-2):9–23, 1980.

CJ Baker. The oscillation of horseshoe vortex systems. *Journal of Fluids Engineering*, 113(3):489–495, 09 1991.

Cüneyt Baykal, B Mutlu Sumer, David R Fuhrman, Niels Gjøl Jacobsen, and Jørgen Fredsøe. Numerical investigation of flow and scour around a vertical circular cylinder. *Philos. Trans. R. Soc. London, Ser. A*, 373(2033):20140104, 2015.

Christian Binet-Tarbé de Vauxclairs. Effondrement du pont de la rivière saint-etienne sur l'île de la réunion, 2007.

C Bonamy, J Chauchat, Q Clemencot, E Puig Montellà, A Mathieu, R Chassagne, M Renaud, P Höhn, A Bernard, G Gonçalves, M Skorlic, and I Nikiteas. fluiddyn/fluidfoam: v0.2.9, feb 2025. URL `https://doi.org/10.5281/zenodo.14893673`.

Mary C Bourke. Barchan dune asymmetry: Observations from mars and earth. *Icarus*, 205(1):183–197, 2010.

Mary C Bourke and Andrew S Goudie. Varieties of barchan form in the namib desert and on mars. *Aeolian Research*, 1(1-2):45–54, 2009.

HNC Breusers, G Nicollet, and HW Shen. Local scour around cylindrical piers. *J. Hydraul. Res.*, 15(3):211–252, 1977.

William R Brownlie. *Prediction of flow depth and sediment discharge in open channels.* PhD thesis, California Institute of Technology, 1983.

Benoît Camenen. Settling velocity of sediments at high concentrations. In *Proceedings in Marine Science*, volume 9, pages 211–226. Elsevier, 2008.

Benoît Camenen and Magnus Larson. A general formula for non-cohesive bed load sediment transport. *Estuarine Coastal Shelf Sci.*, 63(1-2):249–260, 2005.

Benjamin Campforts, Charles M Shobe, Philippe Steer, Matthias Vanmaercke, Dimitri Lague, and Jean Braun. Hylands 1.0: a hybrid landscape evolution model to simulate the impact of landslides and landslide-derived sediment on landscape evolution. *Geoscientific Model Development*, 13(9):3863–3886, 2020.

Tuncer Cebeci. *Analysis of turbulent boundary layers*. Elsevier, 2012.

Ismail Celik and Wolfgang Rodi. Modeling suspended sediment transport in nonequilibrium situations. *J. Hydraul. Eng.*, 114(10):1157–1191, 1988.

CFSAEORTEMAUP CEREMA. Analyse de risque des ponts en site affouillable, 2019.

F. CHARRU and E. J. HINCH. Ripple formation on a particle bed sheared by a viscous liquid. part 1. steady flow. *Journal of Fluid Mechanics*, 550:111–121, 2006. doi: 10.1017/S002211200500786X.

François Charru. Selection of the ripple length on a granular bed sheared by a liquid flow. *Phys. Fluids*, 18(12), 2006.

François Charru, Bruno Andreotti, and Philippe Claudin. Sand ripples and dunes. *Annu. Rev. Fluid Mech.*, 45(1):469–493, 2013.

Rémi Chassagne, Cyrille Bonamy, and Julien Chauchat. A frictional–collisional model for bedload transport based on kinetic theory of granular flows: discrete and continuum approaches. *Journal of Fluid Mechanics*, 964:A27, 2023.

Patrick Chassaing. *Turbulence en mécanique des fluides: analyse du phénomène en vue de sa modélisation à l'usage de l'ingénieur*. Cépaduès-éditions, 2000.

Julien Chauchat, Zhen Cheng, Tim Nagel, Cyrille Bonamy, and Tian-Jian Hsu. Sedfoam-2.0: a 3-d two-phase flow numerical model for sediment transport. *Geosci. Model Dev.*, 10(12):4367–4392, 2017.

Zhen Cheng, Tian-Jian Hsu, and Joseph Calantoni. Sedfoam: A multi-dimensional eulerian two-phase model for sediment transport and its application to momentary bed failure. *Coastal Engineering*, 119:32–50, 2017.

Yee-Meng Chiew and Bruce W Melville. Local scour around bridge piers. *J. Hydraul. Res.*, 25(1):15–26, 1987.

Yee-Meng Chiew and Gary Parker. Incipient sediment motion on non-horizontal slopes. *Journal of Hydraulic Research*, 32(5):649–660, 1994.

Haecheon Choi and Parviz Moin. Grid-point requirements for large eddy simulation: Chapman's estimates revisited. *Physics of fluids*, 24(1), 2012.

John Crank and Phyllis Nicolson. A practical method for numerical evaluation of solutions of partial differential equations of the heat-conduction type. In *Mathematical proceedings of the Cambridge philosophical society*, volume 43, pages 50–67. Cambridge University Press, 1947.

Mehdi Pierre Daou, Olivier Bertrand, Eric Blayo, and Antoine Rousseau. Tridimensional model coupling using schwarz methodology—application to a water intake of a hydroelectric plant, 2018.

Koustuv Debnath and Susanta Chaudhuri. Laboratory experiments on local scour around cylinder for clay and clay–sand mixed beds. *Engineering Geology*, 111(1-4):51–61, 2010.

Subhasish Dey and Navneet P Singh. Clear-water scour depth below underwater pipelines. *Journal of Hydro-Environment Research*, 1(2):157–162, 2007.

Zhibao Dong, Guangqiang Qian, Wanyin Luo, Zhengcai Zhang, and Ping Lv. Dune types and their distribution in the kumtagh sand sea, northwestern china. *Zeitschrift für Geomorphologie*, 57(2):207–224, 2013.

Sylvain Courrech Du Pont, David M Rubin, Clément Narteau, Mathieu GA Lapôtre, Mackenzie Day, Philippe Claudin, Ian Livingstone, Matt W Telfer, Jani Radebaugh, Cyril Gadal, et al. Complementary classifications of aeolian dunes based on morphology, dynamics, and fluid mechanics. *Earth-Science Reviews*, 255:104772, 2024.

Orencio Duran Vinent, Bruno Andreotti, Philippe Claudin, and Christian Winter. A unified model of ripples and dunes in water and planetary environments. *Nat. Geosci.*, 12(5):345–350, may 2019. ISSN 1752-0894, 1752-0908. doi: 10.1038/s41561-019-0336-4.

Paul A Durbin. Near-wall turbulence closure modeling without "damping functions". *Theoretical and computational fluid dynamics*, 3(1):1–13, 1991.

Paul A Durbin, G Medic, J-M Seo, JK Eaton, and S Song. Rough wall modification of two-layer k- ε. *Journal of Fluids Engineering*, 123(1):16–21, 2000.

Gianmarco D'Alessandro, Cristian Marchioli, and Ugo Piomelli. Large-eddy simulation

of the flow over a realistic riverine geometry. *Journal of Fluid Mechanics*, 1010:A35, 2025.

David L Egholm, Vivi K Pedersen, Mads F Knudsen, and Nicolaj K Larsen. Coupling the flow of ice, water, and sediment in a glacial landscape evolution model. *Geomorphology*, 141:47–66, 2012.

Hans Albert Einstein. Formulas for the transportation of bed load. *Transactions of the American Society of civil Engineers*, 107(1):561–577, 1942.

Hans Albert Einstein. *The bed-load function for sediment transportation in open channel flows*, volume 1026. US Government Printing Office, 1950.

Frank Engelund. Hydraulic resistance of alluvial streams. *Journal of the Hydraulics Division*, 92(2):315–326, 1966.

Frank Engelund and Jørgen Fredsøe. A sediment transport model for straight alluvial channels. *Hydrol. Res.*, 7(5):293–306, 1976.

Felix M Exner. *Zur physik der dünen*. Hölder, 1920.

Hong-Wei Fang and Wolfgang Rodi. Three-dimensional calculations of flow and suspended sediment transport in the neighborhood of the dam for the three gorges project (tgp) reservoir in the yangtze river. *J. Hydraul. Res.*, 41(4):379–394, 2003.

Jorgen Fredsoe and Rolf Deigaard. *Mechanics of coastal sediment transport*, volume 3. World scientific publishing company, 1992.

Jorgen Fredsoe and B Mutlu Sumer. *The mechanics of scour in the marine environment*, volume 17. World Scientific Publishing Company, 2002.

David R Fuhrman, Martin Dixen, and Niels Gjøl Jacobsen. Physically-consistent wall boundary conditions for the k-ω turbulence model. *Journal of Hydraulic Research*, 48 (6):793–800, 2010.

Cyril Gadal, Clément Narteau, Sylvain Courrech Du Pont, Olivier Rozier, and Philippe Claudin. Incipient bedforms in a bidirectional wind regime. *Journal of Fluid Mechanics*, 862:490–516, 2019.

Cyril Gadal, Matthieu J Mercier, Marie Rastello, and Laurent Lacaze. Slumping regime in lock-release turbidity currents. *Journal of Fluid Mechanics*, 974:A4, 2023.

Michael M Gibson and Adil A Dafa'Alla. Two-equation model for turbulent wall flow. *AIAA journal*, 33(8):1514–1518, 1995.

Alban Gilletta, Cyrille Bonamy, Marie Robert, and Julien Chauchat. Assessment of hybrid rans/les models for the prediction of the flow and scour around a wall-mounted cylinder. *Advances in Water Resources*, 199:104934, 2025.

Andrew S Goudie. Global barchans: A distributional analysis. *Aeolian Research*, 44: 100591, 2020.

Willi H Hager. Du boys and sediment transport. *Journal of Hydraulic Research*, 43(3): 227–233, 2005.

Robert L Haney. On the pressure gradient force over steep topography in sigma coordinate ocean models. *Journal of physical Oceanography*, 21(4):610–619, 1991.

Antti Hellsten, Seppo Laine, Antti Hellsten, and Seppo Laine. Extension of the k-omega-sst turbulence model for flows over rough surfaces. In *22nd atmospheric flight mechanics conference*, page 3577, 1997.

Allen T Hjelmfelt and Charles W Lenau. Nonequilibrium transport of suspended sediment. *Journal of the Hydraulics Division*, 96(7):1567–1586, 1970.

Raad I Issa. Solution of the implicitly discretised fluid flow equations by operator-splitting. *J. Comput. Phys.*, 62(1):40–65, 1986.

Niels Gjøl Jacobsen. *A full hydro-and morphodynamic description of breaker bar development*. PhD thesis, DTU mechanical engineering, 2011.

Niels Gjøl Jacobsen. Mass conservation in computational morphodynamics: uniform sediment and infinite availability. *Int. J. Numer. Methods Fluids*, 78(4):233–256, jun 2015. ISSN 0271-2091, 1097-0363. doi: 10.1002/fld.4015. URL `https://onlinelibrary.wiley.com/doi/10.1002/fld.4015`.

Hrvoje Jasak and Zeljko Tukovic. Automatic mesh motion for the unstructured finite volume method. *Trans. FAMENA*, 30(2):1–20, 2006.

Hrvoje Jasak, HG Weller, and AD Gosman. High resolution nvd differencing scheme for arbitrarily unstructured meshes. *Int J Numer Meth Fl*, 31(2):431–449, 1999.

Hrvoje Jasak, Aleksandar Jemcov, Zeljko Tukovic, et al. Openfoam: A c++ library for complex physics simulations. In *International workshop on coupled methods in numerical dynamics*, volume 1000, pages 1–20. Dubrovnik, (Croatia), 2007.

James T Jenkins and Diego Berzi. Dense inclined flows of inelastic spheres: tests of an extension of kinetic theory. *Granular Matter*, 12(2):151–158, 2010.

Hakeem K Johnson and Julio A Zyserman. Controlling spatial oscillations in bed level update schemes. *Coastal Engineering*, 46(2):109–126, 2002.

Pierre Jop, Yoël Forterre, and Olivier Pouliquen. A constitutive law for dense granular flows. *Nature*, 441(7094):727–730, 2006.

Mohammadreza Kadivar, David Tormey, and Gerard McGranaghan. A review on turbulent flow over rough surfaces: Fundamentals and theories. *International Journal of Thermofluids*, 10:100077, 2021.

IG Kantardgi. Incipiency of sediment motion under combined waves and currents. *Journal of coastal research*, pages 332–339, 1992.

Takao Kawamura, Munehiko Hiwada, Toshiharu Hibino, Ikuo Mabuchi, and Masaya Kumada. Flow around a finite circular cylinder on a flat plate: Cylinder height greater than turbulent boundary layer thickness. *Bulletin of JSME*, 27(232):2142–2151, 1984.

Aman G Kidanemariam and Markus Uhlmann. Formation of sediment patterns in chan-

nel flow: minimal unstable systems and their temporal evolution. *Journal of Fluid Mechanics*, 818:716–743, 2017.

Serge Kiki Sandoungout. *Caractérisation de la morphologie des dunes dans des écoulements unidirectionnels et alternatifs*. PhD thesis, Université de Bretagne occidentale - Brest, September 2019. URL `https://theses.hal.science/tel-02453140`.

Gokhan Kirkil and George Constantinescu. Flow and turbulence structure around an instream rectangular cylinder with scour hole. *Water Resources Research*, 46(11), 2010.

Tobias Knopp, Bernhard Eisfeld, and Javier Bartolome Calvo. A new extension for k–ω turbulence models to account for wall roughness. *International Journal of Heat and Fluid Flow*, 30(1):54–65, 2009.

Andrej Nikolaevich Kolmogorov. Equations of turbulent motion in an incompressible fluid. In *Dokl. Akad. Nauk SSSR*, volume 30, pages 299–303, 1941a.

Andrey Nikolaevich Kolmogorov. The local structure of turbulence in incompressible viscous fluid for very large reynolds. *Numbers. In Dokl. Akad. Nauk SSSR*, 30:301, 1941b.

Kouamé Kan Jacques Kouakou and Pierre-Yves Lagrée. Evolution of a model dune in a shear flow. *European Journal of Mechanics-B/Fluids*, 25(3):348–359, 2006.

George J Kynch. A theory of sedimentation. *Transactions of the Faraday society*, 48: 166–176, 1952.

Yong G Lai, Larry J Weber, and Virendra C Patel. Nonhydrostatic three-dimensional model for hydraulic flow simulation. i: Formulation and verification. *Journal of Hydraulic Engineering*, 129(3):196–205, 2003.

Yong G Lai, Xiaofeng Liu, Fabián A Bombardelli, and Yalan Song. Three-dimensional numerical modeling of local scour: A state-of-the-art review and perspective. *Journal of Hydraulic Engineering*, 148(11):03122002, 2022.

Robin B Langtry and Florian R Menter. Correlation-based transition modeling for unstructured parallelized computational fluid dynamics codes. *AIAA journal*, 47(12): 2894–2906, 2009.

Brian Edward Launder and Dudley Brian Spalding. The numerical computation of turbulent flows. In *Numerical prediction of flow, heat transfer, turbulence and combustion*, pages 96–116. Elsevier, 1983.

DR Laurence, JC Uribe, and SV Utyuzhnikov. A robust formulation of the v2- f model. *Flow, Turbulence and Combustion*, 73(3):169–185, 2005.

Cheng-Hsien Lee. Rough boundary treatment method for the shear-stress transport k-ω model. *Engineering Applications of Computational Fluid Mechanics*, 12(1):261–269, 2018.

Giles R Lesser, JA v Roelvink, JA Th M van Kester, and GS Stelling. Development and

validation of a three-dimensional morphological model. *Coastal Eng.*, 51(8-9):883–915, 2004.

Dongfang Liang, Liang Cheng, and Fangjun Li. Numerical modeling of flow and scour below a pipeline in currents: Part ii. scour simulation. *Coastal engineering*, 52(1):43–62, 2005.

F-S Lien and MA Leschziner. A pressure-velocity solution strategy for compressible flow and its application to shock/boundary-layer interaction using second-moment turbulence closure. *Journal of fluids engineering*, 115(4):717–725, 1993.

Phillip M Ligrani and Robert J Moffat. Structure of transitionally rough and fully rough turbulent boundary layers. *Journal of Fluid Mechanics*, 162:69–98, 1986.

Xiaofeng Liu and Marcelo H García. Three-dimensional numerical model with free water surface and mesh deformation for local sediment scour. *J. Waterw. Port. Coast.*, 134 (4):203–217, 2008.

DA Lyn. A similarity approach to turbulent sediment-laden flows in open channels. *J. Fluid Mech.*, 193:1–26, 1988.

Ye Mao. The interaction between a pipeline and an erodible bed. *Series Paper Technical University of Denmark*, (39), 1987.

Vincent Marieu, Philippe Bonneton, Diane L. Foster, and Fabrice Ardhuin. Modeling of vortex ripple morphodynamics. *J. Geophys. Res.*, 113(C9):2007JC004659, sep 2008. ISSN 0148-0227. doi: 10.1029/2007JC004659. URL `https://agupubs.onlinelibrary.wiley.com/doi/10.1029/2007JC004659`.

Marco Mazzuoli and Laurent Lacaze. *Physics of Granular Suspensions*. Springer, 2024.

F. R. Menter. Two-equation eddy-viscosity turbulence models for engineering applications. *AIAA J.*, 32(8):1598–1605, aug 1994. ISSN 0001-1452, 1533-385X. doi: 10.2514/3.12149. URL `https://arc.aiaa.org/doi/10.2514/3.12149`.

Florianr Menter. Zonal two equation kw turbulence models for aerodynamic flows. In *23rd fluid dynamics, plasmadynamics, and lasers conference*, page 2906, 1993.

Eugen Meyer-Peter and Robert Müller. Formulas for bed-load transport. In *IAHSR 2nd meeting, Stockholm, appendix 2*. IAHR, 1948.

SA Miedema. An analytical method to determine scour. *WEDA XXVIII & Texas A&M*, 39(1):8–11, 2008.

MC Miller, IN McCave, and P_D Komar. Threshold of sediment motion under unidirectional currents. *Sedimentology*, 24(4):507–527, 1977.

Gaurav Misuriya and TI Eldho. Turbulent structures and local scour around a cylindrical pier under unsteady flows. *Environmental Fluid Mechanics*, 23(6):1359–1380, 2023.

M Muste, K Yu, I Fujita, and R Ettema. Two-phase versus mixed-flow perspective on suspended sediment transport in turbulent channel flows. *Water Resour. Res.*, 41(10), 2005.

Tim Nagel, Julien Chauchat, Cyrille Bonamy, Xiaofeng Liu, Zhen Cheng, and Tian-Jian Hsu. Three-dimensional scour simulations with a two-phase flow model. *Adv. Water Resour.*, 138:103544, 2020.

CR Neill. Mean-velocity criterion for scour of coarse uniform bed-material. 1967.

Peter Nielsen. *Coastal bottom boundary layers and sediment transport*, volume 4. World scientific, 1992.

Johann Nikuradse. Stromungsgesetze in rauhen rohren. *vdi-forschungsheft*, 361:1, 1933.

Thomas Pähtz, Eric J. R. Parteli, Jasper F. Kok, and Hans J. Herrmann. Analytical model for flux saturation in sediment transport. *Phys. Rev. E*, 89:052213, May 2014. doi: 10.1103/PhysRevE.89.052213. URL `https://link.aps.org/doi/10.1103/PhysRevE.89.052213`.

AS Paintal. A stochastic model of bed load transport. *Journal of Hydraulic Research*, 9 (4):527–554, 1971.

Chris Paola and Vaughan R Voller. A generalized exner equation for sediment mass balance. *J. Geophys. Res.: Earth Surf.*, 110(F4), 2005.

Gary Parker. Surface-based bedload transport relation for gravel rivers. *Journal of hydraulic research*, 28(4):417–436, 1990.

Gary Parker and Peter C Klingeman. On why gravel bed streams are paved. *Water Resources Research*, 18(5):1409–1423, 1982.

Suhas V Patankar and D Brian Spalding. A calculation procedure for heat, mass and momentum transfer in three-dimensional parabolic flows. In *Numerical prediction of flow, heat transfer, turbulence and combustion*, pages 54–73. Elsevier, 1983.

V. C. Patel. Calibration of the preston tube and limitations on its use in pressure gradients. *Journal of Fluid Mechanics*, 23(1):185–208, 1965. doi: 10.1017/S0022112065001301.

Damien Pham Van Bang, Emmanuel Lefrancois, Philippe Sergent, and Francois Bertrand. Mri experimental and finite elements modeling of the sedimentation-consolidation of mud. *HOUILLE BLANCHE-REVUE INTERNATIONALE DE L EAU*, (3):39–44, 2008.

Ludwig Prandtl. 7. bericht über untersuchungen zur ausgebildeten turbulenz. *ZAMM-Journal of Applied Mathematics and Mechanics/Zeitschrift für Angewandte Mathematik und Mechanik*, 5(2):136–139, 1925.

Luke J Prendergast and Kenneth Gavin. A review of bridge scour monitoring techniques. *Journal of Rock Mechanics and Geotechnical Engineering*, 6(2):138–149, 2014.

J Radebaugh, R Lorenz, T Farr, Philippe Paillou, C Savage, and C Spencer. Linear dunes on titan and earth: Initial remote sensing comparisons. *Geomorphology*, 121 (1-2):122–132, 2010.

A Recking. A comparison between flume and field bed load transport data and conse-

quences for surface-based bed load transport prediction. *Water Resour. Res.*, 46(3), 2010.

Hans Reichardt. Vollständige darstellung der turbulenten geschwindigkeitsverteilung in glatten leitungen. *ZAMM-Journal of Applied Mathematics and Mechanics/Zeitschrift für Angewandte Mathematik und Mechanik*, 31(7):208–219, 1951.

M. Renaud, O. Bertrand, C. Bonamy, and J. Chauchat. sedexnerfoam 2412: A 3d exner-based sediment transport and morphodynamics model. *EGUsphere*, 2025:1–36, 2025. doi: 10.5194/egusphere-2025-2375. URL `https://egusphere.copernicus.org/preprints/2025/egusphere-2025-2375/`.

Osborne Reynolds. Xxix. an experimental investigation of the circumstances which determine whether the motion of water shall be direct or sinuous, and of the law of resistance in parallel channels. *Philosophical Transactions of the Royal society of London*, (174): 935–982, 1883.

Osborne Reynolds. Iv. on the dynamical theory of incompressible viscous fluids and the determination of the criterion. *Philosophical transactions of the royal society of london.(a.)*, (186):123–164, 1895.

Jan S Ribberink. Bed-load transport for steady flows and unsteady oscillatory flows. *Coastal Engineering*, 34(1-2):59–82, 1998.

Everett V Richardson, Stanley R Davis, et al. Evaluating scour at bridges. Technical report, United States. Federal Highway Administration. Office of Bridge Technology, 2001.

JF Richardson and WN Zaki. The sedimentation of a suspension of uniform spheres under conditions of viscous flow. *Chem. Eng. Sci.*, 3(2):65–73, 1954.

Anatol Roshko. Experiments on the flow past a circular cylinder at very high reynolds number. *Journal of fluid mechanics*, 10(3):345–356, 1961.

Andreas Roulund, B Mutlu Sumer, Jørgen Fredsøe, and Jess Michelsen. Numerical and experimental investigation of flow and scour around a circular pile. *J. Fluid Mech.*, 534: 351–401, 2005.

WW Rubey. Equilibrium-conditions in debris-laden streams. *Eos, Transactions American Geophysical Union*, 14(1):497–505, 1933.

Philip Geoffrey Saffman. A model for inhomogeneous turbulent flow. *Proceedings of the Royal Society of London. A. Mathematical and Physical Sciences*, 317(1530):417–433, 1970.

Ahmed MA Sattar, Hrvoje Jasak, and Vanja Skuric. Three dimensional modeling of free surface flow and sediment transport with bed deformation using automatic mesh motion. *Environ. Modell. Software*, 97:303–317, 2017.

Günter Schewe. On the force fluctuations acting on a circular cylinder in crossflow from subcritical up to transcritical reynolds numbers. *Journal of fluid mechanics*, 133:265–285, 1983.

Hermann Schlichting and Joseph Kestin. *Boundary layer theory*, volume 121. Springer, 1961.

R Schwind. The three-dimensional boundary layer near a strut. *Gas Turbine Lab. Rep.*, 1962.

Haoran Shi, Maria-Eletta Negretti, Julien Chauchat, K Blanckaert, U Lemmin, and DA Barry. Unconfined plunging of a hyperpycnal river plume over a sloping bed and its lateral spreading: Laboratory experiments and numerical modeling. *Water Resources Research*, 58(8):e2022WR032633, 2022.

Albert Frank Shields. *Anwendung der Ähnlichkeitsmechanik und der Turbulenzforschung auf die Geschiebebewegung*. PhD thesis, 1936.

Tsan-Hsing Shih, William W Liou, Aamir Shabbir, Zhigang Yang, and Jiang Zhu. A new $k-\epsilon$ eddy viscosity model for high reynolds number turbulent flows. *Computers & fluids*, 24(3):227–238, 1995.

J Dungan Smith and SR McLean. Spatially averaged flow over a wavy surface. *Journal of Geophysical research*, 82(12):1735–1746, 1977.

Yalan Song, Yuncheng Xu, Hassan Ismail, and Xiaofeng Liu. Scour modeling based on immersed boundary method: A pathway to practical use of three-dimensional scour models. *Coastal Eng.*, 171:104037, 2022.

Richard Soulsby and Whitehouse. *Threshold of Sediment Motion in Coastal Environments*, volume 1. Centre for Advanced Engineering, University of Canterbury, Christchurch, N.Z.: Centre for Advanced Engineering, CEA, 1997. ISBN 978-0-908993-15-4. Meeting Name: Australasian Coastal and Ocean Engineering Conference.

Philippe Spalart and Steven Allmaras. A one-equation turbulence model for aerodynamic flows. In *30th aerospace sciences meeting and exhibit*, page 439, 1992.

Dudley B Spalding et al. A single formula for the law of the wall. *Journal of Applied mechanics*, 28(3):455–458, 1961.

Arne Stahlmann. Numerical and experimental modeling of scour at foundation structures for offshore wind turbines. In *ISOPE International Ocean and Polar Engineering Conference*, pages ISOPE–I. ISOPE, 2013.

George Gabriel Stokes. *Mathematical and physical papers*, volume 3. Cambridge University Press, 1901.

B Mutiu Sumer and Jørgen Fredsøe. Scour below pipelines in waves. *Journal of waterway, port, coastal, and ocean engineering*, 116(3):307–323, 1990.

B Mutlu Sumer et al. *Hydrodynamics around cylindrical strucures*, volume 26. World scientific, 2006.

Rui Sun and Heng Xiao. Sedifoam: A general-purpose, open-source cfd–dem solver for particle-laden flow with emphasis on sediment transport. *Computers & Geosciences*, 89:207–219, 2016.

Prabhata K Swamee and Akalank K Jain. Explicit equations for pipe-flow problems. *Journal of the hydraulics division*, 102(5):657–664, 1976.

Pablo Tassi, Thomas Benson, Matthieu Delinares, Jacques Fontaine, Nicolas Huybrechts, Rebekka Kopmann, Sara Pavan, Chi-Tuan Pham, Florent Taccone, and Régis Walther. Gaia-a unified framework for sediment transport and bed evolution in rivers, coastal seas and transitional waters in the telemac-mascaret modelling system. *Environmental Modelling & Software*, 159:105544, 2023.

Brian J Todd. Morphology and composition of submarine barchan dunes on the scotian shelf, canadian atlantic margin. *Geomorphology*, 67(3-4):487–500, 2005.

Gregory E Tucker and Gregory R Hancock. Modelling landscape evolution. *Earth Surface Processes and Landforms*, 35(1):28–50, 2010.

Zeljko Tukovic and Hrvoje Jasak. Simulation of free-rising bubble with soluble surfactant using moving mesh finite volume/area method. In *Proceedings of 6th International Conference on CFD in Oil & Gas, Metallurgical and Process Industries, no. CFD08-072*, 2008.

Tessa Uroić, Hrvoje Jasak, and Henrik Rusche. Implicitly coupled pressure–velocity solver. In *OpenFOAM®: Selected Papers of the 11th Workshop*, pages 249–267. Springer, 2019.

WM van der Sande, PC Roos, T Gerkema, and SJMH Hulscher. Nonlinear modeling of river dunes: Insights in long-term evolution of dune dimensions and form roughness. *Geomorphology*, page 109649, 2025.

Milton Van Dyke. An album of fluid motion. *NASA STI/Recon Technical Report A*, 82: 36549, 1982.

Leo C van Rijn. Sediment transport, part i: bed load transport. *J. Hydraul. Eng.*, 110 (10):1431–1456, 1984a.

Leo C. van Rijn. Sediment transport, part ii: Suspended load transport. *J. Hydraul. Eng.*, 110(11):1613–1641, nov 1984b. ISSN 0733-9429, 1943-7900. doi: 10.1061/(ASCE) 0733-9429(1984)110:11(1613).

Leo C van Rijn. *Principles of sedimentation and erosion engineering in rivers, estuaries and coastal seas including mathematical modelling package (toolkit on CD-ROM)*. 2005.

Vito A Vanoni. Measurements of critical shear stress for entraining fine sediments in a boundary layer. 1964.

Nathalie M Vriend and Karol A Bacik. The dynamics of sand dunes. *Annual Review of Fluid Mechanics*, 58, 2025.

D. Keith Walters and Davor Cokljat. A three-equation eddy-viscosity model for reynolds-averaged navier-stokes simulations of transitional flow. *Journal of Fluids Engineering*, 130(12):121401, 10 2008.

Kumalasari Wardhana and Fabian C Hadipriono. Analysis of recent bridge failures in the united states. *J. Perform. Constr. Facil.*, 17(3):144–150, 2003.

John C Warner, Christopher R Sherwood, Richard P Signell, Courtney K Harris, and Hernan G Arango. Development of a three-dimensional, regional, coupled wave, current, and sediment-transport model. *Comput. Geosci.*, 34(10):1284–1306, 2008.

Peter R Wilcock and Joanna C Crowe. Surface-based transport model for mixed-size sediment. *Journal of hydraulic engineering*, 129(2):120–128, 2003.

David C Wilcox et al. *Turbulence modeling for CFD*, volume 2. DCW industries La Canada, CA, 1998.

Charles HK Williamson. Oblique and parallel modes of vortex shedding in the wake of a circular cylinder at low reynolds numbers. *Journal of Fluid Mechanics*, 206:579–627, 1989.

Russell B Wynn, Douglas G Masson, and Brian J Bett. Hydrodynamic significance of variable ripple morphology across deep-water barchan dunes in the faroe–shetland channel. *Marine Geology*, 192(1-3):309–319, 2002.

Anqi Xie, Xuguang Chen, Xixi Liu, Kehu Li, Su Chen, and Fengpeng Zhang. New methods for the scour protection around the pile foundation based on oyster reef cover. *Ocean Engineering*, 335:121682, 2025.

Conghao Xu and Zhenhua Huang. A laboratory study of wave-induced local scour at an emergent pile breakwater. *Ocean Engineering*, 270:113618, 2023.

Jin Xu, Jihong Xia, Lingling Wang, Eldad J Avital, Hai Zhu, and Yin Wang. An improved eulerian method in three-dimensional direct numerical simulation on the local scour around a cylinder. *Applied Mathematical Modelling*, 110:320–337, 2022.

VSASTBCG Yakhot, Steven A Orszag, Siva Thangam, TB Gatski, and CG1167781 Speziale. Development of turbulence models for shear flows by a double expansion technique. *Physics of Fluids A: Fluid Dynamics*, 4(7):1510–1520, 1992.

Mehmet Selim Yalin and Emin Karahan. Inception of sediment transport. *Journal of the hydraulics division*, 105(11):1433–1443, 1979.

UCE Zanke. On the influence of turbulence on the initiation of sediment motion. *Int. J. Sediment Res.*, 18(1):17–31, 2003.

Ming Zhao, Liang Cheng, and Zhipeng Zang. Experimental and numerical investigation of local scour around a submerged vertical circular cylinder in steady currents. *Coastal Engineering*, 57(8):709–721, 2010.

Zhenjiang Zhao, Ling Zhou, Ling Bai, Bo Wang, and Ramesh Agarwal. Recent advances and perspectives of cfd–dem simulation in fluidized bed. *Archives of Computational Methods in Engineering*, 31(2):871–918, 2024.

Lu Zhou. *Numerical modelling of scour in steady flows*. PhD thesis, Université de Lyon, 2017. URL `http://www.theses.fr/2017LYSEC015/document`.